

*École Doctorale Mathématiques, Sciences de l'information et de l'ingénieur
(MSII)*

THÈSE présentée par :
Azhar Ali Ayaz Pirzado

Soutenue le: 12 juin 2015

pour obtenir le grade de : **Docteur de l'Université de Strasbourg**

Discipline: **Sciences of engineering**

Spécialité: **Microelectronics and Photonics**

**Integration of Few Layer Graphene
Nanomaterials in Organic Solar Cells as
(Transparent) Conductor Electrodes**

DIRECTEUR DE THÈSE:

M. François Le Normand

Dr. Hab., ICube, CNRS-Université de Strasbourg

CO-ENCADRANTE:

Mme Izabela Janowska

Dr., ICPEES, CNRS-Université de Strasbourg

RAPPORTEURS:

M. Costel Sorin COJOCARU

Dr., LPICM, CNRS-École Polytechnique

Mme Brigitte VIGOLO-GREFFIER

Dr., Institut Jean Lamour, CNRS-Université de Lorraine

EXAMINATEURS:

M. Philippe TUREK

Professeur, Institut de Chimie, Université de Strasbourg

M. Alain CELZARD

Professeur, ENSTIB, Université de Lorraine

The idea is to try to give all the information to help others to judge the value of your contribution; not just the information that leads to judgment in one particular direction or another.

Richard P. Feynman



To

My parents,

- for unconditional love, support and providing with innumerable opportunities

....Wife, Family members

- for their inspiration, support, laughter and joy

Contents

List of Variables and Abbreviations	1
1 Introduction: Transparent Conductor Materials/Electrodes for Organic Solar Cells	8
1.1 Criteria for Choosing TCEs	10
1.2 Role of Electrodes in Organic Solar Cells	14
1.3 Carbon-based TCEs/TCMs for OSCs	14
1.3.1 Characterizations of Graphene and Graphene Films	21
1.3.2 Graphene Production Methods	26
1.3.2.1 Micro-mechanical cleavage/ Mechanical ablation/Ball-milling	28
1.3.2.2 Liquid-phase exfoliation (LPE)	28
1.3.2.3 Graphene Oxide	29
1.3.2.4 Bottom-up Approaches and Growth on Substrates	31
1.3.3 Charge Transport in Graphene and in FLG	32
1.3.4 Charge Transport in Carbon Nano Tubes (CNTs)	38
1.3.5 Charge Transport in graphene/FLG films	41
1.4 Introduction to Organic Solar Cells	44
1.4.1 Types and Architectures of Organic Solar Cells	47
1.4.1.1 Equivalent Circuit for a p-n Junction Solar Cell .	49
1.4.2 Organic Solar Cell Mechanism	51
1.4.2.1 Photon Absorption	51
1.4.2.2 Exciton diffusion and charge separation	52
1.4.2.3 Charge Transport	53
1.4.2.4 Charge Collection	53
1.4.3 Characterization of Organic Solar Cells	55

1.5	Performance and Properties of Graphene TCEs	58
1.5.0.1	Carbon Nanotubes and their Hybrids	65
1.6	Aim of Thesis	68
1.7	Organization of Thesis	68
2	Experimental: Materials and Techniques	70
2.1	Materials	70
2.2	Methods and Techniques Used for Preparations of Materials . . .	73
2.2.1	Few Layer Graphene Synthesis by Mechanical Ablation . .	74
2.2.1.1	Few Layer Graphene Synthesis by Mechanical Ab- lation of Pencil Lead	74
2.2.1.2	Homogenization and Crystallization of Few Layer Graphene by μ -waves-assisted Oxidation in Water Oxidation in Water	75
2.2.1.3	Few Layer Graphene Synthesis by Mechanical Ab- lation of Synthetic Graphite	76
2.2.2	Microwave-assisted Liquid Phase Exfoliation of FLG and Reduced Graphene Oxide (rGO)	76
2.2.2.1	Few layer Graphene by Microwave-assisted Liquid Phase Exfoliation (LPE) of Expanded Graphite in Toluene	77
2.2.2.2	Reduced GO from Graphene Oxide (GO) and Expanded Graphite (EG) Composite in Ethylene Glycol	78
2.2.3	CNTs dispersion	80
2.3	Film Formation for charge transport devices by Hot-spray Method	81
2.3.1	Electrodes Deposition by Thermal Evaporation	81
2.4	Solar Cell Preparation	82
2.5	Characterizations Techniques	84

2.5.1	Electrical Characterizations for Charge Transport Measurements by Two Probes, Four-Point Probes (FPP) and Hall Effect (HE)	84
2.5.1.1	Two Probes for Electrical Resistance Measurements	85
2.5.1.2	Four-Point Probes (FPPs) for R_s Measurements .	86
2.5.1.3	Hall Effect Measurement System for Mobility, Resistivity and Charge Carrier Concentrations Measurements	87
2.5.1.3.1	Basic Measurements:	90
2.5.2	Scanning Electron Microscopy (SEM)	91
2.5.3	Transmission Electron Microscopy (TEM)	93
2.5.4	Spectrophotometry: UV-Vis spectroscopy	95
2.5.5	Photoelectron Spectroscopy (PES)	96
2.5.5.1	X-Ray Photoelectron Spectroscopy (XPS) Analysis	99
2.5.5.2	Ultraviolet Photoemission Spectroscopy (UPS) .	101
2.5.6	Photoluminescence spectroscopy (PL)	102
2.5.7	Raman Spectroscopy	103
2.5.8	Thermogravimetric Analysis (TGA)	104
2.5.9	Temperature-programmed desorption coupled with mass spectrometry (TPD-MS)	105
2.5.10	Profilometer	105
2.5.10.1	Arithmetic average roughness, R_a	106
2.5.10.2	Geometric Average Roughness, R_q	106
2.5.11	Atomic Force Microscope (AFM)	107
2.5.12	Nuclear reaction analysis (NRA)	109
3	Results: Few Layer Graphene	112
3.1	Few Layer Graphene by Ablation of Pencil Lead (FLG-Abl) . . .	112

3.1.1	Summary of the article: Electrical Transport in "Few-Layer Graphene" Film Prepared by the Hot-Spray Technique: The Effect of Thermal Treatment	113
3.1.2	Article: Charge Transport in FLG Films Prepared by Hot-spray Method: Effect of Thermal Annealing, with Supporting Information	116
3.1.3	FLG Charge Transport Device Mobility, Resistivity and Carrier Concentration in FLG Film Studied by Hall Effect	128
3.1.4	FLG Charge Transport Device Studied by Four-Point Probes (FPPs): Sheet Resistance	131
3.2	Charge Transport in FLG by Mechanical Exfoliation of Synthetic Graphite (HOPG)	139
3.3	Homogenization and Crystallization of Few Layer Graphene by μ -waves-assisted Oxidation in Water	144
3.4	Roughness and Thickness Determination	146
3.4.1	Surface Profile for Roughness by Profilometer	146
3.4.2	Surface Profile for Roughness by AFM	147
3.4.3	Thickness by NRA	151
3.5	Determination of Work Function	154
3.6	Percolation in FLG-Abl	158
3.7	FLG by Microwave-assisted Liquid Phase Exfoliation (LPE) of Expanded Graphite in Toluene (FLG- μ w)	159
3.7.1	Preparation and Characterizations of FLG- μ -w	159
3.7.2	Charge transport in FLG-MW	163
3.8	Conclusion	167
4	Results: Reduced Graphene Oxide (rGO) and rGO/FLG Composite	169

4.1	Preparation of rGO and rGO/FLG Composite Materials/Charge Transport Devices	169
4.2	Characterizations	171
4.2.1	Charge Transport in rGO and rGO/FLG	171
4.2.2	Morphology and Roughness	175
4.2.3	Work-function Determination	178
4.3	Percolation threshold in rGO and rGO/FLG	182
4.4	Conclusion	183
5	Results: Carbon Nanotubes/Few Layer Graphene Hybrids	184
5.1	Preparations of CNTs/FLG Hybrid Films/Devices	185
5.2	Characterizations of CNTs/FLG-HOPG devices	186
5.2.1	Charge transport in CNTs/FLG-HOPG Hybrids	186
5.2.2	Morphology and Roughness Profiles of CNTs/FLG-HOPG Hybrids	191
5.3	Charge transport in CNTs/rGO	193
5.3.1	Morphology and Roughness of CNTs/rGO Hybrids	196
5.4	Work-function of CNTs	198
5.5	Conclusion	199
6	Results: Organic Solar Cells based on Carbon TCEs	200
6.1	Conclusion	204
7	Concluding Discussion and Perspectives	205
7.1	Concluding Discussion	205
7.2	Perspectives	212
7.2.1	Materials	212
7.2.2	Automated Mobile Air-gun for Hot-spray	213
7.2.3	Polishing/Etching to Smoothen the Surface of Films	213
7.2.4	Polymer as Smoothing Agent	213

7.2.5	Volume-thickness Study	213
7.2.6	Optimization of FLG Obtained by Exfoliation of Expanded Graphite in Toluene via Microwave Irradiation and Use of Large Diameter Spray-nozzle	214
7.2.7	FLG as Counter Electrode for OSCs	214
7.2.8	rGO as Buffer Layer	214
8	Appendix	256
8.1	ITO and Related TCOs	256
8.2	Other Candidates for TCEs	261
8.3	Bottom Up Techniques: Epitaxial Growth, CVD and Chemical Synthesis	268
8.3.1	Epitaxial Growth	268
8.3.2	Chemical Vapor Deposition and Transfer	268
8.3.3	Chemical Synthesis	270
8.4	Charge Transport in Organic Semiconductors	271
8.5	Four-point Probes manual for calculation of geometrical factor . .	273

List of Variables and Abbreviations

A	Absorption/Acceptor/Anode
Abl	Ablation
α	Visible Absorption coefficient
A/D	Acceptor/Donor
AFM	Atomic Force Microscope
Å	Angstrom
Ag	Silver
AgNW	Silver Nanowires
Al	Aluminum
Al ₂ O ₃	Aluminum oxide
AM	Air Mass
A-GNRs	Armchair Graphene Nanoribbons
ATO	Sb-doped ITO
Au	Gold
AZO	Aluminum-doped ZnO
BCP	Bathocuproine
BHJ	Bulk heterojunction
BLG	Bi layer Graphene
C	Centigrade/Cathode/Carbon
c	concentration
Ca	Calcium
c.a.	circa (around, about)
cm	centimeter
CNTs	Carbon Nanotubes
Cr	Chromium
CTCEs	Carbon-based Transparent Conductor Electrodes

CTCFs	Carbon-based Transparent Conductor Films
CuPc	Copper Phthalocyanine
CVD	Chemical Vapor Deposition
CVD-G	Chemical Vapor Deposition Graphene
D	Donor
d	pathway/thickness of film/sheet
D/A	Donor/Acceptor
σ_{DC}	DC Conductivity
DC	Direct Current
DSSCs	Dye-sensitized solar cells
DMF	N,N-dimethylformamide
DWNTs	Double Wall Nanotubes
EBL	Electron Blocking Layer
EFM	Electrostatic force microscope/Microscopy
EG	Expanded Graphite
E_g	Energy gap
e	elementary charge (electron)
e.g.	exempli gratia (for example)
ε	Epsilon (the absorption coefficient)
ε^* c)	Epsilon (the absorption coefficient of graphene)
EQE	External Quantum Efficiency
ETL	Electron Transport Layer
eV	Electron Volt
FET	Field-effect transistor
F	Fluorine
FF	Fill Factor
FLG	Few Layer Graphene
FTO	Fluorine-doped Tin Oxide

FWHM	Full width half minimum
GME	Graphene mesh electrode
GO	Graphene Oxide
G_o	Conductance quantum
GPa	Giga pascal
GFeTCs	Graphene-ferroelectric transparent conductor electrodes
GraHEL	Graphene Hole Extraction Layer
GTCEs	Graphene-based Transparent Conductor Electrodes
GTCFs	Graphene-based Transparent Conductor Films
GZO	Gallium-doped Zinc Oxide
HEL	Hole Extraction Layer
H ₂ O	Dihydrogen Monoxide (Water)
HOMO	Highest occupied molecular orbital
HOPG	Highly Ordered Pyrolytic graphite
HTL	Hole Transport Layer
I	Current (intensity)/Transmitted light
i.e.	id est (that is)
IEEE	Institute of Electrical and Electronics Engineers
I_{mpp}	Current at maximum output power point
In ₂ O ₃	Indium oxide
I_o	Incident light
IPCE	Incident photon to electron conversion efficiency
IQE	Internal Quantum Efficiency
IR	Infra red
I_{sc}	Short-circuit current
ITO	Indium-doped Tin Oxide
I ₃	Triiodide
I-V	Current-Voltage

J	Current density
J_o	Reverse bias saturation current density
JPC C	Journal of Physical Chemistry C
J_{sc}	Short-circuit current density
J-V	Current density-Voltage
K	kelvin
k	kilo
k_B	Boltzman's constant
L	Length
l	electron mean free path
LBL	Layer by layer
LB-rGO	Langmuir-Blodgett-reduced Graphene Oxide
LiF	Lithium Fluoride
LED	Light emitting diode
Log	logarithm
LPE	Liquid Phase Exfoliation
LPE-G	Liquid Phase Exfoliation Graphene
LrGO	Laser-reduced Graphene Oxide
LUMO	Lowest unoccupied molecular orbital
M	Mega
m	meter
Mg	Magnesium
mg	milligram
min	minute/minimum
mL	milli litter
MIM	Metal Insulator Metal
MLG	Multi-layer graphene
MoO ₃	Molybdenum oxide

MPP	Maximum power point
μ	mu (mobility/micro)
MW	Microwaves
MWCNTs	Multi-walled Carbon Nanotubes
MWI	Microwaves irradiation
MWNTs	Multi-walled Nanotubes
N	Newton
n	n-type, concentration, diode ideality factor
NH ₂	Hydrazine
nm	nanometer
NMP	N-methyl-2-pyrrolidone
NP	Nano particles
O	Oxygen
1D	One-dimensional
ODCB	orthoDichlorobenzene
OLED	Organic light emitting diode
Ω	Omega (ohm)
OPV	Organic Photovoltaic
OSC	Organic Solar Cell
O ₂	Oxygen plasma
P	Power
p	p-type
Pa	pascal
PAHs	Polycyclic aromatic hydrocarbons
PC ₆₀ BM	[6,6]-phenyl-C61-butyric acid methyl ester
PCE	Power Conversion Efficiency
ϕ_c	Phi (critical point)
PEDOT:PSS	Poly(3,4-ethylenedioxythiophene) polystyrene sulfonate

PET	Polyethylene terephthalate
PI	Polyimide
P_{in}	Incident solar radiation (Input power)
P3HT	poly-(3-hexylthiophene)
PLD	Pulsed Laser Deposition
PMMA	Poly-methyl-methacrylate
Pt	platinum
PV	Photovoltaic
PVA	Polyvinyl alcohol
QE	Quantum Efficiency
R	Resistance/Reflectance
rGO	reduced Graphene Oxide
ρ	Resistivity
RPM	Rotations Per Minute
R_s	Sheet resistance, series resistance
R_{sh}	Shunt resistance
s	second/space/spacing
SCM	Scanning Capacitance Microscope/Microscopy
σ	Conductivity
σ_{gt}	Conductivity of transparency
SEM	Scanning Electron Microscope/Microscopy
S	Silicon/Siemens
SiO ₂	Silicon dioxide
SKPM	Scanning Kelvin Probe Microscope/Microscopy
SLG	Single Layer Graphene
SM	Small Molecule
SnO ₂	Tin
SWNTs	Single Wall Nanotubes

T/ T	Temperature/Transmittance/Transmission
t	thickness
TCE	Transparent Conductor Electrode
TCF	Transparent Conductor Film
TCM	Transparent Conductor Material
TCO	Transparent Conductor Oxide
TEM	Transmission Electron Microscope/Microscopy
3D	Three-dimensional
TiO ₂	Titanium dioxide
TPa	Tera pascal
2D	Two-dimensional
UPS	Ultraviolet Photoemission Spectroscopy
US	United States
USD	United States Dollar
UV-Vis	Ultraviolet-visible
V	Volt/Voltage/volume/volumic
V_F	Fermi velocity
VI	Voltage-Current
V_{mpp}	Voltage at maximum output power point
V_{oc}	Open-circuit voltage
W	Width Watt
WF	Work function
WO ₃	Tungsten oxide
wt	weight
ZD	Zero-dimensional
ZnO	Zinc Oxide

1 Introduction: Transparent Conductor Materials/Electrodes for Organic Solar Cells

Transparent Conductor Electrodes (TCEs) are crucial for the range of electronic and optoelectronic devices ranging from touch screens, Liquid Crystal Displays (LCDs), Organic Light Emitting Diodes (OLEDs), Photovoltaic (PV) Solar Cells, E-readers, Electro-chromic Windows and Stretchable Touch Sensors. Figure 1.1 shows several illustrations and applications of TCOs.



Figure 1.1: *Transparent Electrodes applications in LCDs [1].*

Several metal oxides and their combinations have been investigated and used at the interface of light and electricity in the above devices as their function is to allow the light and current to pass through them. Oxides of Indium (In_2O_3), Tin (SnO_2) and Zinc (ZnO) and their combinations; Fluorine doped Tin Oxide (FTO), and Indium Tin Oxide (ITO) are hitherto the most-widely used TCEs [2, 3, 4], with ITO taking the lion's share of current TCE applications being the the leading and a popular choice with a work function of 4.8-5.0 eV, a transmittance of $>80\%$ and a sheet resistance of $10\text{-}30\ \Omega/\square$ in organic solar cells [3]. These oxides are referred in the literature as Transparent Conductor Oxides (TCOs) or Transparent Conductive films (TCFs). Table 1.1 shows the

Table 1.1: Criteria for choosing TCO materials [4].

Property	Materials
Highest transparency	$ZnO:F$, Cd_2SnO_4 , Zn_2SnO_4
Highest conductivity	$In_2O_3:Sn$
Highest mobility	CdO , $In_2O_3:Ti$, $In_2O_3:Mo$
Lowest work function	$ZnO:F$
Highest work function	$SnO_2:F$, $ZnSnO_3$
Best thermal stability	$SnO_2:F$, TiN , Cd_2SnO_4
Best mechanical durability	TiN , $SnO_2:F$
Best chemical durability	$SnO_2:F$
Best resistance to water	$SnO_2:F$
Best resistance to H plasma	$ZnO:F$
Easiest to etch	$ZnO:F$, TiN
Lowest deposition temperature	$In_2O_3:Sn$, $ZnO:B$
Least toxic	$ZnO:F$, $SnO_2:F$
Lowest cost	$SnO_2:F$

most important transparent conductor oxides with different properties, which are required depending upon future application [4]. Further details on ITO and other related TCOs are presented in the appendix 8.1. Figure 1.2 shows the evaluation of sheet resistance for different applications of TCEs.

A TCO can be defined as a wide band-gap semiconductor having a relatively high concentration of free electrons in its conduction band. Free electrons can be tuned by controlling the defects or extrinsic dopants in the material. The high electron-carrier concentration (assumed that the materials are n-type) is responsible for causing absorption of both the visible and infrared radiation of the electromagnetic spectrum, while for photovoltaic applications, the absorption in the visible portion is more important. A balancing compromise between electrical

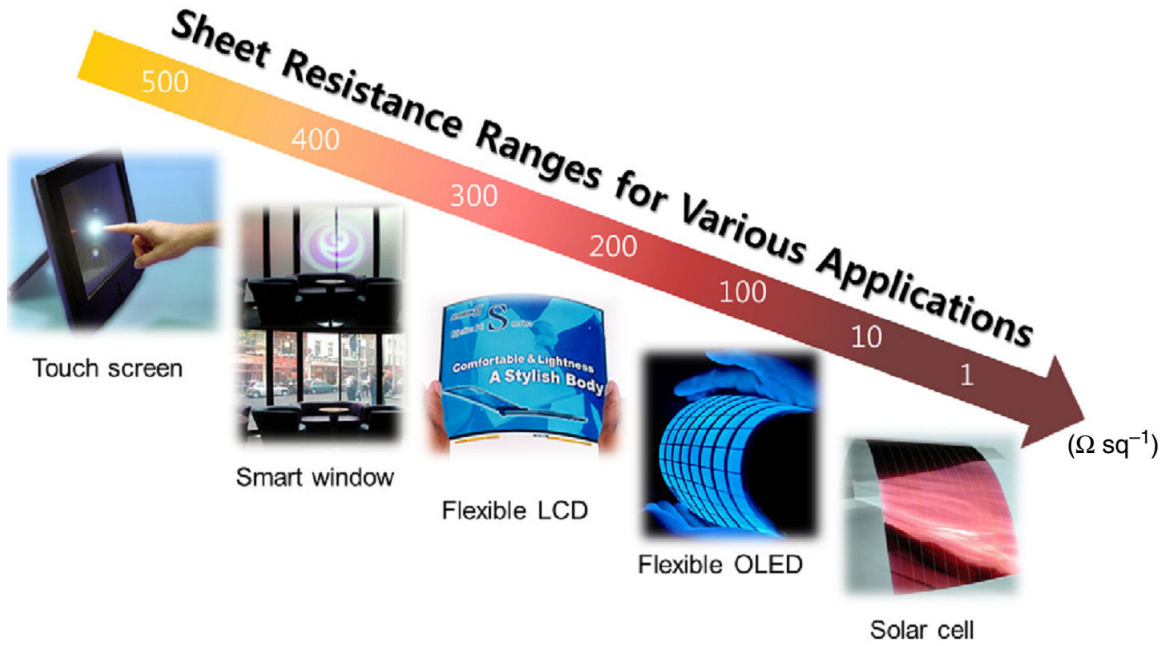


Figure 1.2: Sheet resistance requirement for different applications of TCEs.

conductivity and optical transmittance is required for most TCE applications [5].

1.1 Criteria for Choosing TCEs

Choice of the TCE is dictated by its potential application. Different criteria/figure of merit can be defined and established for different applications. However, optical transparency and electrical conductivity are the two broad factors which are at the helm of TCEs.

DC electrical conductivity (σ) defines the ability of a material/electrode to allow the DC current to pass through it and it is defined either in Siemens per centimeter (or meter) or the inverse, the resistance in Ohms (Ω), more frequently by sheet resistance (R_s). The latter defines the resistance of a uniform two-dimensional film, expressed in ohms per square (Ω/\square). The lower the sheet resistance, the better conductivity is. For a rectangle shaped film of length L ,

width W , the resistance R is:

$$R = \frac{\rho/t \times L}{W} = \frac{R_s \times L}{W} \quad (1.1)$$

The term L/W can be seen as the number of squares of side W that can be superimposed on the resistor without overlapping. Thus, even if R_s has units of ohms (as R does), it is called ohms per square (Ω/\square), due to historical reasons for simpler description. R_s is related to bulk resistivity ρ by:

$$R_s = \rho/t. \quad (1.2)$$

Where t is the film thickness, $\rho=1/\sigma$ is the resistivity, The electrical (and electronic) properties of materials (and devices) are measured by I-V (current-voltage curve, also called V-I) characteristics, from which their behavior can be determined. Resistance is generally characterized by a relationship called current-voltage characteristic and typically represented as a chart or graph. The graph shows the electric current through a circuit, device, or material, and the corresponding voltage, or potential difference across it.

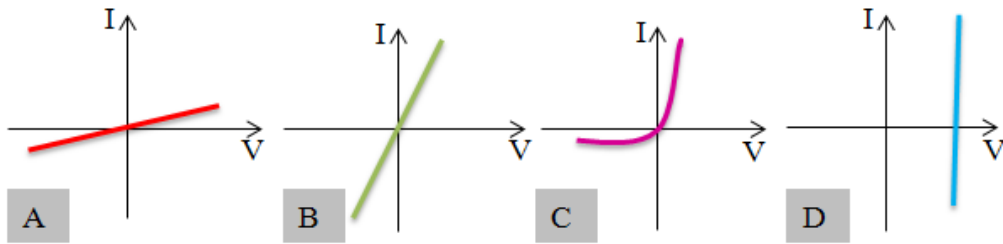


Figure 1.3: *I-V curves for different electrical and electronic devices: for a large resistance (resistor) A); a small resistance B); a p-n junction diode C) and a battery D).*

Figure 1.3 shows I-V curves for ohmic (resistor) and non-ohmic (p-n junction/Schottky diode) different electrical and electronic devices.

Optical transparency defines the ability of a material/electrode to let the light pass through it without scattering. It is often described as per cent of light passing through a material as function of wavelength, normally in the visible range of spectrum from 350 to 800 nanometers (nm), and it is commonly given at 550 nm. The higher the transparency, the better. The transmittance and/or absorbance can be derived from the Beer-Lambert-Bouguer law. The transmittance of a sample T is referred as a function of the wavelength of UV-visible light as:

$$T = \frac{I}{I_0} \quad (1.3)$$

where I is the portion (%) of light coming out of sample and I_0 is the incident light (100 % light). The transmittance is related to the absorbance A and the reflectance R ($A+R+T=1$). Thus with R negligible:

$$A = -\log_{10}T = \varepsilon^* c d; \quad (1.4)$$

Where ε^* is the extinction coefficient; c is the concentration; d is the pathway of the light (thickness of graphene/film in this case).

A transparent conductor film/electrode has ideally the lowest possible sheet resistance R_s and the highest possible transmittance (for optoelectronic devices such as organic solar cells, OLEDs, displays, touch screens). A good standard is the ITO film which has a transparency of >80 % with a sheet resistance of 30-40 Ω/\square for organic solar cells. Thus let us recall that the resistance of thin two-dimensional films is given as $R_s=\rho/t$.

Each of these parameters, transparency and sheet resistance alone, is of little value for the TCE applications. There is always a trade-off between two parameters depending upon the application. The effectiveness of TCE based on the ratio of electrical conductivity σ to visible absorption coefficient α can be defined quantitatively. This ratio is known as the figure of merit for TCEs and

is given by:

$$\sigma/\alpha = -\{R_s \log(T + R)\}^{-1} \quad (1.5)$$

Where α is the absorption coefficient in visible range, T and R are the total visible transmission and reflectance, respectively. Higher the value of σ/α , better is the TCE. Another figure of merit is described for thin semiconductor films, mostly based on carbon materials, allowing a combination of opto-electronic properties of TCE without knowing the thickness (t) of the film [6]. This is called Conductivity of Transparency (σ_{gt}) expressed in Siemens per cm ($S \cdot cm^{-1}$) by:

$$\sigma_{gt} = \frac{\varepsilon_{graphene}}{-\log(I/I_0)\rho_{sample}} = \frac{301,655 cm^{-1}}{-\log(I/100\%)\rho_{sample}} \quad (1.6)$$

Where σ_{gt} is the conductivity of transparency based at 550 nm; ρ_{sample} (often used interchangeably as R_s) is surface resistance of a transparent conductive graphene sample; $\varepsilon_{graphene}$ is the absorption coefficient, I/I_0 is the transmission. The $\varepsilon_{graphene}$ is determined from the dependency of absorption coefficient on intensity change of light, the length of the pathway, and the concentration. Since the perfect graphene (single sheet) structure has no variable concentration, there is no dependence on the concentration, hence $\varepsilon_{graphene}$ ($=\varepsilon^* c$) is the absorption coefficient of graphene in this case [6]. Thanks to its near perfect structure (in our work because this is not the case of chemical vapor deposition graphene), graphene has no variable concentration and it is taken as constant. So it does not affect the absorption coefficient (equation 1.6). The interlayer distance in highly oriented pyrolytic graphite (HOPG) graphite is well known to be 0.335 nm (0.340 nm for other graphite). A single sheet of graphene absorbs $\sim 2.3\%$ of white light, so the transparency is 97.7%. Hence, it is possible to calculate the absorption coefficient of graphene to $301,655 cm^{-1}$ as follows:

$$\varepsilon_{graphene} = \frac{-\log(I/I_0)}{d_{graphite}} = \frac{-\log(97.7\%/100\%)}{3.35 \cdot 10^{-8} cm} = 301,655 cm^{-1} \quad (1.7)$$

Certain applications like E-Readers need very high transparency, around 99 % but sheet resistance as high as few $k\Omega$ may be acceptable. For organic solar

cells (OSCs) on the other hand, the criteria require a transparency of 80 % with a sheet resistance of few tens of ohms per square.

Apart from conductivity and transparency, other important factors affecting the behavior of TCE are: chemical, thermal, mechanical and physical properties like band gap, Fermi level (carrier generation), work function, and energy level alignment at hetero-interfaces [4], [7] (Some of the other general criteria were earlier shown by the table 1.1). Therefore, for choosing a TCE, one has to take into consideration all these factors affecting the performance of TCE as well as the TCE employing device. Depending upon application, some of other material properties become critical. For example, for OSCs, the TCE has to be resistant to environmental conditions like humidity, heat, and oxidation among others.

1.2 Role of Electrodes in Organic Solar Cells

An OSC consists of an active layer sandwiched between two electrodes chosen with suitable work-function, where, one of them is the transparent conductor oxide/electrode. The active layer consists of a heterojunction of organic semiconductors with an electron donor and an electron acceptor material. Organic semiconductors absorb the incident light via transparent conductor anode electrode (ITO) and convert it to electrical energy [8]. The converted energy is collected by the counter cathode electrode (Al). Further details of OSC and electrodes will be discussed later in section 1.4 in this chapter.

1.3 Carbon-based TCEs/TCMs for OSCs

In this section, carbon-based transparent conductive films and electrodes as alternative to commonly-used TCOs will be discussed. With the increase in demand for TCEs for various emerging applications, amidst challenges of increased cost of existing TCOs, especially the scarcity of indium (limited sources) and

price fluctuations, difficulty in processing, sensitivity to acidic and basic chemical environments and brittleness of ITO, new materials are being studied for their suitability in the growing market of TCEs, especially for the applications involving flexible devices. Last two decades' progress in controllable synthesis, purification, and analyses of novel nanomaterials has opened new possibilities to investigate optical, electrical, thermal and mechanical properties of thin percolating films as well as bulk materials. Many methods have been studied to produce thin percolating networks/films. Nanomaterial thin films can achieve higher in-plane conductivity (due to percolation networks) than the bulk materials of the same species with additional benefits of flexibility, ease of processing and stability. These small materials in the form of sheets, nanotubes and wires, not only have high aspect ratio/large active surface area but are relatively easy to disperse in inexpensive solutions. The nanomaterials, which can be cast from their suspension into thin conducting films have revolutionized thin film electronics, and the dependency upon high cost (high temperature and high vacuum) film growth has been significantly curtailed. Solution processable dispersions give good promise to produce high volume, high throughput, large scale thin films with low cost. One of the promising and readily reachable applications for solution-processable nanomaterials is the use as transparent conductor films and electrodes. Nano-scale carbon-based materials, like graphene (single, bi, tri, few/multi layer graphene), Carbon Nanotubes (CNTs), Reduced Graphene Oxide (rGO) have recently joined this pool due to their attractive properties [9]. Other candidates as metal nanowires and metal grids have also shown great potential to be investigated as TCEs [2, 7, 10].

High values of intrinsic dc conductivity of thin and transparent films including carbon-based ones of up to 100 nm is key driving agent for these materials. Typically, high aspect ratio of these materials and web-like topology make low materials density films with reasonable sheet resistance a viable possibility and they are worth applying in opto-electronics applications along with additional

advantages of mechanical flexibility and thermal stability. Low cost starting materials and simple deposition techniques coupled with good properties mentioned below make these rapidly advancing nanomaterials very attractive transparent electrodes [2].

Considerable amount of research efforts have added knowledge to improve synthesis methods, to better understand their material properties and to demonstrate their potential as alternate TCEs/TCFs. Here, the most important work which deals with Carbon-based TCEs/TCFs (CTCEs, CTCFs) is reviewed. The methods of preparations (synthesis) and transfer of material itself and characterizations are not detailed (until later in this chapter). Other materials such as: conducting polymers, metal grids and silver nanowires have also joined the race, and their potential is discussed as other candidates for TCEs in the appendix 8.2.

Table 1.2: Strengths and weaknesses of TCF technologies [11].

TCF Technology	Film Properties							Examples of Commercial Suppliers
	Conductivity	Flexibility	Printability	Stability	Color	Haze	Stretchability	
TCO	●	●	●	●	●	●	●	Many suppliers (film)
Silver grids	●	○	●	●	●	○	●	PChem Associates Inc. (ink); Cabot Corporation (ink)
Silver nanowires	●	○	●	●	●	●	●	Cambrios Technologies Corp. (film); Carestream Advanced Materials (film)
PEDOT	○	●	●	●	●	●	○	Agfa Specialty Products (ink, film); Heraeus Precious Metals (ink)
CNTs	○	●	●	●	●	●	●	SouthWest NanoTechnologies, Inc. (ink); Unidym, Inc. (film)

● Excellent, ○ Good, ● Poor.

CNT, carbon nanotube; PEDOT, poly(3,4-ethylenedioxythiophene); TCO, transparent conducting oxide.

Table 1.2 shows the strengths and the weaknesses of transparent conductive film (TCF) technologies including TCOs, Carbon nanotubes, silver grids and

nanowires [11]. This table gives a quantitative view of the properties of TCF technologies and does not include the price of material/film which can be also a deciding factor in the commercialization of a given technology. From this table it is evident that CNTs have superior properties for flexible TCF applications. One can see that CNTs out perform metal-based TCFs. Table 1.3 gives a more quantitative analysis of properties of materials for TCF technologies including graphene. This table includes cost and failure strain % as well as thickness of

Table 1.3: *Properties of various materials for TCF technologies [12].*

	Thickness (nm)	Transparency (%)	Sheet resistance (Ω/sq)	Failure strain (%)	Cost
ITO	100~200	> 90	10~25	1.4	120 \$/m ²
PEDOT:PSS	15~33	80~88	65~176	3~5	2.3 \$/ml
Silver NWs	~ 160	92	100	~1.2	40 \$/m ²
CNT	7	90	500	~ 11	35 \$/m ²
Graphene	0.34	90	~ 35	~ 7	45 \$/m ²

TCFs apart from two prominent parameters, sheet resistance and transparency [12]. All these films are under investigation for optimum performance and cost of film preparation, which have to undergo evaluation for next several years for potential application in various optoelectronic devices. As the table shows, CNTs (rolled graphene sheets) have good conductivity (though lower than TCOs and Ag nanowires/grids) but surpass in all other parameters.

The most recent and promising carbon nanomaterial for TCE applications, among others, is graphene or few layer graphene (FLG) with favorable work-function. The table 1.4 shows the work-functions of carbon nanomaterials including graphene in comparison with the currently used TCEs [ITO, AZO (Al-doped ZnO), Sn-doped ITO, ATO (Sb-doped), FTO (Florine doped), etc]. As it is evident from this table, carbon materials have similar work-functions to that

of currently-used TCOs [7].

Table 1.4: *Work Function of current TCEs and Carbon-based TCEs.*

TCE	ITO	AZO	ATO	FTO	Graphene	SWNTs	MWNTs
Work func- tion (eV)	4.26-5.6	3.2-4.5	4.0-5.3	4.4-5.0	4.3-4.6	4-70-5.05	4.80-4.95
Reference	[13], [7]	[7]	[7]	[14]	[15], [16]	[17],[18]	[17],[18]

Graphene is an allotrope and a flat, one atom-thick mono layer/sheet of two-dimensional (2D) honeycomb lattice structure of carbon atoms. It is recognized as the basic unit and building block of other graphitic materials of different dimensionalities. Wrapping it will give OD fullerenes, rolling the sheet will form 1D nanotubes, stacking of infinite multiple sheets over each other will yield 3D graphite material, while several stacked sheets give "pseudo" 2D sheets FLG [19], however, it has come under enormous interest during the last decade in many fields of fundamental and applied sciences, since first isolation as stable 2D material in 2004 [20], [21]. Figure 1.4 shows these carbon allotropes: graphite (3D); graphene (2D); carbon nanotubes (1D) and fullerenes (0D).

The most prominent properties of zero-overlap semi-metal graphene (single sheet) include very thin atomic thickness of 0.34 nm [23], very light at 0.77 milligrams per square meter [24, 25], spring constants of 1-5 N/m and a Young's modulus of 0.5 TPa [26], an enormous tensile strength of 130 GPa (100 times stronger than the best steel) [19], having one of the largest specific surface areas of 2630 m²/g [27], the highest in-plane thermal conductivity between 2000-4000 W/m.K for suspended samples at room temperature [28] and mobility above 15000 cm²/V.s (electrical conductivity of 10⁻⁶ Ω-cm) with ballistic transport where both holes and electrons as charge carriers are able to travel sub-micrometer distances without scattering [29], including high current density, chemical inertness, and super

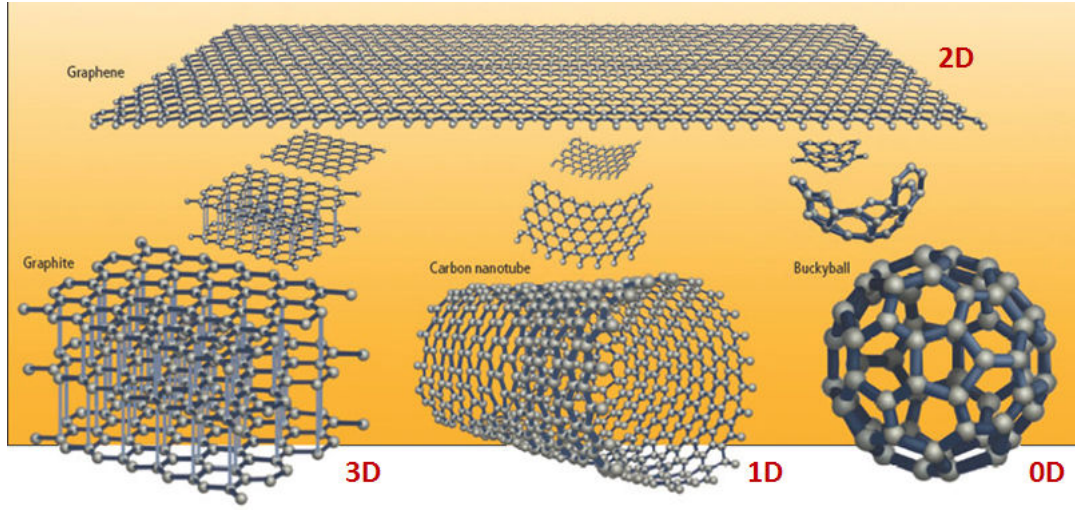


Figure 1.4: Family of carbon allotropes [22].

hydrophobicity at nanometer scale.

Many sheets of graphene (hundreds) piled together, forming a thin film can be referred to as 3D graphite. It is not obvious to draw a clear demarcation line defining when few sheets of graphene make up a 3D material. However, looking at electronic structure and suitability in electronic applications, ten sheets can be referred to as few layer graphene (FLG). A stack thicker than 10 sheets is considered as multi-layer graphene (MLG) and up to 100 sheets thick stack is a thick film of 3D graphite and is of less scientific interest for electronics applications[20, 30]. A distinction between single-, bi- and three- layer can be done for band gap description.

Fullerenes are physically zero dimensional objects with discrete energy states where carbon atoms are arranged spherically [31]. Fullerenes can be thought as wrapped-up graphene as they can be obtained from graphene with the introduction of pentagons that create positive curvature defects.

Whereas, CNTs are thought of as a graphene sheet, rolled up along a given direction and reconnecting the carbon bonds, to form a seamless tube or cylinder, of up to some microns in length and a few nanometers in diameter [32, 33].

The ends of the tube are capped by fullerene-like half-spheres [34]. Hence carbon nanotubes have only hexagons and can be thought of as one-dimensional (1D). They exist in two configurations, with the first one consisting of a single rolled up (strip of) graphene layer, and is called single-walled carbon nanotube (SWNT), while the second one, consisting of several coaxially stacked SWNTs (like a Russian doll) and is named multi-walled carbon nanotube (MWNT). Double-walled carbon nanotubes (DWNTs) are two sheets of rolled graphene and are described separately. Typically the diameter of the latter is about one order of magnitude larger than for SWNTs.

Graphite, a three dimensional 3D allotrope of carbon is made out of stacks of graphene layers that are weakly coupled by van der Waals forces [35] and theoretical 2D graphite (graphene) has been studied since nearly seventy years [36].

The structural flexibility of graphene is reflected from its electronic properties [37]. The sp^2 hybridization between one s orbital and two p orbitals gives a trigonal planar structure with a carbon atoms bond of 1.42 Å. The σ band is responsible for the robustness of the lattice structure in all allotropes and are responsible for the mechanical properties. Due to the Pauli principle, these bands have a filled shell and, hence, form a deep valence band. The unaffected p orbital, which is perpendicular to the planar structure, can bind covalently with neighboring carbon atoms, leading to the formation of a π band. The π band is half filled because each p orbital has one extra electron which is delocalized. These delocalized electrons are available for charge transport and are responsible for exceptional electronic and thermal properties of graphene. Whereas, the van der Waals attraction between different graphene sheets are responsible for the stacking of sheets.

Thickness of graphene is directly proportional to the number of graphene sheets and for few layer graphene the electronic properties change with thickness and by the relative position of atoms in adjacent layers (by added complexity

of stacking order) [19]. Figure 1.5 shows the in-plane σ bonds/atom and π orbitals perpendicular to the plane and the most common structures and stacking sequences of graphene flakes [38]. Structurally, Carbon (C) atoms can be stacked

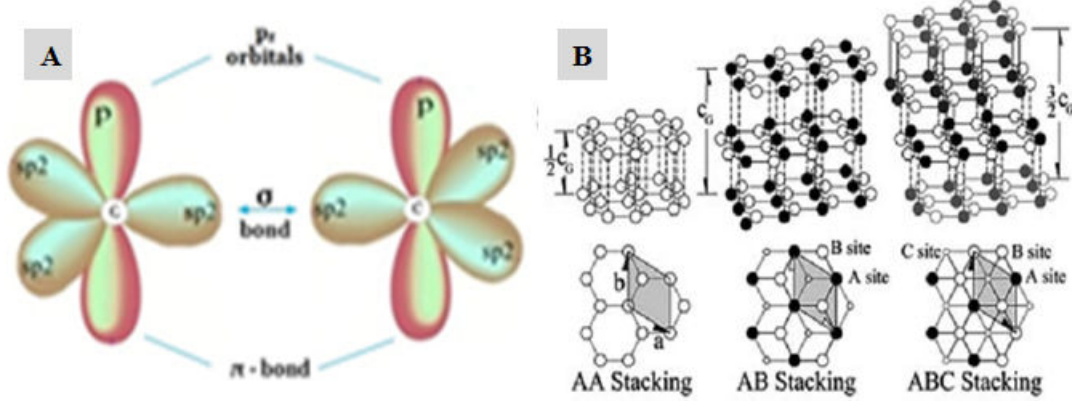


Figure 1.5: Schematic of the in-plane σ bonds and the p orbitals perpendicular to the plane of the graphene sheets forming π bonds A) and three most common stacking sequences of graphene flakes B) [38].

in several ways in graphite to generate hexagonal (AA stacking with each atom on top of another atom), Bernal (AB stacking with atoms on second layer sit on the empty spaces of the layer below) which is the most stable and studied so far and rhombohedral (ABC) arrangement, see figure 1.5B [29], [38]. Bilayer graphene can have AA or AB stacking order, trilayer can show a combination of mono and bilayer stacking, whereas, for FLG no specific fixed stacking order [19].

1.3.1 Characterizations of Graphene and Graphene Films

Graphene morphology especially as thin films can be studied by Scanning Electron Microscope (SEM) which is important for electronic applications. SEM is a non-destructive technique but it is both time consuming and unsuitable because of the absence of clear signatures for the number of atomic layers. Scanning probe is also a slower technique to study graphene due to its low throughput [9]. Better approach to study graphene is Transmission Electron Microscope (TEM)

which, though a destructive technique, can give useful and accurate information on the structural quality and the number of graphene sheets/layers accurately. TEM diffraction mode can detect the single layer of graphene [39]. Figure 1.6 shows TEM and SEM micro-graphs of graphene sheets.

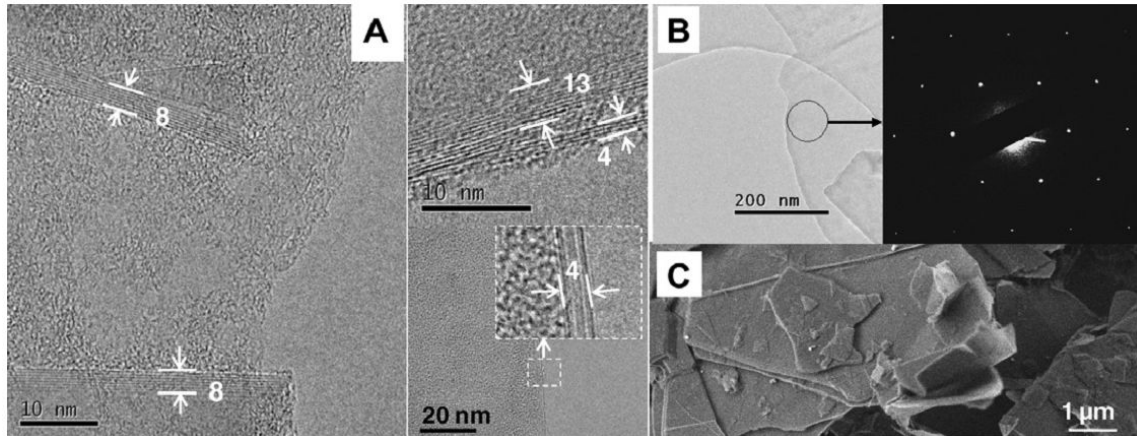


Figure 1.6: TEM micro-graphs of the FLG borders with different graphene sheets numbers A), TEM micro-graph and electron diffraction of a single layer graphene B), SEM image showing the presence of thick FLG in the sample C), [40].

Further detailed topography and to determine the number of graphene layers can be performed by Atomic Force Microscopy (AFM) [41, 42]. Another rather easier way to differentiate thickness of graphene is by optical microscopy on Si substrate with a capping layer of 285-300 nm SiO_2 using contrast spectra [20, 43, 44]. A study showed that visibility of graphene depends strongly on both thickness of SiO_2 capping layer and light wavelength. They claimed, by using monochromatic illumination, that graphene can be made visible for theoretically any SiO_2 thickness (in contrast to 300 nm-thick standard) and showed that 100 nm thickness is the most suitable for visual detection of graphene [45].

Further to study the nanoscale electrical properties of single-layer graphene (SLG), bilayer graphene (BLG) and multilayer graphene electrical properties Scanning Capacitance Microscopy (SCM) and Electrostatic Force Microscopy (EFM) can be employed [46]. Two probes [47], four point probes, and Hall Effect

techniques [48] can be used to study the electrical properties of graphene flakes, sheets and films.

Electronic properties such as: work function (WF) and energy band gap related studies can be carried out using scanning Kelvin probe microscopy (SKPM) [49] and Ultraviolet Photoelectron Spectroscopy (UPS) [50]. An advantage of graphene (few layer graphene) is that its work-function depends upon thickness, mostly increases with number of layers and can be tuned. For epitaxial monolayer graphene on SiC the WF is 4.3 eV, which increases to 4.5 eV for four layers and reaches final saturation value of 4.6 eV for higher numbers of layers. The environment, substrate and other parameters affect the values of WF e.g., a WF value of 4.5 eV for monolayer graphene on SiO₂ was reported, it can be significantly higher at 5.3 eV for monolayer graphene on Al₂O₃. Mostly, the basic trend that holds is that WF can be increased by adding more layers of graphene irrespective of the type of graphene and WF measurement techniques. This tunability can be very useful in its applications in electronic devices [50].

Raman spectroscopy has been largely employed to investigate the structural and electronic characteristics of graphite materials [51, 52]. A Raman spectra by its D, G and 2D peaks/bands from different locations yield important signatures in determining the crystal quality and thickness of graphene based on change in position, intensity and width. The most prominent features in the Raman spectra of single sheet or monolayer graphene are the so-called G band which appears at around 1580 cm⁻¹ (graphite) and the G' band (or 2D) at about 2700 cm⁻¹ using a 514 nm laser. Figure 1.7(a) compares the Raman spectra of graphene and bulk graphite [44]. The G band comes from a normal first order Raman scattering process in graphene and is associated with the doubly degenerate (iTO and LO) phonon mode (E_{2g} symmetry) at the Brillouin zone center. Whereas, the G' and D bands originate from a second-order process involving two iTO phonons near the K point for the G' band or one iTO phonon and one defect in the case of the D band. Since the width (location by wavelength) of the G' band is approximately

twice the width of D band ($\omega_{G'} \sim 2\omega_D$), G' band is often called as the 2D band. From the figure 1.7(a), We can also see the so-called disorder-induced D band,

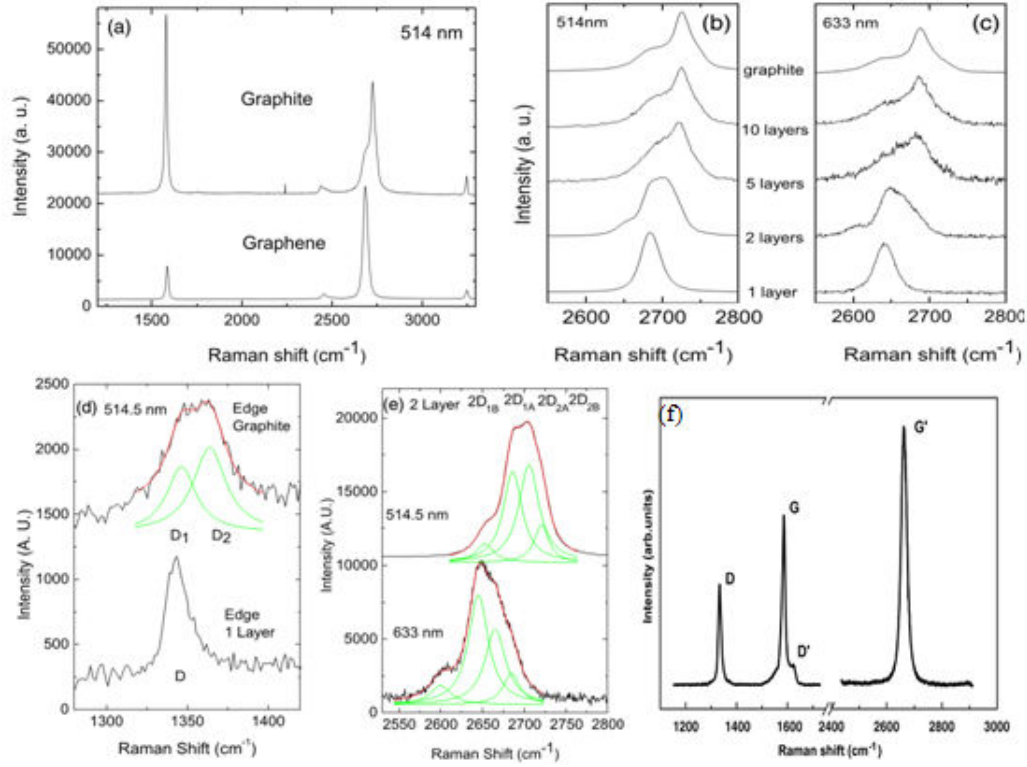


Figure 1.7: Comparison of Raman spectra at 514 nm for bulk graphite and graphene (scaled to have similar height of the 2D peak at 2700 cm⁻¹) (a). Evolution of the spectra at 514 nm with the number of layers (b). Evolution of the Raman spectra at 633 nm with the number of layers (c). Comparison of the D band at 514 nm at the edge of bulk graphite and single layer graphene (d). The fit of the D₁ and D₂ components of the D band of bulk graphite is shown. The four components of the 2D band in 2 layer graphene at 514 and 633 nm (e) [44]. Raman spectrum of a graphene fragment, recorded at an edge, showing the main Raman features, i.e. the D, G, D' and G' bands taken with a laser excitation energy of 2.41 eV [53].

at about half of the frequency of the G' band (around 1350 cm⁻¹ for a disordered sample or at the edge of a graphene [53]). As expected, a D peak is mostly observed at the sample edge, it is not itself a quantitative and accurate measure

of defects in the graphene lattice, figure 1.7(d). A significant change in shape and intensity of the 2D peak of graphene compared to bulk graphite is observed in figure 1.7(a). The 2D peak in bulk graphite is comprised of two components $2D_1$ and $2D_2$ roughly $1/4$ and $1/2$ the height of the G peak, respectively. A single, sharp 2D peak in graphene, with a roughly $4 \times$ more intensity than that of G peak was measured for graphene. Observably, the G peak intensity of single layer and bulk graphite is comparable [note that figure 1.7(a) is rescaled to show a similar 2D intensity] and the G position is $3\text{-}5 \text{ cm}^{-1}$ higher than bulk graphite showing an upshift. The G band peak however, will down-shift with number of layers. The change in shape of the 2D band is evidently confirmed in figure 1.7(d), which compares the D peak of the graphite and graphene edges, respectively. The D peak for graphene is a single sharp peak, while in graphite it shows a band consisting of two peaks D_1 and D_2 [44]. Figures 1.7(b)- (c) show the evolution of the 2D band as a function of layer number for two different laser excitations: 514.5 and 633 nm, respectively. The immediately observation reveals that a bilayer has a much broader and up-shifted 2D band with respect to graphene. This band is very different from bulk graphite as well with 4 components, $2D_{1B}$, $2D_{1A}$, $2D_{2A}$, $2D_{2B}$; two of which, $2D_{1A}$ and $2D_{2A}$, have higher relative intensities than the other two, as evident in figure 1.7(e). Also a further increase in number of layers leads to significantly important decrease of the relative intensity of the lower frequency $2D_1$ peaks as shown in figure 1.7(b)-(c). For this reason, Raman spectrum becomes hardly distinguishable from that of bulk graphite for more than 5 layers. Hence Raman spectroscopy is capable of clearly distinguishing a single layer, from a bilayer from few (less than 5) layers with its changes in shape, width and position of 2D-band. The intensity ratio I_D/I_G increases with a decrease in the number of layers/thickness. The thinner is graphene, the higher is the ratio, (approximately 3.6 for a single layer) [29, 40, 44, 54]. An area ratio A_D/A_G can be used for small disorder [55], whereas, an intensity ratio of I_D/I_G coupled with full wave half minimum (FWHM) can give better approximation

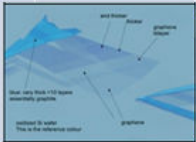

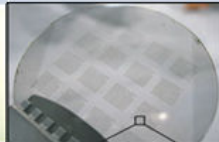

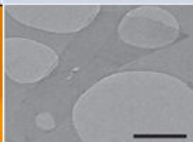
of defects/graphene quality for a large disorder. Some variations in the peak positions are also reported for the in-plane vibration of sp^2 carbon atoms (G band at $\sim 1582\text{ cm}^{-1}$) as well as the stacking order (2D band at $\sim 2670\text{ cm}^{-1}$) and defects band around 1350 cm^{-1} laser excitation at 2.41 eV [figure 1.7(f)] [53]. The notation D' band is used to denote another weak disorder-induced feature which appears at $\sim 1620\text{ cm}^{-1}$ when laser directly lands at the edge of a graphene fragment [figure 1.7(f)].

1.3.2 Graphene Production Methods

There are several general ways to make graphene based upon top-down (mechanical and liquid exfoliation) or bottom up approaches (CVD and epitaxial growth) and the choice is dictated by the final application, the cost of production and the efficiency. The first isolation of graphene (in 2004 by top-down method) published in 2005 which used a micro-mechanical technique to exfoliate graphite into thin graphene sheets [56]. This technique is still considered as the best one in order to get defect free, highly pure material with the best electro-optical properties. However, the yield is low, large area coverage and transfer to other substrates and upscaling for large quantities are still unresolved challenge with this technique [56]. Since then, number of other methods have emerged or already existing methods have been employed to produce graphene in order to get high quality, high yield graphene for various applications. High quality single and few layer graphene is grown by Chemical Vapour Deposition (CVD by bottom-up) on the metal substrates and is subsequently transferred onto other substrates for electronic applications [23, 52, 57, 58]. Later, roll-to-roll production of 30-inch single sheet of graphene films were grown by CVD on flexible copper substrates [59]. CVD is an existing technique which was already in use for the production of CNTs. Multi-walled and Single-walled CNTs were reported using CVD, a decade earlier before the graphene was discovered by micro-mechanical exfoliation

[60, 61]. A segregation of carbon-containing substrates or simply by heating and cooling down a SiC substrate, commonly known as epitaxial growth is used for growth of graphene on large area substrates [62, 63, 64, 65]. These methods have gained substantial importance currently due to potential to produce better yields, controllability, and growth on large area surfaces/substrates [9]. Although CVD is scalable, epitaxial growth on SiC is not. Most epitaxial or CVD graphene needs to be transferred on to arbitrary substrates for electronics applications. Transfer is usually done via polymethyl methacrylate (PMMA), polymer support. Some traces of PMMA may still be present on graphene as an impurity while the catalyst is etched away (and lost) by acid treatment. Liquid Phase Exfoliation (LPE) of graphite or expanded graphite method is also known for decades [66, 67, 68, 69]. Table 1.5 shows five representative methods for production of graphene and related characteristics of the produced graphenes (adapted from [68, 70, 71]).

Table 1.5: Five representative methods of graphene production [70].

Method	Mechanical exfoliation	Reduction of graphene oxide	Epitaxial growth on SiC	CVD growth on Ni, Cu, Fe,	Liquid phase exfoliation
Size	10-100 μm	>6 inch (152 mm, film)	<4 inch (101 mm)	>6 inch (152 mm)	few 10s of μm
Mobility	best	bad	high	high	low
Transfer	yes	yes	no	yes	yes
Applications	no	yes	little	most	little
Scalable					

Graphene produced by liquid phase method is the viable low cost technique of large-scale production but there are quality related issues such as, structural defects formed by oxidation products and reduction treatment and poor electrical

conductivity. We will mainly describe further the top-down approaches to get FLG or graphene flakes.

1.3.2.1 Micro-mechanical cleavage/ Mechanical ablation/ Ball-milling

Inspired from the scotch-tape micro-mechanical ablation, few layer graphene produced by mechanical ablation of pencil lead was produced with a very high yield of FLG (percent of exfoliated sheets/flakes from the original materials used) of around 60 percent [40]. Some other groups reported few layer graphene production by the means of ball milling. Few-layer graphenes was reported from ball-milling of graphite with melamine in solid phase. Melamine was removed from FLG by a thermal annealing step up to 300 °C [72]. Another study used Triazine derivatives under ball-milling conditions to exfoliate graphite. They compared their results with those obtained using melamine as an activating agent in exfoliation [73]. Ball milling methods are low cost route, however, they often involve activation agents/intercalants and the resultant graphene sheets are of smaller, random size and shapes due to poor controllability and selectivity of the process.

1.3.2.2 Liquid-phase exfoliation (LPE)

Graphene can be prepared in liquid media with varied conditions and environments. This consists of a chemical wet dispersion followed by ultrasonication, including organic solvents, ionic liquids, and water/surfactant solutions [74]. LPE can be either surfactant-free or surfactant-assisted and allows upscaling the production towards mass production of graphene [71, 75]. The simplest way consists in dispersing the graphite in an organic solvent which appropriately matches the surface energy of graphite [76]. This will reduce the energy barrier to overcome the force between adjacent sheets and thereby detaching a graphene layer from the 3D graphite. The solution is then ultrasonicated in a bath sonicator for

several days/weeks (hundreds of hours). Alternatively, a voltage is applied [77]. After the dispersion, a step of centrifugation is carried out to dispose off/separate the thicker flakes in the solution. The quality of the obtained graphene flakes varies from moderate to high depending upon the experimental conditions. Reproducibility is good but the process is not yet controllable. The complexity is low and this method allows preparing large amounts of graphene. A high percentage (up to 70 % of total product) of SLG can be obtained, by sonication of graphite in water, using sodium deoxycholate surfactant and followed by ultracentrifugation [78]. The use of graphite-intercalation compounds to exfoliate the expanded graphite has also been studied via LPE [67, 79]. The first sonication-assisted exfoliation of graphite was demonstrated using N-Methyl-2-pyrrolidone (NMP, an organic solvent) with 28% of single sheets of high purity and quality with conductivity as high as 6500 S.m^{-1} for semi-transparent ($T = 46\%$) films [68]. Later a liquid medium exfoliation method was reported to produce single to three graphene sheets varying in shape and size, after the exfoliation of graphite in N,N-dimethylformamide (DMF) solution [80]. Graphene nanoribbons of widths up to few nanometers have been demonstrated as well from expanded graphite [81]. The main advantage of LPE is that it is a low cost and scalable method and it does not need expensive growth substrates. Furthermore, it is more suitable to produce thin films due to being in the solution/liquid media [9].

1.3.2.3 Graphene Oxide

An extension of LPE is used to exfoliate graphite oxide by the means of sonication to obtain graphene oxide (GO) using for example, Hummers' method [66, 82]. The method is based on a chemical process that can be used to generate graphite oxide through the addition of potassium permanganate to a solution of graphite, sodium nitrate, and sulfuric acid (figure 1.8 shows the general strategies for preparation of graphene oxide/graphene, structure and dispersion of GO)

[25, 83, 84]. GO is subsequently reduced by (i) Thermal reduction (TR), (ii) Chemical reduction (CR) or (iii) Electrochemical reduction (ER) methods to produces reduced graphene oxide (rGO)/graphene.

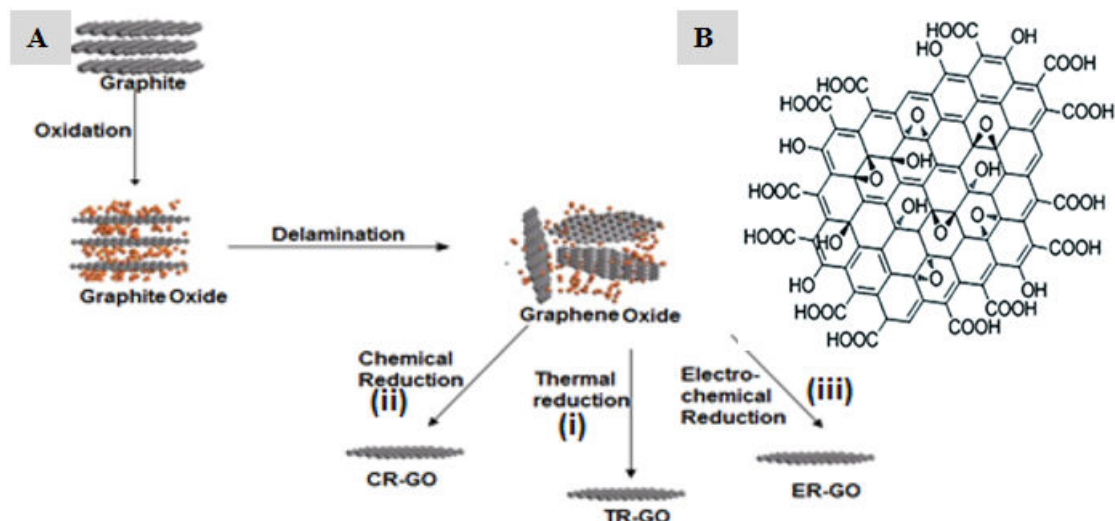


Figure 1.8: General strategies for preparation of graphene oxide/graphene from graphite followed by types of reduction treatments A) and chemical structure of graphene oxide B).

Graphite oxide is hydrophilic and thus can be solved in water by sonication or stirring, thanks to the presence of several oxygen groups at the plane and edges. The ultrasonication in liquid makes the dispersion negatively charged. The sp^2 network is disrupted in the material and hydroxyl or epoxide groups are introduced [85]. This makes a detaching of individual sheets possible and sheets turn to become graphene oxide from Graphite Oxide (GO). Additional step of centrifugation may be required to separate the thin graphene oxide from the thicker. Due to the high oxygen content ($>50\%$), graphene oxide is an insulator and it has to be reduced in thermal or chemical environment under Ar, H_2 or N_2 gas at high temperature, most common being hydrazine (NH_2) [86, 87, 88]. Then this material changes to be called reduced Graphene Oxide (rGO). Even after thermal reduction, some oxygen remains present in rGO. In fact, a C/O

atomic ratio lower than 10 is imperatively desirable [84]. An effective reduction GO suspended paper was achieved by performing a two step reduction and a minimum temperature treatment of 1500 °C [89]. This method adds to complexity and cost by adding the further need to reduce GO. However, if cheaper starting graphite oxide is used, it can be really a cheap method on the whole to produce large sheets of graphene with moderate to high quality rGO [90]. Several other thermal and chemical methods involving high temperature treatments and use of chemicals, respectively, and their combinations exist for reducing the graphene oxide [91]. Another method uses the rapid heating of expanded graphite (EG) or graphene oxide in a solvent by μ -waves irradiation (MWI) to ~ 165 , °C using commercially available microwave oven to exfoliate EG, and simultaneously exfoliate and reduce the GO. This is an extension of the LPE in a way that the GO/EG have been been ultrasonicated or stirred in an organic solvent for intercalation between the sheets to reduce the strong Van der Waal forces. The method shifts the approach to lower the reduction temperature or to avoid the use of chemicals. The microwave brings an advantage of heating GO/EG in a very short time resulting not only in a pre-exfoliation process but also in thermal reduction for a rapid production [91]. The use of μ -waves for GO reduces the weight% of oxygen-containing groups up to less than 10% with a conductivity as high as 10,000 S/m [92]. GO can also be reduced in a powder form with a rapid microwave irradiation treatment without the use of solvents [93]. Fast photo-reduction by photo-irradiation, by xenon lamps or by femtosecond lasers have also been reported, but their conductivity is on the lower side [94].

1.3.2.4 Bottom-up Approaches and Growth on Substrates

Methods to grow graphene directly on different surfaces/substrates has shown potential towards high quality SLG and FLG. In CVD, carbon is decomposed on metal surfaces to grow graphene layers. The size of obtained graphene

layers is independent of the initial graphite crystal. However, CVD is a high cost, requires transfer to arbitrary substrates and potential problems occur due to grain boundaries. A recent study demonstrated that multi-layer graphene can be grown by high temperature carbon implantation into nickel film (supported on SiO₂/Si substrate) [95]. Further details on CVD, epitaxial and chemical synthesis methods are given in the appendix 8.3. In epitaxial growth, the carbon already exists in the substrate, i.e. the substrate and the layer of graphene are the same material. Another bottom-up technique called total organic synthesis involves well-defined, nanosized polycyclic aromatic hydrocarbons (PAHs). They are extensively present in the remains of coal, wood, and other organic materials, and even in interstellar, after domestic and natural combustion. PAHs are two-dimensional graphite fragments of all-sp² carbon composition which offer synthesis versatility but the challenge lies in preserving distributed and a planar geometry for large PAHs [96].

1.3.3 Charge Transport in Graphene and in FLG

Various types of electrical transport exist. For example, charge transport processes which occur via localized states of the charge carriers in the conductor like variable range hopping [97] or polaron hopping [98], are known as hopping conduction. In the cases, where the charges are not localized, but scattered on dislocations, phonons or magnetic impurities (Kondo effect [99]) or even among one another along their way in the conductor, the charge transport is based on diffusive conduction process. If the charge carriers do not suffer any scattering, the charge transport is called ballistic [34]. Due to similarity of graphene structure to organic semiconductors, a brief introduction to charge transport in organic semiconductors has been presented in the appendix 8.4. The figure 1.9 shows the energy dispersion for the entire graphene lattice with zooming in on the linear energy dispersion near a Dirac point.

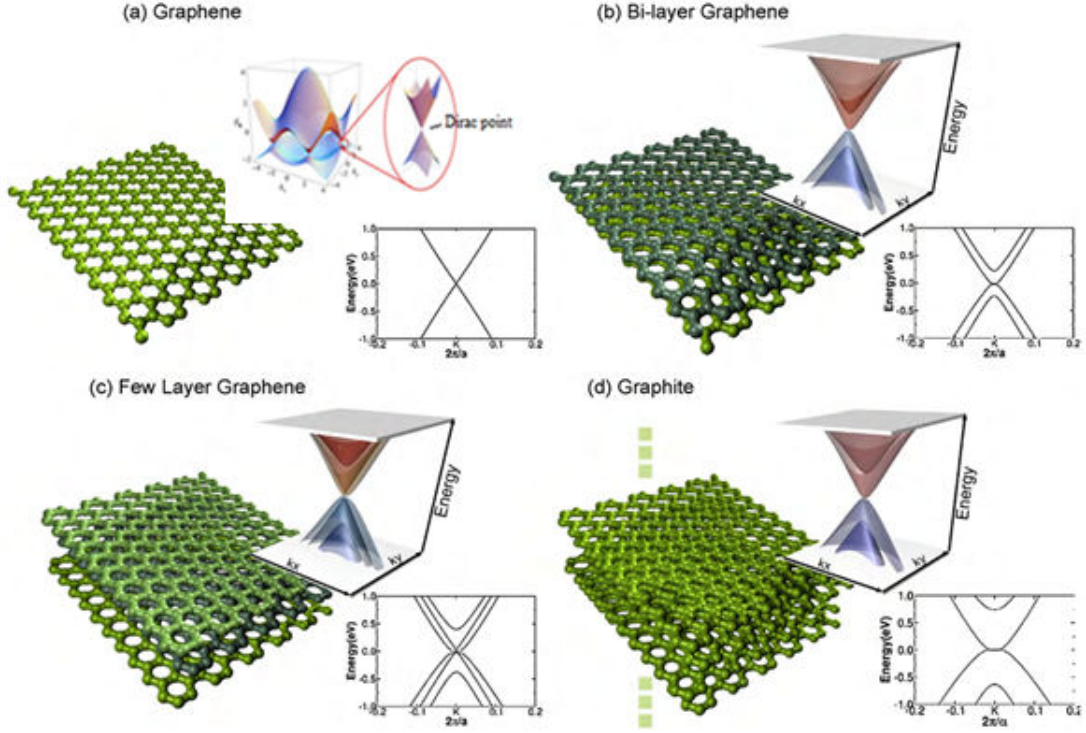


Figure 1.9: Low energy DFT 3D band structure and its projection on k_x close to k point K for graphene showing graphene honeycomb lattice and the Brillouin zone (a), bilayer graphene (b), trilayer graphene (c) and graphite (d). The Dirac point (i.e., relativistic fermion characteristic) is lost in bilayer graphene (b), but appears again in trilayer graphene (c); (d) shows the 3D graphite structure which displays a semimetallic band structure with parabolic-like bands. The Fermi level has been set at zero in all cases [19] An enlargement close to the K and K' point shows Dirac cones [37, 100].

In the first Brillouin zone, the inequivalent corners K and K' are called the Dirac points. A pure graphene sheet (SLG without any defects) exhibits a unique electronic band structure with a linear dispersion relation close to the charge neutrality point (Dirac point) [37]. This crystal structure of graphene can be considered as two equivalent carbon triangular sub-lattices. The linear dispersion for this structure leads to massless excitons, described by the Dirac equation. These Dirac fermions (electrons or holes) behave very differently and exhibit un-

usual properties compared to ordinary electrons, thus leading to new phenomena. The chiral nature of charge excitations in 2D graphene has been shown to result in unconventional quantum transport features, such as unusual quantum Hall effects, or anomalously weak localization phenomena at low temperature [101].

The structure of bi- and few layer graphene differs from that of single sheet of graphene. The figure 1.9 provides further explanations of energy dispersion by density functional theory (DFT) calculations [19] in comparison to single sheet. Stacking of few layers can change the electronic properties (empty dispersions) considerably and the layering structure can be used in order to control the electronic properties. As with any physical system, the charge carriers in graphene are affected by structural disorder and doping (the most common factors influencing the transport properties) as well as by hopping between sheets in the case of FLG. Possible sources for disorder in graphene systems many and possibly include but are not limited to the charged impurities in the form of surface adsorbates or trapped charge in the supporting substrate, neutrally charged impurities, ripples, carbon vacancies, edges (stable defects due to oxygen groups attached), topological Stone-Wales defects, interstitial defects, and lattice strain, adatoms, and interlayer adatoms for FLG case [102, 103, 104]. The examples of structural and potential kind of oxygen groups are presented in figure 1.10. A direct consequence of a single atomic layer structure of graphene is that all electronic conduction takes place at the surface of graphene [37]. For this reason, the charge transport properties such as mobility, Dirac point, and minimum conductivity are expected to be sensitive to the surrounding environment. Such dependence of charge transport on the environmental factors and also possibility to tailor graphene's properties through intentional doping with adsorbates or lattice defects have been demonstrated both theoretically and experimentally [106]. Due to its extreme sensitivity to molecular adsorbents, chemical functionalization means can also introduce band gap opening in graphene which will give rise to a change in work function [107]. The band gap opening leads to a shift in

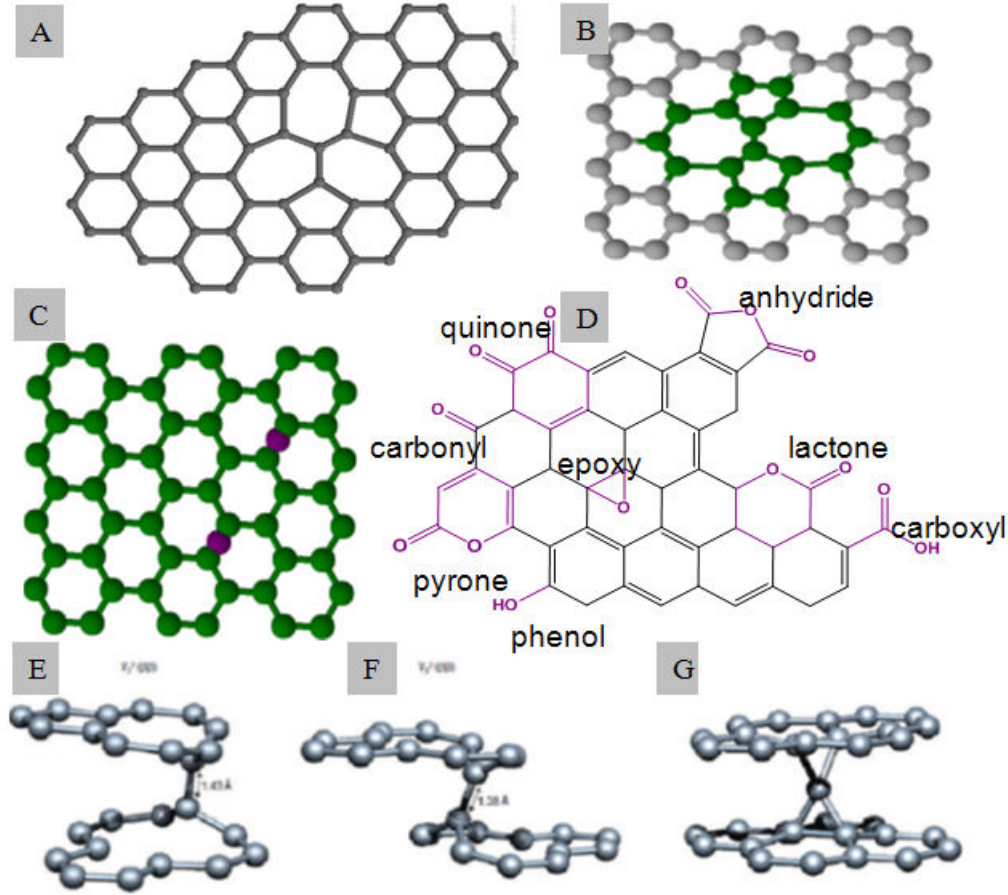


Figure 1.10: Examples of structural defects and oxygen groups in single sheet of graphene. The 5-8 double vacancy A), stone-wales defects B), adatoms C) oxygen functional groups mainly on the edges D). Interlayer double vacancy structures in bilayer graphene V_2^1 ($\beta\beta$) E), V_2^2 ($\beta\beta$) F), and spiro-interstitial (a four-coordinated carbon atom between the layers) G) [105].

the Fermi level as well [25]. It was shown by simulations that the band gap and other electronic properties of few-layer graphene can be strongly modulated by the interlayer distance and fluorination (also experimentally) [19, 108]. Whereas, the armchair graphene nanoribbons (A-GNRs) are semiconductors with energy gaps which is demonstrated to decrease by increasing the widths of ribbons [19].

The presence of disorder due to the presence of charged impurities results in an inhomogeneous distribution of conducting electron and hole puddles at low

carrier concentrations [109]. Due to these electron-hole puddles a residual carrier density, n^* , on the order of 10^{11} cm^{-2} for graphene on SiO_2 is observed [density fluctuations (electron-hole puddles) experimentally measured using a scanning single electron transistor) and prevents truly probing Dirac point physics, where carrier concentration vanishes (figure 1.11). Even at an average carrier density of zero (Dirac point) electronic conduction occurs locally through sections having electron and hole concentrations, represented by the blue and red regions respectively (figure 1.11).

These puddles qualitatively explain the presence of the observed minimum conductivity and indicate that the physics near the Dirac point is different than the physics at higher carrier densities. Several theoretical works have investigated the behavior of massless dirac fermions [110, 111, 112, 113], for quantum conductance. The conductance quantum, denoted by the symbol G_0 is the quantized unit of electrical conductance and is defined by Landauer formula [114, 115]:

$$G_0 = \frac{e^2}{\pi h} \approx 7.7480917346(25) \times 10^{-5} S \quad (1.8)$$

Where e is the electron charge (most of quantum transport is the transport of electrons) and the h is the Planck constant (this indicates the role of quantum mechanics). In fact, under certain conditions, Dirac fermions are immune to localization effects observed in ordinary electrons [116] and it has been demonstrated by experimental studies that electrons can propagate without scattering over large distances, typically of the order of micrometers in graphene, thus giving rise to ballistic transport [21].

Many reports have predicted a universal minimum conductivity value of $4e^2/\pi h$, where the factor of 4 stands for the spin and valley degeneracy [37]. Yet, experimental works reported $\sigma_{min} \sim 4e^2/h$ [20], and further studies found a non-universal σ_{min} generally greater than $4e^2/h$ (for ideal graphene) [117]. Investigations focused on resolving the issue of the missing π between theoretical predictions and experimental values, demonstrated that $4e^2/\pi h$ is accessible in

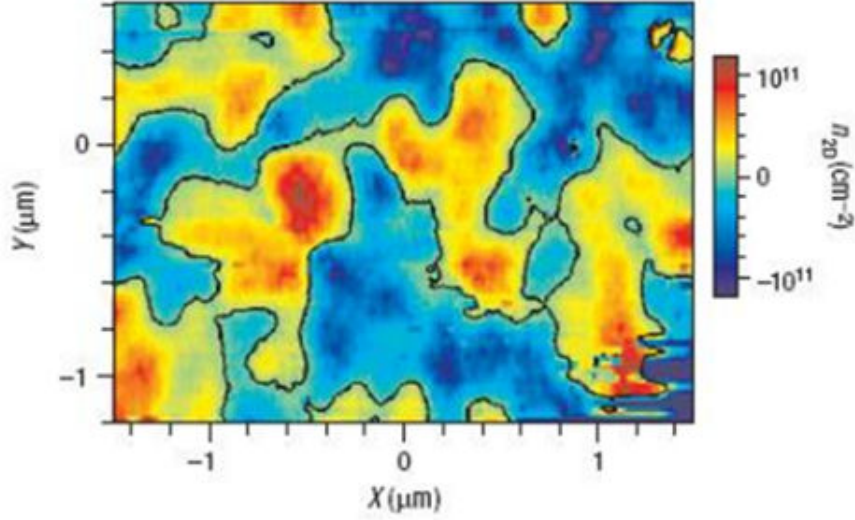


Figure 1.11: Disorder in graphene obtained by micromechanical exfoliation (scotch tape) of synthetic graphite. Using a scanning single electron transistor the spatial density fluctuations in graphene are measured. The black line shows the contour between electron (red) and hole (blue) puddles at an average carrier density of zero [109].

the ballistic transport regime for samples where length is much shorter than width [118]. While the three experimental works discussed here [20, 117, 118] demonstrate a wide variety of measured values for σ_{min} , a common feature in pristine graphene devices is a $\sigma_{min} > 4e^2/\pi h$. Away from the Dirac point, disorder also plays a role in the measured transport properties through the mobility μ and gate dependent conductivity. Charge mobilities in the range $1\text{-}20 \times 10^3 \text{ cm}^2/\text{Vs}$ were reported in graphene samples with various levels of disorder [101]. The equation 1.9 relates to the scattering of charge carriers and is an indication of the quality of electronic transport.

$$\mu = \frac{\sigma}{ne} \quad (1.9)$$

While graphene devices supported by Si/SiO₂ have exhibited impressive mobility between $\sim 1 \times 10^4 \text{ cm}^2/\text{V.s}$ $\sim 2 \times 10^4 \text{ cm}^2/\text{V.s}$, it is still dramatically

less than the predicted intrinsic limit of $\sim 2 \times 10^5 \text{ cm}^2/\text{Vs}$ [119, 120]. Additionally, the symmetry of the experimentally measured conductance indicates that hole and electron mobilities should be nearly the same. The large disparity is an indication of extrinsic sources of electronic scattering. Scattering effect of electrons by optical phonons of the substrate is larger than the effect of scattering by graphene's own phonons. Contacts to graphene can strongly dominate charge transport and mobility as well as significantly modify the charge transport environment local to the contacts by creating pn-type (pp, nn) metal/semiconductor junctions depending upon the materials used as metal contacts but usually Cr/Au contacts are free from such additional contact effects except sometimes creating junctions [106].

1.3.4 Charge Transport in Carbon Nano Tubes (CNTs)

First multiwall nanotubes (MWNTs) were synthesized (1991) with diameters ranging from a few nanometers to several hundred nanometers for the inner and outer shells, respectively. They extend the length over several microns. Single-wall carbon nanotubes (SWNTs) were synthesized shortly after the discovery of MWNTs by arc-discharge methods using transition-metal catalysts [33]. Carbon-based tubular molecular structures (nanotubes) with a high aspect ratio with a strong one-dimensional (1D) character are investigated as photoactive material and semi-transparent electrodes in photovoltaic and other applications due to their superior electronics, thermal and mechanical properties [121]. MWNTs are generally composed of a few to tens of shells with random helicities weakly coupled through van der Waals interactions, exhibit additional geometrical complexity due to the coupling between shells, resulting in a multi shell transport (figure 1.12A). They displayed a weak localization and negative magneto-resistance as well as incorporating them in to Y-shaped junctions shows that they behave as intrinsic nonlinear devices, displaying strong rectifying be-

havior at room temperature (figure 1.12) [33, 122].

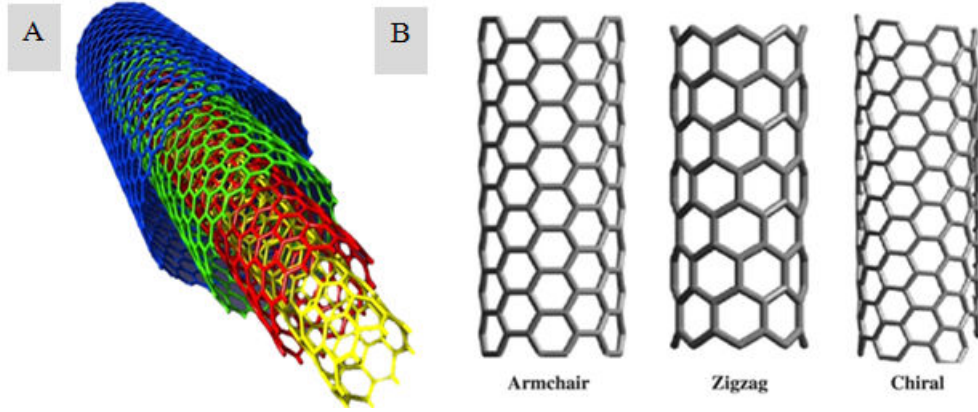


Figure 1.12: Schematic structure of MWNTs A) and chiralities of single wall CNTs B) [123, 124].

They are cheaper alternative (2-3 orders of magnitude lower cost as compared to SWNTs), produced in large quantities even if their R_s is on the higher side in thin films with $\approx 250 \text{ k}\Omega/\square$ at 80% transmittance as compared to $0.15\text{-}2 \text{ k}\Omega/\square$ for same transparency for SWNTs [124]. The electrical properties of single and multi-walled CNTs are mainly determined by their diameter, their wrapping angle and the direction in which the graphene sheet is rolled up (out of many ways). The diameter and the wrapping angle determine whether a CNT is metallic or semiconducting with a band gap varying from zero to a few tenths of an eV. As a consequence, all armchair tubes are metallic whereas zigzag nanotubes can exist as either metallic or semiconducting molecular structures [125]. Figure 1.12B shows types of single wall CNTs depending on the chirality. The conduction in CNTs can be ballistic, diffusive, or based on tunneling/scattering. The investigation of the electrical transport properties of CNTs has shown that various effects have been observed such as single-electron tunneling (Coulomb blockade) [126, 127] ballistic transport at room temperature [128, 129]. Metallic SWNTs have a Fermi velocity (v_F) of $8 \times 10^5 \text{ m/s}$ that is comparable to typical metals. Semiconducting SWNTs have a bandgap E_g 0.9 eV/d , where d is the diameter

of the tube in nanometers [130]. By the Landauer formula, the conductance is given by:

$$G_0 = \left(\frac{4e^2}{h}\right) \times T \quad (1.10)$$

Where T is the transmission coefficient describing the probability that an electron will be transmitted along the channel through the sample. A SWNT has four 1D channels in parallel due to spin degeneracy and the sublattice degeneracy of graphene. Conduction in SWNTs is quantized due to their one-dimensionality and the number of allowed electronic states is limited, if compared to bulk graphite. The nanotubes behave consequently as quantum wires and charge carriers are transmitted through discrete conduction channels. When ballistically conducted, the electrons travel through the nanotubes channel without experiencing scattering due to impurities, local defects or lattice vibrations (no resistance and no energy dissipation in the conduction channel). The transport properties of MWNTs are similar to those of SWNTs, however some differences exist due to the transport coupling between the walls of the tube. For SWNTs bundles, the coupling between tubes requires to be taken in account [125]. In order to estimate the current in the carbon nanotube channel, the Landauer formula can be applied, which considers a one-dimensional channel, connected to two contacts source and drain in a FET structure.

Assuming no scattering and ideal (transparent) contacts, the conductance of the one-dimensional system is given by:

$$G = G_0 N T \quad (1.11)$$

Where N is the number of the channels available for transport, and G_0 is the conductance quantum $2e^2/h \approx 12.9k\Omega^{-1}$. Perfect contacts, with reflection $R = 0$, and no back-scattering along the channel result in a transmission probability $T = 1$ and the conductance of the system becomes: $G = (2e^2/h) N$. Thus each channel contributes $2G_0$ to the total conductance [131].

If the transport is ballistic and the tube has perfect contacts, this equation predicts a quantized conductance of $4e^2/h$ associated with each 4-fold degenerate 1D subband. Metallic nanotubes very often approach this quantized conductance value even at room temperature [132, 133]. Conductance less than the quantized value can arise from additional resistance contributions due to either the contacts or the tube which add up incoherently at or near room temperature. At lower temperatures, coherence effects and the Coulomb blockade become important as well. If we neglect coherence effects, the total resistance $R=G^{-1}$ of a nanotube device with a uniform channel can be written as:

$$R = R_{contacts} + R_{tube} \quad (1.12)$$

Where the contact resistance obeys:

$$R_{contacts} = \left(\frac{h}{4e^2}\right) \quad (1.13)$$

and for a uniform tube with diffusive scattering:

$$R_{tube} = \left(\frac{h}{4e^2}\right) \times \left(\frac{L}{l}\right) \quad (1.14)$$

where L is the tube length, l is the electron mean-free path for momentum relaxation. For example, electric force microscopy can measure the potential drop along the tube under current bias [129, 134, 135], directly probing the relative contributions.

1.3.5 Charge Transport in graphene/FLG films

There are several methods of growing graphene/rGO/FLG films on arbitrary substrates, such as spray [136, 137], spin coating [138], casting [139] transfer via vacuum filtration, Langmuir-Blodgett assembly/deposition [140, 141, 142] charge drop-casting, dip coating, electrophoresis [12] and inkjet-printing for

metal-graphene hybrid structure [143] for transparent conductor films (TCFs) have been demonstrated. The charge transport in these films is influenced by grain boundaries (CVD method), junction dependency (between two sp^2 hybridized species, FLG-FLG, interflakes stacking), however a minimum amount called critical point (ϕ_c) is required to cover the surface to form a percolation in the conducting film is necessary which depends upon several parameters: shape, size, texture, chemical nature (phase of grains), orientation of domains, homogeneity, density of materials and other physical and chemical properties among others [144]. percolation (most solution-processable films) including other factors already mentioned earlier.

Table 1.6 provides summary of pristine, doped and reduced graphene oxide materials with sheet resistance, transmittance characteristics along with conductivity of transparency (σ_{gt})[6, 145].

For a CVD graphene (CVD-G) film, R_s of $280 \Omega/\square$ with 76 % (at 550 nm) transmittance (T) was reported with a high σ_{gt} of $9.0 \times 10^3 \text{ S.cm}^{-1}$ [23]. For the doped CVD-G, respectively with HNO_3 and AuCl_3 , even better results were reported with lower values of R_s of 30 and $150 \Omega/\square$, higher transmittance of 90 and 87 %, and σ_{gt} of 2.2×10^5 and $3.3 \times 10^4 \text{ S.cm}^{-1}$, respectively [59, 146]. A non-volatile ferroelectric polymer spin coated on top of CVD-G in a hybrid structure what the authors call graphene-ferroelectric transparent conductors (GFeTCs) yield R_s of $120\text{-}130 \Omega/\square$ with T of 95% with σ_{gt} of $3.1 \times 10^3\text{-}10^4 \text{ S.cm}^{-1}$ [147]. A mono layer of reduced graphene oxide (rGO) by Langmuir-Blodgett (method of forming mono-and multimolecular films of an amphiphilic substance on the water surface and then transfer it to a solid substrate) was transferred to transparent glass substrate to form a LB-rGO film, and very high R_s of $1.9 \times 10^7 \Omega/\square$ and T of 95% (at 650 nm) were reported [141]. Lower R_s ($1100 \Omega/\square$) and T (91% at 550 nm) were reported by similar method (LB-rGO), giving slightly higher σ_{gt} (670 S.cm^{-1}) than previous ($6.7 \times 10^{-1} \text{ S.cm}^{-1}$) result [149]. Currently, there are not so many results available for films made from exfoliated (mechanical or liquid)

Table 1.6: Sheet resistance, transmittance and conductivity of transparency (σ_{gt}) of graphene, graphene oxide and doped graphene films produced by various methods.

Graphene Film (ref.)	R_s (Ω/\square)	Transmittance % (Wavelength in nm)	Conductivity of Transparency (σ_{gt}) (S/cm)
CVD-graphene (G) ([23])	280	76 (550)	9.0×10^3
CVD-G doped with HNO_3 ([59])	30	90 (550)	2.2×10^5
CVD-G doped with AuCl_3 ([146])	150	87 (550)	3.3×10^4
Ferroelectric polymer/CVD-G (GFeTCs) ([147])	10^2 - 10^3	95 (500)	3.1×10^3 - 10^4
LB-rGO ([141])	1.9×10^7	95 (650)	6.7×10^{-1}
Electrochemically exfoliated graphene ([148])	2.4×10^3	73 (N/A)	92
Vacuum filtered rGO ([88])	4.3×10^4	73 (550)	51
LB-rGO ([149])	1100	91 (550)	670
LB-chemically modified G ([67])	8×10^3	83 (1000)	465
LPE-G by ultrasonication ([78])	1000	65 (550)	1.6×10^3
rGO ([143])	2.5×10^3	93 (550)	3.8×10^3
rGO-Ag-NP ([143])	640	87 (550)	7.8×10^3

graphene, however, LPE-G obtained by ultrasonication showed a R_s 1000 Ω/\square and T of 65% (550 nm) with high σ_{gt} of 1.6×10^3 S.cm⁻¹ [78]. The rGO films displayed a higher R_s of 2.5×10^3 with 93 % T (550 nm) yielding a σ_{gt} of 3.8×10^3 S.cm⁻¹ [143], whereas rGO coupled with Ag nanoparticles shows better performance with a lower R_s of 640 Ω/\square at T of 87% giving improved σ_{gt} of 7.8×10^3 S.cm⁻¹ [143].

1.4 Introduction to Organic Solar Cells

Organic Solar Cells (OSCs) are the technology which has attracted strong attention in recent years, due to the numerous advantages. They contain certain organic molecules and polymers for solar energy harvesting. Organic molecules/polymers have good absorption/light capture efficiency, possess semi-conducting properties, are easy to process at room temperature (the most of the cases), and provide good promise for low-cost solar cells manufacturing at large scale. Though, they did not hit the commercial market due to lower efficiencies (record up to 11.1%) as compared to inorganic cells technology, matured over 50 years (record efficiency up to 44.4 % for triple-junction compound solar cells). Figure 1.13 shows the graph with the progress in different solar cells and technologies to date (2014).

The fundamentals of OSCs and their progress during last decade will be covered briefly. In simplest terms, an organic solar cell contains a photo-active layer, consisting of an electron donor (D) and an electron acceptor (A) materials sandwiched between two electrodes. One of the electrodes is transparent (anode, ITO) and facilitates light absorption by acting as window to the active layer and the other (cathode) usually is a metal (Al, Ca etc), all deposited on a rigid glass or flexible plastic transparent substrate [8]. They are fabricated in the form of successive thin films where spin-coating, spray, printing and vacuum deposition techniques are applied to form the complete cell.

The active layer can be a planar or a bulk hetero-junction of two materials. The commonly used materials are a blend of poly-(3-hexylthiophene)/phenyl-C₆₁-butyric acid methyl ester (P3HT/PC₆₁BM) [151]. P3HT is used as a donor and PCBM as an acceptor material (figure 1.14, [?]). Architectures will be discussed later in the section 1.4.1. .

To facilitate an efficient charge collection, one or more additional buffer layer(s) can be added for hole and/or electron extraction/transport. These layers,

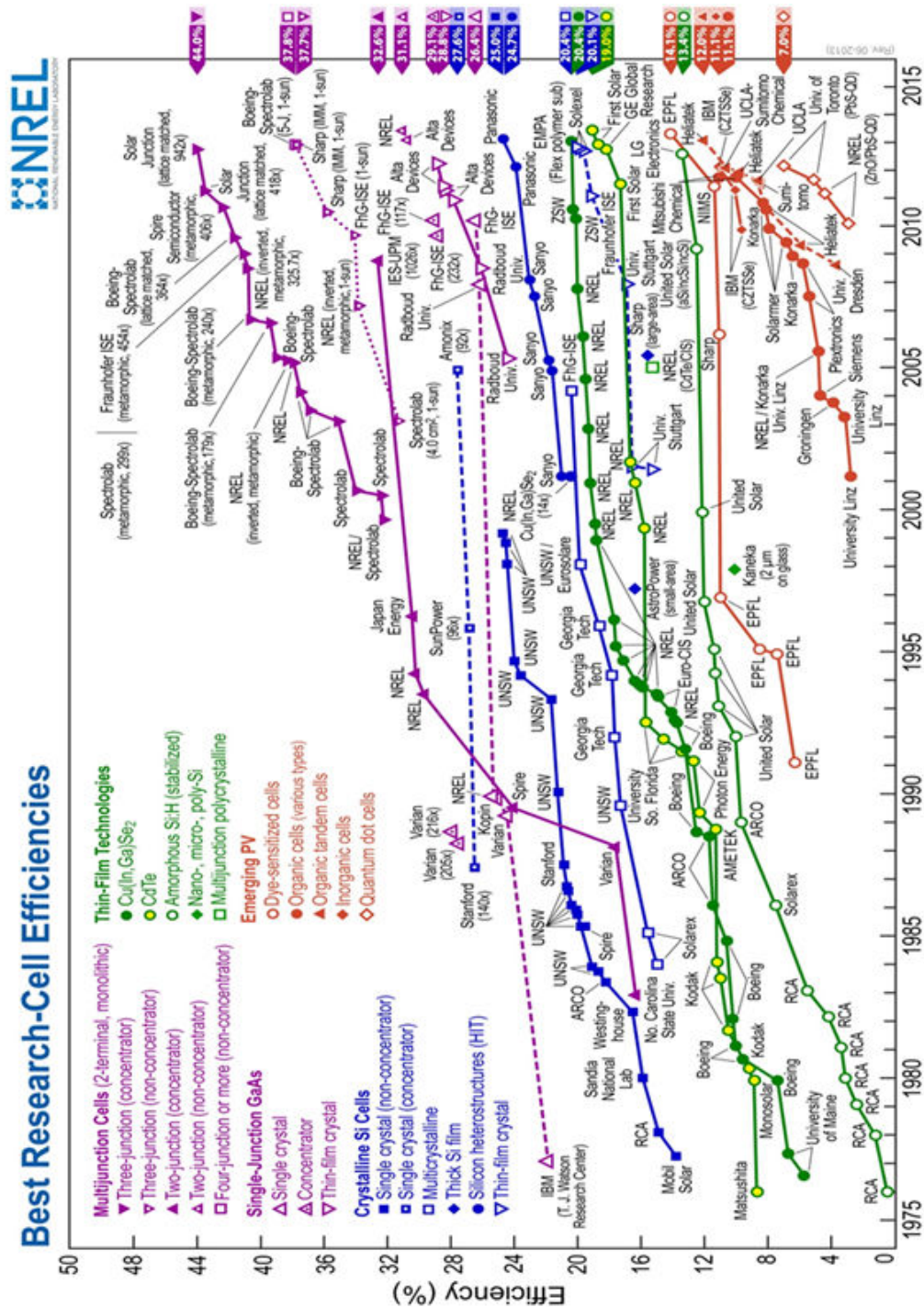


Figure 1.13: The graph shows the record solar-cell efficiencies over time, highlighting the progress in different solar cells and technologies up to the end of 2014. [150].

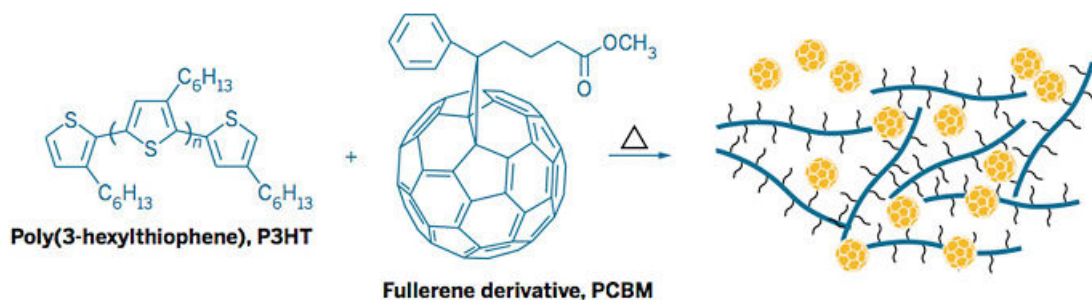


Figure 1.14: P3HT and PCBM materials, and their blended D/A structure [?].

according to the function they perform in the cell, can be named as hole transport layer (HTL) or hole extraction layer (HEL). Poly(3,4-ethylenedioxythiophene) Polystyrene sulfonate (PEDOT:PSS) is the most popular choice polymer material for HTL [152]. Bathocuproine (BCP) is an example of an electron transport layer (ETL) [153]. One of the functions of ETL or HTL is to block the opposite charge carriers from the infiltrating P3HT and PCBM, respectively, after charge separation. Following layers make up the OSC: first electrode, electron transport layer, photo-active layer, hole transport layer, and second electrode. But HTL and ETL may not always be the integral part of an OSC structure. Thickness of organic solar cells made of thin layers of organic materials is of the order of 100-120 nanometer range [154]. A rather general concept of solar cells is defined as: light is absorbed by photo-active materials via transparent and conductive electrode, absorbed light generates charge carriers (excitons= electron-hole pair) by photo-excitation process, both electrons and holes are separated by the electric field present near contacts to be subsequently delivered to contacts in the form of electrical power. The basic difference between inorganic and organic solar cells lies with the mechanism of the way charge carriers are created and separated. In the former, charge carriers are generated directly by incident light when it strikes the photo-active material which are then collected by the electrodes. In the later, light absorption does not generate free carriers instantly, rather an electron-hole

pair called exciton is generated due to coulomb-interaction which has typical binding energy (0.3-0.5 eV) [151]. Since organic components have low dielectric constant (~ 3), photo-excitation leads to a strongly bound exciton, which needs to be dissociated into free carriers [155]. The necessary electric field ($>10^6$ V/cm) is usually required for charge separation which is not available inside the active layer, so exciton has to travel (depending upon lifetime of charge carrier and hole/electron mobility of polymer) to the D/A interface in order to be separated in the presence of sufficiently strong field at the hetero-junction. This requires energy alignment of materials (D/A interface) for efficient separation of excitons and minimize the loss of energy during conversion process [151].

1.4.1 Types and Architectures of Organic Solar Cells

There are three types of organic solar cells based on the materials used in the fabrication of an OSC, namely: conjugated polymer (macromolecules with a molecular weight larger than 10000 atomic mass unit), small molecular (SM) weight (consist of lighter molecules usually called oligomers or small molecules,) SM solar cells and dye-sensitized solar cells (or Gratzel cell) in which dye molecules are adsorbed on a highly porous layer of titanium dioxide (an electron transport layer) [154]. Usually, physical vapor deposition in vacuum methods dominate for SM solar cells and spin-coating and ink-jet printing methods are used for deposition of polymers (vacuum deposition techniques are needed for electrodes deposition/evaporation purposes in polymer cells also). In Gratzel cells, screen-printing is the method used for deposition of titanium dioxide which is followed by sintering and dying steps.

Conjugated polymers (alternating single and double bonded carbon) possess delocalized (not associated with a single atom) electrons that can absorb photons. They are attractive class of semiconductors for photo-voltaic cells due to their strong absorbing ability and low-cost deposition on various substrates. The light

that is absorbed by conjugated polymers generates power in the solar cell by photo-voltaic effect. For these reasons, the devices which include the polymers are also called organic photo-voltaic (OPV) cells/ solar cells. One of the most common and best performing active layer in OPVs is comprised of a polymer-fullerene cell with poly (3-hexylthiophene) (P3HT) as the donor and the fullerene [6,6]-phenyl-C61 butyric acid methyl ester (PCBM) as the acceptor.

The simplest of the OPV devices is Single-layer OPV. This contains only one layer of conjugated polymer, sandwiched between two electrodes. A high work function, transparent conductor electrode such as ITO is used as anode, whereas, low work function metal cathode such as Ag, Al, Ca, or Mg may be used, as schematized in figure 1.15 [151]. The Highest Occupied Molecular Orbital (HOMO) and Lowest Unoccupied Molecular Orbital (LUMO) will be explained later in the section 1.4.2.

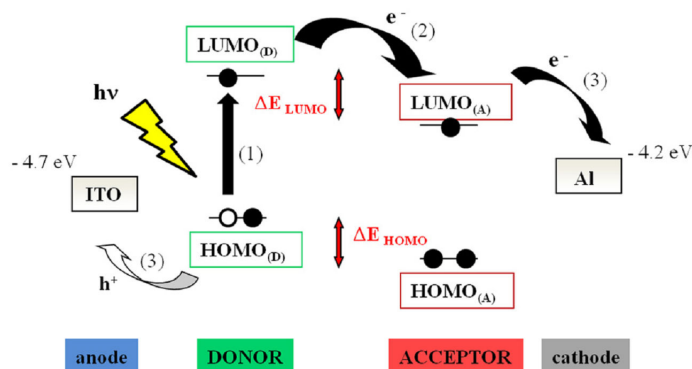


Figure 1.15: Structure of conventional OSC with ITO anode and Al cathode electrodes, highlighting the importance of WF [151].

This difference of work-function between two electrodes sets up an electric field in the active layer and this field helps separate the charge carriers (electrons and holes) from exciton (electron-hole pair). Based on the number of conjugated polymer(s) and the way of arrangement in the active layer, four device architectures are possible (see figure 1.16a-d). Ideally, electrons and holes are pulled towards positive and negative electrodes, respectively, under the influence of elec-

tric field. Practically, single layer OPVs (see figure 1.16a) are inefficient devices because the photo-generated excitons usually do not split by the built-in electric field, arising from work functions difference of electrodes, and single layer is not sufficiently thick to absorb all the visible light [156]. In order to increase the efficiency, the exciton splitting must occur at the interface between two semiconductors with offset energy levels. A rather improved design of OPV is made as bi-layer device structure which involves an electron donor and an electron acceptor materials placed separately over one another in the planar structure, and sandwiched between high and low work-function electrodes (refer to 1.16b) [157, 158]. However, a lot of excitons, due to small diffusion length (10-20 nm) recombine or decay (radiatively or non-radiatively) before reaching the D/A interface. A better approach to harness the most excitons is to reduce the distance that excitons have to travel. This can be achieved by mixing the donor and the acceptor materials together to form a polymer blend so that D/A blend has more interfaces throughout the bulk structure of blend (refer to 1.16c-d). If the exciton diffusion lengths are comparable to the length scales of the polymer blend, then most of the excitons generated in either material may reach the interface and they break efficiently to disassociate to become electron and holes. The charge carriers (electrons and holes), after the exciton break-up, are efficiently collected at their respective electrodes, while traveling through the blend [156, 159].

1.4.1.1 Equivalent Circuit for a p-n Junction Solar Cell

The figure 1.17 shows the equivalent circuit and the equation for the solar cell (diode). It describes the solar cell J-V behavior into four constituent parts, mathematically expressed by the diode equation in figure 1.17B: a photocurrent source, a diode, a series resistor and a shunt resistor. This model is based on inorganic p-n junction (a boundary between p-type and n-type material in a semiconductor device) model [160, 161]. Starting with the photocurrent source

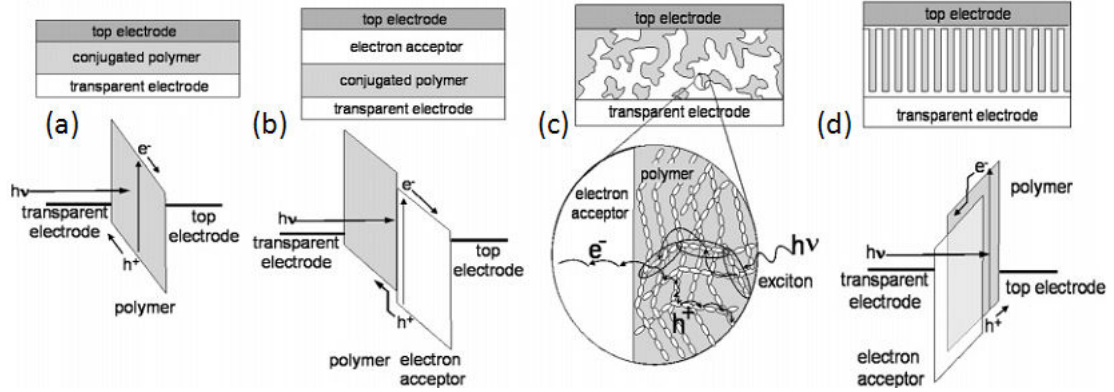


Figure 1.16: Four device architectures of conjugated polymer-based photo-voltaic cells: (a) single-layer PV cell; (b) bilayer PV cell; (c) disordered bulk hetero-junction; (d) ordered bulk hetero-junction [159].

which is simply the result of converting absorbed photons to free charge by the solar cell, then the diode representing the electron-hole recombination at the $p-n$ junction, the internal resistance of the cell to current flow is denoted by the series resistor, and finally, the leakage current through the cells (e.g., via pinholes) is accounted by the shunt resistor [160, 161]. Although the active layer in an OSC is a blend of two materials in heterojunction structure which is difficult to describe by a $p-n$ junction model used for the inorganic solar cells but this model is used

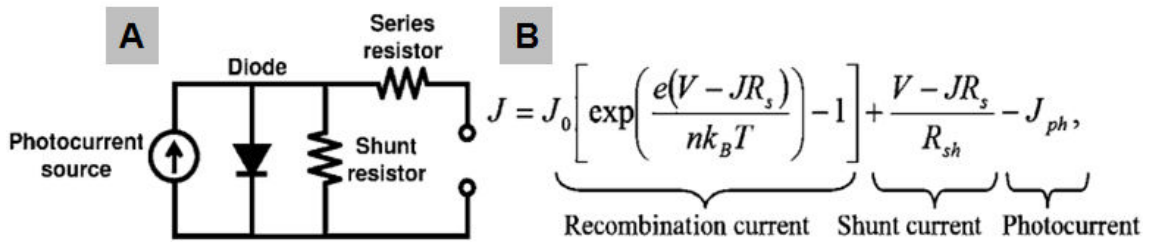


Figure 1.17: The commonly used equivalent circuit for a $p-n$ junction diode A) and the current density equation B) for solar cells. Note that the diode represents recombination current [160, 161].

commonly to consider active layer as roughly equivalent to the inorganic $p - n$ junction by considering the donor (P3HT an electron rich material, hence type n) and PC₆₀BM (acceptor, hole rich material, hence type p) as shown in the figure 1.18 [161, 162].

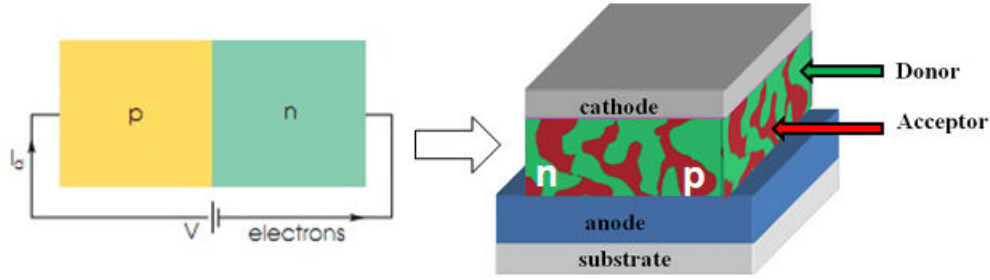


Figure 1.18: Bulk heterojunction in organic solar cells described by the $p - n$ junction in inorganic solar cells.

In the equation, J_0 is the reverse bias saturation current density, e is the elementary charge, R_s is the series resistance, n is the diode ideality factor, k_B is Boltzmann's constant, T is temperature, and R_{sh} is the shunt resistance. According to the original $p - n$ junction theory of Shockley, J_0 represents the saturation current density at reverse bias for an ideal $p - n$ junction diode [163].

1.4.2 Organic Solar Cell Mechanism

In a bi-layer organic solar cell, D/A active layer is the center of activity. The related four steps are briefly explained here [8, 164, 165].

1.4.2.1 Photon Absorption

In the first step in a PV process, the incident light strikes the active layer by passing through transparent electrode (ITO) and photons are absorbed by the active organic material (D/A). Upon the absorption of a photon, an electron in

the organic semiconductor is excited from the Highest Occupied Molecular Orbital (HOMO) to the Lowest Unoccupied Molecular Orbital (LUMO) of donor material. In organic semiconductors, HOMO and LUMO refer to energy bands that correspond to different hybridization states of the p-bonds and are analogs to the valence band and conduction band respectively in inorganic semiconductors. Upon absorption of photon, not only electron is excited from HOMO to LUMO in an organic semiconductor, but the electrons within other energy levels are excited as well. This is in contrast to the actual excitation of a free electron from the valence band to the conduction band in inorganic semiconductors. The strong Coulombic attraction between the electron-hole pair form an exciton [166, 167]. Since organic semiconductors have high absorption coefficients (typically $>10^5/\text{cm}$), hence a layer of a few hundred nanometers thickness is normally sufficient to absorb the incident light. High band gap limits the absorption of light hence, hence low band gap materials are preferred to maximize the absorption.

1.4.2.2 Exciton diffusion and charge separation

Once excitons are generated, they diffuse through the active layer (donor) towards D/A interface. As the potential difference between LUMO of donor and HOMO of acceptor is lower than that of the energy of the exciton, the transfer of an electron from the exciton to LUMO is an energetically favorable process whereas the hole remains in the donor material. However, they recombine and decay by giving away the energy (radiatively or non-radiatively) before dissociating at the D/A interface. After dissociation, electron-hole pairs form a charge pair called a geminate pair. These are still coulombically bound charges and have to be separated by an internal field. Common exciton diffusion lengths (the distance that excitons can diffuse before recombination) in organic semiconductors are very short, typically a few tens of nanometers [154, 168].

1.4.2.3 Charge Transport

After the exciton dissociation, the geminate pairs have to travel to electrodes for collection before they decay or recombine on the way. The main driving forces for the transport of holes to the anode and electrons to the cathode are drift and diffusion currents [169]. Electrodes are chosen in a way that their difference of potential creates a built-in electric field inside the solar cell. The drift current corresponds to carrier movement along the potential gradient within the solar cell. A high work function anode and a low work function cathode determine the open circuit voltage (V_{oc}) of the cell. The potential gradient is mainly determined by the choice of band alignment of donor and acceptor materials for hetero-junction electrodes in a solar cell. With the application of an external bias voltage, the internal electric field set by electrodes' work-function changes and hence the drift current changes also. The carriers then drift along the resultant internal electric field of the solar cell toward the respective electrodes for collection. Diffusion current also participates in carrier transport. This is the diffusion of carriers along the carrier concentration gradient developed around the hetero-junction. As the geminate pairs keep generating around hetero-junction of the cell, the concentration of electrons and holes tend to grow around the hetero-junction. This higher concentration of charge carriers is responsible for build up of concentration gradient. Thus, charge carriers diffuse along the concentration gradient away from the hetero-junction, resulting into the diffusion current. The diffusion current mainly dominates when the applied bias modifies in a way that internal electric field is nearly zero, while drift current dominates when the internal electric field is large [8].

1.4.2.4 Charge Collection

Once the charge carriers approach to the active layer/electrode interface, they are extracted from the active layer to the electrodes. The potential barrier

at the active layer/electrode interface has to be minimized so that maximum charge can be collected. Thus, the electrodes are chosen in a way that the work function of the anode ideally matches the donor HOMO, while the work function of the cathode is expected to match the acceptor LUMO. With this set up, the contacts are called ohmic contacts and at the same time, V_{oc} correlates positively with the difference between the acceptor LUMO and donor HOMO [170]. On the other hand, a corresponding ohmic contact cannot be established between active layer/electrode interface if the work functions of anode and cathode materials are not near from the donor HOMO or acceptor LUMO. If they are not, this will result in the carrier extraction behavior dominantly governed by the metal-insulator-metal (MIM) model [171]. ITO does this job well as an anode because its work function of 4.7 eV matches well with the HOMO of donor material P3HT [172] and low work function metals, such as Al, with work function of 4.2 eV match the LUMO of PCBM. Besides choosing right electrodes, certain materials can be inserted as interlayers between the electrodes and the active layer to better align the electrode work function and the active layer LUMO or HOMO. For example, a very thin layer of LiF, is usually evaporated on the active layer before fabricating the cathode to form an ohmic contact [173, 174]. TiO_2 [175, 176] and ZnO are solution-processable materials which have been used to enhance electron collection [177, 178]. For ohmic contact at anode electrode, some transition metals oxides, such as MoO_3 or WO_3 as interlayer/hole collector are used [178, 179, 180, 181]. The overall operation of solar cells is summarized in figure 1.19 showing the four steps: (1) Photon absorption leading to exciton generation; (2) Exciton diffusion to a donor/acceptor heterojunction; (3) Exciton dissociation at a heterojunction to form geminate pairs; (4) Carrier transport and carrier extraction at the electrodes.

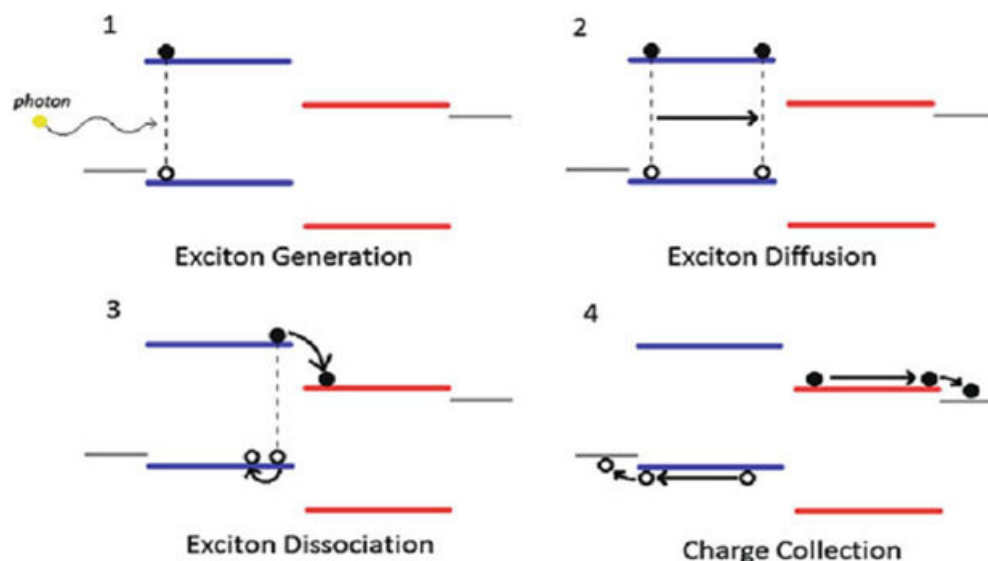


Figure 1.19: Illustration of the principle of charge separation in solar cell [8].

1.4.3 Characterization of Organic Solar Cells

Characterization of Organic Solar Cells involves some measurements which need to be described. The terminology used in the characterization of OSCs will briefly be explained. It is important to begin with by understanding what happens to an OSC in the dark and upon exposure to illumination. This is explained by Current-Voltage (J-V) characteristics curve/graph, also called I-V graph. In dark, the J-V curve passes through the origin of graph. No current flows if there is no potential applied to the electrodes of device. But once the device is under illumination, the J-V curve shifts downward. Figure 1.20 shows the J-V characteristic curve. The following terms are often used to characterize solar cells, some of the items can be seen on the J-V curve:

Air Mass (AM) is the measure of atmosphere sunlight that must travel to the earth's surface and is denoted by "AM(x)", where x is the inverse of the cosine of the zenith (the highest point that the Sun or the Moon reaches in the sky, directly above you) angle of the Sun. A typical value for solar cell measurements is 1.5,

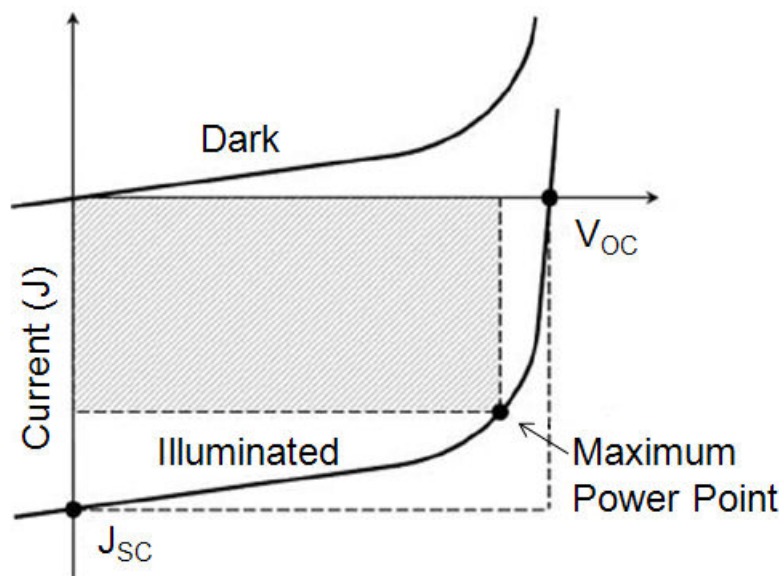


Figure 1.20: Graph of current (J) versus Voltage for photo-voltaic devices. The figure shows how the device characteristics change upon illumination. Key points on the graph are also indicated,[182].

which means that the sun is at an angle of about 48° . Air mass describes the spectrum of radiation, but not its intensity. For solar cell purposes, the commonly used value of intensity is fixed at 100 W/cm^2 .

Open-Circuit Voltage (V_{oc}) is the maximum possible voltage (V) across a photo-voltaic cell, the voltage at which the current density output is 0 A . V_{oc} mainly depends on the difference of work function of metal contacts. It depends on the difference of HOMO-LUMO between the donor and the acceptor when an ohmic contact at the electrodes is formed.

Short-Circuit Current Density (J_{sc}) is the current (I_{sc}) intensity per surface (A/m^2), the current that flows through an illuminated solar cell when there is no external resistance (i.e., when the electrodes are simply connected or short-circuited) or the current at which the externally applied voltage is 0 V . The short-circuit current is the maximum current and represents the number of charge carriers that are generated and eventually collected at the electrodes at short

circuit condition. This can be improved by a small band gap, a high absorption coefficient, a smaller phase separation, or a high carrier mobility.

Maximum Power Point (MPP) the point (I_{mpp} , V_{mpp}) on the J-V curve is the maximum power (P, a product of current and voltage, $P=JV$) and is illustrated in the figure as the area of the rectangle formed between a point on the J-V curve and the xy axes. The maximum power point is the point on the J-V curve, where the area of the resulting rectangle is the largest.

Fill Factor (FF) is the ratio of a photo-voltaic cell's actual maximum power output to its theoretical power output if both current and voltage were at their maxima, J_{sc} and V_{oc} , respectively. This is an important factor that helps measuring the performance of cell. It also defines the shape of J-V curve as the measure of the squareness of the J-V curve. The squarer the shape of J-V, the better the device is. The formula for FF in terms of the above quantities is:

$$FF = J_{mpp} \times V_{mpp} / J_{sc} \times V_{oc} \quad (1.15)$$

where J_{mpp} and V_{mpp} are the current density and the voltage at the point of maximum output power respectively.

Power conversion efficiency (PCE) is the ratio of power output to power input and represents the efficiency of the solar cell. In other words, PCE measures the amount of power produced by a solar cell relative to the power available in the incident solar radiation (P_{in}). P_{in} is commonly fixed at 100 W/cm² when solar simulators are used. This is the most general way to define an efficiency. The formula for PCE, in terms of quantities defined above, is:

$$\eta_e = J_{mpp} \times V_{mpp} / P_{in} = J_{sc} \times V_{oc} \times FF / P_{in} \quad (1.16)$$

Quantum Efficiency (QE), is the efficiency of a device as a function of the wavelength or the energy of the incident radiation. For a particular wavelength, it specifically relates the number of charge carriers collected to the number of photons shining on the device. QE can be reported in two ways: internal QE and external QE.

External Quantum Efficiency (EQE) also called Incident Photon to Current Efficiency (IPCE), is the measure of incident photon to electron conversion efficiency. This type of quantum efficiency includes losses by reflection and transmission. This gives the percentage of incident photons that are converted to carriers that are finally collected at the electrodes under short circuit conditions.

Internal Quantum Efficiency (IQE) refers to the efficiency with which photons that are not reflected or transmitted out of the cell can generate collectable carriers. By measuring the reflection and transmission of a device, the external quantum efficiency curve can be corrected to obtain the internal quantum efficiency curve.

1.5 Performance and Properties of Graphene TCEs

The interest in the graphene-based TCEs is introduced in this part. Apart from high optical transparency, high electrical conductivity and good thermal and chemical stability [183], [20], graphene is flexible unlike ITO which yields cracks on bending. Due to these attractive properties, graphene is investigated in several applications as TCE. Graphene is being envisaged as an enabling material which will not only replace ITO in mainstream application but will energize the drive for flexible electronics devices. Here, we will focus on the performance of graphene based TCEs for Organic Solar Cells. A single sheet or a mono-layer of graphene absorbing light between 400 nm and 6 mm in the UV region through direct inter-band transitions, while its absorption intensity remains nearly flat, approximately 2.3 %, throughout this spectrum as shown in the figure 1.21(a) and (b), it indicates that 4 sheets/layers (or less) of graphene can be applied to obtain comparable or even higher transmittance than provided by ITO (figure 1.21) [183, 184].

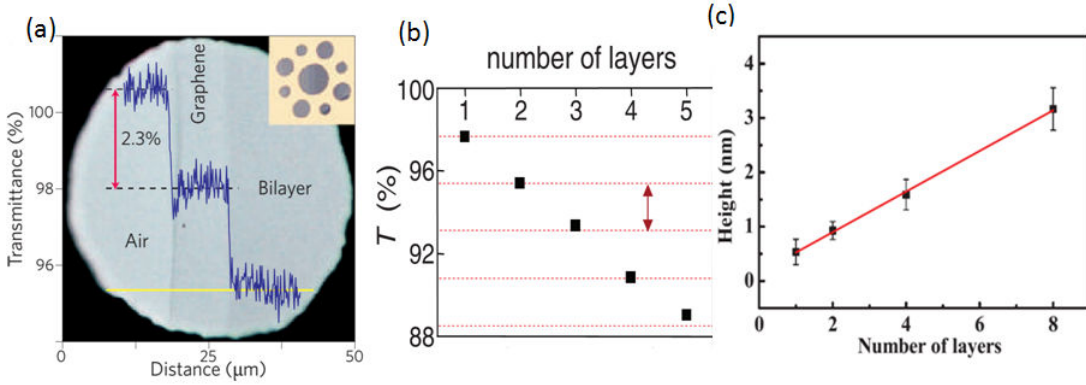


Figure 1.21: Transmission of SLG, and BLG (a), and up to five layer FLG (b), and AFM height as function of thickness of graphene (height obtained by AFM tapping-mode profile) up to 8 layers of graphene (c) [183], [46].

In terms of sheet resistance, single to few (up to 5) layers graphene from epitaxial and CVD methods can give best performance (sheet resistance $\sim 30\Omega/\square$, but generally one order of magnitude higher) [145]. LPE graphene has moderate values of sheet resistance. RGO, as starting material, is insulating (sheet resistance of 10^{12}), but can give resistance in the range of 10^2 to $10^5 \Omega/\square$, depending upon the rate of reduction, the type of reduction environment and the thermal conditions [88, 185, 186]. Most of the production methods render values of sheet resistance that are not sufficient for organic solar cells and hence they are doped with different types of materials to modify the conductivity and the type of carriers in thin films.

Sheet resistance can be reduced by nitric acid, a p-type dopant up to 108 from $272 \Omega/\square$ [59] for roll-to-roll (CVD) SLG. Polyvinyl alcohol (PVA) induces a n-type doping, and the sheet resistance for graphene obtained by micromechanical exfoliation can be dramatically decreased from value of $4 \text{ k}\Omega/\square$ to $400 \Omega/\square$, whereas transmittance remains unaffected [187]. One of the problem, however, of the doping approach is the long-term stability of doping, which is susceptible to degradation due to instability of doping and absorbance of moisture. This

issue warrants the use of chemical doping requiring long-term use/application. A curable polymer (poly(4-vinylpyridine)) coating can be applied over the doped graphene film to protect the properties of doped graphene film. This technique has displayed reliable protection of film and its sheet resistance stayed unaltered under ambient conditions for a period over 2.5 months [188].

Many groups have used graphene-based (graphene, few layer graphene or rGO) transparent conductive films (GTCF) into organic solar cells as transparent electrode and have demonstrated beyond the proof of concept and comparable with ITO electrode performance with graphene materials, on rigid and flexible substrates [189], [190]. Solution-processable rGO provides lower efficiency up to 1 % in OSC devices due to its high R_s which is in the range of 1-18 K Ω . Highly-doped, CVD-grown multi layer graphene used as a top (anode) electrode, and P3HT:PCBM as the active layer, was reported to show excellent efficiency of 3.2 % in flexible OSC device on a plastic substrate [191]. Figure 1.22 shows two device structures for OSCs: conventional and inverse, and their Current-Voltage (J-V) characteristics. Figure 1.22(a) shows a conventional device (Glass/LrGO/PEDOT:PSS/P3HT:PCBM/Al) structure using one step, fast laser reduced (LrGO) as an anode on a glass substrate [192]. Figure 1.22(b) shows an inverse structure device on a flexible polyimide (PI) substrate (PI/Metal/ZnO/P3HT:PCBM/PEDOT:PSS (Au)Graphene/PMMA) with CVD graphene used as anode [191]. J-V characteristics of both devices are shown by (c) and (d) for different thickness of LrGO and graphene (with variable number of sheets) conventional and inverse devices, respectively.

In a recent report, very high efficiency was obtained by using doped-CVD graphene on a flexible substrate with modified PEDOT:PSS (Graphene hole extraction layer (GraHEL), also called hole transport layer (HTL) to improve wettability of HEL which otherwise can hamper the homogeneous deposition of pristine PEDOT:PSS due to opposing nature of graphene (hydrophobic) and HEL (hydrophilic) (figure 1.23). They demonstrated that 3 sheets of graphene using a

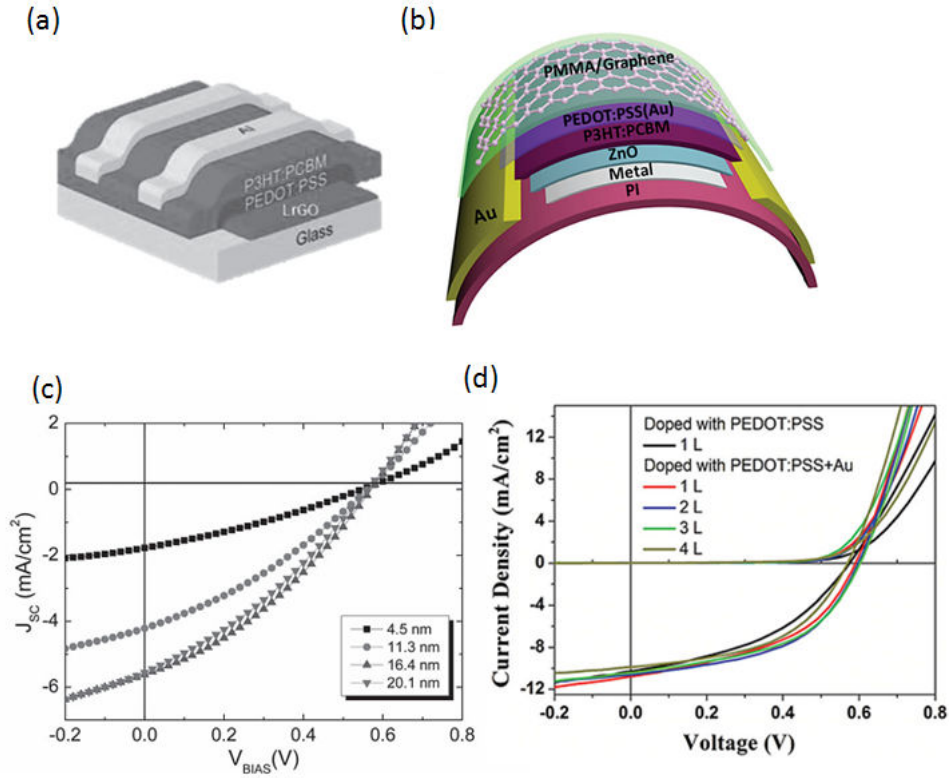


Figure 1.22: Organic Solar Cell structure using GTCEs. (a) Conventional device (Glass/LrGO/PEDOT:P3HT:PCBM/Al) structure for using LrGO as an anode, (b) Inverse structure device on flexible substrate (PI(substrate)/Metal/ZnO/P3HT:PCBM/PEDOT:PSS (Au)Graphene/PMMA) with CVD graphene used as cathode, (c) J-V characteristics of OPVs with different number of layers of graphene anode doped with PEDOT:PSS+Au or PEDOT:PSS only, and (d) J-V curves of the solar cells with various LrGO film thicknesses [192], [191].

more efficient bulk heterojunction (BHJ) provides highest reported efficiency of 4.33 %, so far [193].

Figure 1.23 shows the device structure and its J-V characteristics, showing flexibility of graphene and FLG and use as interlayer in a high efficiency device. Inset shows optical image of the fabricated device on flexible substrate.

These cells have also been demonstrated with active layer consisting of small molecular weight molecules, such as copper phthalocyanine (CuPc)/fullerene

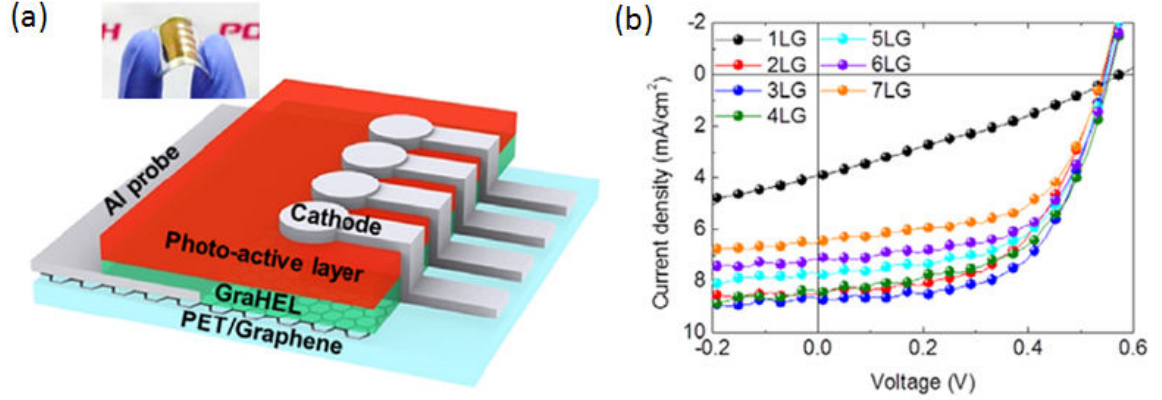


Figure 1.23: (a) Organic Solar Cell structure using modified PEDOT:PSS (GraHEL) and (b) J-V curves of the solar cells with varying film thickness/sheets of graphene [193].

C60/bathocuproine (BCP) as well. Earlier, an OSC with CuPc/C₆₀/BCP on rGO with a film thickness of 20 nm, an optical transmittance of 80 %, and a variable sheet resistance from 5 K Ω to M Ω /square was reported with poor device characteristics, efficiency of only 0.4 %, due to the enormously large sheet resistance [189]. CVD graphene with sheet resistance of 230 Ω /square at 72 % transparency showed power conversion efficiency of 1.18 % which was comparable with ITO-based control device (efficiency 1.27 %) [189]. Device structure consisted of Graphene/PEDOT:PSS/CuPc/C₆₀/BCP/Al where CuPc/C₆₀ formed the heterojunction, PEDOT:PSS and BCP served as Hole Transport Layer (HTL) and Electron Transport Layer (ETL) for anode (graphene) and cathode (Al) respectively. Figure 1.24 shows the band diagram of graphene-based device with small molecules and the J-V characteristics with bending cycles.

The conventional structure of OSC has evolved from ITO/PEDOT:PSS/photo-active layer/Al due to instability and performance degradation caused by oxidation of the top Al electrode to inverse structure by incorporating air-stable and high work function electrodes as Ag, CNT and ITO, which gave efficiencies of

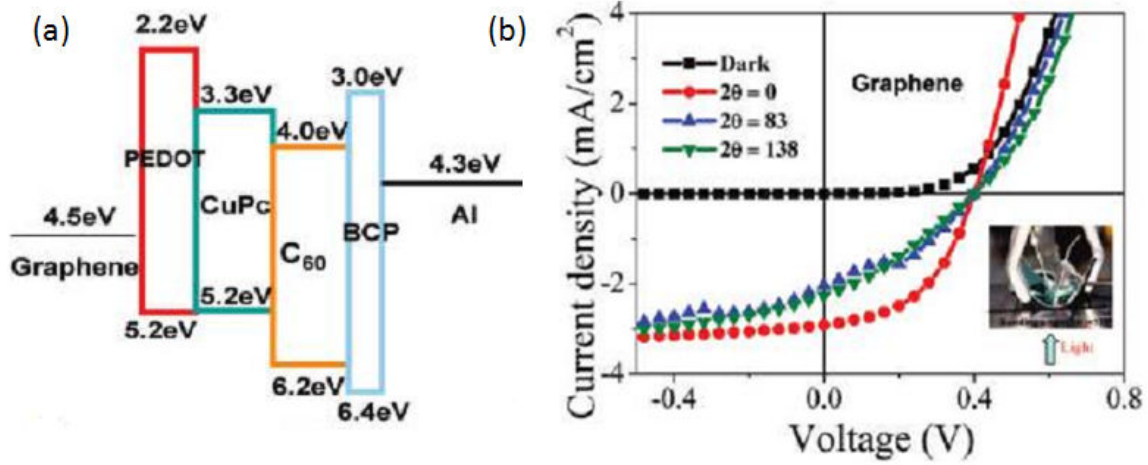


Figure 1.24: (a) Organic Solar Cell structure using small molecules and graphene-based TCE (b) J-V curves of the solar cells for different bending cycles [189].

1.3 % up to 3.2 % [194], [195], [196]. There are examples where graphene films have been used as cathode electrode, investigated towards their suitability for semi-transparent inverse structure solar cells. Laminated graphene was used in as top electrode in ITO/ZnO/P3HT:PCBM/GO/G structure, using a simultaneous thermal releasing/annealing technique. The device demonstrated PCE up to 2.5 % [197]. Later, an improved performance was demonstrated by using highly doped single-layer graphene as the top electrode of semitransparent organic solar cells. An efficiency of 2.7 % was reported by illumination of the device from graphene electrode side under the AM1.5 solar simulator. Further, it was stated that devices showed higher efficiency from the graphene than ITO side, due to the better transmittance of the graphene electrodes [198]. Table 1.7 shows the performance of some selected organic solar cell devices made using graphene-based transparent conductor films/electrode [145].

Recently, graphene cathode-based hybrid solar cells using two different photo-active materials, PbS quantum dots and the conjugated polymer P3HT, demonstrated power conversion efficiencies of 4.2 % and 0.5 %, respectively, under AM 1.5G solar simulator conditions [199].

Table 1.7: Performance of GTCFs in organic solar cells [145].

Graphene type	Sheet resistance	T (%)	PCE (%)
rGO*	1 k Ω sq ⁻¹	80	1.01
rGO*	17.9 k Ω sq ⁻¹	85–95	0.13
rGO-CNT	240 k Ω sq ⁻¹	86	0.85
LiGO	700 Ω sq ⁻¹	44	1.1
CVD-G doped with PEDOT:PSS	350 Ω sq ⁻¹	88	2.7
CVD-G doped with PEDOT:PSS and Au	158 \pm 30 Ω sq ⁻¹	90	3.2
CVD-G doped with SOCl ₂	450 Ω sq ⁻¹	90	2.5
CVD-G doped with HNO ₃	36.6 Ω sq ⁻¹	85	4.33

* Chemical reduction of exfoliated graphene oxide (GO).

Another type of organic solar cells which use organic dyes are the Dye-sensitized solar cells (DSSCs). DSSCs have attracted scientific community since last two decades due to low cost production, simplicity, and high conversion efficiencies with very recent report at 13 % efficiency [200]. Potential of graphene as conductor counter electrode has been investigated in this category of devices as well. Function of a counter electrode is to inject electrons into the electrolyte and help catalyze iodine reduction after charge injection in DSSCs [201]. Fluorinated multilayer graphene was shown to display a promising electro-catalytic activity toward triiodide (I₃) reduction in DSSC device. The device platinum-free multilayer graphene counter electrode demonstrated power conversion efficiency (PCE) of 2.56 %. Another report using a graphene nanosheet counter electrode claimed high PCE of 6.81 % in DSSC [202]. rGO films, when used as transparent counter-electrodes displayed an encouraging 2.64 % efficiency [87]. Later, a graphene film coated with conducting polymer, used as counter electrode displayed a high efficiency of 6.26 % (comparable to 6.68 % efficiency of the control device comprising Pt/ITO) in a platinum-free and inexpensive flexible device [203]. A short duration nitric acid treatment and a PEDOT:PSS film over graphene contributed to lower the sheet resistance and enhancement of PCE for the device. These results highlight the importance of graphene materials as counter electrodes in DSSCs.

However, to be fully commercialized, graphene production methods have to be optimized for low cost and high quality graphene films on a large scale. GTCFs are promising, environmentally favorable and flexible alternatives for TCEs to replace ITO. Pristine graphene, stacked FLG, doped graphene and rGO have demonstrated gradual improvement in performance in the TCFs in polymer and small molecule OSCs as bottom and top electrodes. Best performance in terms of PCE is demonstrated for doped CVD graphene, whereas large quantity graphene with compromised material properties is obtained by the LPE method. However, future of graphene TCEs is promising, as further optimization of production methods, deposition and non-volatile doping techniques continue to improve the material.

1.5.0.1 Carbon Nanotubes and their Hybrids

Since the first experimental observations of CNTs in 1991 [204], fundamental transport properties of more tubes have been studied, and a decade later it was reported that charge mobilities as high as $10^5 \text{ cm}^2/\text{V.s}$ can be attained in individual CNTs [205]. Despite their attractive electrical, optical and mechanical properties, the progress in CNTs applications has been slower than initially expected. Fundamental problems linked with CNTs are their production in large quantities with appropriate purity.

It is difficult to separate carbon impurities and catalyst-free CNTs. Further, as-produced CNTs contain a mixture of nanotubes of various lengths, diameters, tube number and chiralities. It involves therefore, tremendous effort and time to get nanotubes of suitable/desired features in large scale without the substantially increasing cost of CNTs production. There are several reviews which cover synthesis, yield, purification, transport and other important features of CNTs in detail, thus we will not focus on it here [206], [130], [207]. Thin films of nanotubes comprising random percolated networks of CNTs have emerged as

transparent material for opto-electronics applications [208], [209], and have been used as transparent conductor electrodes by several groups [210], [211], [212]. In order to obtain good quality flexible and transparent films, the transfer from a filter membrane onto a desired support via solvents [212] or in the form of LBL adhesive film grown by CVD method is necessary [213]. A study showed that films prepared by arc-discharge show good conductivity and transparency [214]. Vertically aligned CNTs with high thermal and good electrical conductivity have been reported as well [215].

Mostly, single wall nanotubes (SWNTs) have been studied for transparent conductive electrodes applications due to their good quality and good transparency for a larger spectrum from UV-Vis to near IR region (3-5 μ meter) [212]. Work-function of SWNTs (4.8-4.9 eV) networks matches well with that of ITO (4.7 eV), indicating that SWNTs can function as efficient hole charge collectors in the OSC anodes [121]. SWNTs films exhibit sheet resistance of few hundreds of Ω/\square which is an order of magnitude higher than in the case of graphene. In contrast to ITO, SWNTs can be deposited on PET substrates via solution-processable means, they are thermally conductive to sustain heat dissipation, and they offer high chemical inertness, even in an oxygen environment. CNT films made from solution-processable methods were demonstrated as anodes in opaque organic solar cells [138]. SWNTs were used as transparent conductor anode on glass substrate to replace ITO with a low efficiency of 1% due to low transmittance (45%) [216]. Soon, another report demonstrated organic solar cell with CNTs network as transparent electrode on flexible PET substrate with 85% transparency and sheet resistance of 200 Ω/\square , showing efficiency of 2.5% [217].

Later study suggested that CNTs electrodes can perform dual function as TCE and as an efficient Hole Transport Layer (HTL), thus eliminating PEDOT:PSS from the structure [218]. The structure replacing ITO with SWNTs (SWNTs/PEDOT/P3HT:PCBM/Al) demonstrated a device efficiency of 2.61% and the second one replacing ITO and PEDOT with single layer of SWNTs (SWC-

NT/P3HT:PCBM/Al) gave an efficiency of 1.43% whereas showing an inherent compatibility of SWNTs with the chlorobenzene solvent.

HNO₃-doped SWNTs demonstrated an efficiency of 3.1% for an OSC, close to the efficiency of control ITO device (3.6%) [219]. To support the concept of eliminating PEDOT:PSS, a device entirely made up with carbon nanotube network electrodes displayed a power conversion efficiency of 2.65% without PEDOT [220]. At the same time, multi-wall nano tubes (MWNTs) film used as a counter electrode in DSSC displayed higher performance with 7.7% of conversion efficiency [221]. The hybrid films consisting of Graphene-CNT have also been integrated as TCE in organic solar cells. One way to improve the properties of transparent film is using rGO/CNT hybrid film which could help lower the sheet resistance and/or modify the work function of TCF [222]. In order to understand how CNT/graphene hybrid will change the opto-electronic properties of thin film, a study [223] demonstrated that with the increase of graphene content (wt%), there was slight gradual decrease in transmittance of hybrid film but sheet resistance was improved. They achieved best transmittance of 80% with a sheet resistance of 100 Ω/\square for optimized hybrid films after acid treatment steps. Recently, Graphene Mesh electrode (GMEs) was produced from rGO using the standard industrial photo-lithography and O₂ plasma etching process on Si/SiO₂ substrate. This functioned as TCE with poly-(3-hexylthiophene)/phenyl-C₆₁-butyric acid methyl ester (P3HT/PC₆₁BM) as the active layer and displayed efficiency of 2.04 % [224].

1.6 Aim of Thesis

The aim of thesis is to integrate few layer graphene (FLG) nanomaterials as transparent conductor electrodes in the organic solar cells (OSCs) in place of the widely-used Indium tin oxide (ITO) anode electrode but also to envisage the potential use of these nanomaterials as conductive counter electrode (cathode). This consists of several subtasks including the production and optimization of FLG by low cost, high yield and facile mechanical and liquid exfoliation methods; and next establishment and optimization of deposition method to obtain (semi) transparent and conductive thin films of FLG materials by hot-spray method which has advantages of being simple, low-cost, scalable and potentially suitable for an unlimited surface coverage. After thin film deposition, investigation of (opto) electronic (electrical) properties and morphology/roughness of prepared thin films/charge transport devices are to be performed to find out their suitability for integration in the OSCs. Several other characterizations are also envisaged to increase the predictive understanding of FLG materials in general and FLG thin films in particular.

1.7 Organization of Thesis

This thesis is divided in to seven chapters. Each of which contains specific information from introduction, methods and materials to results and conclusions.

The introduction to the subject and literature review is presented in the chapter 1. This include the criteria for choosing a transparent conductor electrode and provides the general overview of carbon-based (graphene, FLG, reduced graphene oxide and carbon naotubes) materials by briefly over-viewing their general characteristics, synthesis methods, charge transport properties, integration in thin, transparent conductor films (TCFs) and their optoelectronic properties. Moreover, this chapter provides a brief introduction to OSC devices

and further develops to survey the performance of carbon-based transparent films in OSCs as carbon-based transparent conductor electrodes (CTCEs). The chapter 2 covers the description of the materials and methods used to carry out this work. This includes the preparations of methods for obtaining different FLG materials and film formation by hot-spray method. Further the details of the characterization techniques that were applied for the investigation, are given. The chapter 3 contains the results of thin FLG films/charge transport devices for the materials obtained by mechanical ablation/exfoliation of pencil lead and synthetic graphite, and microwaves-assisted liquid exfoliation of expanded graphite (EG), respectively. These results include charge transport studies, transparency, roughness/thickness, morphology and work-function studies of these films/devices. The chapter 4 further presents the results for reduced graphene oxide (rGO) and rGO/FLG composite materials obtained by simultaneous exfoliation and reduction by microwaves-assisted liquid exfoliation of graphene oxide (GO) and GO/EG composite in ethylene glycol medium. Their investigations are similar to those presented in chapter 3. The chapter 5 presents the results for hybrid devices that were prepared with carbon nanotubes (CNTs), i.e. CNTs/FLG and CNTs/rGO. The preliminary results for OSC devices fabricated by integrating the carbon-based transparent conductor electrodes are presents in the Chapter 6. Finally, the general conclusions and perspectives for future work are given in the chapter 7.

2 Experimental: Materials and Techniques

The information about the materials, the methods and the characterizations that have been used to carry out research work in this thesis, is presented in this chapter. This will begin with listing the materials first in the section 2.1, then further details on their preparation and synthesis methods for materials will be presented in the section 2.2. Film formation by Hot-spray method and device fabrication will be described in the section 2.3. Solar cells preparation will be discussed in the section 2.4. Characterization techniques that have been employed will be discussed finally in the section 2.5.

2.1 Materials

The following materials have been used during experiments:

A) Carbon/graphitic materials used in the powder form, for film formation and preparation of charge transport devices

1. Few Layer Graphene (FLG) powder obtained by mechanical ablation of Pencil Lead (commercially available B9 pencil).
2. FLG powder obtained by mechanical ablation of synthetic graphite: Highly Ordered Pyrolytic Graphite (HOPG).
3. FLG flakes obtained by μ -waves assisted liquid phase exfoliation (LPE) of expanded graphite (EG) in toluene purchased from Carbone Lorraine TM.
4. Graphene Oxide (GO) obtained by the modified Hummer's method.
5. Reduced Graphene Oxide (rGO) obtained by μ -waves assisted reduction of graphene oxide alone by microwave irradiation.
6. Reduced Graphene Oxide-Few Layer Graphene (rGO-FLG) obtained from μ -waves assisted liquid phase exfoliation of graphene oxide and expanded graphite

composite.

7. Multiwalled Carbon Nanotubes (CNTs): NanocylTM (3100 Series Thin Multi-wall Carbon Nanotubes) produced by the Catalytic Chemical Vapor Deposition (CCVD) process with carbon purity >95%, metal oxide content <5%, average length and diameter of 1.5 μm and 9.5 nm, respectively. CNTs were used as received without further purification.

Table 2.1 provides the summary of these materials with their abbreviations. Further details on the methods will be presented later in the section 2.2.

Table 2.1: Summary of carbon/graphitic materials used.

Raw Material	Type/ Form	Obtained by (Method)	Obtained from (Material/Company)	Short Name
Few Layer Graphene (FLG)	Solid/ Flakes	Mechanical Ablation Exfoliation	Pencil Leads (B9)	FLG-Abl
Few Layer Graphene (FLG)	Solid/ Flakes	Mechanical Ablation Exfoliation	Synthetic Graphite	FLG-HOPG
Expanded Graphite (EG)	Solid/ Flakes	Thermal expansion of graphite	Carbone Lorraine	EG
Few Layer Graphene (FLG)	Solid/ Flakes Powder	μ -waves-assisted liquid phase exfoliation	Expanded Graphite	FLG- μ -w
Graphene Oxide (GO)	Solid/ Flakes	Modified Hummer's Method	Graphite Flakes	GO
Reduced Graphene Oxide (rGO)	Solid/ Flakes	μ -waves-assisted liquid phase exfoliation	Graphene Oxide	rGO
Reduced Graphene Oxide (rGO)	Solid/ Flakes	μ -waves-assisted liquid phase exfoliation	GO and EG	rGO/FLG
Multi-wall Carbon Nanotubes (MWCNTs)	Solid/ Flakes	catalytic chemical vapor deposition (CCVD)	Nanocyl	CNTs

B) Materials used in the fabrication of Organic Solar Cells

1. Poly(3-hexylthiophene-2,5-diyl) (P3HT) (4002-E(2013)) electronic grade powder/flakes with purity of 98.8% purchased from Rieke Metals, IncTM, used as received.

2. [6,6]-Phenyl C61 butyric acid methyl ester (PC₆₀BM) powder, with purity of 99.5%, purchased from Solenne b.v.TM, powder used as received.

3. Poly(3,4-ethylenedioxythiophene)-poly(styrenesulfonate) (PEDOT:PSS) liq-

uid form, with conductivity (σ) of 1 S/cm, purchased from CLEVIOSTM HTL Solar and used as purchased.

C) Substrates

Glass and quartz substrates of 1 cm \times 1 cm and 2 cm \times 2 cm size were used for film formation.

ITO with $R_s=15 \Omega/\square$ and patterned contacts on glass substrates were purchased from the Luminescence Technology CorporationTM Taiwan.

D) Solvents

Various solvents were used to prepare dispersions of the above materials and/or to clean the substrates. The table 2.2 lists the specific use of these solvents.

Table 2.2: List of solvents and their use.

Solvent (formula)	Purity (%)	Purchased from	Used for
Ethanol (C ₂ H ₆ O)	99.8	Sigma Aldrich	Dispersion of FLG
Toluene (C ₇ H ₈)	99.3	Sigma Aldrich	Dispersion of EG
Ethylene Glycol (C ₂ H ₆ O ₂)	99.5	FLUKA	Dispersion of GO and GO/EG hybrid materials
Chloroform (CHCl ₃)	99	Carlo Erba	Dispersion of CNTs
Acetonitrile (C ₂ H ₃ N)	99.9	Acros Organics	Dispersion of CNTs
Isopropanol (C ₃ H ₈ O)	99.7	Carlo Erba	Dispersion of CNTs/ Cleaning ITO/glass substrates
Acetone (C ₃ H ₆ O)	99.8	Carlo Erba	Cleaning ITO/glass substrates
De-ionized water (H ₂ O)	(pH \sim 7)	home-purified	Cleaning ITO/glass substrates
Orthodichlorobenzene (ODCB) (C ₆ H ₄ Cl ₂)	99	Sigma Aldrich	Dispersion of PC ₆₀ BM/P3HT blend

E) Gases

Gases used in thermal treatment/reduction steps were purchased from SOL France and are used as purchased:

Argon, Hydrogen, Helium, and Nitrogen

F) Sonicators and stirrers

The following sonicators/stirrers were used for FLG, CNT, EG, GO and GO/EG

dispersions:

1. Low-power bath sonicator (Elmasonic 102168022) with mild sonication for different durations.
2. Finger/tip sonicator (Bandelinsonoplus uw 2200) at 30% power for different durations.
3. Flasher Blobblock Scientific MR 3001 K Stirrer was used for stirring the PC₆₀BM/P3HT blend in ODCB suspension at 800 rotation per minute (RPM) of 60 °C for 48h.

G) Spray-coating apparatus The following materials were used during spray-coating method, the details of which will be presented in the section 2.3:

1. Air used as a carrier medium
2. Airgun (Hi-line Iwata)
3. Hot plate

H) Ovens and reactors for thermal annealing and reduction

The reactors are in quartz tubes

The ovens are tubular ovens, Early(max. temp. 1000 °C)

They were used for thermal annealing and reduction of FLG, rGO and CNT and hybrid films.

2.2 Methods and Techniques Used for Preparations of Materials

In this section, the details of the methods used to obtain the materials for preparing transparent conductor films are presented.

2.2.1 Few Layer Graphene Synthesis by Mechanical Ablation

This section describes how the FLG materials (powder form) used in this work, were obtained. These materials were subsequently used to prepare FLG dispersions in ethanol and to prepare FLG films on planar substrates by hot-spray method. Later, these FLG films will be called charge transport devices after the deposition of contact electrodes for the study of charge transport properties of FLG. This FLG was produced by mechanical ablation from different starting materials, such as pencil lead (B-9 grade) and synthetic graphite: Highly Ordered Pyrolytic Graphite (HOPG). FLG from pencil lead will be introduced first and then FLG from synthetic graphite will be presented. Both types of FLG were obtained by mechanical thinning/ablation process but the difference was in the starting material and post-synthesis treatments, which will be briefly discussed below.

2.2.1.1 Few Layer Graphene Synthesis by Mechanical Ablation of Pencil Lead

This method was prepared by our group and reported in an earlier work [40]. Commercially available pencil leads were used to synthesize FLG by a mechanical thinning principle displayed in figure 2.1 [40]. These pencil leads were ablated against the rough glass disk continuously, in an automated system, and assisted with simultaneous ultrasonication, in order to get FLG in powder form. Further, the obtained FLG in ethanol suspension has to undergo harsh filtering, purification and drying steps involving acid and base treatments for several hours, to remove the impurities such as the inorganic binder contained in the pencil lead. After these steps, FLG was obtained in powder form for further use [40]. These FLGs had an average lateral size of few micrometers, and consisted of 1-20 sheets. Analyses showed that the method produced good

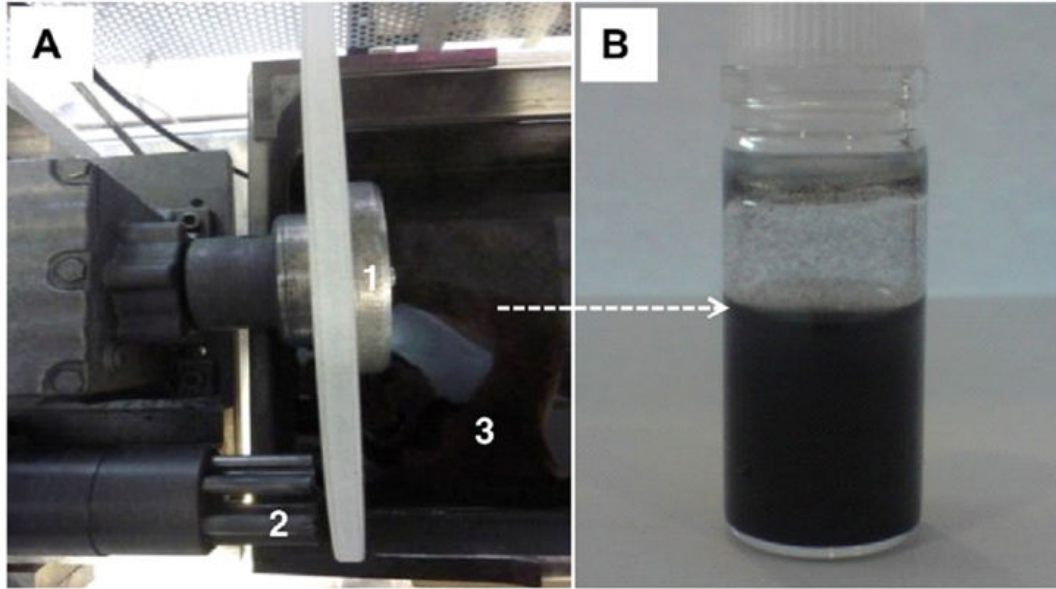


Figure 2.1: A) Optical photo showing the main part of the mechanical set-up to produce the FLG from the pencil lead by a mechanical ablation where: (1) is the glass disk with rough surface, (2) pencil leads, (3) an ultrasonication bath containing solvent, B) suspension of the FLG in the ethanol medium.

quality graphene with high yield (60% yield of the starting material) with added advantages of being simple, fast, low-cost and scalable but was poorly selective for the number of sheets, the lateral size of flakes, and size of sheets within individual flakes. This FLG will be further called FLG-Abl in the text to indicate FLG from Ablation (mechanical exfoliation) of pencil lead.

2.2.1.2 Homogenization and Crystallization of Few Layer Graphene by μ -waves-assisted Oxidation in Water Oxidation in Water

A 30 mL amount of distilled water was added to 300 mg of FLG and the suspension was stirred and heated at 160 °C for 1h under the μ -waves irradiation of 400 W (FLG-H₂O). The powder was next filtered and dried at room temperature for 24h and at 110 °C for 2h, respectively. Prior to oxidative treatment, the FLG-Abl (solid/powder) was annealed in Ar at 900 °C for 2h.

2.2.1.3 Few Layer Graphene Synthesis by Mechanical Ablation of Synthetic Graphite

On the pattern of FLG from pencil lead, disks of synthetic graphite materials like HOPG was ablated against a rough glass surface in a home-grown set-up to obtain FLGs. During ablation process, a controlled flow of ethanol was carried on in order to collect the ablated FLGs in a beaker. The suspension of FLGs in ethanol was kept for 24h for decantation in order to let the thicker flakes settle down. The thinner FLGs floating in the ethanol (supernatant) will be collected from the suspension after 24h. These FLGs will be called FLG-HOPG24h in the manuscript. The approximate concentration of HOPG24h was determined to be 0.1mg/mL ethanol. For all the materials obtained by ablation as explained above, hot-spray method was applied for film formation, which will be described later in 2.3.

2.2.2 Microwave-assisted Liquid Phase Exfoliation of FLG and Reduced Graphene Oxide (rGO)

Expanded Graphite and Graphene Oxide were used as starting materials to obtain FLG and reduced graphene oxide (rGO) by the microwave irradiation method, respectively. The Mars (CEM Corp.) microwave oven was used for these experiments with the following characteristics: adjustable power between 300 and 1200 W and maximum temperature of 250 °C. First, the synthesis of Few layer Graphene from Expanded Graphite in Toluene will be presented, then Ethylene Glycol-mediated reduction of graphene oxide and expanded graphite will be described.

2.2.2.1 Few layer Graphene by Microwave-assisted Liquid Phase Exfoliation (LPE) of Expanded Graphite in Toluene

400 mg of raw expanded graphite (EG) was mixed with 200 mL toluene (2 mg/mL), dispersed in the liquid phase and homogenized in a low-power sonic bath (Elma sonic 102168022) for 5 minutes and a tip sonicator (Bandelinsonoplus uw2200) at 10% power for 10 minutes, respectively. Prior to μ -waves heating, the EG-toluene suspension was sonicated in closed vessel and then stirred for 24h, in order to help intercalation of toluene at the edges, cracking of EG. The suspension was then ready for microwave irradiation experiment. Suspension was then put into four reactors in equal quantity (50 ml \times 4) and they were placed inside the chamber of the microwave oven within the following conditions:

- The microwave irradiation was set at the power of 600 W with a ramp of 1 min and a duration of plateau for 10min.
- Maximum infra-red (IR) temperature and pressure were set to 160 °C and 40 bars, respectively.
- The suspension was cooled for 15 min.

The FLG sheets were formed as a suspension in toluene phase above the solid residual EG which remains at the bottom. First there is an intercalation of toluene at the edges, at the nano-cracks, and than the very fast heating (by μ -waves) helps to exfoliate (extract) the sheets due to the rapid rise of local surface temperature. The suspension was left for decantation for 90 min and the FLG sheets in toluene were extracted from the supernatant, which was formed above the precipitated residual EG. After decantation they were kept in an oven for drying at 120 °C for 20h. The final mass of the FLG was measured to be 27 mg (around 7 % yield) after this drying step. The yield was improved up to \sim 20% by adding an additional 24h stirring step prior to μ -waves treatment. A similar procedure was already reported for NH_4OH exfoliated EG in [225].

2.2.2.2 Reduced GO from Graphene Oxide (GO) and Expanded Graphite (EG) Composite in Ethylene Glycol

Graphene oxide (GO) was reduced under μ -waves in ethylene glycol to obtain rGO. Expanded graphite (EG) and GO were sonicated in ethylene glycol separately, and the two suspensions were mixed and treated by μ -waves to help exfoliation (extraction) and reduction in rGO-FLG. Graphene oxide was prepared by a modified Hummer's method from graphite plates as described in [226]. Two solutions were prepared by mixing GO alone in ethylene glycol with a concentration of 1 mg/mL (100 mg/100 mL), and GO/EG (0.33:1 wt%) composite in ethylene glycol with a concentration of 2 mg/mL (60 mg/120 mL), respectively. The suspensions were dispersed by tip sonicator (Bandelinsonoplus uw2200) at 15% power for 3h at 40 °C. After sonication, about 80% of both suspensions were taken in flasks in order to separate heavier from lighter material to maximize the chances of obtaining thin FLGs. The figure 2.2 shows the raw materials and the sonication steps for both materials which allows the adsorption of GO on EG and probably to induce the exfoliation of EG before performing the μ -waves experiment for exfoliation and reduction. Both suspensions (GO alone and GO/EG composite) were separately put into four reactors (15ml \times 4) each, and reactors were then placed inside the microwave oven. Various conditions were attempted and the following conditions were retained for both suspensions:

- The microwave irradiation was set at 800 W with a ramp of 1 min and a duration of 15 min.
- Maximum IR temperature and pressure were set to 200 °C and 40 bars, respectively.
- The suspensions were cooled for 15 min.

After the exposure to microwaves, the reduced graphene oxide was recovered with a yield of 0.7 mg/mL (70%) and 1 mg/mL (50%) for starting material GO and GO/EG composite (now called rGO and rGO/FLG), respectively. The suspen-



Figure 2.2: A) Raw materials, B) Sonication and exfoliation procedure before the microwave experiment.

sions were further diluted by adding ethanol twice the volume of ethylene glycol (e.g. 20 mL of ethanol was added in 10 mL of ethylene glycol-containing product after microwave irradiation, modifying the concentration to ≈ 0.25 mg/mL and 0.33 mg/mL for GO and GO/EG composite, respectively). This was done in order to lower the boiling point of the solvent which was high for ethylene glycol alone (c.a. 190°C). The rGO samples obtained from both GO and GO/FLG in ethylene glycol-based solutions were used to grow thin films on glass/quartz substrates with various deposition quantities using the spray-coating method. These films are further called rGO and rGO/FLG, respectively. Table 2.3 provides the summary of the prepared FLG/rGO materials by different methods discussed in this section.

Table 2.3: Summary of methods of producing FLG/rGO materials.

Exfoliation/Reduction Method	Raw Material/Precursor	Media/Solvent	Obt. Product	Short Name
Mechanical Exfoliation	Pencil Leads (B-9)	Rough glass disk/Ethanol/Toluene	FLGs	FLG-Abl
Mechanical Exfoliation	Synthetic Graphite (HOPG)	Rough glass disk/Ethanol	FLGs	FLG-HOPG24h
Liquid Exfoliation/ μ -waves	Expanded Graphite	Toluene/ μ -waves	FLGs	FLG- μ -w
Liquid Exfoliation/ μ -waves	Graphene Oxide	Ethylene Glycol/ μ -waves	rGO	rGO
Liquid Exfoliation/ μ -waves	Graphene Oxide/Expanded Graphite Composite	Ethylene Glycol/ μ -waves	rGO/FLG	rGO/FLG

2.2.3 CNTs dispersion

Different solvents with different concentrations were tested to prepare CNTs dispersions in order to find the suitable solvent and concentration, respectively 2 mg each was initially put into 40 mL (0.05 mg/mL) of a solvent such as: ethanol, chloroform, ethylene glycol, acetonitrile, and isopropanol. By visual examination, it was found that CNTs had formed better dispersion in acetonitrile or isopropanol and was stable for several hours as compared to the other three solvents. To further homogenize the dispersions, the suspensions were diluted to a concentration of 0.025 mg/mL by doubling the volume of solvents and this concentration was retained for further use of these suspensions in the formation of thin films. CNTs dispersions were used to prepare the hybrid films with other materials, such as FLG and rGO by spray method. These films made up of CNT/FLG, CNT/HOPG and CNT/rGO hybrids were prepared by always depositing CNTs ahead of other materials (FLG/HOPG/rGO) to minimize the roughness issues.

2.3 Film Formation for charge transport devices by Hot-spray Method

Hot-spray method was used to prepare thin films of FLG and rGO materials obtained by the above methods (mechanical and μ -waves-assisted liquid exfoliation), which would serve as transparent conductor films for the study of charge transport properties by electrical measurements. Hybrid films of these materials were also prepared with CNTs. Different concentrations of these materials were tested in different solvents. Films were prepared on a preheated glass/quartz plates ($1/2 \text{ cm}^2$, respectively) at 120°C under ambient air. Glass plates were cleaned in ethanol for 15 min in sonic bath before deposition. Different volumes of FLG/rGO suspensions (mostly in ethanol) were deposited using Airgun (Hi-line Iwata).

The glass/quartz plate substrate was continuously heated during the material deposition and the temperature fluctuated between $80\text{-}120^\circ\text{C}$ during deposition. Air was used as the carrier gas at a variable inlet pressure between $0.5\text{-}1.5$ bar. The nozzle diameter of the gun was variable ($0.22\text{-}0.3 \text{ mm}$) and its distance from the substrate was 12 cm .

Some of the $2 \text{ cm} \times 2 \text{ cm}$ (4 cm^2) samples were used as transparent conductor electrodes for fabricating OSCs. These will be called carbon-based TCEs (CTCEs) as when used as group term and they will be referred to, with their generic names as FLG-Abl, FLG-HOPG, rGO, CNTs/FLG-Abl and so on so forth when used as individual films. Figure 2.3 shows the FLG dispersion in ethanol and hot-spray set up.

2.3.1 Electrodes Deposition by Thermal Evaporation

Before Au evaporation, a new configuration of masks for Hall Effect measurements was designed, using Labview interface for a laser (YAG epitherm610

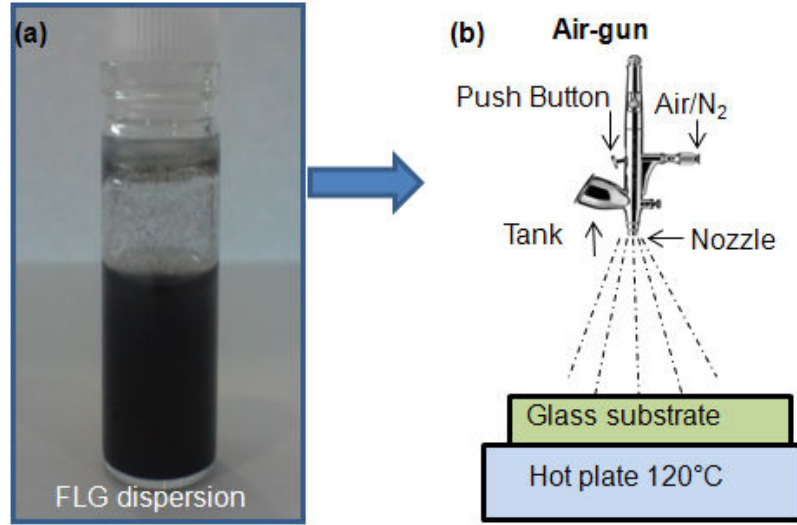


Figure 2.3: (a) FLG dispersion in ethanol, (b) set-up of spray coating by air-gun on hot plate.

quantronix model 114). The laser has the following specifications: Intensity 30A, repetition rate 25kHz, wavelength 1064 nm, pulse 100 ns, laser focus spot on sample 100 μm , continuous power 6 W, and cutting speed of 100 μ/sec . The masks were cut with the following conditions: 60 mm/s at 30A intensity.

Chromium/Gold (Cr/Au) electrodes were deposited on the top of the FLG films by evaporation (Home-made evaporator at the rate of evaporation of 3-7 $\text{\AA}/\text{s}$ for Au and 1 $\text{\AA}/\text{s}$ for Cr with a vacuum of 4×10^{-7} mbar) to prepare charge transport devices for electrical measurements. The thicknesses of deposited chromium and gold electrodes on the top of graphene film were 2.5 nm and 30 nm, respectively, for each sample.

2.4 Solar Cell Preparation

Solar cell preparations steps are outlined here.

The donor-acceptor solution (P3HT/PC₆₀BM)

The prepared solution (40 mg of PC₆₀BM/P3HT (1:0.7)) was taken in a small

flask and mixed with ODCB (40 mg/mL) and placed on the stirrer for stirring the blend in ODCB suspension at 800 rpm at 60 °C for 48 hours inside the glove box.

Thermal evaporation and substrate cleaning

Cr 2.5 nm and Au 25 nm were deposited by thermal evaporation on all substrates/samples (CTCFs/CTCEs and reference ITO).

The ITO reference cell was cleaned three times for 15 min, each in acetone, isopropanol and deionized water in mild ultrasonic bath at 45°C.

UV Ozone treatment

Few samples (CTCF/CTCE) were treated under UV to activate the surface before PEDOT:PSS deposition for 2 min and some of them were retained as untreated. Subsequently, the reference ITO substrate/cell was treated for 15 min under UV ozone.

PEDOT: PSS deposition

PEDOT:PSS was deposited using spin-coating method with the following conditions:

Few hundreds of μL of PEDOT:PSS was spin-coated on all cells with speed=3000 rpm and acceleration=1000 rpms/s for 60s. CTCF/CTCE samples without UV ozone treatment remain hydrophobic and the deposition of PEDOT:PSS is then not uniform on the surface of CTCFs/CTCEs. All samples were thermally-annealed on a hot plate at 140 °C for 30 min inside the glove box.

Active layer

The spin-coating method was used for deposition of P3HT:PCBM blend as well with following conditions in 2 steps: step 1: speed=1250 rpm and acceleration=200 rpm/s for 90s; step 2: speed=2000 rpm; and acceleration=200 rpm/s for 120s. All samples were thermally-annealed on a hot-plate at 140 °C for 15 min inside glove box.

Counter electrodes (Ca/Al) deposition

Ca (20 nm) and Al (120 nm) electrodes were deposited by thermal evaporation

inside the glove box.

J-V characterization

The current density-voltage (J-V) characteristics of the reference ITO device and carbon-based OSCs were measured with a Keithley source 4200 SCS measurement unit, under darkness and illumination in conjunction with a solar simulator under AM 1.5 G conditions (Oriel Xenon 150 W) and a 100 mW/cm² power flux on an active device surface of 0.12 cm². The device performances in terms of V-I response and efficiency were measured in glove box under nitrogen atmosphere. Mr. Thomas Regrettier and Nicolas Zimmermann helped with solar cells fabrication and characterizations.

2.5 Characterizations Techniques

The following characterization techniques have been employed to study the structural, (opto) electronic properties, and the morphology of graphene materials and films. This section will start with the description of electrical characterization first.

2.5.1 Electrical Characterizations for Charge Transport Measurements by Two Probes, Four-Point Probes (FPP) and Hall Effect (HE)

In order to study the charge transport of these carbon-based (FLG/rGO and hybrids with CNTs) films, electrodes must be deposited on these films to facilitate the electrical measurements by providing ohmic contact and preserving underlying films from degradation. Further details on electrical characterizations are provided for each technique below.

2.5.1.1 Two Probes for Electrical Resistance Measurements

A Keithley 4200-SCS semiconductor characterization system was used for two-probes electrical resistance (R) measurements with a 4200-SMU card unit in ambient environment. The SMU card unit operates as a voltage or current source (depending upon source function) in series with an I-Meter (ampere meter), and connected in parallel with a V-Meter (volt meter). Current and voltage are regulated (limited) by respective limiting circuits (I-Limit and V-Limit, respectively) to the programmed compliance value of the unit. By injecting a current (I), the potential difference (V) can be measured across the same terminals and vice versa. Figure 2.4A shows the device (Organic Field Effect Transistor, OFET device supplied by FRAUNHOFER IPMS) configuration with variable gaps between electrodes (2.5, 5, 10 and 20 μm) for two probes and figure 2.4B shows the SEM image of a 2.5 μm device after FLG deposition over it.

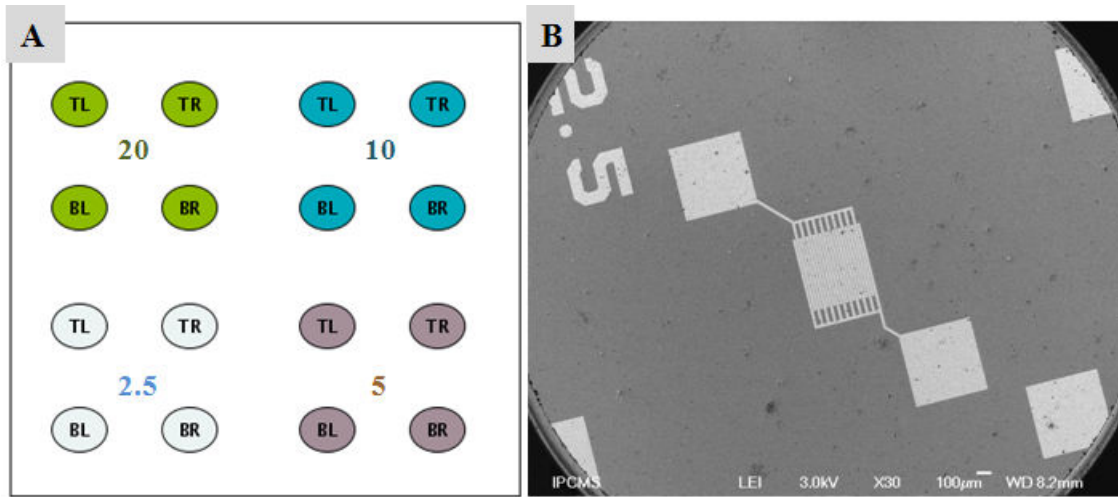


Figure 2.4: A) Device configuration with variable gaps between electrodes (2.5, 5, 10 and 20 μm) for two probes measurement (T =top, B = bottom, R = right and L =left) and B) SEM image of the 2.5 μm device after FLG deposition.

2.5.1.2 Four-Point Probes (FPPs) for R_s Measurements

The resistivity, expressed in units of ohm-centimeters (ohm.cm) can be determined using either a four-point probe or a Van der Pauw configuration/measurement technique. The most common method for measuring resistivity is the four-point probes method (FPPs). A Keithley 220 programmable current source in conjunction with a Hewlett-Packard 34401A multimeter was used for four-point probes sheet resistance measurements (R_s) in ambient environment.

FPPs also allow to measure two-dimensional sheet resistivity of thin films by injecting/inducing the current through two extreme (external) probes, and measuring voltage difference (V) between two middle probes, created by current flowing through the sample. The scheme is given in figure 2.5.

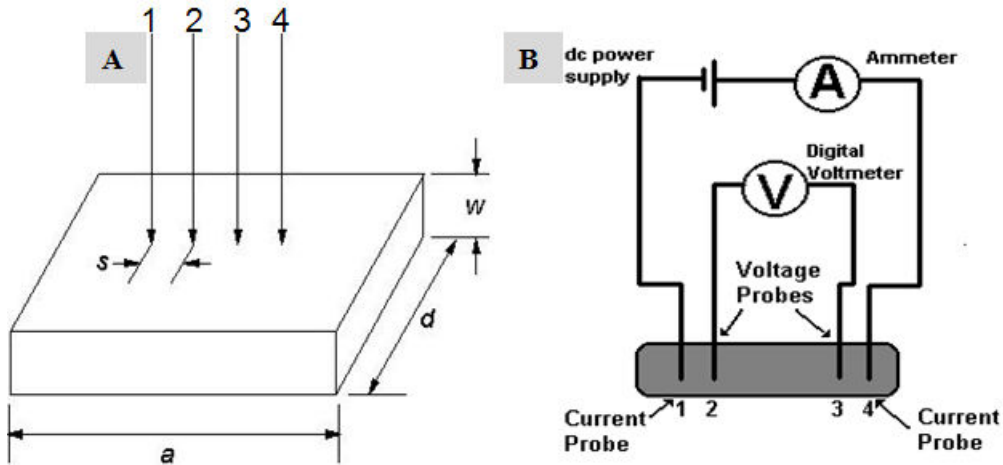


Figure 2.5: A) Scheme showing the geometry of sample and probes in FPPS measurement, B) scheme showing the measurement principle, where extreme probes are used to inject the current in the sample under investigation and middle probes measure the voltage drop caused by the induced current across the sample. The spacing between probes is equal to s and is constant for all four probes from 1 to 4 as shown in A. The distance among probes in B is arbitrarily exaggerated for a better visualization only.

If the spacing between the probe points is constant, the conducting film thickness is less than 40 % of the spacing, and the edges of the film are more than

4 times the spacing distance from the measurement point, the sheet resistance (R_s) of the film is given by Ohm's law and a geometrical correction factor as follows:

$$R_s = \frac{V}{I} \times F2 \quad (2.1)$$

The R_s is the calculated sheet resistance of sample in Ω/\square , V is the measured potential difference in Volts, I is the induced current in Amperes, and $F2$ is a geometrical correction factor which takes into account the length (a) to width (d) ratio (a/d) of the sample, and the spacing s between the probes for rectangle or square samples. It is precisely based on the ratio of the width to the probe spacing (d/s) and sample size or length to width ratio (a/d) [227]. Since our samples are $2 \text{ cm} \times (4 \text{ cm}^2)$, and the spacing (s) is 0.635 mm , d/s ratio is around 31, so a factor 4.45 or 4.51 corresponding to the $d/s < 40$ can be applied. In our calculations, a value of 4.45 was chosen. Further, chart with calculations of geometrical factor for different sample geometries is provided in the manual pages of FFPs in the appendix 8.5.

The measurements were done by inducing different current (I) values, starting from $1 \mu\text{A}$ to 1 mA and occasionally up to 10 mA depending upon the stability of the FLG transport device and the compliance of the Keithly measurement system in order to get evaluation of R_s with increasing current. For each device, a pair of electrodes (Au/Cr) was deposited (by Nicolas Zimmermann) as shown in Figure 2.6.

2.5.1.3 Hall Effect Measurement System for Mobility, Resistivity and Charge Carrier Concentrations Measurements

A Microworld HMS-500 Hall Effect (HE) measurement system was used to make electrical characterizations. The van der Pauw configuration is commonly used in measuring the resistivity and the Hall coefficient of a sample [228]. Usually, highly conductive materials such as Au and Ag are used for electrodes, but

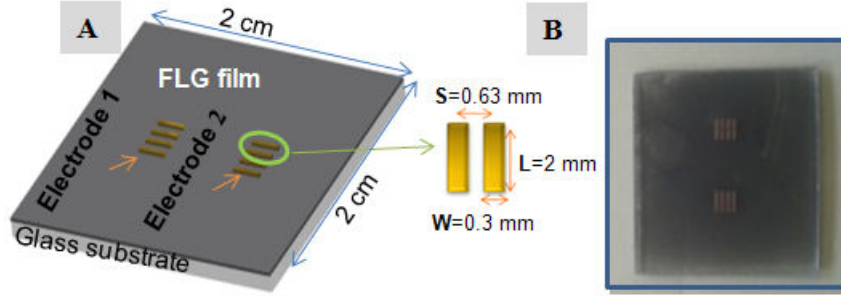


Figure 2.6: A) Geometry for charge transport device sample with dimensions of electrodes and spacing (s) between them, B) Optical image of actual device after electrodes deposition.

paste of Indium Gallium (InGa) is also used. Figure 2.7(b-d) shows the possible geometries for HE measurements. A cloverleaf geometry is preferred, however a square sample with contacts at the perimeter is acceptable. The contacts are numbered from 1 to 4 in a counter-clockwise order, beginning at the top-left contact (figure 2.7(b)). The Hall effect can be observed when the combination of a magnetic field through a sample and a current along the length of the sample creates an electrical current perpendicular to both the magnetic field and the current, which in turn creates a transverse voltage that is perpendicular to both the magnetic field and the current [229]. Figure 2.7(a) illustrates the schematic of Hall Effect principle and sample geometries in van der Pauw configuration for Hall effect measurements [230]. When an electrical current passes through a sample placed in a magnetic field, a potential proportional to the current and to the magnetic field is developed across the material in a direction perpendicular to both the current and to the magnetic field. The Lorentz force accumulates the carriers on one side of the sample so that a Hall voltage (V_H) is created when the electric force on the carriers counter balances the Lorentz force. The right hand rule allows us to determine the direction of the force on a charge carrier based on its direction of motion and the direction of the applied magnetic field.

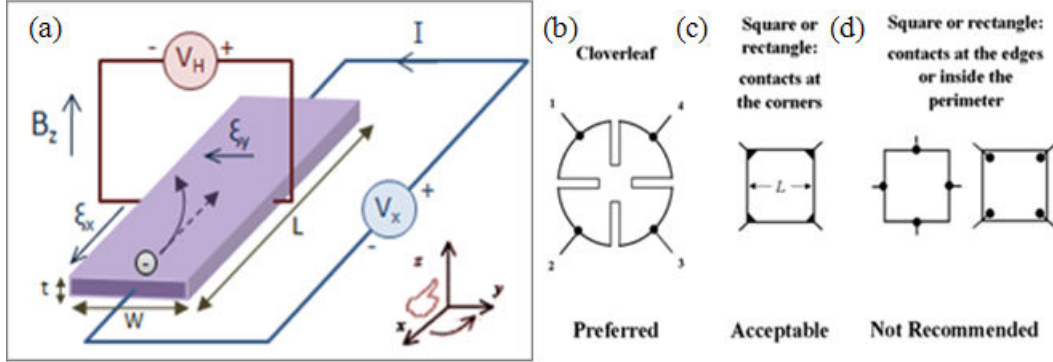


Figure 2.7: Schematic of principle of Hall Effect (a) and sample geometries for Van der Pauw configuration for resistivity and Hall effect measurements (b-d)

Based on this principle, a measurement of Hall Effect can actually be used to determine several important material parameters such as the carrier mobility (μ), the carrier concentration (n), the resistivity (ρ), and the conductivity type (N or P) apart from the Hall voltage (V_H) and the Hall coefficient (R_H). The Hall voltage (V_H) is expressed as:

$$V_H = -\frac{IB}{nte} \quad (2.2)$$

Where I is the current across the plate length (sample), B is the applied magnetic field, t is the thickness of the sample, e is the elementary charge, and n is the charge carrier density of the carrier electrons. The Hall coefficient R_H is defined as:

$$R_H = \frac{E_y}{j_x B} \quad (2.3)$$

Where j is the current density of the carrier electrons, and E_y is the induced electric field. This is expressed in SI units as follows:

$$R_H = \frac{E_y}{j_x \times B} = \frac{V_H t}{IB} = -\frac{1}{ne} \quad (2.4)$$

The units of R_H are generally expressed as m^3/C , or $\Omega \times \text{cm}/\text{G}$, or other variants. As a result, the Hall effect is very useful as a means to measure either

the carrier density. The R_H can also be defined in terms of mobility and charge carriers concentration types, respectively:

$$R_H = \frac{p\mu_h^2 - n\mu_e^2}{e(p\mu_h + n\mu_e)^2} \quad (2.5)$$

Where n is the electron concentration, p is the hole concentration, μ_e the electron mobility, μ_h the hole mobility and e the elementary charge.

Figure 2.8 shows geometry of the prepared devices and an optical image of the device sample.

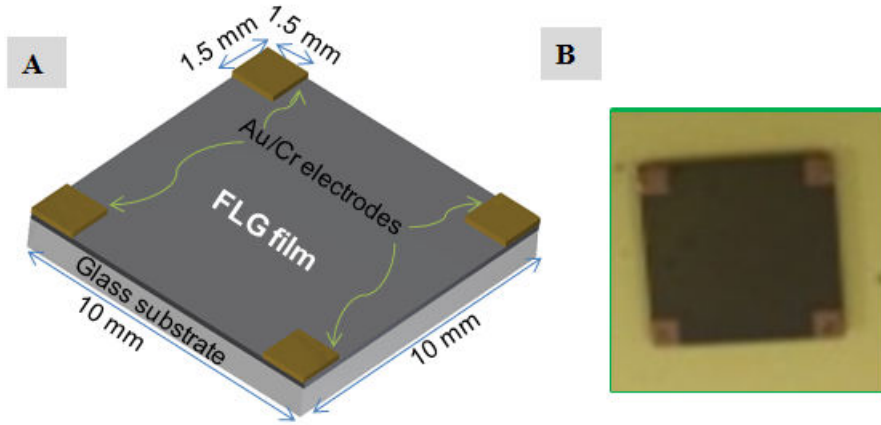


Figure 2.8: A) Schematic for the van der Pauw configuration device for Hall Effect measurement, B) Optical image of the device. Practically, the four contact electrodes have each $1.5 \times 1.5 = 2.25 \text{ mm}^2$ over a surface of $10 \times 10 = 100 \text{ mm}^2$ with a thickness $t = 200 \text{ nm}$ ($t/a = 200 \times 10^{-9}/10 \times 10^{-3} = 2 \times 10^{-6}$).

2.5.1.3.1 Basic Measurements: To make a measurement, a current is caused to flow along one edge of the sample (for instance, I_{12}) and the voltage across the opposite edge (in this case, V_{34}) is measured. From these two values, a resistance, R (for this example, $R_{12,34}$) can be found using Ohm's law:

$$R_{12,34} = \frac{V_{34}}{I_{12}} \quad (2.6)$$

The current I_{12} is a positive DC current injected into contact 1 and taken out of contact 2, in amperes (A). The voltage V_{34} is a DC voltage (V) measured between the opposing contacts (3-4) with no externally applied magnetic field, measured in volts (V). The actual sheet resistance is related to these resistances by the van der Pauw formula:

$$e^{-\pi R_{12,34}/R_s} + e^{-\pi R_{23,41}/R_s} = 1 \quad (2.7)$$

Rearranging for R:

$$R = \frac{R_s}{\pi} \ln 2 \quad (2.8)$$

The average resistivity ρ of a sample is given by:

$$\rho = R_s \times t \quad (2.9)$$

where the R_s is the sheet resistance and t is the thickness of the sample (200 nm in average). Thus equation 2.8 and 2.9 can be combined for R as follows:

$$R = \frac{\rho \ln 2}{\pi t} \quad (2.10)$$

This method was also applied for the HE measurements of our charge transport devices. Measurements were performed in an ambient environment at room temperature, first with the current range of $1\mu\text{A}$ to 1 mA , with magnetic field of 0.55 Tesla and second, as a function of temperature from $-130\text{ }^\circ\text{C}$ to around $80\text{ }^\circ\text{C}$ (from 140 K to 350 K) at a current fixed at $5 \times 10^{-4}\text{ A}$ in N_2 atmosphere on the samples of 1 cm^2 with the electrode configuration described above.

2.5.2 Scanning Electron Microscopy (SEM)

SEM is a type of electron microscope used to produce images of a sample surface by scanning it with a focused beam of electrons. The electrons inter-

acting with atoms of the sample produce different types of signals that can be detected and analyzed subsequently to extract the information about the sample's topography and composition. These different types of signals can be secondary electrons (SE), back-scattered auger electrons (BSE), characteristic x-ray cathodoluminescence (CL) light (see the figure 2.9A), and specimen current and transmitted electrons. The secondary electrons emitted by atoms excited by the electron beam is the most common imaging mode for detection. Since the signals result from the interactions of the electron beam with the atoms at or near the surface of the sample (SEs cannot be detected after a few collisions as their energy is reduced and they are unable to leave the sample), the amount of surface "seen" by the electron beam is very important. Therefore, the contrast in the secondary electron image (SEI) is created by sharp features and tilts on the sample surface. Conductive samples are usually better for reflecting back the electrons. SEM can provide a controllable magnification over a range of up to 6 orders of magnitude from about 10 to 500,000 times. SEM employs condenser and objective lenses to focus the beam to the spot and not to image the sample. Image magnification in SEM is not a function of the power of lens as in the case of transmission electron microscope (TEM) and other optical microscopy techniques. SEM micrographs have a large depth of field (due to narrow electron beam) which yields a three-dimensional characteristic appearance useful for understanding the surface morphology of a sample. For this work, a JEOL 6700-FEG microscope working at 3 kV accelerated voltage, and equipped with a CCD camera was used to characterize the morphology of thin films, FLG-Abl, FLG-HOPG, rGO and their hybrid with CNT, CNTs/FLG, CNTs/FLG-HOPG and rCNT/rGO samples, respectively. Dr. Thierry Dintzer Thierry Romero helped during SEM sessions.

2.5.3 Transmission Electron Microscopy (TEM)

TEM is another electron microscopy technique that uses electron beam produced by an electron gun focused on the sample by a condenser system to form images. The image is formed from the interaction of the electrons with the local electronic potential of the sample in the image producing system. The image producing system consists of objective lens, a movable specimen stage, and image recording system (and intermediate and projector lenses), which focus the electrons passing through the specimen to form a real, highly magnified image (see the figure 2.9B). The images are then fed to an image recording system which converts the electron image into some form perceptible to the human eye. The image recording system usually consists of a fluorescent screen for viewing and focusing. The image is magnified and focused on to an imaging device, such as: fluorescent screen or CCD camera for permanent records. TEM is capable of imaging at a significantly higher resolution than other light microscopes, owing to the small de Broglie wavelength of electrons accelerated by high voltages up to 400 kV (200 kV in our case). The most common modes of operating a TEM is the bright field imaging mode. In this mode, the contrast formation when considered classically is formed directly by the diffusion of electrons in the sample. Thicker regions of the sample or the regions with higher atomic number (Z) will appear dark, whereas, the regions with no sample (or light elements) in the beam path will appear bright. Hence the term bright field is used. During the analysis of the crystalline samples, a "dark-field" mode exists opposed to the bright-field mode. In this mode, the detector is placed at a certain angle with respect to the transmitted beam and analyzes one of the diffracted beams due to interference with a given family of crystal planes of the sample. In fact, when the sample is crystalline it acts as a diffraction grating and the image on the screen is composed of a series of spots or rings. A selected-area (electron) diffraction (SAED) pattern provides information on the local structural properties of the

sample. The TEM can be modified to work in scanning transmission electron microscopy (STEM) mode by addition of movable stages and detectors. In this mode, the electron beam, which is not parallel anymore but convergent on the sample, moves across (rasters) the sample to form the image. Modern TEMs include aberration correctors for better quality of imaging. The figure 2.9 shows the basic principles for SEM and TEM microscopes.

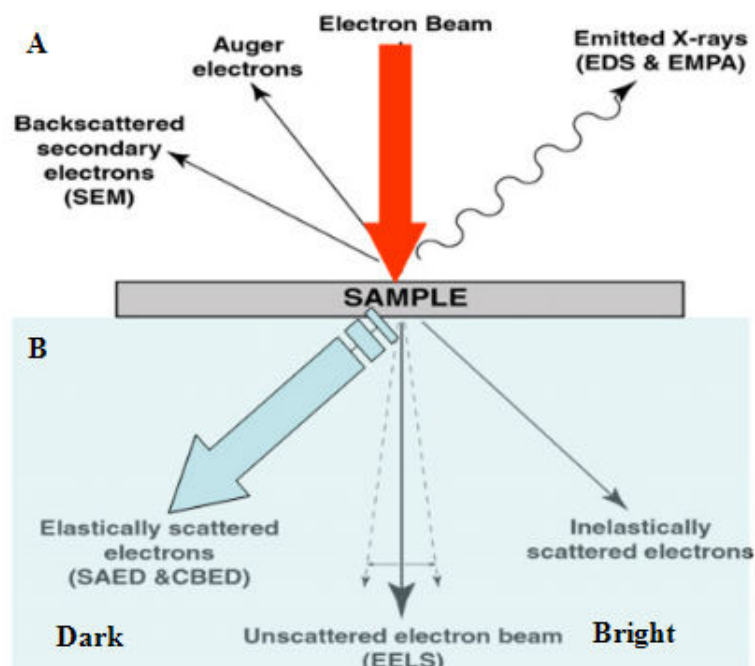


Figure 2.9: Principle of SEM and TEM respectively, showing back-scattered electrons and transmitted electrons.

In addition, a vacuum system, consisting of pumps and their associated gauges and valves, and power supplies are required. A JEOL 2100 field-emission gun (FEG) microscope operated under an acceleration voltage of 200 kV was used to study the structural quality and the number of FLG sheets accurately. Dr. Baaziz Walid helped with TEM sessions. TEM analysis were made by drop casting of the FLG dispersion onto holey carbon grids. The number of sheets in few layer graphene can be counted on the slightly curved flakes edges. The HR-TEM allows to see the crystallinity of FLG, but with very low number of

sheets the graphene becomes unstable for the standard electron acceleration (200 KV) and for the monolayer graphene, the lower acceleration is required. [58], [40].

2.5.4 Spectrophotometry: UV-Vis spectroscopy

Ultraviolet-visible spectroscopy or ultraviolet-visible spectrophotometry (UV-Vis or UV/Vis) refers to absorption spectroscopy or reflectance spectroscopy in the ultraviolet-visible spectral region. Transmittance is the fraction of incident light (electromagnetic radiation) at a specified wavelength that passes through a sample. The basic principle involves sending monochromatic light on the sample and analyzing the absorbed, reflected or transmitted light. Generally, the transmittance measurements are performed at normal incidence unlike reflectance measurements which are performed at 8° from the normal for technical reasons. The instrument used in ultraviolet-visible spectroscopy is called a UV/Vis spectrophotometer. It measures the intensity of light passing through a sample (I), and compares it to the intensity of light before it passes through (100 % light) the sample (I_o). Transmittance of a sample is given by (T) as function of wavelength of UV-visible light, and is usually expressed as a percentage (%).

$$T_\lambda = \frac{I}{I_0} \quad (2.11)$$

The basic parts of a spectrophotometer include a light source, a sample holder, a diffraction grating in a monochromator or a prism to separate the different wavelengths of light, and a detector. The radiation source is often a tungsten filament (300-2500 nm), a deuterium arc lamp which is continuous over the ultraviolet region (190-400 nm), a Xenon arc lamp, which is continuous in the range 160-2000 nm, or more recently a light emitting diode (LED) for the visible wavelengths. The detector is typically a photomultiplier tube, a photodiode, a photodiode array or a charge-coupled device (CCD). A spectrophotometer can be either single beam or double beam. In a double-beam instrument, the light is split

into two beams before it reaches the sample. One beam is used as the reference; the other beam passes through the sample. The reference beam intensity is taken as 100 % Transmission (or 0 % Absorbance), and the measurement displayed is the ratio of the two beam intensities.

For our samples, a VARIAN Cary 100 Scan UV-Visible spectrometer having both a deuterium arc lamp and a tungsten halogen lamp was used to study the transmittance of thin films in solid mode. Transmission spectra were measured for films of few layer graphene, reduced graphene oxide and their hybrids with carbon nanotubes on glass/quartz substrates (prepared by hot-spray method, see section 2.3) in the UV-Vis range (200-900 nm and occasionally between 300-800 nm) with double beam mode (blank sample as a reference) without baseline correction. The measurement was repeated at three locations at least on the sample in order to check the homogeneity of the transmittance over whole sample. The photon energies in the visible region range from 36 to 72 kcal/mole and the near ultraviolet region up to 200 nm it extends to 143 kcal/mole.

2.5.5 Photoelectron Spectroscopy (PES)

Photoelectron spectroscopy (PES), also called photoemission spectroscopy, refers to energy measurement (kinetic energy distribution) of electrons emitted (photoelectrons) from solid, gas or liquid by the photoelectric effect, in order to determine the surface composition, the binding energies of electrons in a substance, and electronic state of surface region. PES uses a well-characterized photon source directed onto a sample. Due to the photoelectric effect, this leads to liberation of photoelectrons which possess information on the chemical and the orbital character of elements of surface material. This information is gained with respect to emission angle and kinetic energy by an electrostatic analyzer. Traditionally, when the technique has been used for surface studies it has been subdivided according to the source of exciting radiation into two categories (XPS

and UPS) but the general equipment requirements are the same, (see figure 2.10):

- A source of fixed-energy radiation (an X-Ray source for XPS or, typically, a

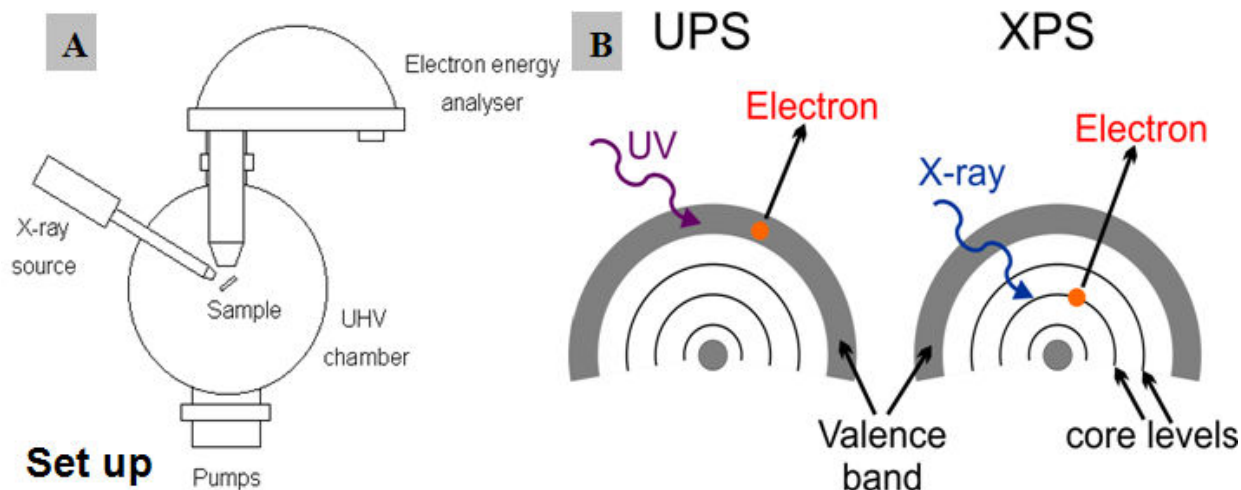


Figure 2.10: A) The basic apparatus required and B) the schemes of photoelectron spectroscopy, XPS and UPS.

He discharge lamp for UPS).

- An electron energy analyzer which can disperse the emitted electrons according to their kinetic energy, and thereby measure the flux of emitted electrons of a particular energy.
- A high vacuum environment to enable the emitted photoelectrons to be analyzed without interference from gas phase collisions.

X-Ray photoemission spectroscopy (XPS) using soft x-rays (with a photon energy of 200-2000 eV) is used to examine core-level states at higher binding energies. By XPS, the chemical composition of the sample can be determined since the binding energy of an electron is characteristic of the element, of the electronic level and of the chemical environment. Ultraviolet photoemission spectroscopy (UPS) uses vacuum UV radiation with a photon energy of 10-45 eV to examine the valence levels with a high selectivity.

Photoelectron spectroscopy is based upon a single photon in/electron out process. The energy of a photon of all types of electromagnetic radiation is given by the Einstein relation:

$$E = h\nu \quad (2.12)$$

Where h is the Planck constant (6.62×10^{-34} J s) and ν is the frequency (Hz) of the radiation. Photoelectron spectroscopy uses monochromatic sources of radiation (i.e. photons of fixed energy). In XPS, the photon is absorbed by an atom in a molecule or a solid, leading to the ionization and the emission of a core (inner shell) electron. By contrast, in UPS, the photon interacts mainly with valence levels of the molecule or solid, leading to ionisation by removal of one of these valence electrons.

The kinetic energy (KE) distribution of the emitted photoelectrons (i.e. the number of emitted photoelectrons as a function of their kinetic energy) can be measured using any appropriate electron energy analyzer and a photoelectron spectrum can thus be recorded. This is shown by a simple model representation in the figure 2.11.

Although the process of photoionization can be considered in several ways, but most the widely used relation depends upon the relation between the Kinetic Energy of emitted photoelectrons and the Binding Energy, BE (the ionization energy, which is synonymous with electron binding energy, of the electron or the energy difference between the ionized and neutral atoms) by Einstein's photoelectric law. The measured kinetic energy of an emitted photoelectron is given by:

$$KE = h\nu - BE \quad (2.13)$$

The BE is now taken to be a direct measure of the energy required to just remove the electron concerned from its initial level to the vacuum level and the

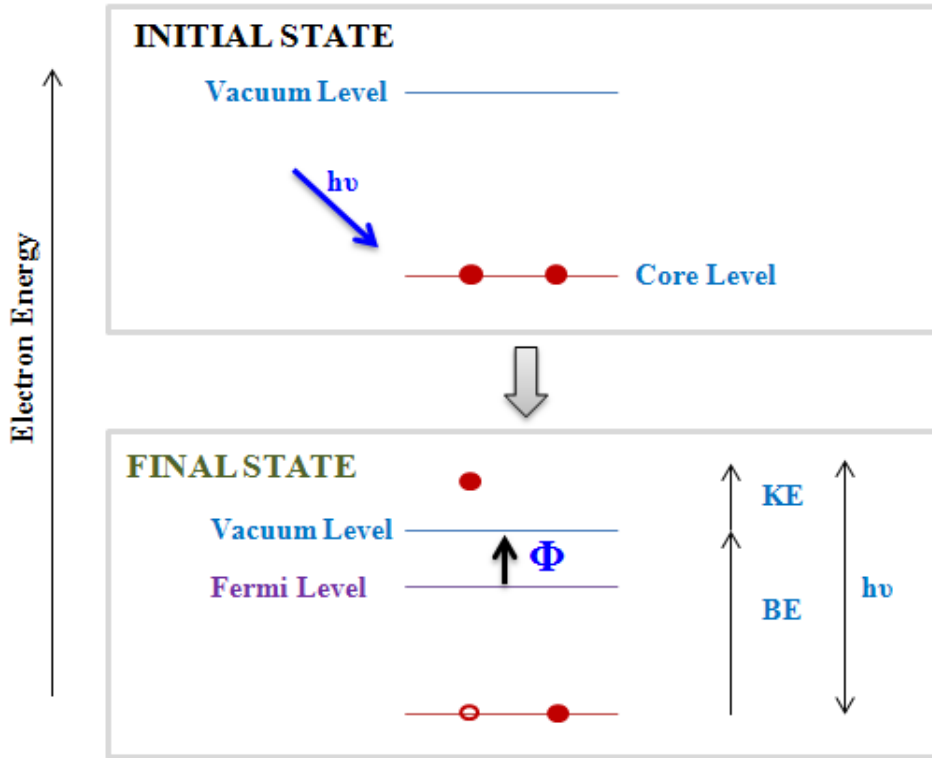


Figure 2.11: The simple model representing the energies in XPS.

KE of the photoelectron is again given by the equation above 2.13. Note that the binding energies (BE) of energy levels in solids are conventionally measured with respect to the Fermi-level of the solid, rather than the vacuum level. This involves a small correction to the equation 2.13 given above in order to account for the work function (ϕ) of the solid (equation 2.14):

$$KE = h\nu - BE - \phi \quad (2.14)$$

2.5.5.1 X-Ray Photoelectron Spectroscopy (XPS) Analysis

X-Ray Photoelectron Spectroscopy (XPS) is also called Electron Spectroscopy for Chemical Analysis (ESCA) is a surface sensitive technique and is widely used technique to investigate the chemical composition of surfaces, more precisely, the elemental composition down to parts per thousand molar concentration. The depth of the analyzed surface is c.a. 10 nm. The XPS instrument

measures the kinetic energy of all collected electrons. The electron signal includes contributions from both photoelectron and Auger electron lines. For each element, there will be a characteristic binding energy associated with each core atomic orbital, i.e. each element will give rise to a characteristic set of peaks in the photoelectron spectrum at kinetic energies determined by the photon energy (Auger lines) and the respective binding energies (2.11).

The presence of peaks at particular energies therefore indicates the presence of a specific element in the sample under study and it is also possible to estimate the percentage of oxygen and carbon in FLG materials from the areas of the peaks. Furthermore, the area of the peaks is related to the concentration of the element within the sampled region. Thus, the technique provides a quantitative analysis of the surface composition

The emitted photoelectrons will therefore have kinetic energies in the range of ca. 0-1250 eV or 0-1480 eV.

For our measurements, the XPS measurements were performed in an ultrahigh vacuum (UHV) setup equipped with a VSW Class WA hemispherical electron analyzer (150 mm diameter; multi-channeltron detector). Dr. Vasiliki Papaefthimiou performed the XPS measurements. The base chamber pressure was 1×10^{-9} mbar. A monochromated MULTILAB 2000 (THERMO) spectrometer equipped with an $\text{AlK}\alpha$ X-ray source ($h\nu=1486.6$ eV; anode operating at 240 W) was used as incident radiation. Survey and high resolution spectra were recorded in constant pass energy mode (100 and 22 eV, respectively). Prior to individual elemental scans, a survey scan was taken for all the samples to detect all the elements present. The CASA XPS program with a Gaussian-Lorentzian mix function and Shirley background subtraction was employed to deconvolute the XPS spectra. The binding energy scale of the FLG/rGO was corrected for electrostatic charging using the C 1s peak at 284.5 eV as an internal reference. The content (% mol) of oxygen was calculated by recording the O 1s and C 1s core level peaks, respectively, properly normalized to the photoemission cross section

and assuming a homogeneous distribution arrangement model [225], [231], [232].

2.5.5.2 Ultraviolet Photoemission Spectroscopy (UPS)

The work functions ϕ of graphene, rGO and other materials can be determined by UPS mode [233], [234], [235]. During the measurements of the work functions by UPS, the HeI source at 21.23 eV was used and a bias of 15.31 V was applied to the sample, in order to avoid interference of the spectrometer threshold in the UPS spectra, for our samples. Dr. Vaso Papaefthymiou performed the UPS measurements. The figure 2.12 shows a simple example of the work function measurement by UPS for a Au(111) surface.

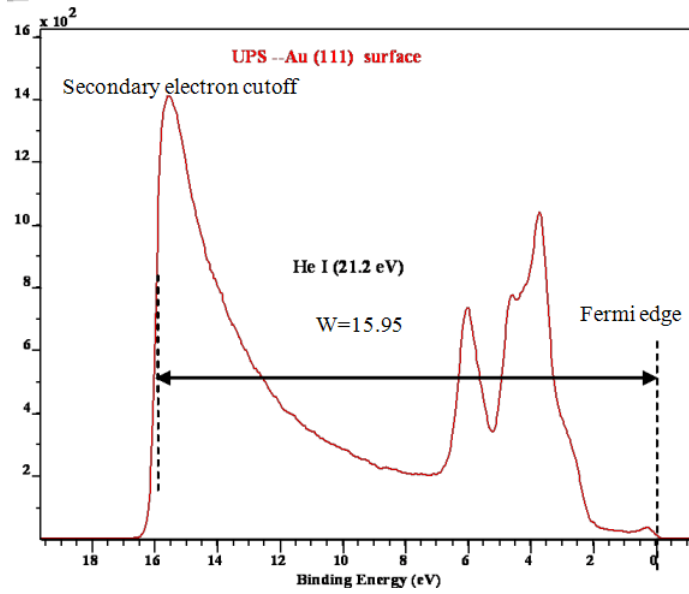


Figure 2.12: A simple example of UPS spectra for Au(111) surface.

The work function of the surface of the sample can be determined by measuring the width of the emitted electrons (W) from the onset of the secondary electrons cutoff up to the Fermi edge E_F ($W = \text{secondary electron cutoff} - E_F$) and subtracting W from the energy of the incident UV light, $h\nu$. Hence in the figure

2.12 the work function ϕ is calculated for the Au(111) surface:

$$\phi = hv - W = 21.23 - 15.95 = 5.33\text{eV} \quad (2.15)$$

2.5.6 Photoluminescence spectroscopy (PL)

Most materials emit photons upon absorbance of photons (electromagnetic radiation), thereby giving rise to phenomena called Photoluminescence (abbreviated as PL), and is initiated by photo-excitation (excitation by photons), hence the prefix photo. Some other forms are of luminescence (light emission) include Cathodoluminescence (electrons impacting on luminescent materials), electroluminescence (due to electric fields and currents) and radioluminescence (due to high energy particles), etc

In PL, the excitation process consists of the excitation of electrons to higher energy states. The excited electrons undergo various relaxation processes and some re-radiate the photons. The time periods between absorption and emission may be very short, between femtoseconds and milliseconds.

PL is an important technique for measuring the purity and the crystalline quality of semiconductors and for quantification of the amount of disorder present in a system. In fact, defects and impurities often introduce electronic states in the band gap associated with relative radiative transitions.

In a typical PL experiment, a semiconductor is excited with a light source that provides photons with energy larger than band gap energy. When electrons are excited high in the conduction band, the carrier temperature initially decreases quite fast via emission of optical phonons. This is a quite efficient due to the comparatively large energy associated with optical phonons and their rather flat dispersion, allowing for a wide range of scattering processes under conservation of energy and momentum. Once the carrier temperature decreases below the value corresponding to the optical phonon energy, acoustic phonons dominate the relaxation. Here cooling is less efficient due to their dispersion and small energies

and the temperature decreases much lower beyond the first ten of picoseconds.

For our samples, PL was carried out with Spectra Physics B10 THG YAG Laser Pulsed Laser with Continuous Wave (CW) 355 wavelength at 100 mW CW power and at 20000 Hz repetition rate for 5 ns duration, and an integration time of 2000 ms. Miss Karima Bouras helped with PL measurements.

2.5.7 Raman Spectroscopy

Raman Spectroscopy is a spectroscopic technique used to study vibrational, rotational, and other low-frequency modes in a system [236]. It relies on inelastic scattering, or Raman scattering, of a monochromatic light, usually from a laser in the visible, near infrared or near ultraviolet range. The laser light interacts with molecular vibrations, phonon band in a solid or other excitations in the system, resulting in the energy of the laser photons being shifted up or down. The resulting inelastically scattered photon which is "emitted"/"scattered" can be either of higher (anti-Stokes) or lower (Stokes) energy than the incoming photon. The difference in energy (or wavelength) of the scattered light from a material is characteristic for a particular bond in its molecular structure (figure 2.13).

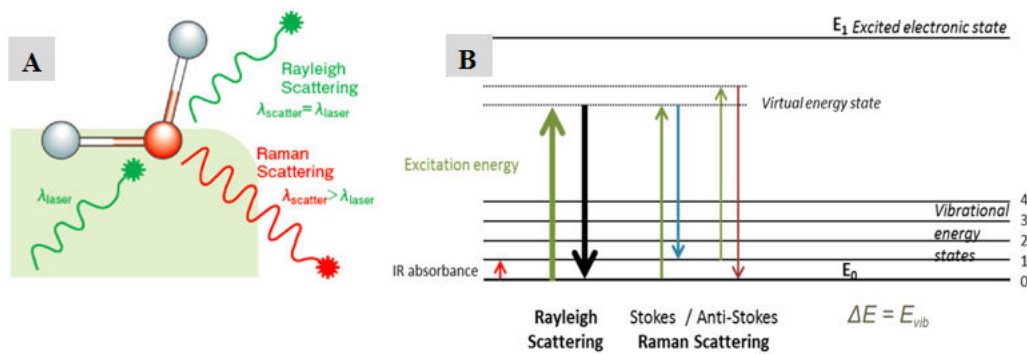


Figure 2.13: A) Raman and Rayleigh scattering of light, B) Energy diagrams. Note that difference of thickness of lines for Rayleigh and Raman, respectively, indicates the intensity of each scattering by which Rayleigh scattering is stronger/more intense in comparison to Raman scattering which is weak.

The shift in energy (or wavelength) gives information about the vibrational modes in the system. Typically, a sample is illuminated with a laser beam. Electromagnetic radiation from the illuminated spot is collected with a lens and sent through a monochromator. Elastic scattered radiation at the wavelength corresponding to the laser line (Rayleigh scattering) is filtered out, while the rest of the collected light is dispersed onto a detector by filter.

Raman spectroscopy was performed using a Horiba Scientific Labram Aramis Raman Spectrometer (JobinYvon technology) in order to study thickness (number of sheets) and crystal quality of FLG materials from its D, G and 2D bands with the following conditions: laser wavelength of 532.15 nm, D2 filter (1% power, ~ 1 mW) and spectrum were recorded in regions from 1250 to 1650 cm^{-1} and from 2600 to 2800 cm^{-1} , with an integration time of 100s for each phase. The Raman and PL spectroscopies were performed on the FLG samples deposited from ethanol suspension on silica (100 SiO_2 , 300 nm thick) substrate by a Pasteur pipette. Miss Karima Bouras and Mr. Fitsum Aweke helped with Raman measurements.

2.5.8 Thermogravimetric Analysis (TGA)

Thermogravimetric Analysis technique was employed to characterize most types of materials including inorganic materials, metals, polymers and plastics, ceramics, glasses, and composite materials used in various environmental, food, pharmaceutical, and petrochemical applications. It measures weight (the mass of a substance is monitored) changes in a material as a function of temperature (usually between 25°C to maximum 1000°C) or time under a controlled atmosphere (nitrogen, helium, air, other gas, or in vacuum) inside a furnace. Its principal uses include measurement of a material's thermal stability and composition. A TGA consists of a sample pan that is supported by a precision balance. This pan resides in a furnace and is heated or cooled during the experiment. A

sample purge gas controls the sample environment. This gas may be inert or a reactive gas that flows over the sample and exits through an exhaust. Sample weight can range from 1 mg to 150 mg. Sample weights of more than 25 mg are preferred. Typically, weight change sensitivity of 0.01 mg or higher is used. Samples can be analyzed in the form of powder (mostly) or small pieces. For our samples TGA were carried out in a Q5000 apparatus (TA instrument) under air flow (20 mL/min), up to 1000 °C with a heating rate of 120°C/min. Mr. Secou Sall performed the TGA measurements.

2.5.9 Temperature-programmed desorption coupled with mass spectrometry (TPD-MS)

In order to gain more insight about changes occurring during thermal treatment in the FLG material, a TPD-MS analysis was performed on the pristine FLG and thermally annealed FLG under Ar (FLG-Ar) materials up to 950 °C. The experiments were performed in a custom-made experimental setup under vacuum at a maximum pressure of 10^{-4} Pa. Approximately 30 mg of graphene powder was placed in a fused silica tube and heated from room temperature to 950°C with a heating rate of 5°C/min. The mass spectrometer was calibrated using N₂, H₂, H₂O, CO, CO₂ gas references [237]. From the TPD-MS analysis, the desorption rate of each gas was determined, and the total amount of each gas released was computed by time integration of the TPD-MS curves. TPD-MS was performed by Camelia Matei Ghimbeu

2.5.10 Profilometer

Profilometer is useful in the analyses of rough surfaces of films and materials. It can provide information, such as Average Step height (ASH), Average Height (AvgHt), arithmetic average roughness (R_a) and Geometric Average Roughness (R_q). Most interesting are the R_a and R_q because they provide a simple value

for roughnesses of surface of film/material. Roughness can also be determined by other methods of surface study such as AFM and interferometry.

2.5.10.1 Arithmetic average roughness, R_a

Arithmetic average roughness, R_a , is the arithmetic average height of roughness-component irregularities (peak heights and valleys) from the mean line measured within the sample length, L (figure 2.14). The measurements are taken as the fine point of the stylus on a profilometer crosses a length L on the surface being measured and expressed by equation 2.16 in nanometers or micrometers.

$$R_a = \int_0^L |Z(x)| dx \quad (2.16)$$

Where L is the evaluation length and $Z(x)$ is the profile height function.

2.5.10.2 Geometric Average Roughness, R_q

Geometric Average Roughness, R_q , also called root-mean-square (RMS) is more sensitive to occasional high and low features, making it a valuable complement to R_a . R_q is the geometric average height of roughness-component irregularities from the mean line measured within the sample length, L and expressed by equation 2.17.

$$R_q = [(1/L) \int_0^L Z(x)^2 dx]^{1/2} \quad (2.17)$$

The main difference in the two scales is that R_q amplifies occasional high or low readings, while R_a , simply averages them. For a given surface, therefore, the R_q value will be higher than the R_a value by a minimum 10%. Figure 2.14 shows the difference between two measurements.

The roughness measurements (R_a and R_q) of our samples were measured by a Veeco DEKTAK 150 profilometer with the following parameters: Stylus radius $12.5 \mu\text{m}$; Stylus force of 1-2 mg and scan duration of 30-60s; measurement range set to $6.5 \mu\text{m}$ with a variable scan length typically few 100s of μm .

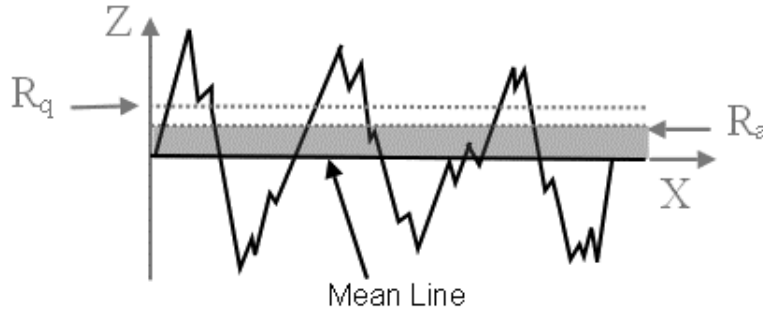


Figure 2.14: Surface roughness: R_a and R_q .

2.5.11 Atomic Force Microscope (AFM)

The AFM is a technique used to characterize the surface morphology of relatively flat surfaces at very high resolution and to extract quantitative information. A sharp probe (tip) attached to a cantilever is brought into close proximity with the sample to be analyzed. When the probe is brought into proximity of the sample surface, forces between the probe and the sample lead to a deflection of the cantilever. During measurement, the probe moves relative to the sample (in our case) in a raster pattern to perform the surface scan, and a quantity is measured in a serial fashion at discrete locations (pixels) (figure 2.15A).

Usually, the deflection is then measured using a laser spot reflected from the top surface of the cantilever and fed to a split photodetector, usually an array of photodiodes (figure 2.15B). The roughness measurement can also be performed by other methods, such as: optical interferometry, capacitive sensing, and piezoresistive cantilevers. In order to adjust the probe-to-sample distance by maintaining the constant force between them, a feedback mechanism is employed. The constant force makes sure that the sample surface is not damaged by the collision and minimizes the chances of breaking of the probe.

AFM can be made to work in either contact mode or non-contact mode

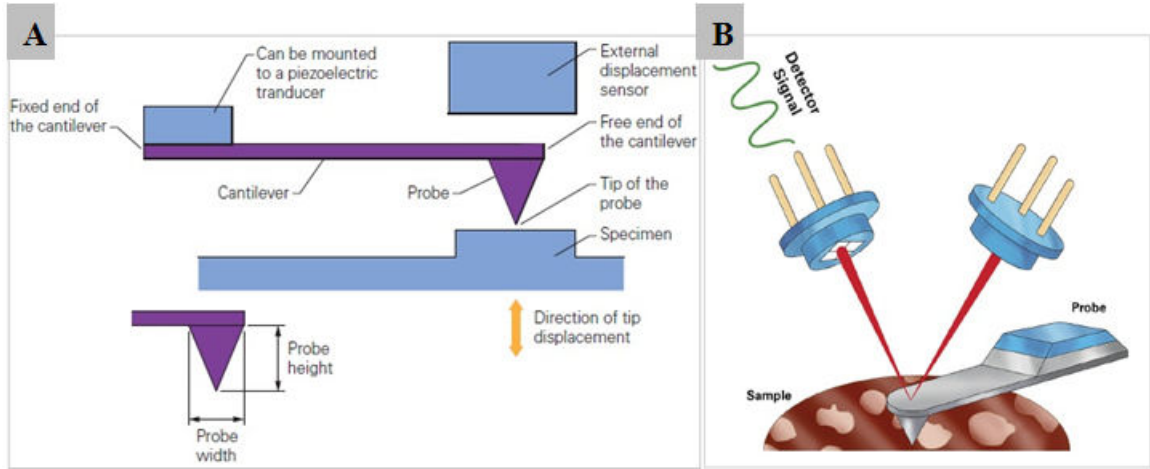


Figure 2.15: A) Schematic of the cantilever-tip assembly used in an AFM, B) Schematic of light source, cantilever, and photo detector reassembling the basic components of the light-lever AFM detection system.

but a combination of both modes gives a good compromise, which is called the tapping or semi-contact mode. When the cantilever approaches the sample, Van der Waals Forces start acting upon it. Figure 2.16 shows the probe sample interaction potential during different modes of AFM with the forces acting during these modes.

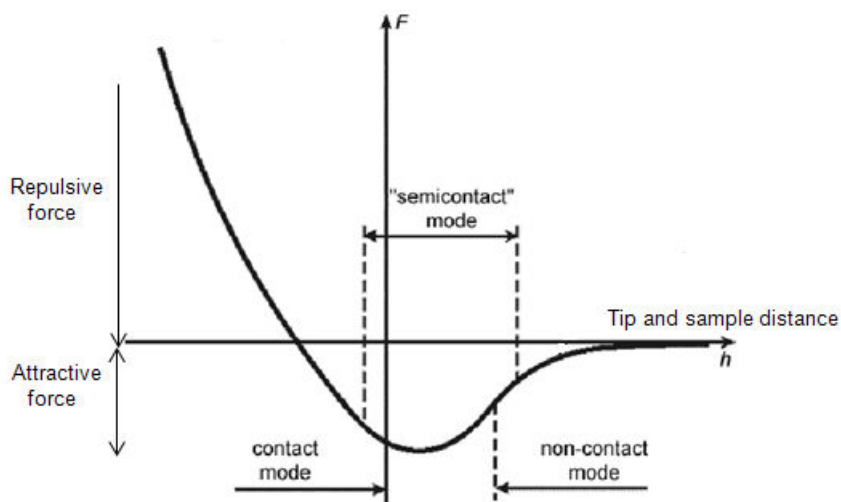


Figure 2.16: Probe-sample interaction potential.

The tapping mode is usually chosen to take the advantage of contact mode while avoiding the damage to the surface of sample by not continuously rubbing against the surface of the sample. In tapping mode, the cantilever is vibrated above the surface close to its resonance frequency to get the topographic information. The probe touches and bounces off the surface of sample at short intervals by a calculation method. The interaction with the surface causes the amplitude of the oscillation to decrease and the topography image is reconstructed from the feedback movement necessary to keep the amplitude constant. Although, AFM provides detailed surface analysis, roughness profile and topographic images but its scan area is relatively small (few tens of microns) and depth range is also limited.

The AFM measurements presented in this manuscript were performed on a NT-MDT stand alone SMENA AFM microscope using tapping mode with the following conditions: HQ:NSC/8/NoAl tip having tip radius of 8 nm, tip height of 15 μm , cone angle of 40° , force 2.8 N/m, frequency 0.5 Hz. The AFM was calibrated on 520 nm to adapt to the morphology variation (rough morphology of our samples can vary up to micrometers range) of the FLG film, for different scan sizes of $10 \times 10 \mu\text{m}$ and $50 \times 50 \mu\text{m}$, respectively in raster scan mode: Horizontal (512 lines scan) with precision of $< 2 \text{ nm}$.

2.5.12 Nuclear reaction analysis (NRA)

Material characterization can be performed by means of Nuclear Reaction Analysis (NRA) to investigate quantitatively the content and the concentration of the light elements with atomic number $Z < 15$ (carbon, nitrogen, oxygen, fluorine, etc) in depth (up to few μm) of thin solid films [238]. This method uses accelerated particles which initiate a nuclear reaction with specific target atoms in the sample. The emitted radiation is characteristic for this reaction and can be detected. From the intensity of the radiation one is able to determine

the concentration of a particular atomic species which can be further used to deduce the density of elements, knowing independently the thickness of the film. Furthermore NRA is a highly sensitive tool with which concentrations of few 10 ppm can be verified.

When an incident ion beam a interacts with an atomic core A , it forms a highly excited atomic core B , which is disintegrated or de-energized by the emission of a charged particle b , (figure 2.17).

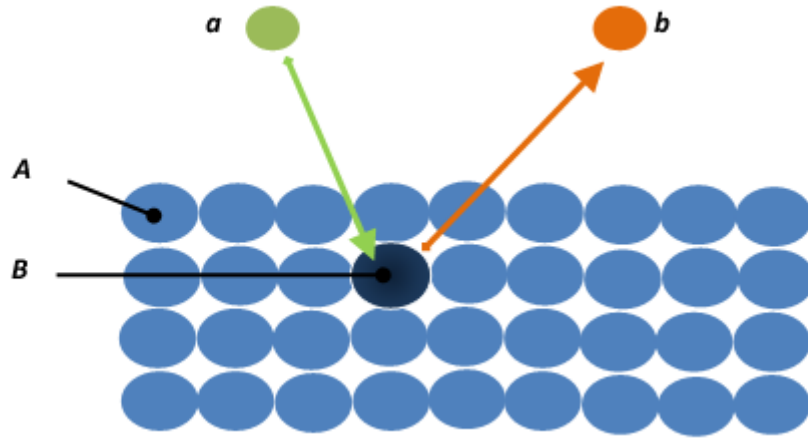


Figure 2.17: Principle of the Nuclear Reaction Analysis.

The detection of an element depends upon the possible existence of an appropriate nuclear reaction and its corresponding cross section. The reaction is usually written as $A(a,b)B$. Moreover, to produce these nuclear reactions, it is necessary that the incident particles overcome the Coulomb barrier of the atomic core. As their energy is generally less than 3 MeV, this method can only detect light elements (atomic number, $Z < 15$). The ion beam analysis was performed using a 4MV Van De Graff accelerator facility. In our study we used a deuterium (^2H) as an incident ion with an energy of 900 keV and a scattering angle of 150° . The experimental spectra were calibrated by using a SiO_2 sample [95]. A 150 mm^2 silicon surface barrier detectors was mounted at an angle of 150° to the beam direction resulting in a total solid angle of Ω 60 mili-steradian (msr).

An absorber of 11.8 μm Mylar foil was attached above the detector to stop the alpha particles generated by the $^{16}\text{O}(\text{d}, \alpha) ^{14}\text{N}$ reaction and the backscattered deuteron particles. The experimental spectra were calibrated by using bare SiO_2 (with a thickness of 200 nm) and SiC samples for oxygen and carbon using the standard oxygen nuclear and carbon reactions [$\text{O}^{16}(\text{d}, \text{p}_0) \text{O}^{17}$], [$\text{O}^{16}(\text{d}, \text{p}_1) \text{O}^{17}$] and [$\text{C}^{12}(\text{d}, \text{p}) \text{C}^{13}$], respectively, using deuterium (^2H) ions. The spectra were then fitted with the SIMNRA software. Fitsum Aweke helped with AFM and NRA measurements and analyses.

3 Results: Few Layer Graphene

In this chapter, a brief introduction to FLG (FLG-Abl) material obtained by mechanical ablation of pencil lead will be presented in section 3.1, followed by a summary of an article published in the Journal of Physical Chemistry C in section 3.1.1, article which is fully displayed with the supporting information in section 3.1.2. Further additional charge transport results obtained by Hall Effect and four point probes will be presented in sections 3.1.3 and 3.1.4, respectively. Next, charge transport in the films obtained by mechanical ablation of synthetic graphite will be presented in section 3.2. Apart from charge transport, some additional characterizations such as scanning electron microscopy micrographs will be presented in sections 3.1.4 and 3.2 to show the morphology of the films. The procedure for homogenization and crystallization of FLG-Abl by μ -waves-assisted oxidation in water is presented in section 3.3. The roughness and thickness analysis by profiler, AFM and NRA techniques are presented in the section 3.4, followed by the work-function analysis by UPS in the section 3.5. Percolation study for FLG-Abl is presented in section 3.6. In section 3.7 the characterization and charge transport in FLGs obtained by expanded graphite will be presented. At the end, a summary of the chapter will be presented in section 3.8.

3.1 Few Layer Graphene by Ablation of Pencil Lead (FLG-Abl)

Synthesis of Few Layer Graphene (FLG) was already demonstrated (see also figure 2.1 in section 2.2.1 in chapter 2 details on method) by our group in an earlier work (see SEM and TEM images in figure 1.6 for morphology) [40], (). The principle involves the ablation the commercially available pencil leads (B-9

and HB) against a rough glass disk, assisted by a continuous ultrasonication. The ablation process is followed by an acid/base treatment to purify FLG flakes obtained in the form of powder, from the inorganic binder (15 to 30 wt%) present in pencil leads. The FLGs obtained from the B-9 pencil (with 15% binder) leads were used in this work.

An automated system was established to produce FLGs on large scale. The present method of mechanical ablation (exfoliation) of graphite based materials is a low-cost, high yield, up to 60%, facile method but weakly selective to the size and number of sheets within an individual flake. Flakes from mono layer to 8 layers and occasionally up to 20 can be obtained with this method. The size of the graphene flakes was of the order of micrometers ($0.5\text{-}3\mu\text{m}$) with sufficiently high structural quality. These flakes produce a good dispersion in ethanol and are compatible with the hot-spray deposition method (see section 2.3 of chapter 2). Due to the above synthesis advantages the FLGs obtained by this method was next used for the FLG film formation in order to investigate charge transport properties.

3.1.1 Summary of the article: Electrical Transport in "Few-Layer Graphene" Film Prepared by the Hot-Spray Technique: The Effect of Thermal Treatment

The results of the charge transport study of FLG-Abl films (charge transport devices) supported on a quartz plate, prepared from randomly stacked few-layer graphene (FLG), by Hall Effect (HE) measurements, were published in the Journal of Physical Chemistry C. The film was prepared by a simple, cheap and rapid hot-spray technique from a FLG suspension in ethanol. Some of the samples were further treated at $900\text{ }^{\circ}\text{C}$ in Argon for 2h. Charge transport was studied by the Hall Effect measurements. The study reveals that thermal treatment (annealing) has a strong effect on the conductivity of the FLG film despite initial low

oxygen/defects content. The later was demonstrated X-ray photoelectron (XPS), Raman, temperature programmed desorption coupled mass spectroscopy (TPD-MS), and photoluminescence (PL) spectroscopies. Results also indicate that the amount of induced current also has an impact on the conductivity. The large range of currents, from μA to mA was gradually induced. The initial sheet resistance (R_s) for the as-prepared FLG sample is around $756 \text{ k}\Omega/\square$ for an induced current intensity of $1\mu\text{A}$ which is reduced to $5 \text{ k}\Omega/\square$ at a current intensity of 1 mA . This could be either due to low sensitivity of material or measurement apparatus at lower currents. The contact resistance of Cr/Au electrodes could be one of the reasons as well. By contrast, the thermally-annealed samples show the conductivity improvement and displays a very stable behavior throughout the range of currents. R_s of $1 \text{ k}\Omega/\square$ or even less ($0.7 \text{ k}\Omega/\square$) are then obtained. Thanks to the TPD-MS analyses we can state that as high improvement of conductivity of FLG film is attributed mainly to the desorption of toluene (hydrocarbons) from the FLG surface and not only to the oxygen decrease as generally stated [47]. The O/C atomic ratio calculated from the total area of O1s and C1s XPS peaks only slightly decreases from initially 0.05 to 0.04 after thermal annealing at 900°C in Ar for 2h. These oxygen groups are mostly attached at the sensitive edges of individual graphene sheets (steps), vacancy or topological defects in the basal plane. The carboxylic groups (OH-C=O) are mostly localized at the edges, and act as stable defects [239]. Some other groups, such as the C-OR group decrease, while the COOR increases after the thermal treatment. A significant increase of the π - π^* transition loss peak was also observed, suggesting higher delocalization of electrons, which is in accordance with the lower full width half minimum (FWHM) of C1s and the low C-OR contribution from basal plane defects as well as increasing conductivity. In general, some hydrocarbon species are also adsorbed on the surface of FLGs and can modify the electronic states depending upon the interaction with graphene (physi- or chemisorbtion). We have shown by TPD-MS analyses, that desorption of toluene requires high

temperature ($\sim 450^\circ\text{C}$ at 10^{-4}Pa), which means that toluene has strong interaction with the surface of FLG sheets. This information can be useful for the sensor applications. The toluene-graphene interactions are strong due to the π - π stacking and possible charge transfer due the electron donor nature of toluene occurs.

The Raman spectroscopy analyses after thermal treatment show a decrease in the I_D/I_G ratio from 0.12 to 0.07. This is a good indication of an improvement of quality and a decrease in defects in FLG.

Further study was carried out to investigate the effect of temperature on conductivity. Two thermally-annealed FLG films were characterized by Hall Effect measurements as a function of temperature from 140 K to 350 K at a current of 0.5 mA. An increase in conductivity was recorded with a decrease of around 20-30% in the R_s and ρ values with the increasing temperature. This shows that the material has a negative-temperature coefficient assuming that this effect is not due to the chemical desorption of impurities (since the samples were thermally-treated at 900°C) hence, most of the impurities have already desorbed and the structure is improved). A negative temperature coefficient (NTC) refers to materials that experience a decrease in electrical resistance when their temperature is raised. Thus, FLGs can find application in thermistor devices.

The thermistors are electrical devices that are used to measure electricity and are often called temperature sensitive resistors. They are usually used to monitor the temperature of certain devices for purposes of regulation. All resistors vary with temperature, but thermistors are constructed of semiconductor material with a resistivity that is especially sensitive to temperature. They are used as inrush current limiters, temperature sensors, self-resetting overcurrent protectors, and self-regulating heating elements. They differ from the resistance temperature detectors (RTDs) which generally use pure metals as by contrast with ceramic, polymer and semi-conducting materials that are used in the construction of thermistors. The temperature response is also different; RTDs are

useful over larger temperature ranges, while thermistors typically achieve a higher precision within a limited temperature range, typically $-90\text{ }^{\circ}\text{C}$ to $130\text{ }^{\circ}\text{C}$ (183-403 K), which are good for low-cost home application devices, [240].

The improvement of conductivity and the charge transport transition from a nonohmic to an ohmic-like behavior for the annealed FLG films could result from conductivity improvement both within individual flakes and at the contacts between them. This in turn means that charge transport here is only restricted by scattering on the topographical defects (like edges) within individual and at the interface between two flakes. The overlapping between adjacent flakes is probably responsible for the low resistance in the FLG film. The SEM analysis confirm this overlapping. It allows to contact the sp^2 carbons from two FLG flakes, making an efficient pathway for electrons that overcome edges defects or at least decreases electron scattering. This contact is additionally strengthened by the annealing treatment during which the surface adsorbents are removed, and stronger Van der Waals interactions are formed between the overlapped parts of two flakes. The junction characterizations require additional study (arrangement between the flakes). The sheet resistance of the FLG film after annealing, obtained here by Hall Effect measurements ($0.76 \pm 1\text{ k}\Omega/\square$), is very close and even lower than the one reported earlier for a single FLG fragment ($1.6\text{ k}\Omega/\square$). Although different technique was used to measure the resistance [40].

3.1.2 Article: Charge Transport in FLG Films Prepared by Hot-spray Method: Effect of Thermal Annealing, with Supporting Information

Electrical Transport in “Few-Layer Graphene” Film Prepared by the Hot-Spray Technique: The Effect of Thermal Treatment

A. A. Pirzado,^{†,‡} Y. Jouane,[‡] F. Le Normand,[‡] R. Akilimali,[†] V. Papaefthimiou,[†] C. Matei Ghimbeu,[§] and I. Janowska^{*,†}

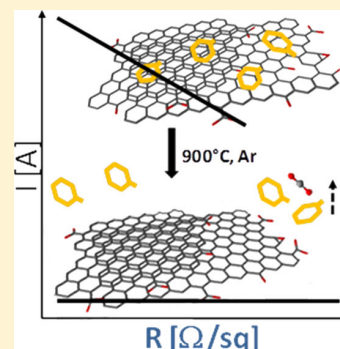
[†]Institut de Chimie et Procédés pour l’Energie, l’Environnement et la Santé (ICPEES), UMR 7515 CNRS, Université de Strasbourg, ECPM, 67400 Strasbourg, France

[‡]Laboratoire des sciences de l’Ingénieur, de l’Informatique et de l’Imagerie (ICube), UMR 7357, CNRS, Université de Strasbourg, 67400 Strasbourg, France

[§]Institut de Science des Matériaux de Mulhouse (IS2M), CNRS UMR 7361, 15, rue Jean Starcky BP 2488, 68057 Mulhouse cedex, France

Supporting Information

ABSTRACT: We investigate charge transport of a randomly stacked few-layer graphene (FLG) film supported on quartz plate, as-prepared and after annealing treatment. The film is prepared by a simple, cheap and rapid hot spray technique from a FLG suspension, while FLG was obtained in our previous report by high yield mechanical exfoliation of pencil lead. According to Hall Effect measurements, the annealing process has strong impact on the conductivity of the FLG film, despite its low oxygen/defect content as confirmed by X-ray photoelectron spectroscopy (XPS), Raman, and photoluminescence spectroscopy. The nonohmic behavior along with a sheet resistance (R_{\square}) decreases from a few tens to a few kilo-ohms is observed for the FLG film, whereas after thermal treatment, a constant R_{\square} of 0.7 k Ω is recorded. The improvement of conductivity in the FLG film is attributed mainly to desorption of toluene from the FLG surface according to the TPD-MS analysis and not only to the oxygen decrease as generally reported.



INTRODUCTION

Since the discovery of graphene in 2004—a promising material mainly due to its electrical properties—a lot of efforts have been dedicated to its synthesis, characterization, and investigations of its properties.¹ Electrical properties of graphene depend on many factors linked purely to material features like crystallinity, number and type of functionalities and/or impurities, number and size of the sheets, and interaction with the support. The last factor is less important in the case of few-layer graphene (FLG), where mostly the sheets directly adhered to the support are affected. Two main approaches are developed for the preparation of large area conductive graphene films. The first one consists of its direct bottom-up synthesis usually by chemical vapor deposition (CVD) method and subsequent transfer of the films on appropriate substrates.^{2,3} The second, which is the top-down approach, focuses on synthesis of graphene flakes with the possibly of high crystallinity, dimension, and low sheet number, followed by the preparation of the films. The most common top-down synthesis bases on the exfoliation of graphite and its intermediates such as expanded graphite and graphite oxide (GO) and reduction in the case of GO.^{4,5} The sheet resistance (R_{\square}) of FLG synthesized by CVD on Ni and measured on a solid substrate is typically 250 Ω /sq or higher (770–1000 Ω /sq).^{3,6,7} N. Rouhi et al. have reported that suspended FLG synthesized also by CVD with an area of 1000 μm^2 exhibits

only 10 Ω /sq, whereas the conductivity decreases about 120 times when FLG is supported on nitride substrate.⁸ Although the authors pointed out that the improvement of conductivity is mainly caused by a decrease of substrate scattering, they do not exclude the impact of other factors such as impurities. The lowest sheet resistance to our knowledge that was measured for pristine suspended graphene was 0.028 k Ω /sq, and for supported graphene was 6.45 k Ω /sq.^{9–12} Many works have been devoted to improvement of the conductivity of reduced graphene oxide (RGO) by applying different chemical and/or thermal reduction treatments, and the conductivity improvements were typically assigned to the decrease of the oxygen/defects ratio in GO. Punckt et al. have reported the change of sheet resistance for the singular supported FLG flake with different C/O ratios, measured by a two-probe technique.¹³ The flake that contains 12% of oxygen shows a nonlinear intrinsic I/V curve due to the lack of percolation between domains of sp^2 carbon and subsequent hopping mechanism of charge. Semiconducting feature of this FLG also causes its Schottky contact with metallic pads. The FLG flake containing 4% of oxygen shows effective sheet resistance of 21 k Ω /sq and an almost linear I/V curve, whereas the FLG flake with 0.6% of

Received: October 18, 2013

Revised: December 13, 2013

Published: December 20, 2013

oxygen exhibits a nearly ohmic behavior with resistance of few kilo-ohms. The lowest sheet resistance of 5 k Ω /sq was measured for FLG that contained only 0.3% of oxygen along with ohmic behavior. The additional obstacles to overcome by charges in the case of assembly of graphene (FLG) in films are the grain boundaries at the contact between adjacent flakes, whereas a different type and degree of stacking can be considered, and different preparation method applied. In view of optoelectronic applications, Pham et al. prepared a film by hot spray technique by mixing graphene oxide (GO) with hydrazine, which exhibits R_{\square} of 2.2 K Ω at 65% of transmittance.¹⁴ Strengthened by temperature-dependent measurements, an investigation of the electrical transport in randomly stacked filtered FLG films shows the change from semiconducting- to metallic-like behavior with increase of graphene density.¹⁵

In this work we investigate the electrical transport of FLG film prepared according to a top-down synthesis method by using a cheap, rapid and simple approach. The FLG, prepared in our previous work by mechanical ablation of a pencil lead, is deposited on quartz substrate by hot spray technique, followed or not by a thermal treatment (900 °C).^{16,17} This technique ensures additionally unlimited surface coating, which is important for potential large-scale application. Due to significant changes of the charge transport in the FLG film measured by the Hall Effect technique together with minimal decrease of the oxygen content after annealing at 900 °C, as confirmed by XPS, a deeper analysis of chemical composition of the FLG (oxygen, impurities) is performed using Temperature Programmed Desorption analysis coupled with Mass Spectrometry (TPD-MS).

EXPERIMENTAL METHODS

FLG Synthesis and Analysis. FLG was obtained by a mechanical ablation of pencil lead assisted by ultrasonication, and followed by acid/base purification as already reported by our group.¹⁷ The final step of the synthesis consisted of separation of the FLG from thick weakly ablated species by their precipitation in toluene.

The average lateral size of graphene sheets (FLG), as determined by TEM, is 2.5 μ m, and the number of graphene sheets varies typically from five to eight, while flakes with higher number up to 15, as well as lower number (monolayers), are observed.¹⁷

Raman spectroscopy was performed using Horiba Scientific Labram Aramis Raman Spectrometer (JobinYvon technology) with the following conditions: laser wavelength of 532.15 nm, D2 filter (1% power) and spectrum in regions from 1250 to 1650 and from 2600 to 2800 cm^{-1} , with integration time of 100s for each phase.

Photoluminescence spectroscopy was carried out with Spectra Physics B10 THG YAG Laser Pulsed Laser with CW 355 wavelength at 100 mW CW power at 20000 Hz RR for 5 ns duration; with integration time of 2000 ms.

The Raman and PL spectroscopy were performed on the FLG material deposited from ethanol suspension on silica with (300 nm SiO_2) wafer by a Pasteur pipet.

The XPS measurements were performed in an ultrahigh vacuum (UHV) setup equipped with a VSW ClassWA hemispherical electron analyzer with a multi-channeltron detector. A monochromated $\text{AlK}\alpha$ X-ray source (1486.6 eV; anode operating at 240 W) was used as incident radiation. The base chamber pressure was 1×10^{-9} mbar. Survey and high-

resolution spectra were recorded in constant pass energy mode (100 and 20 eV, respectively). Prior to individual elemental scans, a survey scan was taken for all the samples to detect all of the elements present. The CASA XPS program with a Gaussian–Lorentzian mix function and Shirley background subtraction was employed to deconvolute the XP spectra. The % oxygen content was calculated by O 1s and C 1s core level peaks, properly normalized to the photoemission cross section and assuming a homogeneous distribution arrangement model.

Temperature-programmed desorption coupled with mass spectrometry (TPD-MS) experiments were performed in a custom-made experimental setup under vacuum at a maximum pressure of 10^{-4} Pa. Approximately 30 mg of graphene powder was placed in a fused silica tube and heated from room temperature to 950 °C with a heating rate of 5 °C/min. The mass spectrometer was calibrated using N_2 , H_2 , H_2O , CO , CO_2 .¹⁸ From the TPD-MS analysis, the desorption rate of each gas was determined, and the total amount of each gas released was computed by time integration of the TPD-MS curves.

FLG Film Formation and Analysis. FLG dispersion: A 15 mg of FLG powder was dispersed in 30 mL of ethanol by ultrasonication with a tip sonicator (Bandelinsonoplus uw 2200) at 30% power for 15 min and in a low-power bath sonicator (Elma sonic 102168022) for 60 min.

Hot spray-coating was carried out on a preheated quartz plate (1 cm^2) at 120 °C under ambient air, where the volume of 1 mL of FLG suspension was deposited using Airgun (Hi-line Iwata). The quartz plate substrate was continuously heated during FLG deposition at 120 °C. Air was used as the carrier gas at an inlet pressure of 1.5 bar. The nozzle diameter of the gun and its distance from the substrate was chosen for 0.22 mm and 12 cm, respectively.

The morphology of the FLG films was examined by scanning electron microscopy (SEM) on a JEOL 6700-FEG microscope.

Thermal annealing of the FLG film deposited on quartz substrate was performed in Ar at 900 °C for 2 h.

Gold/chrome electrodes were deposited on the top of FLG film by evaporation (Home-made evaporator with velocity of 3–7 Å/s for Au and 1 Å/s for Cr with vacuum of 4×10^{-7} mbar). Before Au evaporation, a new configuration of masks for Hall Effect measurements was designed for laser cutting, using a program written with a Labview interface for a laser (YAG epitherm610 quantronix model 114). The conditions for laser specifications were intensity 30A, repetition rate 25kHz, 1064 nm wavelength, pulse 100 ns, laser focus spot on sample 100 μ m, cont. power 6 W, and cutting velocity of 100 μ m/sec. The masks were cut with 30A intensity and velocity of 60 mm/s. Figure 1 shows a schema of electrode configuration and optical image (inset) of FLG sample with Au electrodes. The thicknesses of deposited chrome and gold electrodes on the

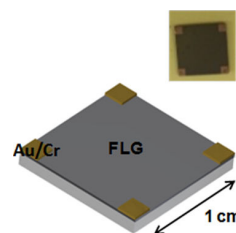


Figure 1. Schema and image (insets) for Au/Cr electrodes/FLG film designed and prepared for Hall Effect measurements.

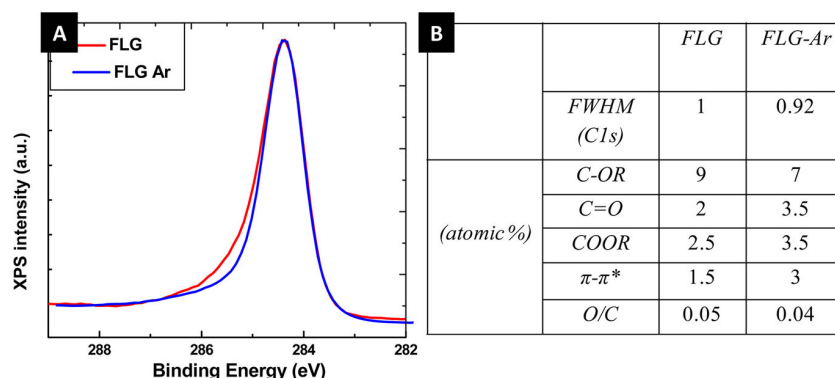


Figure 2. A) C1s XPS spectra of FLG and FLG-Ar, B) table with the percentage of different functionalities obtained by deconvolution of C1s peak and fwhm of C1s peaks.

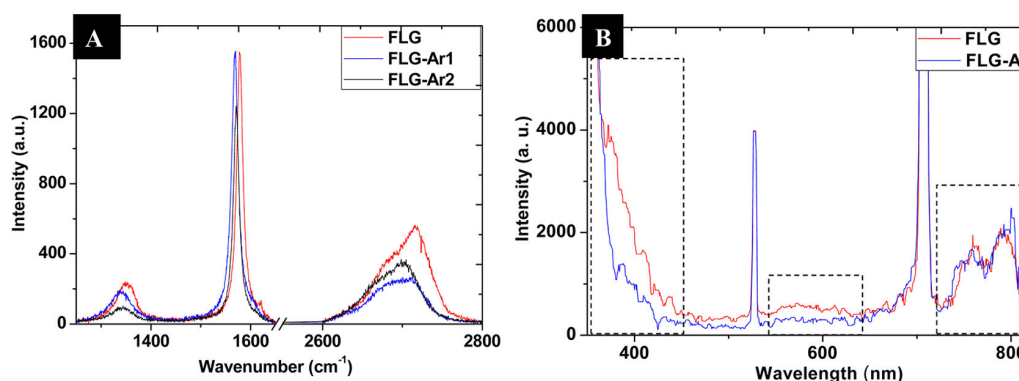


Figure 3. (A) Representative Raman spectra of FLG before (FLG) and after annealing (FLG-Ar1, FLG-Ar2). (B) Photoluminescence spectra of FLG before and after annealing.

top of graphene film were 2.5 and 30 nm, respectively, for each sample.

Hall Effect measurements were performed in an ambient environment at room temperature at the current range of 1 μ A to 1 mA and second as a function of temperature from -130 $^{\circ}$ C to around 80 $^{\circ}$ C (from 140 K to 350 K) at a current of 5×10^{-4} A in N_2 atmosphere on the samples of 1 cm^2 with the electrode configuration described above (Figure 1).

The sheet resistance R_{\square} of FLG film was calculated from the measured resistivity values according to the equation

$$R = \rho/t \quad (2)$$

where t is the thickness of the sample (200 nm) and ρ is the measured resistivity.

The thickness of the sample was measured by a Veeco DEKTAK 150 profilometer.

A Microworld HMS Hall Effect measurement system was used to measure ρ .

RESULTS AND DISCUSSION

FLG material used in this work exhibits low oxygen content according to XPS spectroscopy. The O/C ratio calculated from the total area of O1s and C1s peaks slightly decreases from 0.05 to 0.04 after thermal annealing at 900 $^{\circ}$ C in Ar for 2h. Figure 2 presents the C1s peak for untreated and annealed FLG and the percentage of specific functionalities found by C1s peak deconvolution in the table.¹⁹ The low decrease of the overall oxygen amount in the sample is probably due to the significant presence of edges (steps) within the singular flakes. The HR-

TEM analysis showed that the presence of punctual defects in the graphene lattice (such as carbon vacancies) is weak; however, the lateral size of sheets within the singular flakes varies, exhibiting a high number of edges (steps).²⁰ The edges are the most oxygen-sensitive and stable graphene defects, usually decorated with carboxylic groups, and, contrary to the C-OR group, the COOR increases after the annealing process (table, Figure 2B).

Despite the increase of the COOR group concentration after the annealing process, a significant increase of the $\pi-\pi^*$ transition loss peak is also observed, suggesting higher delocalization of electrons, which is in accordance with the lower fwhm of C1s and the low C-OR contribution from basal plane defects.

Apart from XPS, Raman and photoluminescence spectroscopy were performed on the FLG before and after annealing. Figure 3A shows representative Raman spectra obtained for the FLG sample without annealing and for two samples after the annealing process. Due to the low selectivity of the FLG synthesis method toward the number of the graphene sheets, a detailed investigation of the number sheets was abandoned. Three peaks corresponding to the D (~ 1350 cm^{-1}), G (~ 1600 cm^{-1}) and 2D (~ 2700 cm^{-1}) vibrations, typical for graphene containing materials, are observed in the spectra. The variable number of sheets impedes an analysis of defects content in the sample, as the defect content increases with the decrease of the graphene sheets number.²¹ Nevertheless, the spectra exhibit coherent tendency, and the I_D/I_G ratio decreases for the samples treated at high temperature, I_D/I_G for the annealed

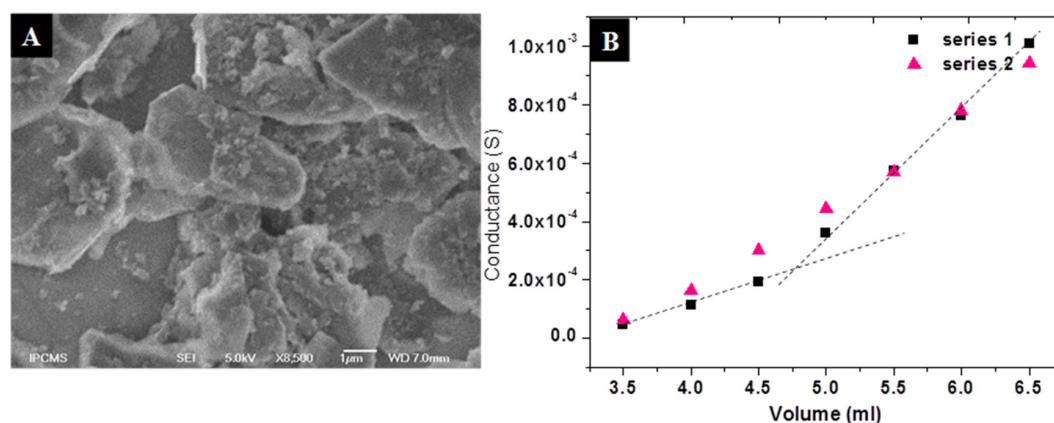


Figure 4. (A) SEM image of FLG deposited on the quartz substrate (1 mL/1 cm²). (B) The conductance as a function of deposited FLG volume on 5 cm² of the total surface (multimeter measurements).

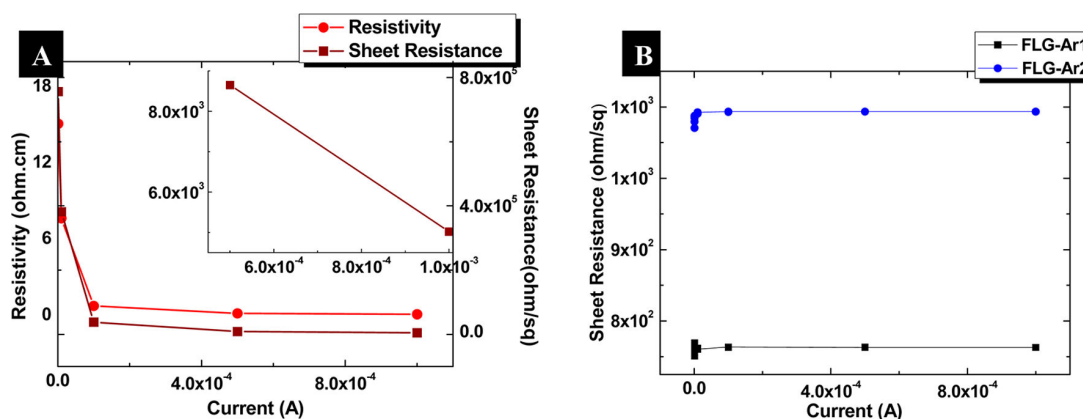


Figure 5. The curves obtained from HE measurements as a function of applied current. (A) ρ and R_{\square} for as-prepared FLG film with the inset for high current. (B) R_{\square} for two annealed FLG films (FLG-Ar1, FLG-Ar2).

samples are 0.12 and 0.07, while for the nontreated FLG it is 0.15. The peaks with higher defects content, corresponding to the pristine FLG, are slightly shifted toward a higher wavenumber compared to the FLG treated at high temperature. The amplitude of this shift is around 10 cm⁻¹ for the G peak. The presence of impurities results in doping of the graphene sheets and may explain this shift.²² The 2D peak of FLG-Ar1 is quasi symmetric (the intensity of D sub-peaks at lower wavenumber is quasi equal to the high wavenumber D subpeaks), which suggests the number of sheets being lower than five and could explain the quite high I_D/I_G compared to the thicker FLG-Ar2 sample.²³

The representative photoluminescence spectra performed on an untreated and annealed sample with laser excitation of 350 nm are presented in Figure 3B. The samples exhibit two main emission peaks, i.e., in the near UV at around 380 nm and at doubled wavelength luminescence in the IR range. The luminescence spectra confirm low defect/oxygen content in the FLG materials. The near UV region emission corresponds to the well crystallized graphene as for reduced graphene oxide (RGO), while the emission at around 600 nm is an effect of the weakly crystallized graphene lattice as is reported in GO.²⁴ Here the peak at 600 nm is pronounced only in the case of FLG without annealing process, confirming distortion of the carbon lattice, while the near UV-peak of FLG-Ar sample is

shifted toward lower wavelengths, confirming higher crystallization of the sample after annealing.

In order to obtain FLG film, the FLG material was dispersed in ethanol, and the obtained suspension was deposited on the preheated (and continuously heated) quartz substrate by the hot spray technique. The statistical SEM analysis shows that with an increase of the deposited volume, an overlapping of the FLG flakes increases, and a minimum volume is required to cover a substrate or rather to ensure a pathway for electron transport through the film. The minimum percolation required to get conductive film was found for 3.5 mL on the support of 5 cm². It was found in our previous studies that the thickness of the sprayed FLG film corresponding to this volume exhibits transparency of around 30–35%, which excludes the application of the as-prepared film as a transparent electrode.²⁵ The FLG suspension behaves like a colloid, and optimal dispersion has to be ensured before its deposition. The SEM images indeed show punctual useless aggregates that do not contribute to the conductive path as well as empty spaces, which make complete control of film homogeneity impossible. Due to the random deposition of flakes, a series of films with varied deposited volume (3.5–6.5 mL) was prepared twice, and the resistance at each added milliliter was measured by a multimeter for both series. The representative SEM image for a deposition of 1 mL/cm² of the FLG is presented in Figure 4A. Figure 4B shows the measured conductance as a function of

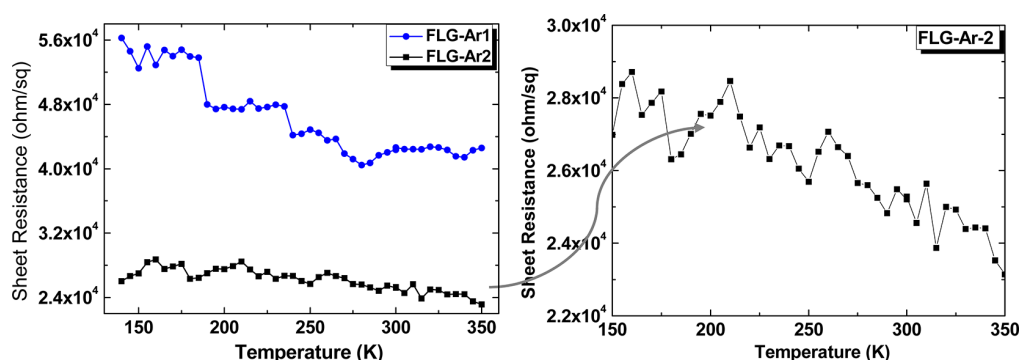


Figure 6. Sheet resistance as a function of temperature (K) for FLG-Ar1 and FLG-Ar2 samples.

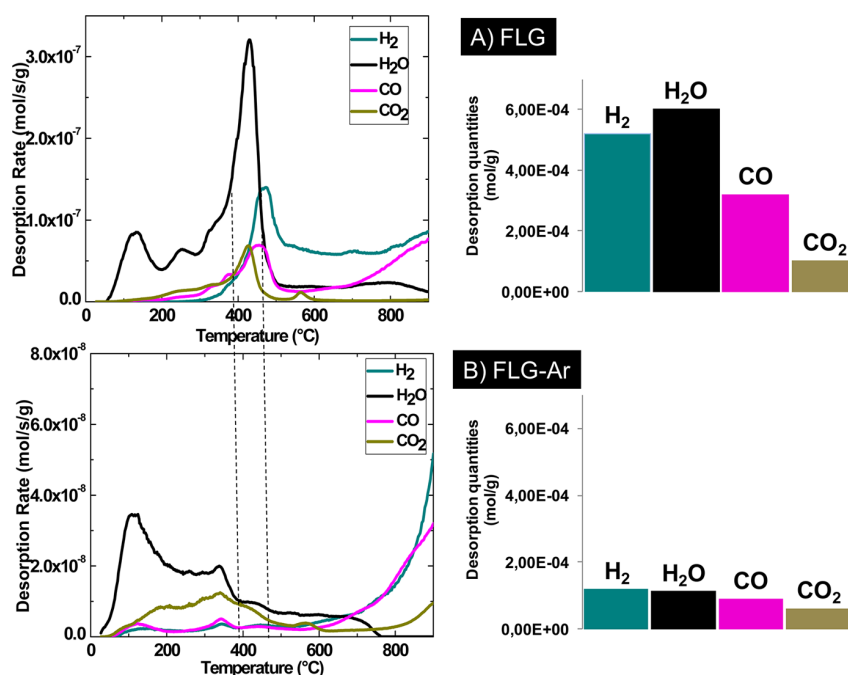


Figure 7. (A/B) (left) Desorption rates of CO, CO₂, H₂O, H₂ gases recorded by TPD analysis with anomaly desorption at around 450 °C from FLG (A) compared to the FLG-Ar (B). (A/B) (right) Desorbed quantity of CO, CO₂, H₂O, and H₂ from FLG and FLG-Ar during TPD-MS analysis (heating up to 900 °C).

volume for both series. Despite random deposition, a recurrence of the results was found: the slopes of increased conductivity as a function of deposited FLG weight (volume) for both series are almost same.

The evolution of conductance (Figure 4B) is very important and highly sensitive in all ranges of added volume. Such important evolution of conductance reveals a transport in the 3-D system and hopping mechanism regime; however, a tendency curve does not have the same slope for the entire volume range: the lower slope at lower volume suggests that the hopping mechanism is weakened toward metallic character.¹⁵ The crossover point of the tendency curve with two slopes corresponds to the volume of ca. 5 mL. An FLG film corresponding to this volume (thickness) was reproduced for Hall Effect (HE) measurements on 1 cm² quartz substrate (1 mL). The resistivity (ρ) was measured for the as-prepared sample and samples thermally treated at 900 °C in Ar (FLG-Ar, both series). The measurements were taken for the current range of 1 μ A to 1 mA at 1 μ A, 10 μ A, 100 μ A, 500 μ A, and 1

mA, and sheet resistance (R_{\square}) was calculated using eq 2 (experimental parts). Figure 5A presents the measured resistivity (ρ), and calculated sheet resistance (R_{\square}) values obtained for the FLG film as a function of the applied current. The obtained results show significant variation of ρ/R_{\square} and its high sensitivity toward injected current (especially at lower current values) for the sample before annealing. The initial ρ of the FLG sample is high (15 Ω .cm) and decreases to 0.1 Ω .cm for the current of 1 mA. The calculated R_{\square} consequently decreases for this current range from 760 k Ω to 5 k Ω . It is expected that the injection of higher currents causes more electrons to drift through the network of sp² carbons and induce desorption of physisorbed species. At higher current range, the change of $\rho(R_{\square})$ is less pronounced but still present, as it can be seen in the inset of the Figure 5A. Figure 5B presents calculated sheet resistance (R_{\square}) for two FLG-Ar samples in the same current range.

In the case of annealed samples, ohmic behavior is observed for the above range of currents, as ρ remains almost stable with

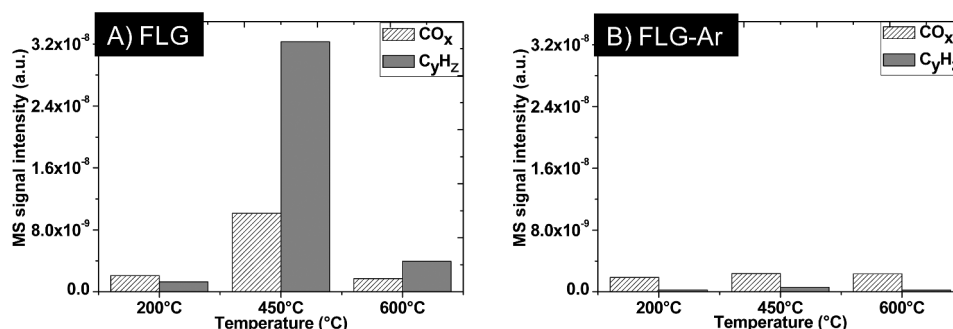


Figure 8. (A/B) MS signal intensities of oxygen (CO_x) and hydrocarbons (C_γH_z) species at three selected temperatures for FLG (A) and FLG-Ar (B).

negligible variation from 1.5×10^{-2} and $2.2 \times 10^{-2} \Omega\cdot\text{cm}$ for 1 μA to 1.5×10^{-2} and $2.2 \times 10^{-22} \Omega\cdot\text{cm}$ for 1 mA for both series. Consequently, the calculated sheet resistance shows very low variation with average value of 760 Ω/\square and 1 k Ω/\square , respectively.

In the second set of Hall Effect measurements the electrical transport of the annealed FLG film (two series) was measured as a function of temperature from 140 K to 350 K at a current of 5×10^{-4} A. The sheet resistance calculated from the resistivity as a function of temperature for both samples is shown in Figure 6. The $R_{\square}/(\rho)$ decreases with the increase of temperature with its final value reduced by 20–30% at 350 K, showing a semiconductive character of the FLG film. A difference in the sheet resistance values obtained for FLG-Ar films by HE and temperature-dependent HE measurements at r.t. (300 K) can be related to the different experimental environments, i.e., air and N₂, respectively.

The improvement of conductivity and charge transport transition from a nonohmic to the ohmic-like behavior for annealed FLG films could result from conductivity improvement in both: within individual flakes and at the contacts between them.

It is expected that for higher oxygen content in an individual FLG flake, i.e., more than 10%, the charge transport is dominated by a hopping mechanism (to overcome the sp³ carbon region), whereas for O₂ content below 10%, a diffusive motion of electrons is only limited by scattering at functional groups and lattice defects.¹³ Punckt et al. have shown that the hopping mechanism results in nonohmic behavior, whereas low-defect graphene exhibits linear behavior.¹³ In our FLG sample, the minimal decrease in the oxygen content, i.e., from 5% to 4% observed by XPS, hardly explains the change of transport mechanism and the significant decrease of sheet resistance of FLG after annealing.

To gain more insight about changes occurring during thermal treatment in the FLG material, a TPD-MS analysis calibrated for CO, CO₂, H₂O, and H₂ was performed on the FLG and FLG-Ar materials up to 950 °C. According to the literature, desorption of the CO and CO₂ species in a specific temperature range is assigned to the specific groups, such as carboxylic acid (CO₂, 100–450 °C), anhydride (CO+CO₂, 350–600 °C), lactones (CO₂, 600–800 °C), phenol, and carbonyl (CO, 500–950 °C).^{26,27} The desorption curves obtained in this work, presented in Figure 7A/B (left) and the total amount of desorbed species presented in Figure 7A/B (right), show decrease of oxygen content after thermal annealing of FLG. The MS at low temperature range shows that the amount of carboxylic groups is higher than the other functionalities in the

annealed sample. It is not surprising that some reoxidation of the annealed samples happens during removal from inert to ambient conditions. This happens especially at the sensitive edges of graphene where mostly carboxylic groups are located.²⁸ Desorption of water is related to physisorbed water and also to water formed during reaction between two different adjacent oxygen functionalities that can occur during analysis at increased temperatures. Hydrogen desorption comes from singas formation, by reaction between graphene and residual water that exists in the set up at high temperature. It should be mentioned that a certain amount of hydrogen desorbed from the FLG at this temperature (~900 °C) could arise from C–H bonds cleavage.

For the untreated sample (Figure 7A, left) an anomaly high desorption was observed for all gases around 450 °C, which is also accompanied by an excessive increase of the experimental overall gas pressure compared to the calibrated pressure for the pristine FLG (SI). The mass spectra indeed reveal the additional m/z peaks at this temperature, which are not corresponding to the calibrated species, i.e., 2, 18, 28, 44. The additional peaks at m/z : 20 (CH_x), 30 (C₂H_y), 44 (C₃H_z), 58 (C₄H_q), 72 (C₅H_u), ..., where $x = 2-4$, $y = 2-5$, $z = 3-7$, $q = 4-9$, and $u = 5-11$ (SI) can be assigned to a desorption of hydrocarbons and their intermediate form decomposition during TPD analysis. The highest m/z of ca. 92 corresponds to toluene. Toluene was used at the final step of the FLG synthesis and it seems that, as strongly adsorbed on the graphene surface, it was not completely removed by the final drying process. The strong interaction of different molecules on the surface of activated carbon was already demonstrated by TPD-MS and it seems to depend strongly on the adsorbed molecule and on the carbon surface chemistry.^{27,29}

Figure 8A,B shows MS signal intensity (not quantity) curves of oxygen containing (CO_x = CO, CO₂) and hydrocarbons (C_γH_z) species at three different temperatures for FLG and FLG-Ar according to the MS analysis. It is clear that even if the oxygen containing groups are present at higher amount in the untreated sample, the desorption rate of hydrocarbons is much higher, especially around 450 °C, contrary to the annealed sample. The desorption of hydrocarbons found here could explain the increase in the $\pi-\pi^*$ transition loss peak and the lower fwhm of the C 1s XPS peak after annealing, despite the minor change in the oxygen content.

Negligible desorption of hydrocarbons, still present in the case of the annealed sample, corresponds to the remaining adsorbed light hydrocarbons and/or other aliphatic, non-graphitized carbon species.

The important adsorption of hydrocarbons still present at temperatures as high as 450 °C indicates that not only the presence of defects/oxygen has an impact on the FLG conductivity, which changes significantly after annealing. Indeed, our previous study has shown that FLG film prepared under the same conditions as in this work, but annealed at lower temperature, 400 °C, showed a sheet resistance of 80 k Ω , which is much higher than the one measured here for the sample annealed at 900 °C, confirming that higher temperature treatments is required to optimize charge transport in the FLG film.²⁵ The change of electrical transport in graphene materials due to the adsorbed species is not surprising, as the adsorbents can modify electronic states depending on the performed bonds.³⁰ Thermal stability of adsorbed toluene is worthy to underline, as many synthesis procedures aiming to obtain graphene materials are encouraged with the use of organic solvents. On the other hand, the reported high temperature treatments aim in general at most to decrease the oxygen functionalities. The adsorbed on graphene surface hydrocarbons observed in this work can simply be considered as impurities. However, very high thermal stability of adsorbed toluene can be useful information for sensor application. Only recently, a chemisensitivity of graphene for toluene detection was investigated, and two different approaches in terms of “conductivity sensitivity” were proposed (of course the amount of detected toluene should be as low as possible). The first one is based on the electron-donor properties of toluene and sensitive “perfect” carbon lattice, and the second one rests in the presence of defects in the graphene lattice. According to the second approach, linear defects or even additional disorder near the edges of the well-ordered islands (closed contour defects) introduced from the postsynthesis remained adsorbed species, are found to be more effective than the punctual ones in the electron hopping regime.^{12,15} According to this approach, the presence of linear defects (edges/steps) within the singular flakes in our FLG, and the presence of thermally stable adsorbed toluene can cause a formation of “defect-like” islands, which need to be overcome by electrons and which results in the hopping mechanism.²⁰ In the case of annealed FLG, where there is a lack of hydrocarbons, a stable resistivity and ohmic behavior is observed, suggesting that the hopping mechanism hardly happens. This in turn means that charge transport here is only restricted by scattering on the topographical defects (edges) within individual and between two flakes. Regarding transport between adjacent flakes, the overlapping is probably responsible for the low resistance. A SEM analysis confirms the overlapping of the FLG flakes (Figure 3A). Two possible ways can be considered to separate two connected graphene flakes; direct atomic bonding at their interface with discrete atomic domain boundary or their overlapping, forming a bilayer boundary region relying on the van der Waals forces.³¹ This overlapping allows one to contact the sp² carbons from two FLG flakes, making a pathway for electrons that overcome edges defects or at least decreases electron scattering. This contact is probably additionally strengthened by the annealing treatment during which the surface adsorbents are removed and stronger van der Waals interactions are formed between the overlapped parts of two flakes (they depend on the staking arrangements between the flakes; a turbostatic stacking cannot be excluded and the experimental analysis and simulation of such stacking are ongoing).

The sheet resistance of the FLG film after annealing, obtained here by Hall Effect measurements (0.76 ; 1 k Ω /sq), is

very close to one reported earlier for a single FLG flake (1.6 k Ω /sq), measured by the two-probe technique.¹⁷ The comparable order of magnitude of sheet resistance for an individual flake and FLG film suggests high contact between the flakes in the film and low impact of grain boundaries on charge transport in the annealed film, although the sample thickness and the measurement technique are not comparable. The “multistep” structure of graphene flake and low selectivity toward the number of sheets in the FLG materials undermine the possibility to obtain high transparency of the conductive film by spray technique deposition; however, conductive coating in a simple and rapid way can be achieved on unlimited surfaces. The conductivity of the FLG film obtained in this work, ~ 60 S/cm ($1/\rho$), is comparable with the one published for the film prepared by filtration on the alumina membrane from the FLG obtained by chemical exfoliation from graphite (65 S/cm), and higher than many films or free-standing paper prepared from reduced graphene oxide or expanded graphite materials.⁵

CONCLUSIONS

In summary, we have shown that FLG film of overlapped FLG flakes prepared by the hot-spray technique with random deposition shows significant improvement of charge transport. This is due to desorption of adsorbed hydrocarbon impurities (toluene and its decomposition intermediates) accompanied by low decrease of oxygen content, once annealed at 900 °C. A desorption of toluene from the FLG surface requires a temperature as high as 450 °C showing strong interaction of this electron-donor species with graphene materials. This information is important to take into account when graphene-based chemisensors are designed. The semiconducting feature of FLG film was observed by nonohmic behavior during Hall Effect measurements, indicating a hopping electron transport mechanism, whereas once the film is annealed, the semiconducting behavior approaches metallic-like. The lowest sheet resistance of 760 Ω /sq was recorded for the annealed FLG film. A divergence of measured values of R_{\square}/ρ observed for different samples is very low despite the random deposition of FLG flakes by the spray-technique. In addition, we assume that the use of a mobile air-gun system for a deposition of FLG could improve homogeneity and continuity of the film, and consequently, reproducibility of the measured electrical characteristics.

ASSOCIATED CONTENT

Supporting Information

The SI contains the mass spectra obtained during TGA analysis for FLG sample without and after annealing. In the case of FLG without annealing, additional peaks detected during analysis correspond to the hydrocarbons adsorbed on the graphene surface. The second data are the overall pressure curves observed during TGA-MS analysis of the FLG sample before and after annealing. This information is available free of charge via the Internet at <http://pubs.acs.org>.

AUTHOR INFORMATION

Corresponding Author

*Tel/Fax: +33 (0) 368852633/+33 (0) 368852674; e-mail: janowski@unistra.fr.

Notes

The authors declare no competing financial interest.

ACKNOWLEDGMENTS

This work was supported by the University of Strasbourg and Higher Education Commission, Pakistan, and program Conectus (Alsace). The authors would like to thank Thierry Romero, Aweke Fitsum, and Debrbouz Draoua Karim for the technical support during SEM analysis, Raman and Photoluminescence spectroscopy and Hall Effect measurements. Nicolas Zimmerman and Jérémy Bartringer are acknowledged for their help in preparation of electrodes.

REFERENCES

- (1) Geim, A. K.; Novoselov, K. S. The Rise of Graphene. *Nat. Mater.* **2007**, *6* (3), 183–91.
- (2) Kholmanov, I. N.; Magnuson, C. W.; Aliev, A. E.; Li, H.; Zhang, B.; Suk, J. W.; Zhang, L. L.; Peng, E.; Mousavi, S. H.; Khanikaev, A. B.; et al. Improved Electrical Conductivity of Graphene Films Integrated with Metal Nanowires. *Nano Lett.* **2012**, *12* (11), 5679–5683.
- (3) Kim, K. S.; Zhao, Y.; Jang, H.; Lee, S. Y.; Kim, J. M.; Kim, K. S.; Ahn, J. H.; Kim, P.; Choi, J. Y.; Hong, B. H. Large-Scale Pattern Growth of Graphene Films for Stretchable Transparent Electrodes. *Nature (London)* **2009**, *457*, 706–710.
- (4) Cai, M.; Thorpe, D.; Adamson, D. H.; Schniepp, H. C. Methods of Graphite Exfoliation. *J. Mater. Chem.* **2012**, *22*, 24992–25002.
- (5) Park, S.; Ruoff, R. S. Chemical Methods for the Production of Graphenes. *Nat. Nanotechnol.* **2009**, *4*, 217–224.
- (6) Li, X.; Cai, W.; Colombo, L.; Ruoff, R. S. Evolution of Graphene Growth on Ni and Cu by Carbon Isotope Labeling. *Nano Lett.* **2012**, *9*, 4268–4272.
- (7) Raina, A.; Jia, X.; Ho, J.; Neizch, D.; Son, H.; Boulvic, V.; Dresselhaus, M. S.; Kong, J. Large Area, Few-Layer Graphene Films on Arbitrary Substrates by Chemical Vapor Deposition. *Nano Lett.* **2009**, *9* (1), 30–35.
- (8) Rouhi, N.; Wang, Y. Y.; Burke, P. J. Ultrahigh Conductivity of Large Area Suspended Few Layer Graphene Films. *Appl. Phys. Lett.* **2012**, *101*, 263101–1–263101–3.
- (9) Castro, E. V.; Ochoa, H.; Katsnelson, M. I.; Gorbachev, R. V.; Elias, D. C.; Novoselov, K. S.; Geim, A. K.; Guinea, F. Limits on Charge Carrier Mobility in Suspended Graphene due to Flexural Phonons. *Phys. Rev. Lett.* **2010**, *105*, 266601–266604.
- (10) Neto, A. H. C.; Guinea, F.; Peres, N. M. R.; Novoselov, K. S.; Geim, A. K. The Electronic Properties of Graphene. *Rev. Mod. Phys.* **2009**, *81*, 109–162.
- (11) Novoselov, K. S.; Geim, A. K.; Morozov, S. V.; Jiang, D.; Katsnelson, M. I.; Grigorieva, I. V.; Dubonos, S. V.; Firsov, A. A. Two-Dimensional Gas of Massless Dirac Fermions in Graphene. *Nature* **2005**, *438*, 197–200.
- (12) Khojin, A. S.; Estrada, D.; Lin, K. Y.; Bae, M. H.; Xiong, F.; Pop, E.; Masel, R. I. Polycrystalline Graphene Ribbons as Chemiresistors. *Adv. Mater.* **2012**, *24*, 53–57.
- (13) Punckt, C.; Muckel, F.; Wolff, S.; Aksay, I. A.; Chavarin, C. A.; Bacher, G.; Mertin, W. The Effect of Degree of Reduction on the Electrical Properties of Functionalized Graphene Sheets. *Appl. Phys. Lett.* **2013**, *102*, 023114–1–023114–5.
- (14) Pham, V. H.; Cuong, T. V.; Hur, S. H.; Shin, E. W.; Kim, J. S.; Chung, J. S.; Kim, E. J. Fast and Simple Fabrication of a Larger Transparent Chemically-Converted Graphene Film by Spray-Coating. *Carbon* **2010**, *48*, 1945–1951.
- (15) Khojin, A. S.; Estrada, D.; Lin, K. Y.; Ran, K.; Haasch, R. T.; Zuo, J. M.; Pop, E.; Masel, R. I. Chemical Sensors Based on Randomly Stacked Graphene Flakes. *Appl. Phys. Lett.* **2012**, *100*, 033111.
- (16) Janowska, I.; Begin, D.; Chizari, K.; Ersen, O.; Bernhardt, P.; Romero, T.; Ledoux, M. J.; Pham-Huu, C. *Preparation de Graphene par Amincissement Mécanique de Matériaux Graphitiques*. No.10-02719; PCT/FR2010/000730.
- (17) Janowska, I.; Romero, T.; Bernhardt, P.; Vigneron, F.; Begin, D.; Ersen, O.; Ledoux, M. J.; Coung, P. H. Few-Layer Graphene Synthesis by Mechanical Ablation of Graphite Material. *Carbon* **2012**, *50*, 3092–3116.
- (18) Ghimbeu, C. M.; Decaux, C.; Brender, P.; Dahbi, M.; Lemordant, D.; Raymundo-piñero, E.; Anouti, M.; Béguin, F.; Vix-Guterl, C. Influence of Graphite Characteristics on the Electrochemical Performance in Alkylcarbonate LiTFSI Electrolyte for Li-Ion Capacitors and Li-Ion Batteries. *J. Electrochem. Soc.* **2013**, *160* (10), A1907–A1915.
- (19) Xia, W.; Wang, Y.; Bergsträßer, R.; Kundu, S.; Muhler, M. Surface Characterization of Oxygen-Functionalized Multi-Walled Carbon Nanotubes by High-Resolution X-Ray Photoelectron Spectroscopy and Temperature-Programmed Desorption. *Appl. Surf. Sci.* **2007**, *254* (1), 247–250.
- (20) Moldovan, M. S.; Bulou, H.; Dappe, Y. J.; Janowska, I.; Begin, D.; Pham-Huu, C.; Ersen, O. On the Evolution of Pt Nanoparticles on Few-Layer Graphene Supports in the High-Temperature Range. *J. Phys. Chem. C* **2012**, *116* (16), 9274–9282.
- (21) Ni, Z.; Wang, Y.; Yu, T.; Shen, Z. Raman Spectroscopy and Imaging of Graphene. *Nano Res.* **2008**, *1*, 273–291.
- (22) Malard, L. M.; Pimenta, M. A.; Dresselhaus, G.; Dresselhaus, M. S. Raman Spectroscopy in Graphene. *Phys. Rep.* **2009**, *473* (5–6), 51–87.
- (23) Ferrari, A. C.; Meyer, J. C.; Scardaci, V.; Casiraghi, C.; Lazzeri, M.; Mauri, F.; Piscanec, S.; Jiang, D.; Novoselov, K. S.; Roth, S.; et al. Raman Spectrum of Graphene and Graphene Layers. *Phys. Rev. Lett.* **2006**, *97*, 187401–1–187401–4.
- (24) Chien, C. T.; Li, S. S.; Lai, W. J.; Yeh, Y. C.; Chen, H. A.; Chen, I. S.; Chen, L. C.; Chen, K. H.; Nemoto, T.; Isoda, S.; et al. Tunable Photoluminescence from Graphene Oxide. *Angew. Chem., Int. Ed.* **2012**, *51*, 6662–6666.
- (25) Akilimali, R.; Macher, N.; Bonnefont, A.; Begin, D.; Janowska, I.; Pham-Huu, C. FLG–High Aspect Ratio MWNTs Hybrid Film Prepared by Hot Spray Technique. *Mater. Lett.* **2013**, *96*, 57–59.
- (26) Figueiredo, J. L.; Pereira, M. F. R. Synthesis and Functionalization of Carbon Xerogels to be used as Supports for Fuel Cell Catalysts. *J. Energy Chem.* **2013**, *22* (2), 195–201.
- (27) Ghimbeu, C. M.; Gadiou, R.; Dentzer, J.; Vidal, L.; Vix-Guterl, C. A TPD-MS Study of the Adsorption of Ethanol/Cyclohexane Mixture on Activated Carbons. *Adsorption* **2011**, *17* (1), 227–233.
- (28) Dreyer, D. R.; Park, S.; Bielawski, C. W.; Ruoff, R. S. The Chemistry of Graphene Oxide. *Chem. Soc. Rev.* **2010**, *39*, 228–240.
- (29) Guo, Y.; Li, Y.; Zhu, T.; Ye, M.; Wang, X. Adsorption of SO₂ and Chlorobenzene on Activated Carbon. *Adsorption* **2013**, *19*, 1109–1116.
- (30) Fowler, J. D.; Allen, M. J.; Tung, V. C.; Yang, Y.; Kaner, R. B.; Weiller, B. H. Practical Chemical Sensors from Chemically Derived Graphene. *ACS Nano* **2009**, *3*, 301–306.
- (31) Robertson, A. W.; Bachmatiuk, A.; Wu, Y. A.; Schaffel, F.; Rellinghaus, B.; Buchner, B.; Rummeli, M. H.; Warner, J. H. Atomic Structure of Interconnected Few-Layer Graphene Domains. *ACS Nano* **2011**, *5* (8), 6610–6618.

Electrical Transport in “Few Layer Graphene” Film Prepared by Hot-Spray Technique; the Effect of Thermal Treatment

A.A. Pirzado^{1,2}, Y. Jouane², F. Le Normand², R. Akilimali¹, V. Papaefthimiou¹, C. Matei Ghimbeu³, I. Janowska^{1*}

* tel/fax: +33 (0) 368852633/+33 (0) 368852674, e-mail: janowskai@unistra.fr

1. Institut de Chimie et Procédés pour l’Energie, l’Environnement et la Santé (ICPEES), UMR 7515 CNRS, Université de Strasbourg, ECPM, France.

2. Laboratoire des sciences de l’Ingénieur, de l’Informatique et de l’Imagerie (ICube), UMR 7357, CNRS, Université de Strasbourg, France.

3. Institut de Science des Matériaux de Mulhouse (IS2M), CNRS UMR 7361, 15, rue Jean Starcky BP 2488, 68057 Mulhouse cedex, France

The SI includes the data dealing with highly adsorbed hydrocarbon species. The Fig.S1 presents the mass spectra obtained during TGA analysis at 450°C for FLG sample before annealing (FLG-(450°C)) and after annealing (FLG-Ar (450°C)). The highest mass ($m/z = 92$) corresponds to toluene, others to the intermediates from decomposition of toluene ($m/z < 20 \Rightarrow \text{CH}_x$; $m/z < 30 \Rightarrow \text{C}_2\text{H}_y$; $m/z < 44 \Rightarrow \text{C}_3\text{H}_z$; $m/z < 58 \Rightarrow \text{C}_4\text{H}_q$; $m/z < 72 \Rightarrow \text{C}_5\text{H}_u$, where $x = 2-4$; $y = 2-5$; $z = 3-7$; $q = 4-9$; $u = 5-11$; in the case of FLG before annealing. These hydrocarbons peaks are almost absent in the case of annealed FLG material.

The colored peaks present on both spectra correspond to calibrated gases, respectively to the: $m/z = 2 \Rightarrow \text{H}_2$ (black); $m/z = 18 \Rightarrow \text{H}_2\text{O}$ (blue); $m/z = 28 \Rightarrow \text{CO}$ (green); $m/z = 44 \Rightarrow \text{CO}_2$ (cyan) .

The fig. S2 presents the overall pressure curves recorded as a function of temperature during TGA analysis (measured) versus calibrated ones, corresponding to the desorption of gases from FLG (A) and annealed FLG-Ar (B). The experimental pressure is much more significant than the calibrated one in the case of FLG sample, especially for the temperature range of 350-500°C, with the max. at c.a; 450°C.

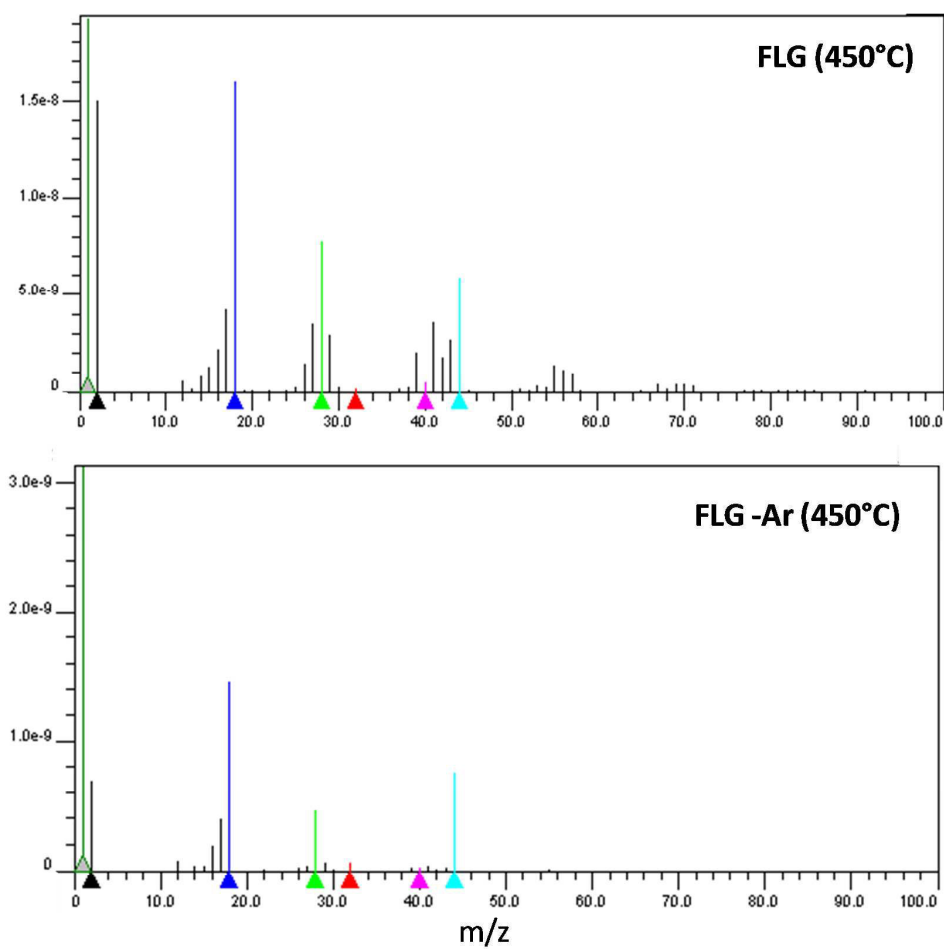


Fig. S1. Mass spectra recorded during TGA analysis at 450°C for FLG before and after annealing (FLG-Ar).

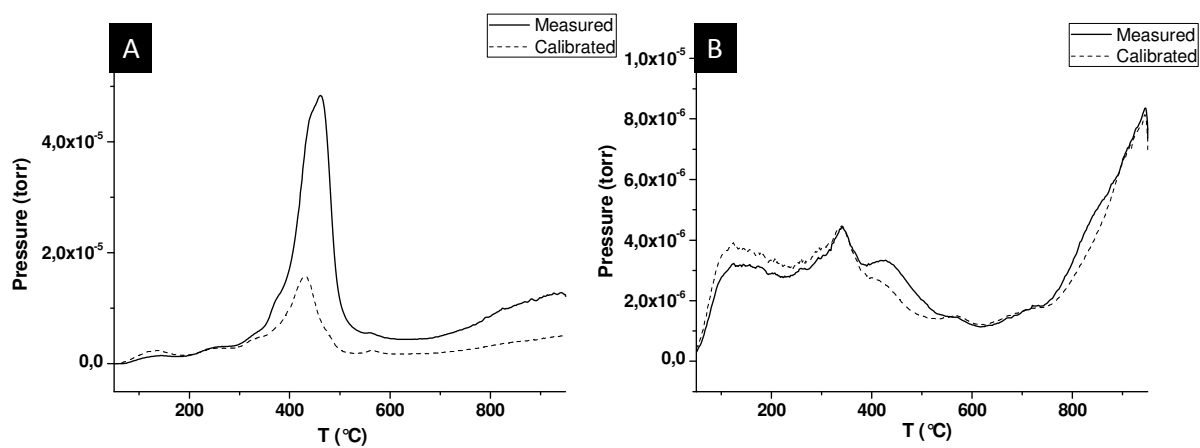


Fig. S2. The overall pressure curves recorded as a function of temperature during TGA analysis (measured) versus calibrated ones, corresponding to the desorption of gases from FLG (A) and annealed FLG-Ar (B)

3.1.3 FLG Charge Transport Device Mobility, Resistivity and Carrier Concentration in FLG Film Studied by Hall Effect

Additionally to the current and temperature dependence resistance investigations, the sheet carrier concentration (n), mobility (μ) and resistivity (ρ) were studied, for 1×1 cm FLG-Abl devices, as-prepared and thermally-treated under Ar at 900°C for 2h, by the Hall Effect measurement system at room temperature. These parameters are extracted from the Hall Coefficient (R_H) as explained in section of chapter 2. Table 3.1 shows the sheet carrier concentration (n), resistivity (ρ) and mobility (μ). The measurements were recorded for different values of the injected currents, starting with 1×10^{-6} A, and then by gradual increase for 1×10^{-5} A, 1×10^{-4} A, 5×10^{-4} A and 1×10^{-3} A, respectively. For each injected current value, the measurements were repeated three times and the average values with \pm error as highest/lowest from mean values for sheet carrier concentration and mobility are presented. The resistivity values remained stable after thermal treatment.

The sheet carrier concentration (n) varies between $5.1 \times 10^{12} \text{ cm}^{-2}$ to $-3.1 \times 10^{15} \text{ cm}^{-2}$, respectively, between, 1×10^{-6} A and 1×10^{-3} A, for the FLG-Abl as-prepared device, which represents approximately 3 orders of magnitude variation, and mixed charge carriers (n and p type) electrons and holes are observed according to positive/negative value of carriers concentration (n). The mobility μ shows mixed trend by increase and decrease with the increasing current intensity for the as-prepared device. It increases from $2.0 \text{ cm}^2\text{V}^{-1}\text{s}^{-1}$ at an initial current of 1×10^{-6} A, to $3.5 \text{ cm}^2\text{V}^{-1}\text{s}^{-1}$ at current value of 1×10^{-4} A, and next exhibits a decrease to $4.0 \times 10^{-1} \text{ cm}^2\text{V}^{-1}\text{s}^{-1}$ at the final current of 1×10^{-3} A. This indicates that with more electrons injected, more carriers are forced to participate in the conduction until a point where scattering effects overcome the liberation of "extra" charge carriers. A small gradual decrease in the resistivity ρ

Table 3.1: *HE measurements results: the carrier concentration n , resistivity ρ and mobility μ for A) the FLG-Abl as-prepared device and B) for the FLG-Abl-900° C-Ar device at room temperature.*

A) FLG-Abl (as-prepared)			
I (A)	Carriers (n) (cm ⁻²)	Mobility (μ) (cm ² V ⁻¹ s ⁻¹)	Resistivity (ρ) (Ω .cm)
1.00.10 ⁻⁰⁶	5.1.10 ¹² ±6-7	2.0.10 ⁰⁰ ±1-1.5	1.5.10 ⁰¹
1.00.10 ⁻⁰⁵	-4.6.10 ¹² ±2-7	2.8.10 ⁰⁰ ±0.4-0.8	7.6.10 ⁰⁰
1.00.10 ⁻⁰⁴	-4.9.10 ¹³ ±1-3	3.5.10 ⁰⁰ ±0.1-0.7	7.6.10 ⁻⁰¹
5.00.10 ⁻⁰⁴	5.1.10 ¹⁴ ±1-2	1.5.10 ⁰⁰ ±0.4-0.5	1.7.10 ⁻⁰¹
1.00.10 ⁻⁰³	-3.1.10 ¹⁵ ±1-5	4.0.10 ⁻⁰¹ ±0.2-0.3	1.0.10 ⁻⁰¹
B) FLG-Abl-900°C Ar			
I (A)	Carriers (n) (cm ⁻²)	Mobility (μ) (cm ² V ⁻¹ s ⁻¹)	Resistivity (ρ) (Ω .cm)
1.00.10 ⁻⁰⁶	3.6.10 ¹⁴ ±0.4-1	2.3.10 ⁰¹ ±0.3-0.7	1.5.10 ⁻⁰²
1.00.10 ⁻⁰⁵	-3.5.10 ¹⁵ ±0.5-1	2.2.10 ⁰⁰ ±0.2-0.6	1.5.10 ⁻⁰²
1.00.10 ⁻⁰⁴	5.7.10 ¹⁵ ±0.5-1	1.4.10 ⁰⁰ ±0.2	1.5.10 ⁻⁰²
5.00.10 ⁻⁰⁴	6.5.10 ¹⁵ ±0.1-0.2	1.3.10 ⁰⁰ ±0.1	1.5.10 ⁻⁰²
1.00.10 ⁻⁰³	6.5.10 ¹⁵ ±0.1	1.3.10 ⁰⁰ ±0	1.5.10 ⁻⁰²

(higher conductivity) is observed for the as-prepared device from $1.5 \times 10^{01} \Omega \cdot \text{cm}$ to $1.0 \times 10^{-01} \Omega \cdot \text{cm}$ when the current is increased. By looking at the \pm error, the carrier concentration and mobility respectively, show stability (less variation) as function of increase in current.

While for the thermally-treated device, sheet carrier concentration (n) varies between $3.6 \times 10^{14} \text{ cm}^{-2}$ and $6.5 \times 10^{15} \text{ cm}^{-2}$, showing an order of magnitude variation dominated mostly by p type carriers (in contrast to the as-prepared sample where mixed type carriers are observed), and indicating a less pronounced effect of injection of more charges by current increase. The concentration type can be affected by many factors including uncontrolled doping by exposure to air at-

mosphere, but preliminary to the presence of defects and hetero-atoms at initial FLG. According to previous investigations of sheet resistance and TPD-MS and XPS analyses, we can state that these impurities are mainly oxygen and hydrocarbon (toluene) species, which influence the electronic state of FLG. The n-type doping is due to the presence of toluene, which has electron donor properties and strongly interacts with graphene. After annealing, the FLG film shows mostly p-type transport which is related to desorption of toluene. Also the presence of N_2 environment can have effect on the type of carriers observed. It is believed that intrinsic FLG is a mixed-carrier material [21]. The resistivity values remain relatively constant for the thermally-treated device around $1.5 \times 10^{-02} \Omega \cdot \text{cm}$ throughout the range of current values, indicating the effect of thermal treatment. It is a good indication of a stable and high conductivity (as presented in the previous sections 3.1.1 and 3.1.2). The mobility also decreases from an initial $2.3 \times 10^1 \text{cm}^2 \cdot \text{V}^{-1} \cdot \text{s}^{-1}$ at $1 \times 10^{-6} \text{A}$ to $1.3 \times 10 \text{cm}^2 \cdot \text{V}^{-1} \cdot \text{s}^{-1}$ at $1 \times 10^{-4} \text{A}$, but afterwards it stays relatively constant. The exact reason for this large decrease in mobility is unclear but the mixed contributions from the scattering effects (phonons, Coulomb, long and short range impurity for example) could have affected it [241]. Although, it is reported that long range scattering in low mobility and short range scattering in high mobility graphene samples (obtained by mechanical cleavage method) are observed [117] but in our case, inhomogeneous connections between the flakes, which we call "multi-step" configuration could be one of the reasons for low mobility, however, this needs further investigation. The mobility is at least two orders of magnitude lower when compared to the generally reported values (for single-, bi- and few layer graphene films from epitaxy and CVD methods) which are in the range of 2×10^3 - $2 \times 10^4 \text{cm}^2 \cdot \text{V}^{-1} \cdot \text{s}^{-1}$ [48, 101, 130]. This can be related to the multi-structure of few layer graphene, where steps/plane ratio is higher than in the flakes with similar lateral sheet size.

Mobility μ is an important parameter for understanding device performance and underlying semiconductor physics of the materials. [241]. Extrinsic scattering

factors, many of them are originated from the surface morphology, chemistry, structural and electronic properties of the widely used SiO_2 substrate, also limit the mobility. Graphene devices fabricated on silicon dioxide substrate have shown field-effect mobilities ranging from 10 to 200 $\text{cm}^2/\text{V.s}$ [117]. The mobility for FLG film is lower (or comparable) to the best values of organic semiconductors (appendix 8.4)

3.1.4 FLG Charge Transport Device Studied by Four-Point Probes (FPPs): Sheet Resistance

In the previous section, charge transport was studied by Hall Effect (HE) for samples of the size of 1 cm^2 . Larger samples of the size two cm^2 are also prepared to investigate charge transport by four-point probes (FPPs). Further, roughness/thickness and work-function measurements are performed as well, which will be presented further in this chapter.

The FLG films were prepared in the same manner as before. Indeed in the bottom contact was covered by graphene film and required penetration of four probes into the film in order to establish a contact. The four point probes allow the local charge transport measurement on a device and then rationalizing the results by taking into account the geometrical dimensions of the sample/film. This is in contrast to the HE measurement, which gives average global resistivity of the sample by measuring the sample by the contacts placed on its perimeter/corners. Cr/Au electrodes were deposited on the top or on the bottom for charge transport studies. The top electrodes configuration was retained due to practical reasons (figure 2.6). The measurement can be performed with Cr/Au electrodes or without and the sample size is not as an issue as it is for HE (a 1 cm^2 with strict geometry and other conditions). Electrodes are used to establish a better ohmic contact between the FLG film and to protect the device (FLG film) from being degraded or etched away by the excessive induced currents or

by the penetration of pointed probes, respectively. Otherwise, this measurement can be performed on any number of locations on the device. The main advantage of FPPs is to avoid the contribution from the contacts that inevitably adds up to the R_s of the sample in the two-probe system.

Current-voltage (I-V) measurements were performed with two sets of electrodes placed on the FLG film (figure 2.6) by inducing different values (range) of current into current probes (extreme probes) and measuring the potential drop across middle probes with the help of a voltmeter. Value of obtained V was divided by the amount of induced current each time and then multiplied by a geometrical correction factor, in order to get the R_s (extracted from the slope of the linear $V(I)$ curve of device, as explained in 2.5.1.2). The figure 3.1A shows the $V(I)$ curve for the evaluation of sheet resistance in the FLG-Abl (deposited volume: 4 ml of FLG/ethanol on 2 cm² quartz substrates) charge transport device before and after a thermal annealing at 900 °C under argon for two hours. Note the measurement points $V(I)$ are arbitrarily joined, only to show the trend in the evaluation of R_s . Additionally, to the I-V measurements, the transparency of the FLG film was performed using UV-Vis spectroscopy. Figure 3.1B shows the transmittance spectra of the related FLG-Abl film and the optical photo of the FLG film bearing the electrodes deposited on top.

The R_s is high for the as-prepared device and it decreases after thermal annealing step, the related transmittance is low, 30-40%. The $V(I)$ curves indicate a marked difference between the as-prepared and the thermally-annealed values of sheet resistances in the same sample, which is in accordance with HE measurements. This is again attributed to the desorption first of toluene (hydrocarbons) and next oxygen groups, and other impurities and possible defects migration/elimination due to annealing at high temperatures. The R_s decreases significantly from 85 k Ω/\square to 15 k Ω/\square with thermal annealing under Ar at 900 °C for 2 hours. However, R_s values are different from the ones measured by HE, i.e. 15 k Ω/\square vs. 750 Ω/\square for the FLG-Abl (thermally-treated). This can be due

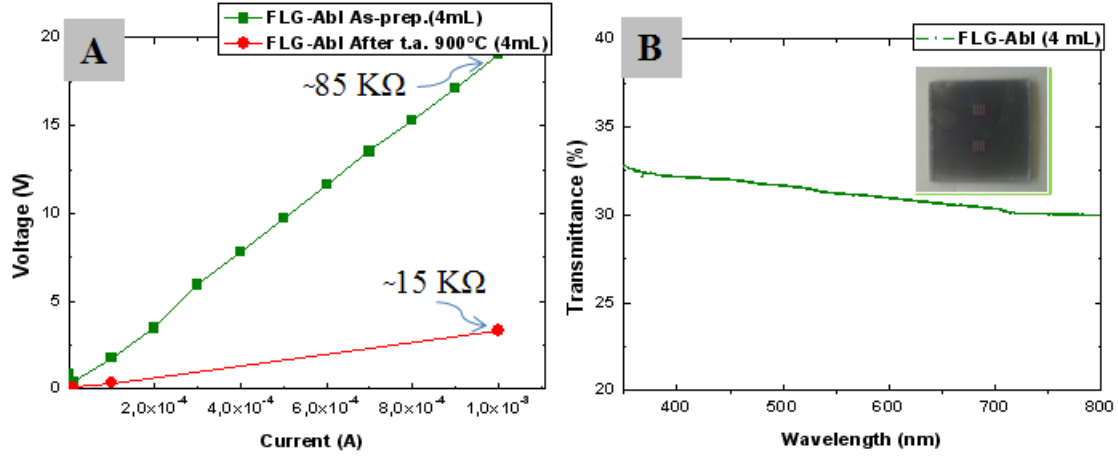


Figure 3.1: $V(I)$ characteristics of FLG-Abl charge transport device, as-prepared and after thermal annealing A), Transmittance spectrum B). Inset: optical image of the device.

to different geometry, environment (air for FPP and N_2 for HE) and local measurement. The $V(I)$ curves for the as-prepared and thermally-annealed devices, show also an important change in the transport, starting from a current value of 10^{-4} A for both devices, showing a different slope towards more linear behavior at this current. Figure 3.2 shows the $V-I$ curves plotted in a log-log scale to better visualize the behavior of the FLG-Abl charge transport devices, as-prepared and after thermal annealing (t.a.) at 900 °C under Argon. This random behavior is more pronounced for the as-prepared device between 10^{-6} and 10^{-4} A. The R_s decreases from $3.74 \text{ M}\Omega/\square$ at an initial current of 10^{-6} A to around $79 \text{ k}\Omega/\square$ at 10^{-4} A. During this regime, the charge transport is unpredictable and resembles to the hopping transport in a disordered materials. This can also be related to the minimum amount of current needed to establish a well-connected path for the flow of charge carriers through randomly deposited flakes of graphene which are not smooth and host large amount of adsorbed impurities. At low currents, charge carriers have difficulty to reach the other end of device, hence the absence of conducting channels in the device could be one of the reason for such high

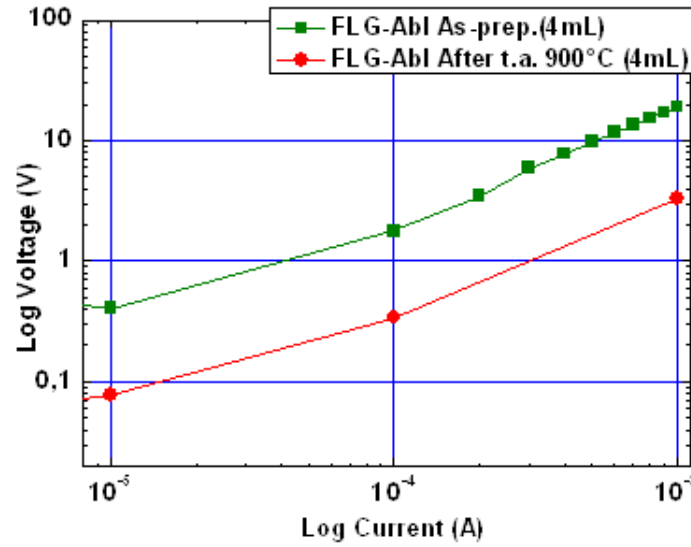


Figure 3.2: Log-log scale $V(I)$ characteristics of FLG-Abl charge transport device, as-prepared and after thermal annealing (as figure 3.1).

and non-ohmic measured resistance. Some of the current is also consumed by the voltmeter itself in practical measurements and its sensitivity could also be the reason of this behavior at low currents. Above 10^{-4} A, the R_s starts to shift towards an ohmic regime up to 10^{-3} A with charge transport dominated by a drift mechanism. However, R_s fluctuates between 77 and 87 $\text{k}\Omega/\square$ for current values between 10^{-4} and 10^{-3} A in this example (a variation of 10 $\text{k}\Omega$ or 12%). This small variation in conducting behavior is understandably normal for most of conducting materials for FLG as some of the oxygen groups are still attached to the sensitive edges of the FLG sheets due to measurement performed in air as well as other factors such as packing density, disorder, impurities and environment apart from scattering [242].

For the thermally-annealed device, the R_s at the starting current of 10^{-6} A is still high (167 $\text{k}\Omega/\square$), but approximately 55% lower than that of the as-prepared device at same current, highlighting the effect of thermal treatment. High starting R_s is not surprising for thermally-treated devices at low current value (10^{-6} A),

possibly due to the lack of a well-connected path for conduction or the measurement artifact related to the noise of the measurement apparatus and adsorbed impurities from environment. The R_s is lowered to $15.1 \text{ k}\Omega/\square$ with a variation of $0.3 \text{ k}\Omega$ or 2% at values within 10^{-4}A - 10^{-3}A is detected. This shows a stable ohmic behavior as compared to the as-prepared device due to a better ordering of structure and to the removal of adsorbants during thermal treatment. The structure is improved to make better contact among the flakes and individual sheets, the evolution indicates a shift towards strong ohmic behavior starting at the current of 10^{-4} A .

To further understand why the $V(I)$ slope always changes at 10^{-4} A , measurements were repeated by going from low currents to high currents (from $10 \times 10^{-6}\text{A}$ to $20 \times 10^{-4}\text{A}$) and coming back in reverse (from high-to-low currents) on several devices several times to check a hysteresis effect (figure 3.3A).

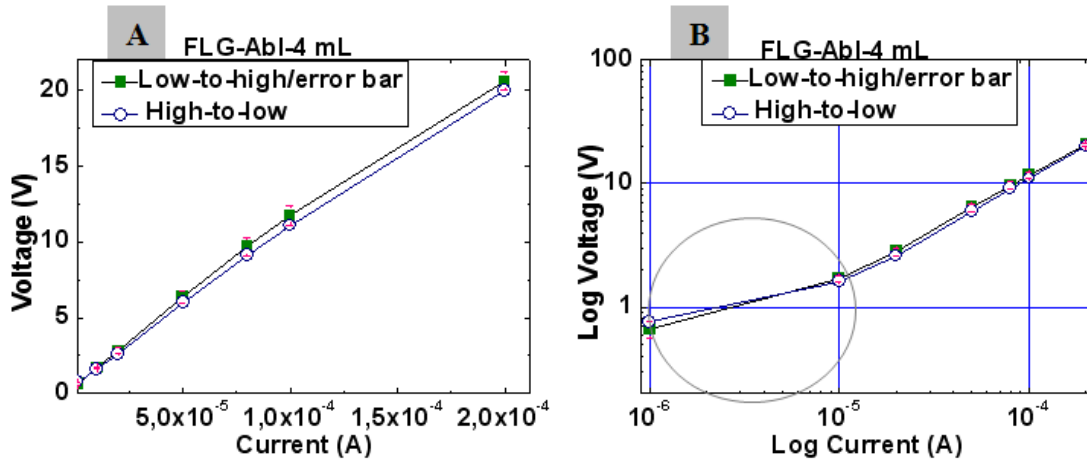


Figure 3.3: $V(I)$ curves for low-to-high and high-to low currents to see hysteresis.

The two curves show that the measured voltage as function of injected current does not change much. The error bar is inserted to show this variation between low-to-high current injection and coming back in the reverse order. Less than 1% (up to 0.065%) change is observed in the measured voltage for the high-to-low current injection measurements. This change is negligible and cannot be

qualified as a hysteresis effect. Figure 3.3B displays the same curves plotted in a log-log scale to verify the ohmic behavior of devices. As it can be seen from the figure, at the current value 10^{-5}A , the device starts to show a clear ohmic behavior.

The results show that at low current values of few μA (10^{-6} to 10^{-5}A), the devices resistance shows high fluctuations (figure 3.3B). Beyond $100\text{ }\mu\text{A}$, (10^{-4}A), the device shows less fluctuations and a stable linear behavior is observed until 10^{-3}A .

Further investigation reveals that the initial strong variation in measured R_s in FLG devices is not related to material itself but it is due to the measurement setup of four probes. The four probes equipment exhibits a problem in measuring low currents. This was then verified with a two-probes technique (see figure 3.4 for measurement set-up).

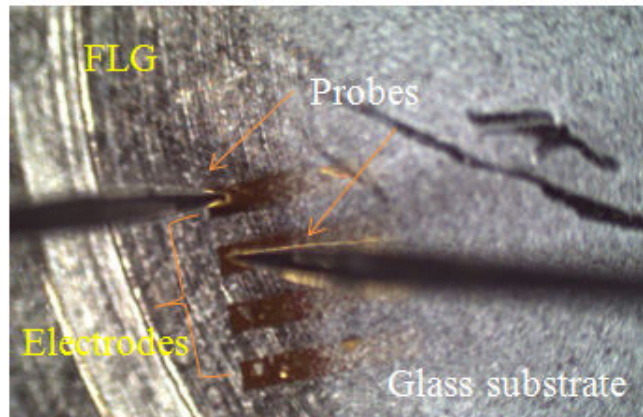


Figure 3.4: Measurement of resistance of FLG film by two-probes technique.

The voltage of the samples (FLG-Abl 4mL) was measured for induced current range with both techniques and the corresponding graphs are shown in figure 3.5. The two-probe technique measures the resistance between two points/electrodes (see section 2.5.1.1 in chapter 2).

As it is clear from these graphs, the curve of four-point probes (FPPs)

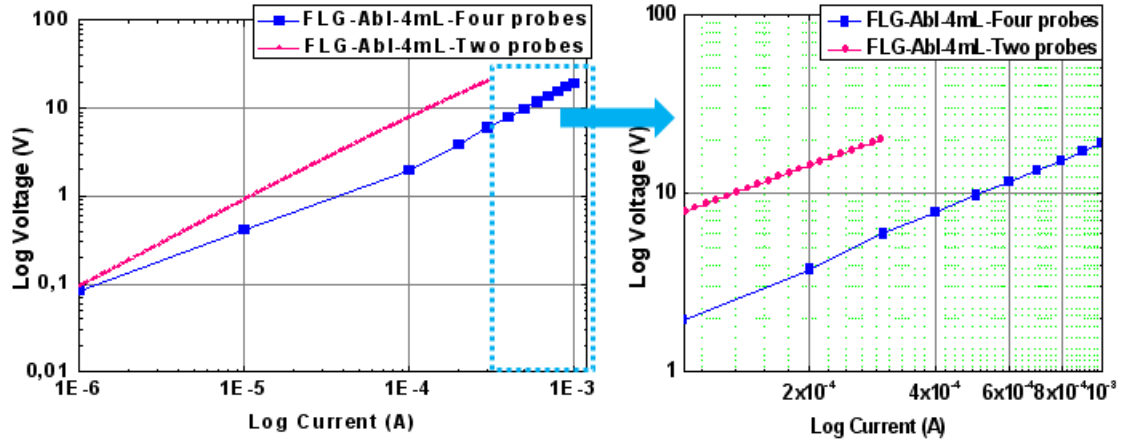


Figure 3.5: Comparison of two-probes and four probes techniques by log-log scale of $V(I)$ curves on left. The log-log plot is magnified between 10^{-4} A and 10^{-3} A on the right.

changes the slope at 10^{-4} A and keeps this behavior for higher currents. This is highlighted by magnifying the part of curve between 10^{-4} A and 10^{-3} A for both measurements. With two probes, the curves display same slopes since the start until the end in contrast to the FPPs. In the case of four electrodes measurements the curves seem to converge at low currents instead of remaining parallel as shown in the magnified part between 10^{-4} A and 10^{-3} A which is due to significant loss of current in contact resistance in four point probes until 10^{-4} A.

Figure 3.6 shows the morphology of charge transport device studied by Scanning Electron Microscope (SEM). The random deposition of the FLG flakes can be observed. We can observe random stacking and piling of flakes with empty spaces between flakes that hamper the percolation, while the excessive stacked amount of flakes is observed in the conduction path which does not necessarily contribute to further conduction. This can explain the high R_s in the FLG device and low transmittance of FLG film.

Despite very low transparency of the FLG films, which excludes the potential application in TCEs, the Conductivity of Transparency (σ_{gt}) which is used

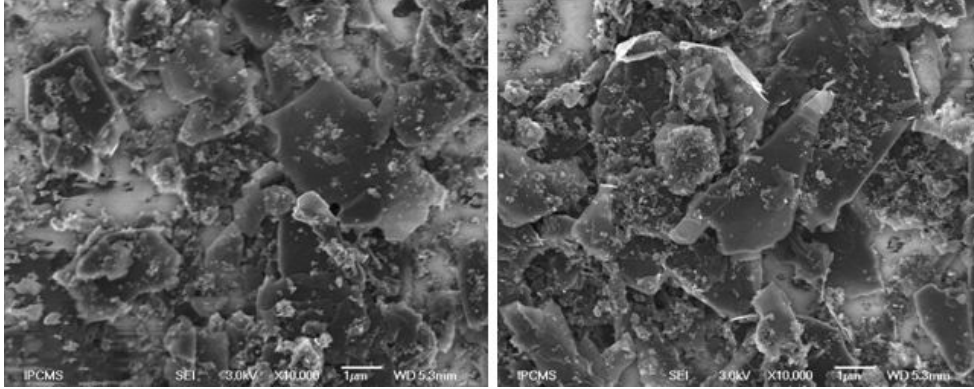


Figure 3.6: SEM images showing the morphology of the charge transport device.

as a figure of merit (see section 1.1 in chapter 1) was calculated for FLG films. Conductivity of Transparency was calculated by taking the average of R_s and transmittance for three measurements. Table 3.2 shows the calculated (σ_{gt}) of representative FLG-Abl devices, along with the \pm error from the mean value of R_s and transmittance at 550 nm, while similar data are provided for two commercially available ITO films [6] for comparison purpose. The heterogeneous random deposition in the films results in local variations of resistance and transparency, that is why measurements are repeated several times for R_s and transmittance at different locations. Comparing these results with that obtained by HE measurements, there is significant difference in the sheet resistance between around $15\text{k}\Omega/\square$ (with FPPs) and around $1\text{k}\Omega/\square$ (with Hall Effect). This can be due to differences in geometry of the FLG film/device and contacts. Note that the R_s is given for the two methods of charge transport used in this study, i.e. the Four-point probes (FPPs) and the Hall Effect (HE).

The highest value of σ_{gt} is obtained for the $1\text{ cm} \times 1\text{ cm}$ sample studied by the Hall Effect, with very low transmittance, which makes it impossible to consider this result for transparent conductor applications. However, conductive electrodes and coatings are well within reach. Comparing the σ_{gt} values with the commercial ITO, it is evident that this type of FLG films are 2-3 orders of magnitude inferior, even after thermal annealing treatment. The low performance

Table 3.2: Conductivity of transparency (σ_{gt}) of FLG-Abl charge transport devices with R_s given for the FPP and HE in comparison to commercially available ITO electrodes.

Sample/Device	$R_{s(avg)}$ ($k\Omega/\square$)	T_{avg} (%)	Conductivity of transparency (σ_{gt}), (S/cm)
FLG-Abl-As-prep.(4mL) (FPP)	85 ± 7	31 ± 4	7
FLG-Abl-900 °C-Ar (4mL) FPP	15 ± 1	31 ± 4	41
FLG-Abl-900 °C-Ar (2mL) (HE)	1 ± 0.3	29 ± 2	801
ITO Sigma-Aldrich Catalog Nos. 576360/639281	0.01/0.1	85/77	$4.3 \times 10^5 /$ 2.7×10^4

of the FLG film is linked directly to high percolation threshold, which is an effect of random deposition plus inhomogeneous and low lateral sizes (and multi-step morphology) of the flakes, and the variable number of the sheets (thickness) within individual flakes.

3.2 Charge Transport in FLG by Mechanical Exfoliation of Synthetic Graphite (HOPG)

FLGs ablated from a pencil lead undergo several filtration and purification treatments in rather harsh conditions, which are necessary to purify the FLGs from binder. To avoid these treatments, Highly Ordered Pyrolytic Graphite (HOPG) was used to synthesize FLG. Other advantage of HOPG material is linked with parallel arrangement of graphene sheets compared to pencil lead during mechanical exfoliation as will be described later.

The FLG was prepared by the same principle of mechanical ablation as for the pencil lead as explained earlier in chapter 2 under section 2.2.1.3. The discs of HOPG was continuously ablated against a rough glass disc with a controlled flow of ethanol to detach the FLGs from the disk surface. The FLGs in ethanol

were collected in a beaker and kept for 24h for a decantation step. After 24h, around 75% of the liquid (ethanol+FLG) was taken in a separate flask in order to get thinner FLG after the settling of the thicker agglomerates of FLG/graphite. Thus, these FLGs are called FLG-HOPG24h. The concentration of FLG was determined to be ~ 0.1 mg/mL.

Charge transport devices were fabricated in the similar way as explained for FLG-Abl (pencil lead) in 2.3. The measurements were repeated three times at different locations on the devices by FPPs. Figure 3.7 shows the representative $V(I)$ characteristics and transmittance for FLG-HOPG24h, as-prepared and thermally annealed at 900 °C under Ar, devices.

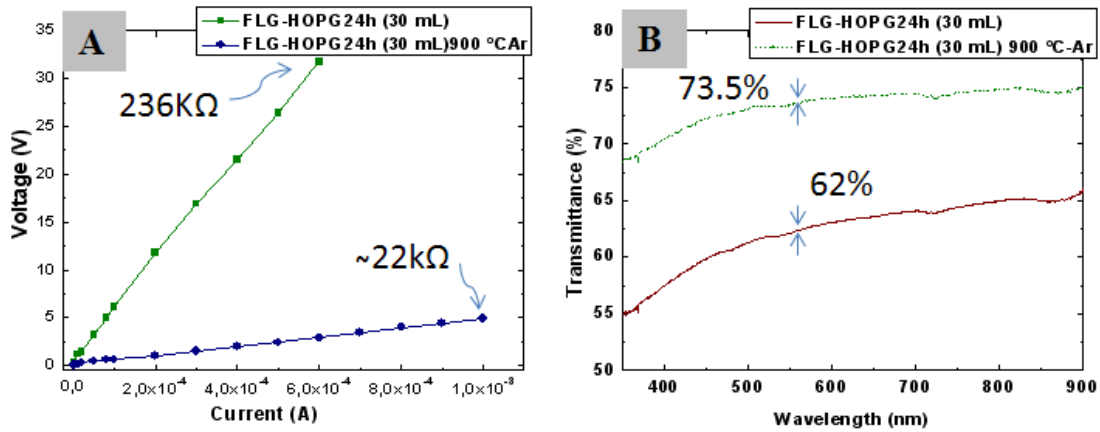


Figure 3.7: A) $V(I)$ characteristics of FLG-HOPG24h charge transport devices, as-prepared and thermally annealed at 900 °C under Ar, B) transmittance.

The $V(I)$ plot always shows a linear variation allowing to calculate a sheet resistance R_s as defined by equation 2.1 in section 2.5.1.2 of chapter 2. The sheet resistance of as-prepared device of ~ 236 kΩ/□ (with an average R_s of $\sim 305 \pm 115$ kΩ/□) is calculated at the transparency of $62 \pm 5\%$. R_s decreases by one order of magnitude with a thermal treatment at 900 °C under Ar for two hours, to ~ 22 kΩ/□ (average of $\sim 23 \pm 11$ kΩ/□) for an average transmittance of $73 \pm 6\%$. Again, the thermal treatment induces the improvement in charge transport as

expected. The transmittance is linked to the volume of FLG deposition, however, a variation of around 18% in the transparency is observed for the same deposition volume of 30 mL for as-prepared (T_{avg} 61%) and thermally-annealed devices ($T_{avg} \sim 73\%$) obtained at 550 nm.

Based upon these results, conductivity of transparency, σ_{gt} is calculated (see the table 3.3 for FLG-HOPG24h devices) by taking into account the average R_s , and T % (at 550 nm) with \pm error bars from mean value.

Table 3.3: Conductivity of transparency of FLG-HOPG24h charge transport devices.

Sample/Device	$R_{s(avg)}$ ($k\Omega/\square$)	T_{avg} (%)	Conductivity of transparency (σ_{gt}), (S/cm)
FLG-HOPG24h (30mL)	305 ± 115	61 ± 5	~ 5
FLG-HOPG24h (30mL)-900°C-Ar	23 ± 11	73 ± 6	61
FLG-HOPG24h (40mL)	167 ± 50	36 ± 4	~ 5

When comparing to the results obtained for FLG-Abl (pencil lead) in previous section (table 3.2), the conductivity of transparency of FLG-HOPG devices is in the same range for as-prepared samples. However, after thermal annealing step at 900°C under Ar for 2h, the value of σ_{gt} has increased up to ~ 61 S/cm compared to ~ 41 S/cm, showing an increase of 40%. For almost same order of R_s , a higher transmittance is achieved with FLG-HOPG devices. The improvement in the σ_{gt} is linked with the improved transmittance which has increased from 31 (for FLG-Abl) to 73% (80% higher for the HOPG devices). We can expect that the HE measurements could lead to a much higher σ_{gt} , as lower R_s should be observed.

The \pm variation for R_s and transmittance between two different samples of FLG-HOPG films is linked to inconsistency in the concentration of FLG-HOPG material in ethanol which was estimated to be around 0.1 mg/mL. Due the difficulty in maintaining the exact concentration of FLG-HOPG24h after the decantation step, it is possible that there are small variations of concentration which can

result in variation of deposited volume (and hence the R_s), transmittance, film thickness and morphology coupled with inconsistencies inherent to the hot-spray method.

Further, a detailed study of the shape, thickness, quality and size of FLG-HOPG24h can bring more information to understand these variations. A drying of the FLG to normalize the concentration is avoided to minimize the stacking of the flakes. The additional factor which could influence the transparency is a decantation process for 24h, which allows to extract the flakes with higher surface/volume ratio.

A possibility to obtain the conductive film with a transparency higher than 70 % for the FLG-HOPG as compared to the 30% in the case of FLG-Abl confirms different morphology of the flakes (larger size of the flakes), as the percolation threshold was decreased. The flakes from ablation of pencil lead have also multi-step structures (the lateral size of sheets within the individual flakes are variable). This was characterized by 3D-TEM [243]. We suppose that this morphology is caused by random directional arrangement of the graphitic parts in the lead during mechanical exfoliation, as it is presented in figure 3.8.

This means that the exfoliated graphitic layers on glass surface are difficult to form connection between two flakes. In the case of HOPG disc all graphitic identities are mostly arranged in the planar, horizontal to the ablation surface direction.

It is clear that the σ_{gt} of this type of FLG is even 2-3 orders of magnitude less than that of the commercial ITO and even after thermal annealing treatment desirable results are not achieved, although HE measurements could provide better HOPG film performance. Figure 3.9 shows the SEM micrographs of several FLG-HOPG-24h devices.

These SEM images recorded in the top-view show that FLG film consists of overlapping flakes forming layers of graphene and few layer graphene sheets with arbitrary shapes and random in-plane orientation. Some of the flakes can

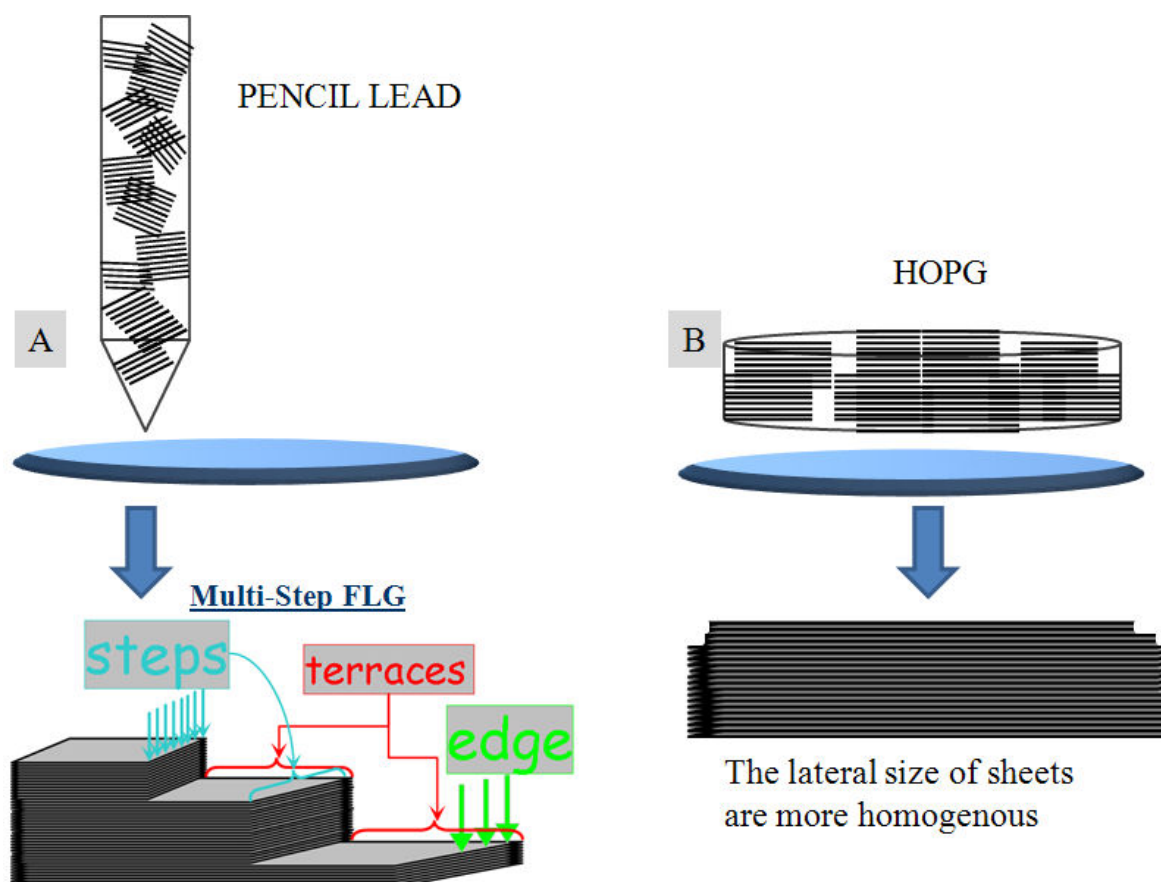


Figure 3.8: The difference and variation of lateral size of sheets within FLGs depending upon the raw materials used. A) FLG-Abl from pencil lead, [239] B) FLG-HOPG from HOPG.

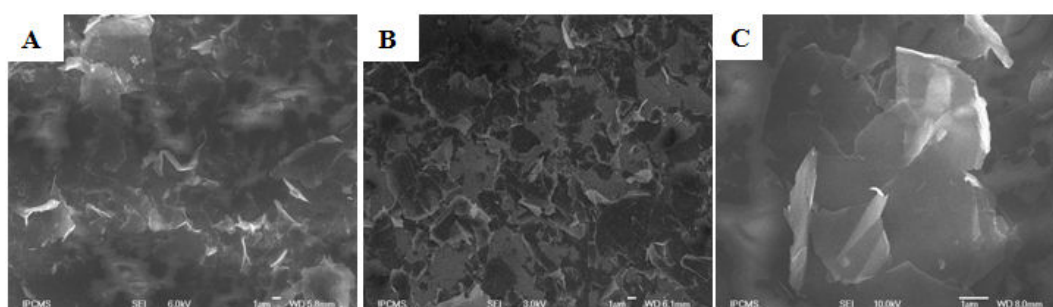


Figure 3.9: SEM micrographs showing morphology of FLG-HOPG24h transport devices.

be seen to have vertical orientation especially as the edges, seen as bright white areas on SEM images [244]. Although R_s can be improved by to some extent by compressing or polishing methods, which might result in better contact/percolation among flakes and hence better charge transport characteristics. However it is not easily practicable without etching away or damaging the surface of film as it can easily be etched with only small applied force. On the other hand this curvature of the flakes towards the "z" direction (opposed to the punctual stacking) or vertical aligned morphology can be an advantage for charge transport in electrodes for dye-sensitized solar cells and storage (lithium ion battery) devices and also can be applied to graphene-based thermal interfacial materials for better thermal management in different electronics devices [39, 245, 246].

Apart from different morphology of the FLG flakes from pencil and HOPG, the important impact on the R_s/T performance could arise from different concentrations of both materials during the preparation of the films. For this reason three series of FLG sheets are possible as visible in figure 3.8.

3.3 Homogenization and Crystallization of Few Layer Graphene by μ -waves-assisted Oxidation in Water

FLG obtained by ablation of pencil lead could be improved in terms of the morphology by two steps: First, μ -waves-assisted oxidation in water, and second oxidation at $\sim 650^\circ\text{C}$.

The first step leads to the double structure, i.e. highly graphitic sheets (due to the action of μ -waves) and carbon nanoballs, which represent 40% of total weight (mass) according to the TGA analyses. The nanoballs are formed from hydrocarbons (toluene) adsorbed on FLG surface (figure 3.10A) and from exfoliation of small sheets of graphene from FLG. The latter probably happens at

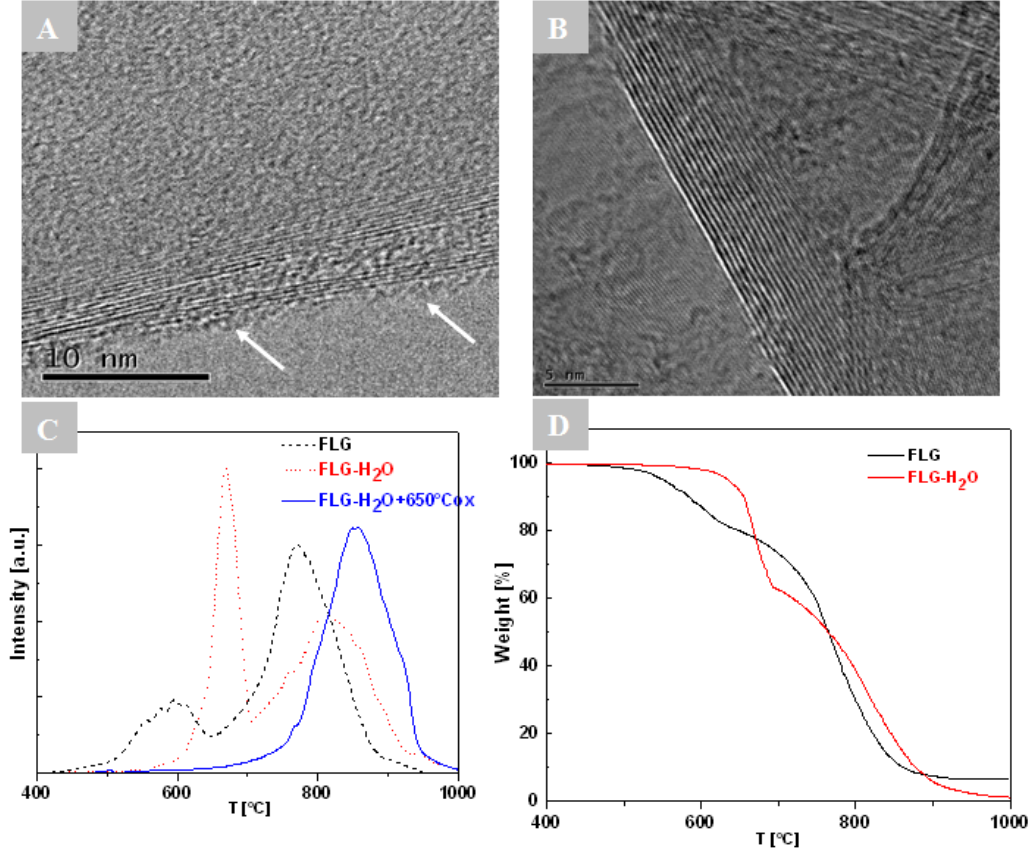


Figure 3.10: TEM micrograph of initial FLG with hydrocarbons layer adsorbed on the sheets (flashes lines), A) TEM micrograph of FLG after μ -waves assisted treatment in water (FLG- H_2O), displaying the highly crystallized FLG sheets, B). TGA (derivatives) profiles of initial FLG (FLG), FLG after μ -waves treatment in water (FLG- H_2O) and FLG after μ -waves treatment in water and additional oxidation at 650° C (FLG- H_2O +650° Cox), C) and FLG and FLG after μ -waves treatment in water (FLG- H_2O) D.

the steps and nanocracks, which decreases the "multi-step" nature of FLG-Abl. Since the nanoballs burn at a temperature significantly lower than graphitic FLG (60%), the temperature at $\sim 650^\circ\text{C}$ can be next applied for selective removal of the balls (figure 3.10B). This results in shift of combustion temperature, and "pure" FLG sheets with high graphitic degree can be achieved (figure 3.10C-

D). This is published article, "Activation of few layer graphene by μ w-assisted oxidation in water via formation of nanoballs- support for Pt nanoparticles" in Journal of Colloid and Interface Science, 2015) [247].

3.4 Roughness and Thickness Determination

The roughness and thickness were studied for different FLG samples from FLG-Abl and FLG-HOPG24h by the Dektak profilometer, AFM and NRA techniques which are presented in the following sections.

3.4.1 Surface Profile for Roughness by Profilometer

Roughness of FLG films from FLG-Abl sample (0.5 mg/mL concentration, 4 mL deposited volume, R_s 85 k Ω /□ and transmittance 31%) was performed for scan length of 400 μ m using Veeco Dektak 150 profilometer and a representative profile image is shown in figure 3.11. Two cylinder bars show the reference and measurement bars in the profile. The narrow green bar is for reference surface at zero and the wider red bar shows the measurement bar with reference to zero.

The roughness can be expressed in several ways but the Arithmetic average deviation from the mean (R_a) and the Root Mean Square of the average roughness (R_q) also called RMS are the two functions that are commonly used. In other words, the R_a is average distance from the mean line whereas, the R_q is the geometric mean of the average roughness R_a , so the later is always higher than the former by 10%, at least. The profile shows that the average roughnesses are around 107 nm by R_a and 130 nm by R_q (RMS), respectively, but several peaks up to 600 nm can be observed. R_q being the geometric mean of R_a is 10% higher than R_a , at least.

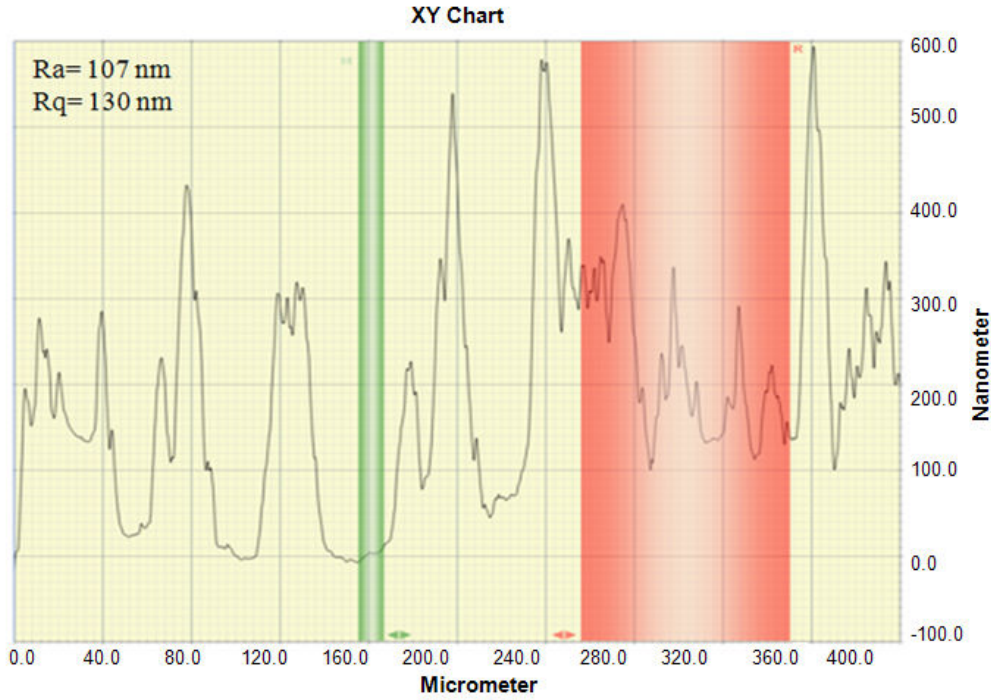


Figure 3.11: Surface profile for average roughness values for a FLG-Abl device.

3.4.2 Surface Profile for Roughness by AFM

To further understand the roughness, the AFM (NT-MDT Stand Alone SMENA Scanning probe Microscope) analyses were performed, working in tapping mode. The AFM profile images and histograms for FLG-Abl devices are given in figure 3.12.

For a relatively flat area without notable feature, the average roughness of FLG films as indicated by Ra and Rq (RMS) are 96 and 118 nm, respectively, (figure 3.12A) which verify the previously obtained results by Dektak profile (Ra 107, Rq 130 nm) with only small variations noting the variation of the scan size in both measurements (Dektak 400 μm distance vs AFM 10 $\mu\text{m} \times 10 \mu\text{m}$). The AFM images correspond well to the SEM images obtained for these films, the presence of thicker points, which are consisted of FLG flakes agglomerates. Figures 3.12B and C provide the 3D image and histogram fitted by Gaussian

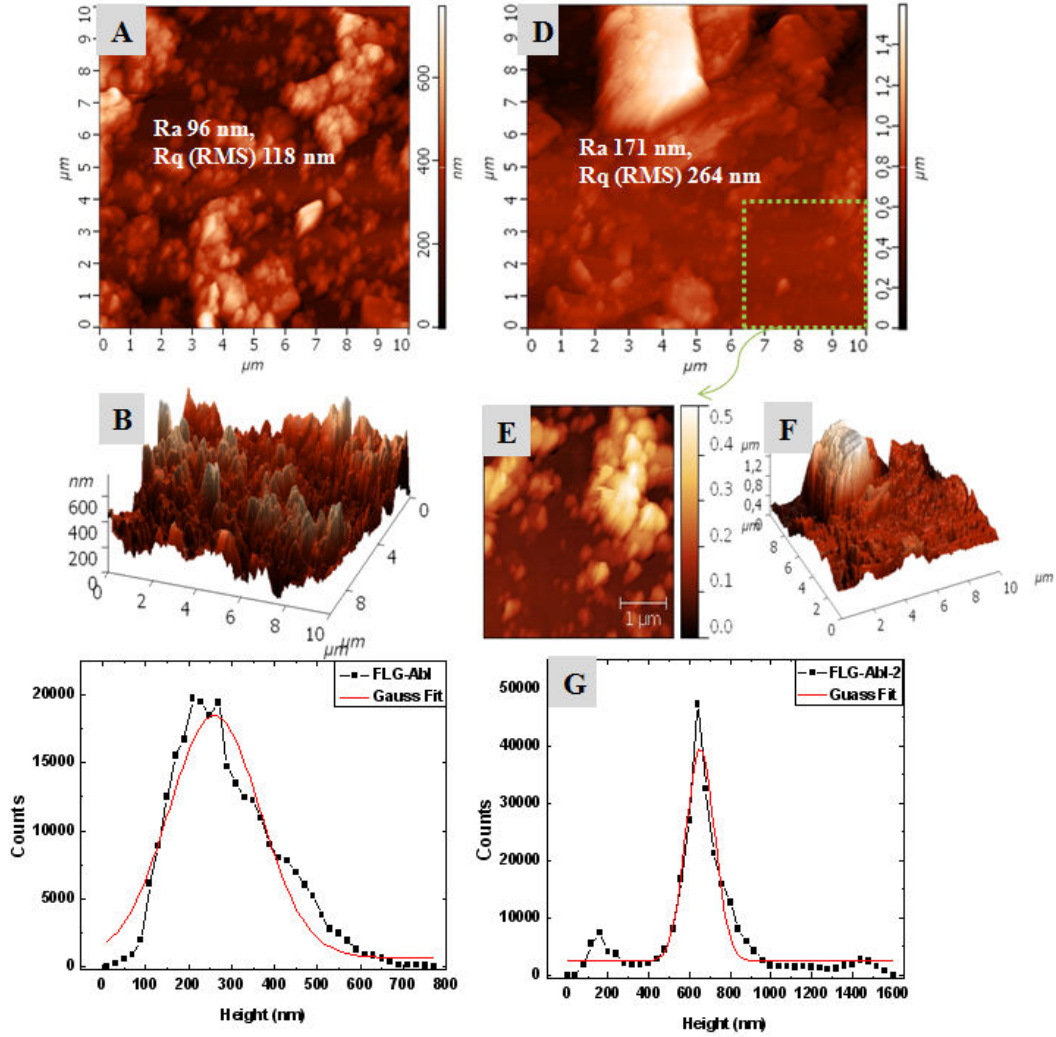


Figure 3.12: A) AFM topography profile image of FLG-Abl device, B) 3D image of the profile, C) Histogram profile fitted by Gaussian curve, D) AFM image at a different location with a big micrometric flake, E) 3D image of profile with large flake F), 2D image of the inset showing smoother area in the profile, G) Histogram profile fitted by Gaussian curve of image in D.

curve, respectively, of the same profile. Note that the step size for height was increased to 20 nm from its original size of 1 nm to get clear evaluation of the roughness by histogram profile. The Gaussian fit, however, absolves the special features or random distribution. However, as noted earlier in the case of the

Dektak profile, very thick flakes/fragments can reach height up to 800 nm as illustrated by the Dektak profile as well by the AFM images. Some fragments can be even accidentally thicker and this can be seen in figure 3.12D for a scan at different location on the same sample, where a thick fragment is seen in light orange/white color. This image shows that the highest peak can attain up to 1.6 μm height (for the same sample at a different location). The R_a and R_q values are also affected (although not significantly) and increased to 171 and 264 nm, respectively. Figure 3.12E shows the scan of a small homogeneous region of $4 \times 4 \mu\text{m} = 16 \mu\text{m}^2$ from the same profile and reveals that there are many areas below 200 nm as indicated by major dark orange color. Figures 3.12F and G show the 3D profile and the histogram fitted by a Gaussian curve, respectively, of the same scan with the thick flake including the highest peak at around 1.6 μm and smaller peaks at around 0.8 μm . The histogram in 3.12G shows a small peak between 50 and 300 nm (height) corresponding to population of smaller peaks in this region (corresponding roughly to the maximum of figure 3.12C) which are overshadowed by the peaks at higher amplitudes.

The interaction of tip with the FLG film under study has not shown any evidence of modification in the roughness or the topography of the films due to repeated scans on the same location under same conditions.

For the FLG-HOPG24h ($\sim 0.1 \text{ mg/mL}$ concentration, 40 mL deposited volume, R_s 167 $\text{k}\Omega/\square$ and and transmittance 36%) sample, larger scans were performed ($50 \times 50 \mu\text{m} = 2500 \mu\text{m}^2$) near the edge and at the center of the device, for approximately same deposited volume as FLG-Abl. Figure 3.13 shows the AFM images and histograms of FLG-HOPG24h device.

The results indicate that the roughness average values increase to $R_a = 159 \text{ nm}$ and $R_q = 240 \text{ nm}$, respectively, for such device (figure 3.13A), compared to $R_a=96$ and $R_q=118$, respectively for FLG-Abl device. It further increases at the center of the device to $R_a = 250 \text{ nm}$ and $RMS = 344 \text{ nm}$ (figure 3.13D), respectively, due to the higher probability of deposition by spray on the center

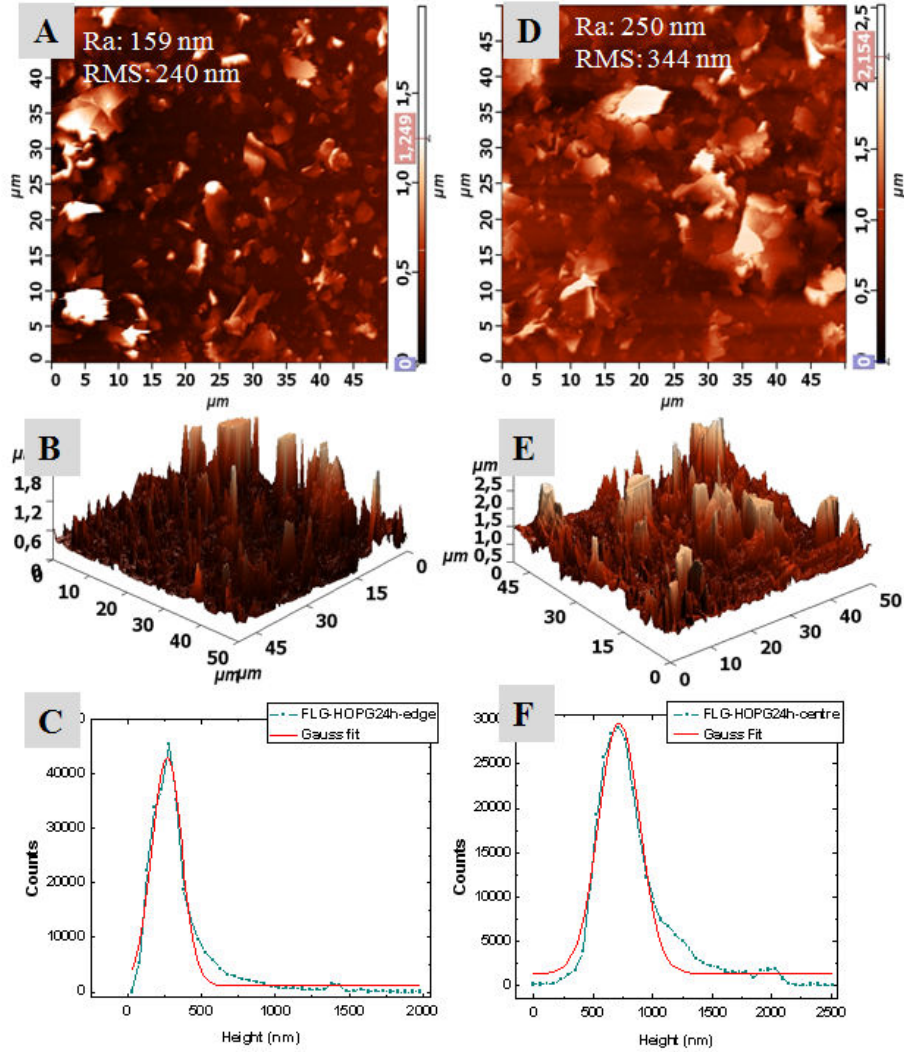


Figure 3.13: A-B) AFM topography profile image of FLG-HOPG24h device at edge and related 3D image, C) Histogram of the profile fitted using Gaussian curve, D-E) AFM topography profile image at center of the device and related 3D image, F) Histogram of the profile fitted using Gaussian curve.

of device, for being directly under the flow of nozzle. Respective 3D images and histogram profiles for scan at the edge and at the center are shown in figure 3.13B-C and 3.13E-F, respectively. The height step size for these histograms were increased to 40 and 61 nm, respectively (which was originally set to 1 nm) for large data points. These results indicate the heterogeneous morphology/topography of

films which not only impedes the charge transport among the flakes but addresses a challenge to obtain uniform films with homogeneous properties for electronics applications as well. If compared to the FLG-Abl, however, the highest points for FLG-HOPG24h are thinner (see AFM images and 3D profiles), which indicates that they are mostly the flakes, which lift vertically from the surface. In the case of FLG-Abl the thick points are mostly stacked in "z" direction flakes. The morphology of FLG-HOPG film seems to be more advantageous for the further application where the charges need to be transported to upper layer.

3.4.3 Thickness by NRA

The Nuclear Reaction Analysis permits to obtain the true atomic density (up to few hundreds of nm deep including the voids) of films by estimating the quantity of elements using their nuclear reactions. Knowing the surface and volume densities of the material, we can estimate the thickness of the material. Reversely, knowing the thickness of the film, we can calculate the volume density of the material. The conversion from channel (arbitrary number slots which are converted to corresponding energy values) to energy is made by using the standard oxygen nuclear reactions [$O^{16} (d,p_0) O^{17}$] and [$O^{16} (d,p_1) O^{17}$] and carbon nuclear reaction using deuterium (2H) ions [$C^{12} (d,p) C^{13}$] on a calibrated SiO_2 sample, with a thickness of 200 nm. Since the resolution of NRA is up to few μm , we have the depth profile through the FLG film and on the SiO_2 substrate that is why we have the two oxygen peaks for two reactions (3.14). The conversion gives us the energy (E) in keV as the function of the Channel (C) is calculated to be $E = 7.04 \times C - 85.00$.

From SIMNRA software (simulation for NRA spectra) spectrum the FLG film is evaluated to contains 6.25×10^{17} atoms/cm² (carbon concentration) which we can call cross-sectional surface density of film (ρ_{sf}). The profile is shown in figure 3.14.

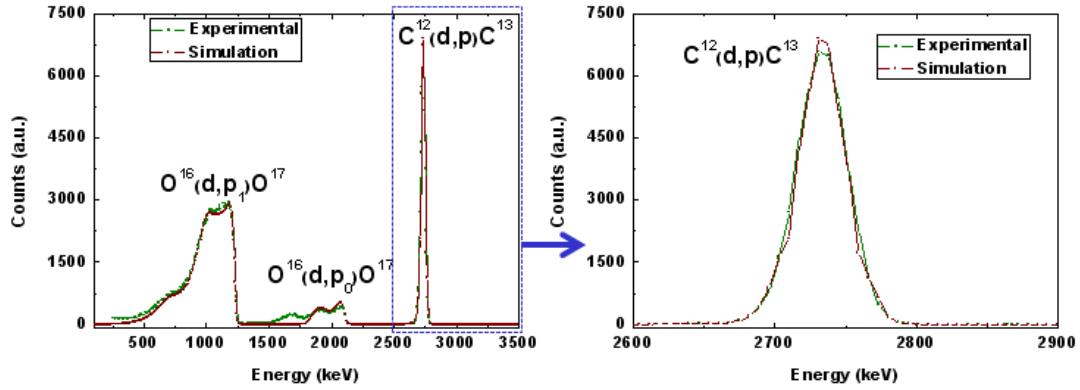


Figure 3.14: NRA profile simulated and experimental for the FLG-HOPG24h-40mL device.

To deduce the thickness of FLG film, we need to know the density of the film. In a first time, assuming that the density of FLG corresponds to the density of bulk graphite material, we can calculate:

Volume density of graphite (gram/cm³), $\rho_{vg} = 2.25 \text{ g/cm}^3$

Avogadro number, $N_a = 6.023 \times 10^{23} \text{ atoms/mol}$

Molar weight of carbon $M = 12 \text{ g/mol}$

Using this information, the atomic density of graphite (atoms/cm³), ρ_{ag} can be calculated by:

$$\rho_{ag} = \frac{\rho_{vg} \times N_a}{M} = \frac{2.25 \times 6.023 \times 10^{23}}{12} = 11.25 \times 10^{22} \text{ atoms/cm}^3 \quad (3.1)$$

The surface density of FLG film (ρ_{sf}) is obtained by NRA measurement, hence, the thickness of FLG film T_{f1} can be calculated dividing the surface density of FLG film (ρ_{sf}) by the atomic density of graphite (ρ_{ag}).

$$\text{Thickness}(T_{f1}) = \frac{\rho_{sf}}{\rho_{ag}} = \frac{6.25 \times 10^{17}}{11.25 \times 10^{22}} = 56 \text{ nm} \quad (3.2)$$

This corresponds to an equivalent thickness of graphite of $\sim 56 \text{ nm}$. The thickness is however, lower than the thickness T_{f2} of 130 nm obtained by the Dektak method. In figure 3.15) the average height of the film is computed from

the zero level. The substrate is obtained by removing the FLG by a sharp line scratch with a needle.

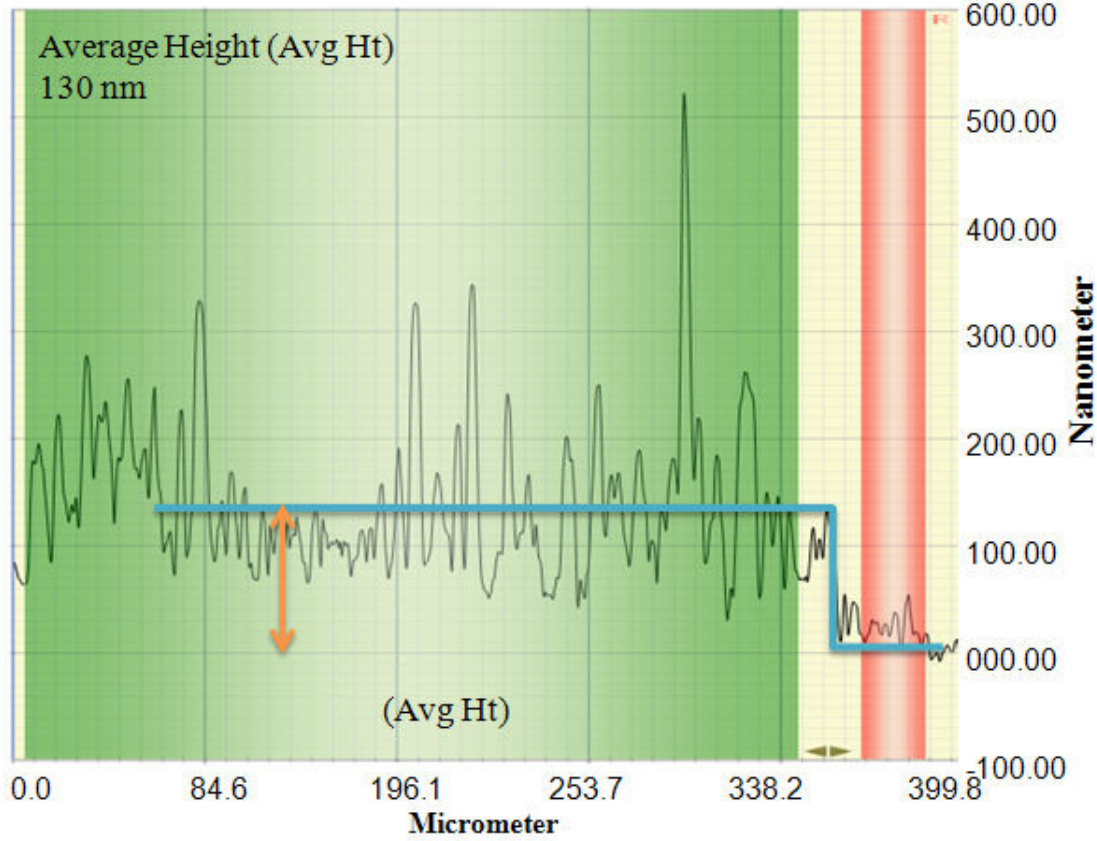


Figure 3.15: Thickness of FLG film obtained by the Dektak profilometer by calculating the average height of the film.

This confirms that the film volume is not completely filled due to the occurrences of voids. From the two different thicknesses obtained by two methods (by dektak and NRA), we can estimate the percentage of voids considering the later thickness values obtained by the Dektak profilometer.

$$Voids(\%) = \frac{T_{f2} - T_{f1}}{T_{f2}} = \frac{130 - 56}{130} = 57\% \quad (3.3)$$

So what is measured by NRA and profilometry is the true density of FLG film in which individual graphene sheets are not perfectly aligned horizontally

and flat over each other, as is also confirmed from SEM and AFM images. Using the value of thickness (T_{f2}), the new volume density of FLG film (ρ_{vf}) can be obtained from atomic density of the cross-section film (ρ_{af}) by:

$$\rho_{af} = \frac{\rho_{sf}}{T_{f2}} = \frac{6.25 \times 10^{17}}{130 \times 10^{-7}} = 4.807 \times 10^{22} \text{atoms} \times \text{cm}^{-3} \quad (3.4)$$

Subsequently,

$$\rho_{vg} = \frac{\rho_{af} \times M}{Na} = \frac{4.807 \times 10^{22} \times 12}{6.023 \times 10^{23}} = 0.96 \text{grams/cm}^3 \quad (3.5)$$

The obtained volumic (ρ_{vf}) and atomic (ρ_{af}) densities in the film are little lower than the half of the volumic (ρ_{vg}) and atomic (ρ_{ag}) densities of graphite, respectively which seems to be unrealistically lower. The causes of error can be the thickness value obtained by Dektak profilometry which calculates an average height of peaks on the surface of the film by scanning with the tip. But it cannot scan below the peaks on the outer surface so the voids that are between and below these peaks are not accounted for by the scanning tip. The reason for this high void content also lies in the fact that the graphene sheets are not of same size and thickness, and with spray deposition, the additional stacking of FLGs in the z direction contributes to increase these voids. The figure 3.16A describes the arrangement of FLG sheets in graphite, showing the voids formed in the film by stacking of FLG fragments of different lateral sizes and thicknesses, and inability of tip-based profilometer to account for these voids by averaging the peaks only.

3.5 Determination of Work Function

For (opto)-electronic applications, one of the most important material characteristic is the work function (WF) of the material (in solid form), denoted by Φ . XPS working in the UPS mode was used to determine the WF. The UPS spectra of FLG ablated from pencil lead (and FLG-B9 obtained by sharpener) and FLG-HOPG showing the valence band spectra are given in the figure 3.17.

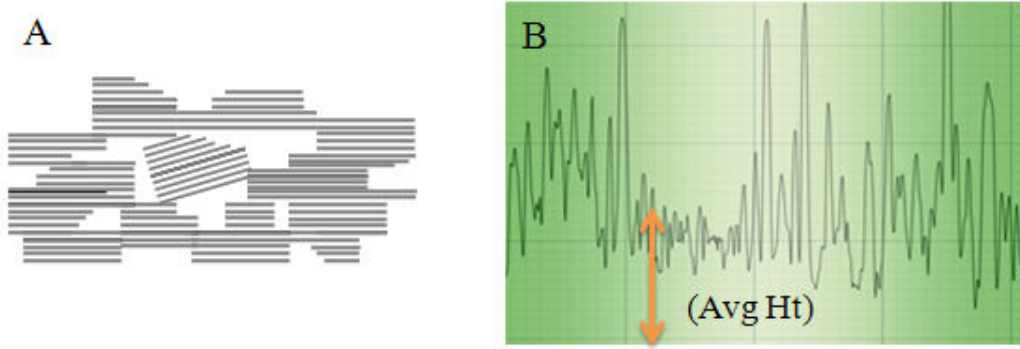


Figure 3.16: A) A possible schematic description of FLG flakes arranged in the film assuming additional stacking in the z direction, B) surface profile of FLG film.

The binding energies of the electrons are given in the increasing mode starting from the HeI line (21.23 eV).

The values of WF of the materials in powder form were determined by subtracting the difference of the UPS secondary electron cutoff (cutoff) and Fermi edge (system calibrated for $V_F=0$, see section 2.5.5.2 in chapter 2) E_F from the excitation energy of the source HeI (21.23 eV).

$$\Phi(\text{eV}) = \text{HeI} - (\text{Cutoff} - E_F) = 21.23 - (\text{Cutoff} - 0) \quad (3.6)$$

These results indicate that the obtained work-functions of FLG-Abl (3.6 and 4.0 eV respectively) materials are lower than those required for TCE (as anode electrode) applications. However, they seem to be suitable to replace low work function counter electrodes materials (like Ag, Al, ... as cathode electrodes), which require a work-function between 4.0-4.3 eV. For FLG-HOPG the work-function can be suitable for anode electrode although it is slightly lower than that of ITO (4.7 eV).

Work function of FLG B-9 (pencil lead) is difficult to ascertain as the spectra displays a large error in the absence of clear inflexion which can be related to inhomogeneous morphology, due to the presence of inorganic binder. It is

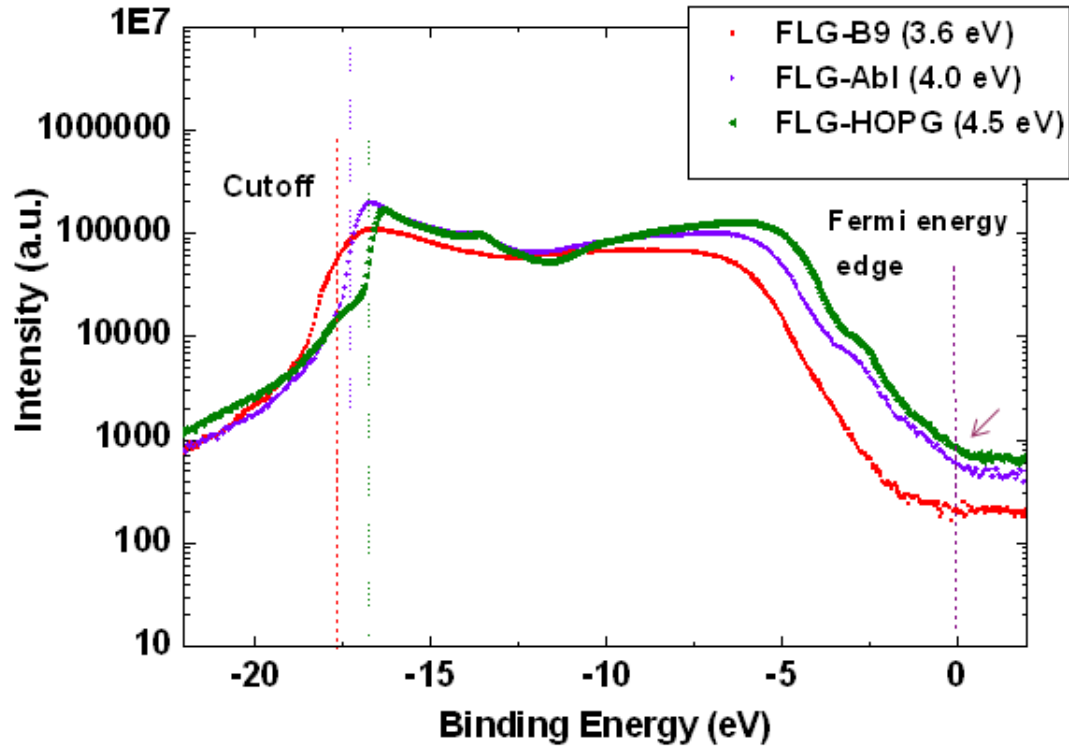


Figure 3.17: UPS work functions of FLG materials.

determined to be very low (3.6 eV), also due to the fact that pencil leads contain minerals (kaolin clay) as inorganic binder (15 wt % kaolin) to maintain the macroscopic form of pencil [40]. FLG-Abl also has a lower work-function than the generally reported value (between 4.2-4.3 eV). This is due to the introduction of oxygen or other functionalities such as CH_3 , OH, carbonyl during the purification steps and adsorbed hydrocarbons [12]. Generally speaking, XPS and UPS are surface-sensitive technique and work function can be affected by many factors including surface morphology/smoothness/roughness, thickness, orientation of material, surface impurity and doping, For thicker FLGs, the work-function approaches that of bulk graphite (4.6 eV) [49]. This order of work-function was here determined for HOPG material. It is known however, that the work-function

of graphene can be tuned by doping. For example, the alkali metal carbonates can n-dope graphene and lower its work-function down to 3.4 eV [248]. During the production of graphene and rGO, and subsequent purification steps, several functional groups can be attached to the edges of the material. They can influence the work-function by increasing/decreasing it, depending upon the type (p or n) of such groups. This is reported that the presence of carbonyl groups (-OH) (electron acceptor) can increase the work-function of graphene, whereas the addition of methyl (-CH₃) or carbonyl groups which are electron donating functionalities to the surface can decrease the WF [25].

In conclusion to this part, the above results of conductivity of transparency of FLG-Abl and HOPG devices prepared with different volumes of spray deposition are low. After thermal treatment, the R_s decreases by one order of magnitude at maximum but remains at least two orders of magnitude higher than the one required for TCE applications. Although the transmittance has been improved for FLG-HOPG up to 73% which is encouraging. The R_s is highly affected by adsorbed impurities as well as by the random stacking of FLGs. The preferential stacking in z direction as well as leaving empty spaces between flakes were analyzed by microscopic techniques. The low work-functions (4.0-4.3 eV) obtained for some of our samples can be useful candidates for counter or conductive electrodes in OSCs and other electronic applications, respectively. The materials with the higher work-functions can be employed as TCEs provided that the R_s and transmittance are in the desired range. To further improve the R_s , our FLG materials have to be improved. It seems also that HOPG provides better FLG flakes to form the film by spray technique and percolation is also easier to obtain than FLG-Abl due to the more homogeneous morphology of the flakes. The morphology where vertical lifting of flakes occurs, can be an advantage for electronics applications including OSCs and other electronic devices.

3.6 Percolation in FLG-Abl

Several samples were prepared with different concentrations to obtain the minimum amount required to attain the percolation for FLG-Abl. The R_s (measured by FPPs) is presented for FLG-Abl material as function of concentration in table 3.18. For each concentration, the R_s decreases with increase of FLG

Weight/Amount (mg)						
	1	1.5	2	2.5	3	3.5
FLG-Abl(0.5 mg/mL)						
$R_{s(\text{avg})}$ (as-prep) ($K\Omega/\square$)	360	280	174	56	12	7
After t.a. 450°C/Ar	300	80	20	26	7	5
FLG-Abl(0.25 mg/mL)						
$R_{s(\text{avg})}$ (as-prep) ($K\Omega/\square$)	-	644	236	100	31	16
After t.a. 450°C/Ar	142	281	89	21	13	12
FLG-Abl(0.1 mg/mL)						
$R_{s(\text{avg})}$ (as-prep) ($K\Omega/\square$)	933	800	78	37	32	16
After t.a. 450°C/Ar	1960	234	34	11	10	3.5

Figure 3.18: Percolation table for FLG-Abl.

amount. The average R_s values suggest that an amount of 1 mg and 1.5 mg is sufficient to cover the surface of $2\text{ cm} \times 2\text{ cm}$ for FLG-Abl and FLG-HOPG24h, respectively. Due to randomness of the spray deposition, effect of different concentrations could not be judged so easily and there is no strict correlation between different concentrations especially, for low amounts of FLG (1-2 mg). For higher amounts, the R_s seems to decrease systematically with decrease of concentration. Random deposition makes that significant increase of conduction pathways (multiple channels) occurs for different amounts of FLG for each concentration. At higher amounts, for example 2 mg onwards a decreasing tendency in the R_s is observed as function of concentration.

3.7 FLG by Microwave-assisted Liquid Phase Exfoliation (LPE) of Expanded Graphite in Toluene (FLG- μ w)

This section presents the preparation of FLG obtained by Microwave-assisted Liquid Phase Exfoliation (LPE) of Expanded Graphite in Toluene, followed by presentation and discussion of the representative results comprising TEM, XPS, Raman and charge transport analyses.

3.7.1 Preparation and Characterizations of FLG- μ -w

Due to the hindrances in obtaining the highly conductive, transparent and uniform films by FLG-Abl and FLG-HOPG materials, another route was envisaged to prepare FLGs by μ -waves-assisted exfoliation of an expanded graphite (EG) in toluene. It was expected that the final FLG product will have higher lateral size of sheets as well as higher conductivity due to the use of μ -waves irradiation. Witnessing an important interaction with FLG-Abl as observed in earlier results [249], toluene was chosen as suspension medium, first to induce the potential intercalation between graphite sheets during dispersion (ultrasonication step), second to stabilize the already exfoliated FLG sheets in suspension, and third due to the low μ -waves absorbance. Figure 3.19 shows the SEM images of expanded graphite. The exfoliation of expanded graphite (EG) was performed by submission of an expanded graphite suspension in toluene with a concentration of 2 mg/mL to μ -waves irradiation at 600W power for 10 minutes, followed by a cooling step (see section 2.2.2.1 in chapter 2 for experimental details). Prior to the μ -waves experiments, EG was sonicated in toluene in a closed vessel and stirred for 24h, which aimed to help intercalation of toluene. The resultant product after μ -waves treatment consisted of settled down EG and a toluene supernatant. The latter contained exfoliated (extracted) few layer graphene flakes (FLGs), which

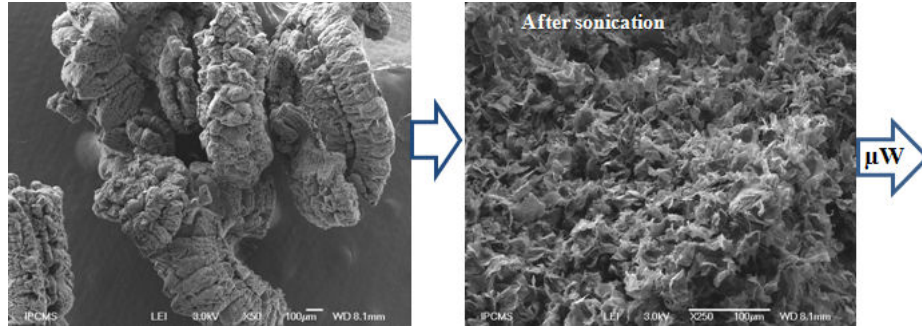


Figure 3.19: SEM micrographs of the expanded graphite A) after sonication B).

were next separated with a yield of $\sim 20\%$. The yield (percentage of exfoliation) was obtained by calculating the percentage of FLG separated to the settled down EG ($EG_{settled}$) from the initial EG ($EG_{initial}$), as follows:

$$Yield_{exfoliation}(\%) = \frac{EG_{initial} - EG_{settled}}{EG_{initial}} 100\% \quad (3.7)$$

The determined here yield is quite high due to the stirring step under pressure for 24h helping intercalation of toluene, (in the absence of the stirring step, the yield of FLG was only $\sim 7\%$). In the present experiment, the exfoliation process is additionally favored by a difference in the μ -waves absorption between EG and toluene, and then a rapid rise of temperatures. Contrary to toluene which displays a low dielectric constant ($\epsilon_0=2.38$ at room temperature), carbon materials are known to be good absorbers of μ -waves [250]. In this regard, we apply short temperature ramp with a high μ -waves power, in order to rapidly reach a demanded high temperature in the reaction media. This high temperature of the medium can be reached rapidly only by high power μ -waves absorption of EG. The figures 3.20A-B plot the curves of temperature-time dependency for EG-toluene, graphite plates-toluene suspensions and toluene alone, respectively, which are registered during 10 min experiments with varied conditions of temperature and power.

The curve in figure 3.20A clearly shows that since toluene cannot be effectively heated by μ -waves, the significant absorption of μ -waves by EG, results

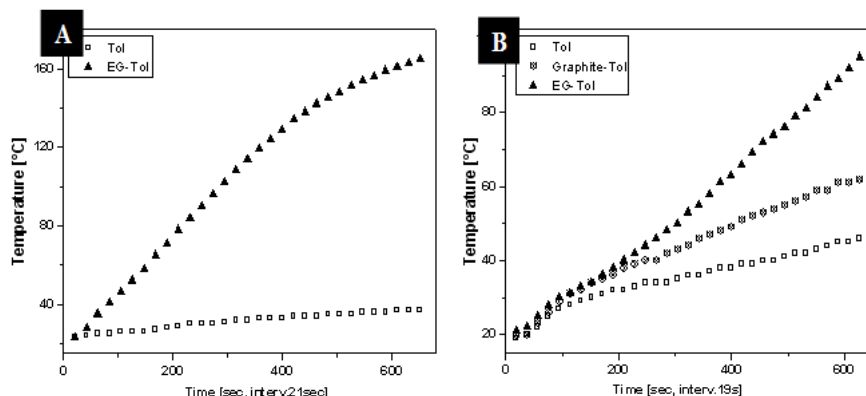


Figure 3.20: A and B. Temperature-time profiles obtained for toluene, EG-toluene and graphite-toluene medium under μ -waves irradiation with two different conditions of μ -wave experiment.

in very fast energy transfer and heating of toluene, and the solution in the reactors reaches a final temperature of 160 °C. This rapid rise of temperature allows the EG separation (exfoliation or extraction), which is probably favorable due to the strong electron donor-acceptor interactions of toluene and graphene by π - π stacking. Such donor-acceptor interactions can be a driving force for both, initial intercalation of toluene between graphene sheets (especially at the cracks) and final dispersion of the flakes in toluene. The last effect (dispersion) will decrease additionally a possible collapsing of exfoliated sheets during the cooling step [251]. A desorption of toluene from the graphene surface required indeed high energy ($T = 450$ °C at 10^{-4} Pa) [249]. For comparison, lower final temperature of toluene and lower heating rate are observed for graphite platelets (figure 3.20B), which is probably related to differences in dielectric permittivity, depending on the sample/size of both materials [252]. A TEM analysis reveals that the number of sheets within singular flakes does not exceed 10 with an average number of 7. Figure 3.21 shows representative low, medium and high resolution TEM images of the FLG flakes as well as a C1s XPS spectrum.

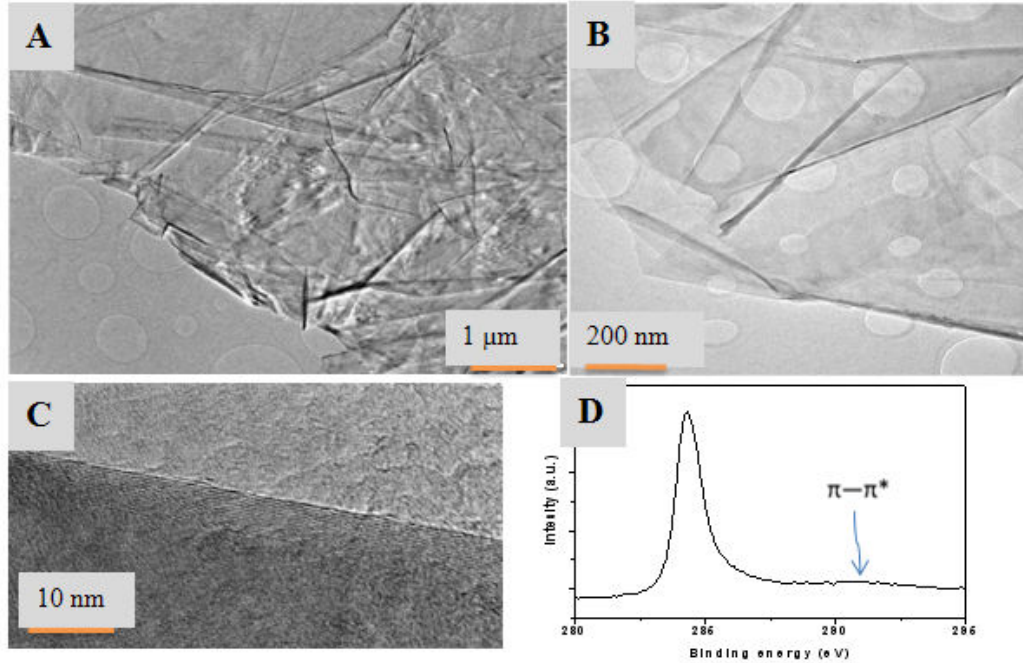


Figure 3.21: TEM micrographs A-C) and XPS C1s peak of FLG D).

The quite low full width at half-maximum (FWHMs) of C1s peak, measured at 1.1eV, indicates a high degree of "sp²" carbon. The progressive broadness of the C1s peak towards higher binding energy is linked to the proper asymmetry of sp² C peak, as well as to some sp³ C linked to oxygen groups (-OH). The tail extend corresponds to gradually increased electro-negativity group (-COH, -COOH) and a small shake-up line of aromatic carbon compounds can be evident at 291 eV ($\pi-\pi^*$ inter band transition). The percentage of oxygen calculated from C1s and O1s peak areas is 5%.

The Raman spectra performed on few different FLG flakes confirm the existence of flakes with varied thicknesses. These flakes are fortunately from highly oriented graphite, therefore the 2D band is sensitive to the material interaction between graphene sheets. Thus, the modification of the 2D peak shape, which consists of four components (asserted by visual examination 2D1B, 2D1A, 2D2A, 2D2B, fit not shown) allow to state that the FLG contains three to five graphene layers (figure 3.22) [44]. Here, broadening towards lower wavenumbers 2D peak

(increase of the relative intensity of the 2D1 component resulting in 2D splitting) indicates the presence of 3-5 layers containing flakes (figure 3.22A) or more than five. The figures 3.22B-D show also the I_G , I_D and I_D/I_G mappings, respectively, which were performed within singular flakes presented on figure 3.22A (insert). The Raman mappings clearly show low (and homogeneous) concentration of defects in the FLG planes, while the highest concentration of defects occur at the edges, when comparing the I_G and the I_D mappings.

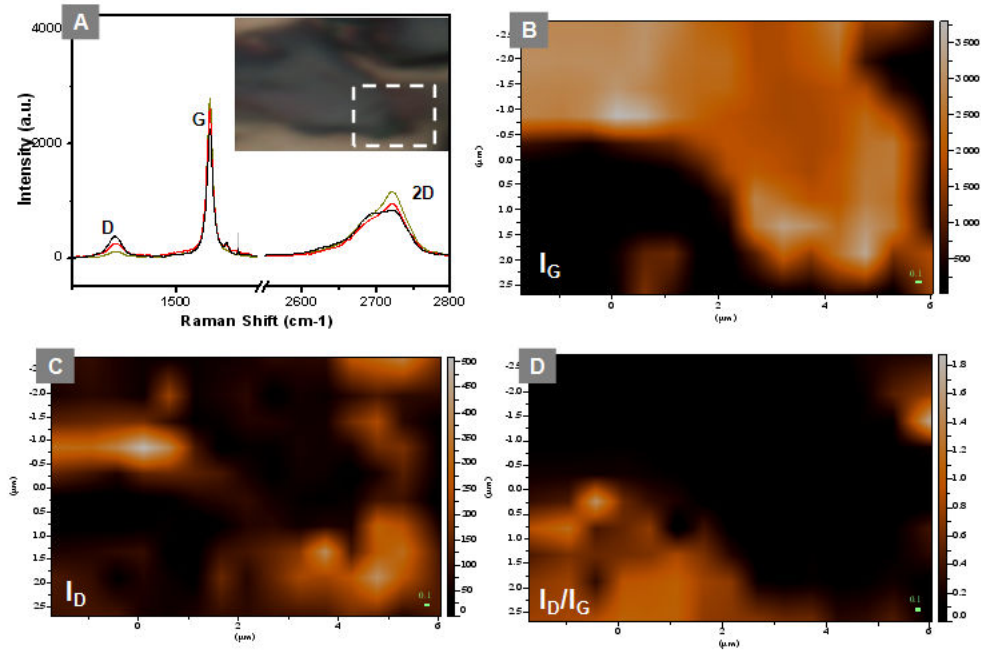


Figure 3.22: A) Representative Raman spectra on FLG flakes. B-D) I_G , I_D and I_D/I_G Raman intensity cartographies obtained (calculated for I_D/I_G) from area of the flake presented at the insert of the image in A.

3.7.2 Charge transport in FLG-MW

The FLG flakes exhibit large lateral size from few and up to tens of microns. Such large surface allows to perform conductivity measurements on varied and significant distance within a singular flakes. Such distance-dependent electron

transport measurements reflect the degree of continuity or homogeneity of the sample. The electrical measurements were performed by the two-point probes (2PPs) technique. The FLG was dispersed in ethanol and deposited on an interdigitated FET-like device between two gold electrodes with gaps of 2.5, 5 and 10 μm , respectively (see section of chapter 2 for device configuration). Deposited flakes were annealed at 200 $^{\circ}\text{C}$ for two hours under Ar prior to the electrical measurements. An examples of flakes deposited between gold electrodes for subsequent measurements is presented in figure 3.23A.

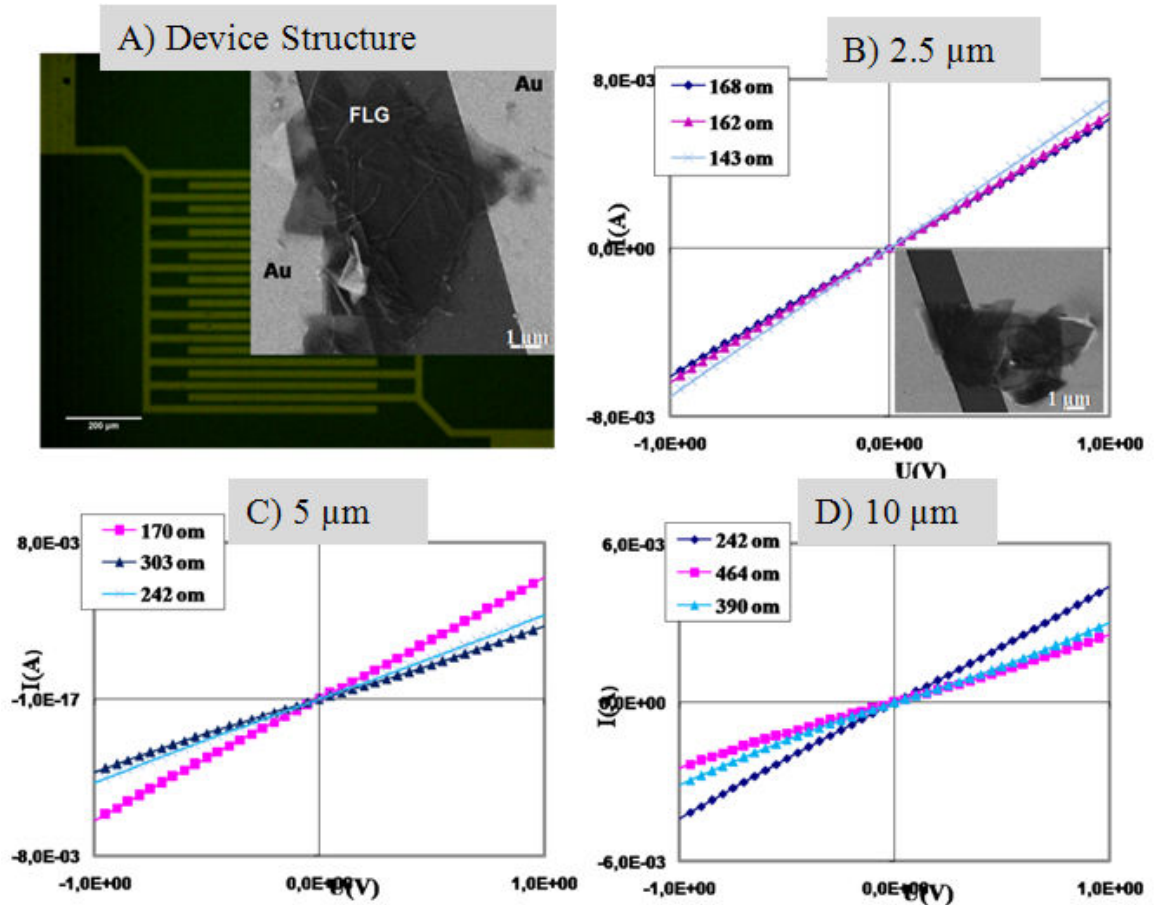


Figure 3.23: A) Representative images of measured FLG flakes between two electrodes in a FET-like device, B-D) The $I(V)$ curves obtained for few FLG flakes with varied electrodes distance at B) 2.5, C) 5 and D) 10 μm , respectively.

The flakes are deposited randomly and the measurements were carried out

by two probes technique (see the figure 3.23B-D, respectively). $I(V)$ curves- measured for several flakes for each distance along with corresponding resistance R values are plotted in figure 3.23B-D. All $I(V)$ curves reveal linear, ohmic behavior. This indicates no (or negligible) scattering of charges, due to the low defect content within the flakes, which is in agreement with the Raman analysis (weak intensity of the D band). The average resistance (R_{avg}) values obtained are 158 ± 15 , 238 ± 70 and $365 \pm 100 \Omega$ at the measured "device distance" of 2.5, 5 and 10 μm , respectively (figure 3.24A).

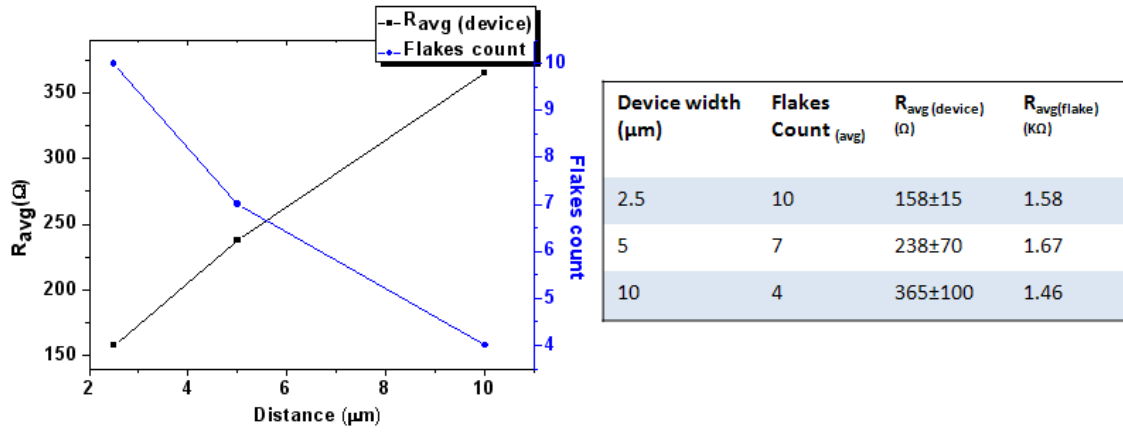


Figure 3.24: The R_{avg} device, FLG flakes count for each device width/distance of 2.5, 5 and 10 μm , respectively A) table enlisting the R_{avg} device, and R_{flake} for each device width/distance along with the flakes count B).

Each device contains variable number of flakes which were determined by HR optical microscopy. This average number of flakes decreases from ~ 10 for 2.5 μm , to ~ 7 for 5 μm and to ~ 4 for 10 μm , which is related to the higher probability of deposited flakes number and making connections with electrodes within lower gap (figure 3.24A). The linear increase of the resistance with the gap increase is due to the number of the flakes, which are measured for each electrode distance. The average resistance for each "flake" is determined by multiplying the obtained average R of each device (distance) with corresponding number

(average) of flakes. These average resistances also include the contribution of inevitable contact resistance and are affected by the substrate scattering.

The calculated values of flake resistance R_{flake} are 1.58, 1.67 and 1.46 k Ω respectively for 2.5, 5 and 10 μm (figure 3.24B). The minimum calculated values according to singular flakes are in the range of 500-700 Ω .

The agreement of the average resistance (R_{avg}) values obtained for each electrodes distance is in agreement with the Raman cartographies revealing homogeneity of the structure and absence of significant defects in FLG flakes even at the higher distance, 10 μm . The conductivity σ for "quasi square" flakes, in Siemens S can be calculated from resistivity ρ :

$$\sigma = \frac{1}{\rho} \quad (3.8)$$

Since resistivity is defined as:

$$\rho = R \times \frac{A}{L} = R \times \frac{W \times d}{L} = R \times d \quad (3.9)$$

Where R is resistance, A, L, W and d are cross sectional area, length, width, and thickness of samples (flakes), respectively. For a square sample W=L. Combining equations 3.8 and 3.9:

$$\sigma = \frac{1}{\rho} = \frac{1}{R \times d} \quad (3.10)$$

Flake resistivity (for a flake containing estimated 7 graphene sheets) is calculated by multiplying the obtained flake resistance ($R_{flake} = 1.6 \text{ k}\Omega$) with thickness of flake (d). The thickness is obtained by multiplying the number of sheets in a flake (n-1, since the number of interlayer distances is always 1 less than the total number of sheets in a flake) with the interlayer distance (d=0.34 nm) between two graphene sheets in the following way:

$$\sigma = \frac{1}{1.6 \times 10^3 \times 6 \times 0.34 \times 10^{-9}} = \frac{1}{3.3 \times 10^{-6}} = 0.3 \times 10^6 = 3 \times 10^5 S/m \quad (3.11)$$

For the "square" flake with 7 sheets and a resistance of 1.6 k Ω , the thickness: $(7-1) \times 0.34 \times 10^{-9}$, and the conductivity according to equation 3.10 is $\sim 3 \times 10^5$ S/m, while for the flakes with 500 Ω , it reaches almost 10^6 S/m (9.8×10^5 S/m). Such high conductivities are comparable with the conductivity (2.27×10^6 S/m, or 2.5×10^6 S/m) parallel to the sheets (horizontal) (σ_{II}), measured for graphite monocrystal or HOPG [144]. The electric property of the FLG is not only comparable with that of CVD-grown materials but also superior to the most of common exfoliation originated graphenes.

3.8 Conclusion

In summary, we have studied different FLG materials obtained by mechanical exfoliation and μ -waves-assisted liquid exfoliation of pencil lead, HOPG, and EG, respectively. FLG by ablation of pencil lead involves several filtration steps but is a high yield, facile and scalable method. The flakes are not larger than 2-3 μm . Charge transport was studied by Hall Effect, two and four-point probes (FPPs) for the devices prepared from these materials. Further, we have shown that the sample prepared by the hot-spray technique leads to overlapped FLG flakes with random deposition. It shows significant improvement of charge transport after thermal treatment. This is due to desorption of adsorbed hydrocarbon impurities (toluene and its decomposition intermediates) accompanied by low decrease of oxygen content, once annealed at 900 $^{\circ}\text{C}$. A desorption of toluene from the FLG surface requires a temperature as high as 450 $^{\circ}\text{C}$ under a pressure of 10^{-4} Pa, showing strong interaction of this electron-donor species with graphene materials. This information is important to take into account when graphene-based chemisensors are designed. A diffusive electron transport mechanism along with the negative temperature coefficient feature of FLG film was observed during Hall Effect measurements which can be useful for potential applications in thermistor devices. The lowest sheet resistance of 760 Ω/\square was recorded for the

annealed FLG film. These results of conductivity make these materials suitable for conductive coatings and electrodes and their low work-function is suitable for cathode electrode for OSCs. The main problem is the random deposition by spray and low percolation between the flakes due to the multi-step structure in FLG from pencil lead (FLG-Abl) and inhomogeneous and low size of the flakes. The roughness of both the FLG-Abl and FLG-HOPG films resulting from the useless agglomerates formed during suspension dispersion and spray are major obstacle to get smooth films with homogeneous surface and repeatable properties. However, significant improvement in the transmittance was achieved in the case of FLG-HOPG24 devices. FLG-Abl flakes were improved by μ -waves treatment in water oxidation at 650 °C.

In the end, the FLG was obtained by liquid exfoliation of EG assisted by μ -waves irradiations. It was observed that few layer graphene flakes with large flake size and high electrical conductivity can be obtained by this method. Significant absorption of μ -waves by EG/FLG allows to reach low defects high range homogeneous conductive materials. Very low sheet resistance together with the large lateral size of FLG flakes, up to tens of microns, are comparable to those of high quality graphenes synthesized by CVD method, while considerable sheets' size is of high interest to reach easy percolation in the further formed films. However, despite the advantages of large lateral size flakes and better electronic properties, FLG from microwave had problems of low yield, forming aggregates in suspension and being difficult to operate in the standard spray-system for film formation (due to the small diameter spray nozzle). To decrease the number of sheets within individual FLG flakes and increase a percolation in films, the rGO-FLG and CNT-FLG hybrids, respectively are further investigated.

4 Results: Reduced Graphene Oxide (rGO) and rGO/FLG Composite

This chapter starts with description of preparation of rGO and rGO/FLG composite materials and the charge transport devices in the section 4.1. Characterizations for these devices are presented in section 4.2, starting with the charge transport studies in subsection 4.2.1, followed by the morphology and roughness profiles and work-function determination in subsequent subsections 4.2.2 and 4.2.3, respectively. Percolation study for the rGO and rGO/FLG is presented in section 4.3. Last, the conclusion is presented in section 4.4.

4.1 Preparation of rGO and rGO/FLG Composite Materials/Charge Transport Devices

Due to the problems with FLG materials discussed in the chapter 3, simultaneous reduction and exfoliation of Graphene Oxide (GO), and Graphene Oxide (GO) and Expanded Graphite (EG) composite have been attempted by the Liquid Phase method with the assistance of μ -waves in a reducing media, e.g. ethylene glycol, (described in the section 2.2.2.2 in chapter 2). Very fast heating rate and conductivity of FLG flakes are obtained from exfoliation under μ -waves (repairing of the crystal lattice) and motivated to use the μ -waves in order to prepare rGO and rGO/FLG composite by reduction/exfoliation process under μ -waves [253], [225]. Since carbon materials are generally good absorbers of microwaves, the combination of the thin-sized large GO and the large lateral sized EG makes a good possibility to obtain thinner and larger sheets which can easily cover the large lateral area on the glass plates/substrates during hot-spray method and provide better percolation [250]. Ethylene glycol is a known reducing agent and

is used as a solvent, which has reductive properties to avoid oxygenation during μ -waves heating, and additionally, can reduce the GO. Both materials resulted in good yield of 50-70% after exfoliation/reduction in the microwave. Later, dispersions were prepared by adding ethanol to the ethylene glycol suspension to lower the boiling point. Ethanol was added at an amount twice the volume of ethylene glycol. This changes the concentration of rGO and rGO/FLG to 0.25 mg/mL and 0.33 mg/mL in ethylene glycol/ethanol, respectively. This was done in order to facilitate the spray on hot plate so that the liquid can evaporate relatively rapidly during the deposition of rGO on glass/quartz substrates. The rGO and rGO/FLG from both GO and GO/EG, respectively, in ethylene glycol were used to grow thin films on glass/quartz substrates with various deposition quantities using spray-coating method (as explained in section 2.3). Several devices were prepared to measure the charge transport in the reduced graphene oxide films. Two types of devices were prepared based on the type of obtained materials: the reduced graphene oxide (rGO) and the reduced graphene oxide and few layer graphene composite (rGO/FLG), respectively. Due to the good ohmic contact and conductive samples/FLG films, the necessity to evaporate Cr/Au electrodes for four-point probes was not kept. So the measurements by FPPs were carried out by landing four probes directly on the rGO- μ waves and rGO/EG- μ waves films. Repetitive measurements confirmed the good ohmic contact between probes and rGO films for charge transport study. The advantage of this omission is that the effects of scattering and contact tunneling can be avoided.

4.2 Characterizations

4.2.1 Charge Transport in rGO and rGO/FLG

The charge transport was studied as function of the induced current by Four-point probes (FPPs) as explained in section 2.5. Representative results of charge transport of reduced graphene oxide devices are shown by $V(I)$ curves in figure 4.1. The results are shown for as-prepared and thermally-annealed devices

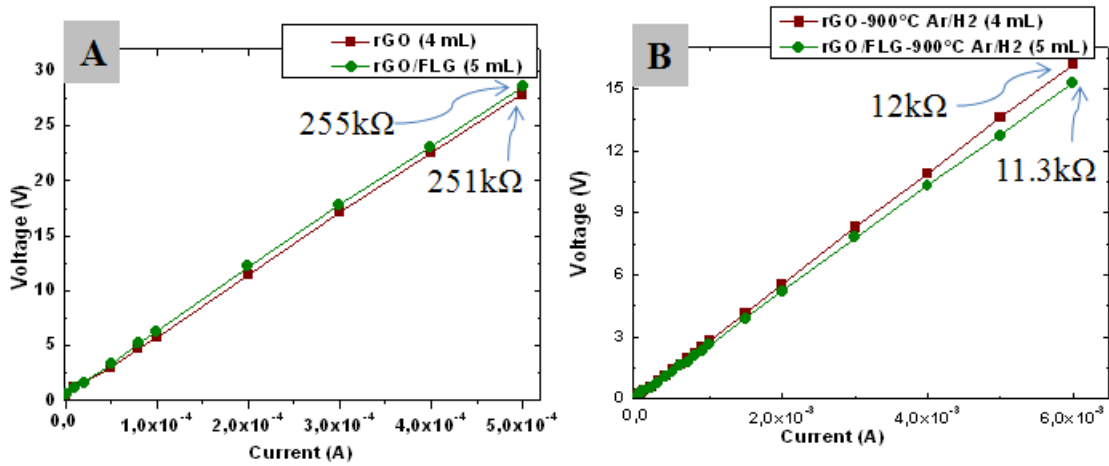


Figure 4.1: Representative $V(I)$ curves of rGO and rGO/FLG charge transport devices by four-point probes. A) as-prepared, B) thermally annealed at 900 °C under Ar/H₂ for 2h.

under H₂/Ar for two hours at 900 °C, respectively. The Ar gas was used during the ramp for the thermal annealing and H₂ was used for 2h at 900 °C. During the cooling step it was switched back to Ar. The charge transport measurements reveal that the sheet resistance is large, up to few hundreds of kΩ/□: 251 kΩ/□ and 255 kΩ/□ for the rGO and the rGO/FLG devices, respectively. This is comparable with our FLG-HOPG device with R_s of 236 kΩ/□, but is larger than FLG-Abl device with R_s of 85 kΩ/□, all of them being un-treated devices. High initial R_s can be also linked to the presence of ethylene glycol (which evaporates at very high temperature), high oxygen content, structural defects among others.

The obtained transmittances are 62% and 73 % for the rGO and rGO/FLG devices, respectively (figure 4.2).

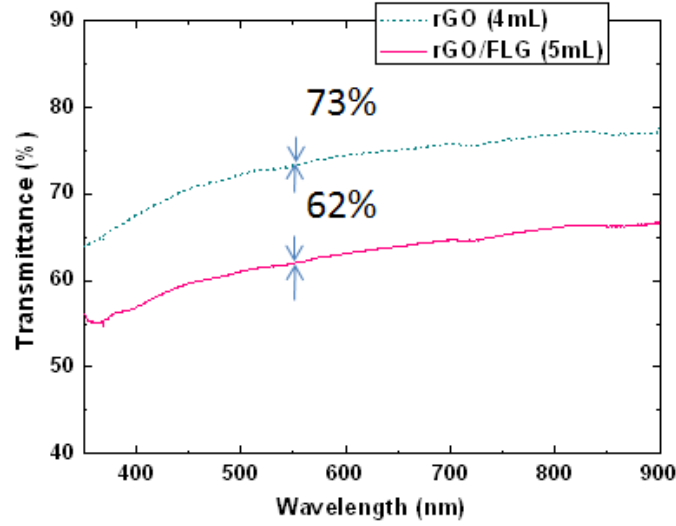


Figure 4.2: Representative transmittance spectra of the rGO and the rGO/FLG devices.

The higher transmittance is probably due to the incomplete reduction of the rGO by μ -waves-assisted reduction (non-reduced GO is transparent) as fully reduced GO will change color to become more darker. The reason is that, because rGO is not completely reduced after μ -waves treatment, is more transparent than rGO/FLG, where FLG is of much lower transparency, (non reduced GO is totally transparent). Note that the R_s and the transmittance were recorded at least two or three times on different locations of the same device, and the representative V-I curves and transmittance spectra plotted here are either average or median values (close to the average/representative value, because it is not possible to generate curves for average R_s or transmittance). Further, the real average values of both quantities (with \pm error) are given in the table 4.1 and are used in the calculation of conductivity of transparency.

Apart from the desorption of unwanted species, there is also a strong possi-

Table 4.1: Conductivity of transparency (σ_{gt}), of the rGO and the rGO/FLG devices.

Sample/Device	$R_{s(\text{avg})}$ k Ω /Sq	T_{avg} (%)	Conductivity of Transparency (σ_{gt}) (S/cm)
rGO (4mL)	250 \pm 20	73 \pm 10	9
rGO (4mL) 900°C Ar/H ₂	14 \pm 5	73 \pm 10	160
rGO/FLG (5mL)	259 \pm 20	62 \pm 2	6
rGO/FLG (5mL) 900°C Ar/H ₂	19 \pm 12	62 \pm 2	77
rGO/FLG (8mL) 900°C Ar/H ₂	4 \pm 2	40 \pm 2	190


bility of further partial thermal reduction of rGO during the thermal treatment in the inert environment which has increased the number of conductive islands with sp^2 electrons and contributed to a better charge transport. The R_s is shown to be lowered by one to two orders of magnitude up to few tens of k Ω /□ or few k Ω /□. The figure 4.1B displays the R_s around 12 k Ω /□ for both the rGO (average $R_s = 14 \pm 5$ k Ω /□) and the rGO/FLG (average $R_s = 19 \pm 12$ k Ω /□) devices, respectively. Further improvement in the R_s (mobility) could have been impaired by electron-phonon and short range scattering (intrinsic defects, e.g. carbon vacancies) and low number of non-conducting islands with sp^3 C remaining even after thermal treatment [254, 255]. These values are comparable with R_s of 22 k Ω /□ and 15 k Ω /□ obtained for the thermally-annealed FLG-HOPG and FLG-Abl devices, respectively. Further, these values are comparable to one of the best reported for CVD-rGO (a two-step thermal reduction and CVD-repair) single layer rGO films which showed an R_s of 14 k Ω /□ by two-probe measurement (transparency not mentioned) [254]. The lowest R_s of 4 k Ω /□ was obtained for the rGO/FLG (8mL)-900°C Ar/H₂ device (with low transmittance=40%).

The conductivity of transparency (σ_{gt}) of these as-prepared devices is 11

(S/cm) and around 6 (S/cm) for the rGO and the rGO/FLG devices, respectively which is comparable to the as-prepared FLG-Abl (7) and FLG-HOPG (~ 5) devices. After thermal treatment however, a significant improvement up to around 160 (S/cm) and around 77 (S/cm) is observed for the rGO and the rGO/FLG devices, respectively. The highest σ_{gt} of 190 (S/cm) however, is achieved for the rGO/FLG (8mL)-900°C Ar/H₂ device. This is almost 500% of the σ_{gt} obtained for thermally-treated FLG-Abl (~ 41 S/cm) and more than 300% higher than obtained for FLG-HOPG (~ 61 S/cm) devices, respectively. However, it falls far from the desired values if we compare with standard ITO by at least two orders of magnitude, even after high temperature thermal treatments under inert environment. Thanks to the large lateral size of the rGO sheets (high 2D aspect ratio) it was possible to make a self-standing paper by filtration of the suspension. The R_s of the rGO suspended paper (films) was measured by the Four-point probes (FPPs) by injecting a current of 4.45×10^{-4} A for the as-prepared and thermally-annealed paper. The measurement was repeated on two or three different locations. The average R_s along with the optical image of the paper are displayed in the table 4.2. The suspended rGO paper films (opaque) display an average R_s of

Table 4.2: R_s of the rGO (films) suspended paper. Insert showing the optical image.

Sample	$R_{s(\text{avg})}$ ($\text{k}\Omega/\square$)
rGO Suspended Paper	127
rGO Suspended Paper 800°C-H ₂	0.027



$\sim 127 \text{ k}\Omega/\square$ for the as-prepared samples. The relatively high R_s of suspended rGO paper, comparable to the R_s obtained for other spray-coated films is the

result of room temperature filtration of GO (preparation of GO paper) and then liquid amount of ethanol/ethylene glycol remaining in the graphene. This lower R_s for rGO suspended film is still lower than other rGO charge transport devices due to the fact that there is no possible effect of substrate scattering as the case might be with films supported on glass/quartz (SiO_2) substrate [256]. The R_s of rGO paper cannot however, be compared directly with sprayed rGO films, since the thickness of rGO paper is incomparably higher than that of the rGO film.

The average R_s is further reduced to around $30 \Omega/\square$ (four orders of magnitude lower) after the thermal treatment at 800°C under H_2 for 2h, which nearly approaches the R_s for conductors/metals. Very low R_s after annealing treatment shows the high conductivity of the rGO due to a high packing density in suspended paper films and testifies the high reduction power brought by the μ -waves-assisted reduction/exfoliation [257] coupled with thermal annealing treatment to the material. The conductivity of paper is 333 S.cm^{-1} , calculated by obtaining the thickness of paper ($\sim 1000 \text{ nm}$) by profiler. This conductivity is higher than most of the values reported for reduced GO in different environments, which range from few to 100 S.cm^{-1} and lower than the higher values of 727 and $\sim 10^3 \text{ S.cm}^{-1}$ [94]. The R_s of charge transport devices does not attain this much higher values primarily due to lower density and thickness and other effects such as substrate scattering.

4.2.2 Morphology and Roughness

Figure 4.3A-B shows the SEM micro-graphs of the rGO/FLG film after exfoliation and deposition on SiO_2 substrate by hot-spray method.

The SEM analysis reveals that the rGO/FLG films exhibit higher homogeneity than FLG-Abl films but roughness remains still high. This was further confirmed by the AFM topographic profiles of the device surface (figure 4.4).

The profiles were obtained near the edge and the center of the sample in

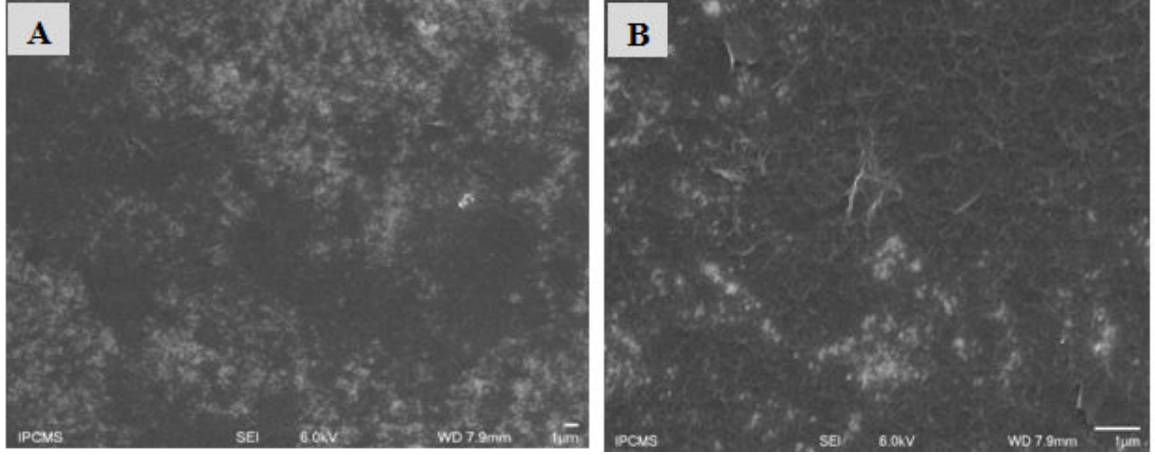


Figure 4.3: SEM micrographs of the rGO/FLG charge transport device.

order to check the homogeneity throughout all the surfaces. The R_a and RMS values are respectively, 35 and 64 nm. While near the edge, these values are slightly lower, down to R_a of 28 and RMS of 49 nm, respectively. The other difference is that the highest peaks (up to 1000 nm) for the profile near the center can be a little bit higher than that near the edge (around 800 nm). This is a potential problem with such spray-deposited films.

Next, a layer of PEDOT:PSS of around 100 nm was deposited over rGO/FLG to smoothen the surface. The optimization of deposition could improve the flatness of the film by decreasing of rGO/FLG concentration and the use of larger diameter nozzle of spray. Also the more effective separation of flakes with different thicknesses would be additional and important advantage.

Although a global roughness (RMS) of 50 to 60 nm is around twice lower than in the case of FLG-Abl, and can be covered by making a PEDOT:PSS layer thicker than usual, there is no immediate and practicable solution to few random peaks reaching up to 800-1000 nm height. The surface profile after the deposition of PEDOT:PSS film (figure 4.5) reveals that the roughness has readily decreased by lowering the R_a and RMS values to 10 and 18 nm, respectively. This shows the film is largely smoother than before and do not display reaching heights of

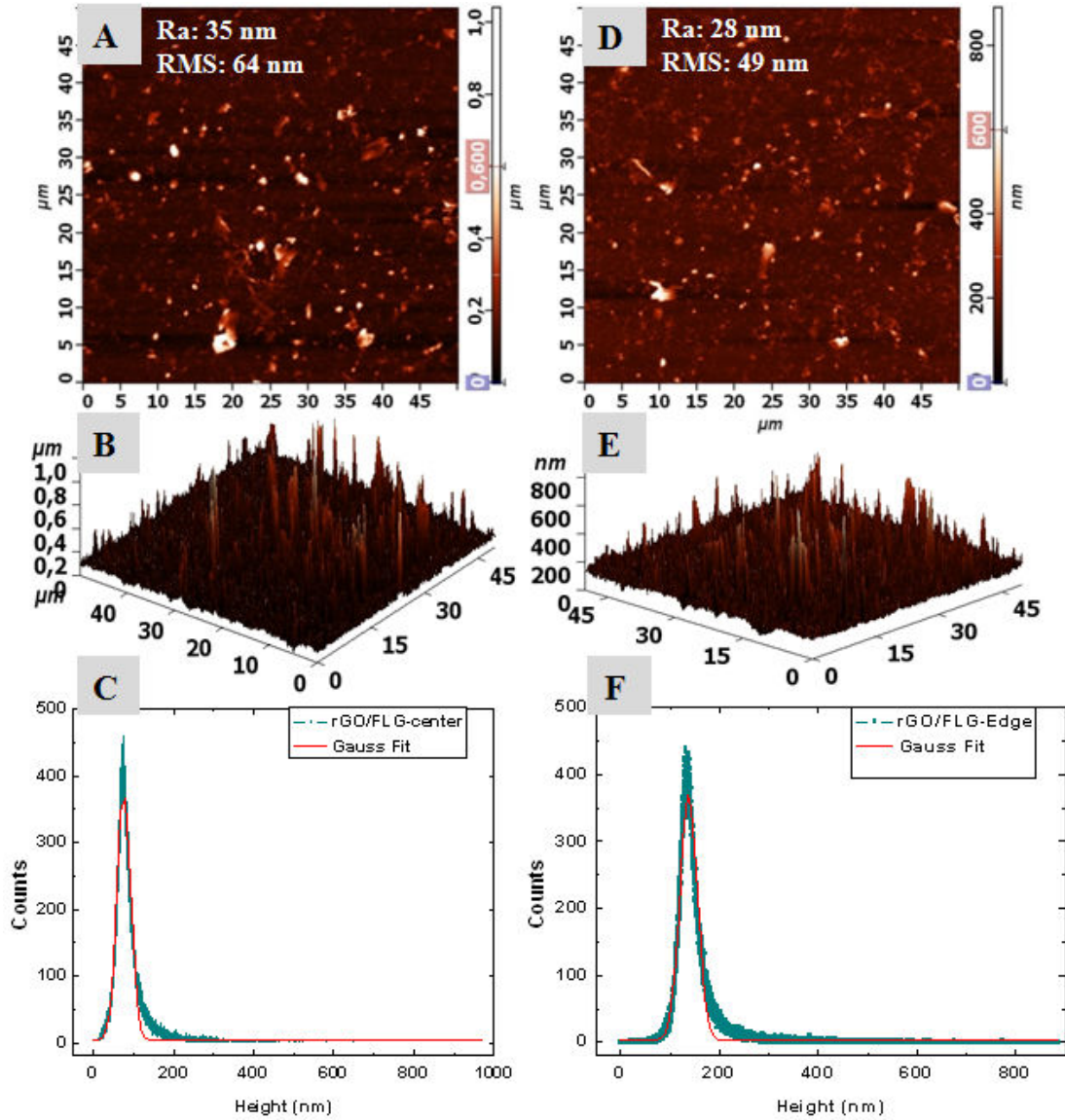


Figure 4.4: AFM roughness analyses of rGO/FLG microwave device.

several hundreds of nanometers very frequently. This is a considerable improvement but the few random peaks of high roughness are still present in the profile. The 3D profile confirms this by indicating that the number/frequency of small as well large peaks has decreased considerably. Further, the SEM micrographs (figure 4.6) display that there are some random delocalized aggregates formed on the surface which cause variations from few hundreds of nm to micrometers.

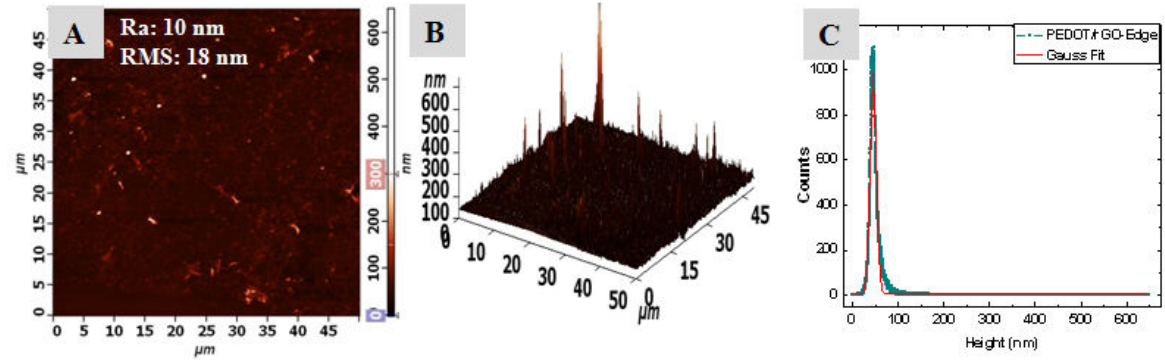


Figure 4.5: AFM roughness analyses of PEDOT:PSS/rGO/FLG microwave device.

These aggregates were already present on the rGO/FLG film and a coating by PEDOT:PSS has taken the shape of these aggregates by covering them. This is a major problem to remove these aggregates to get the smoother film surface.

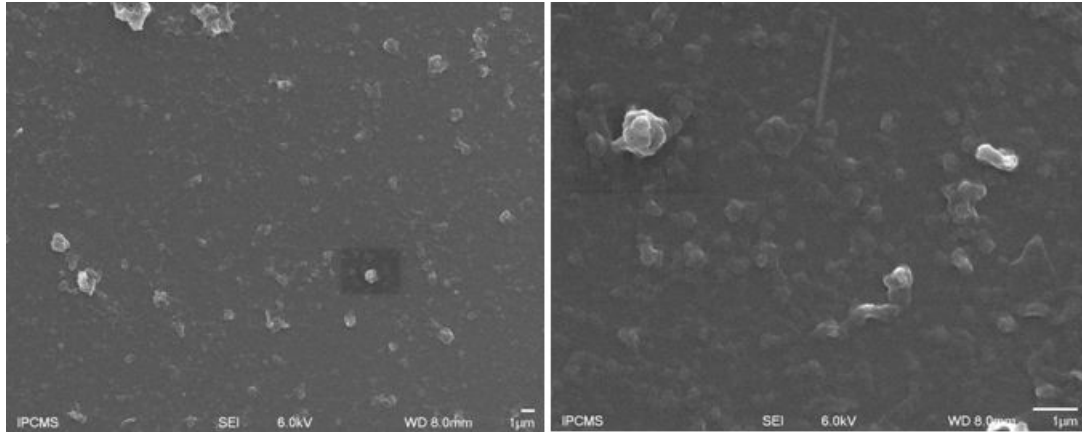


Figure 4.6: SEM of PEDOT:PSS/rGO/FLG microwave device.

4.2.3 Work-function Determination

The work-function of the rGO/FLG is determined by UPS by subtracting the energy difference between secondary electrons at cutoff and the Fermi edge from that of the HeI (figure 4.7 and equation 2.15).

The obtained work-function (WF) according to the equation 2.15 of the

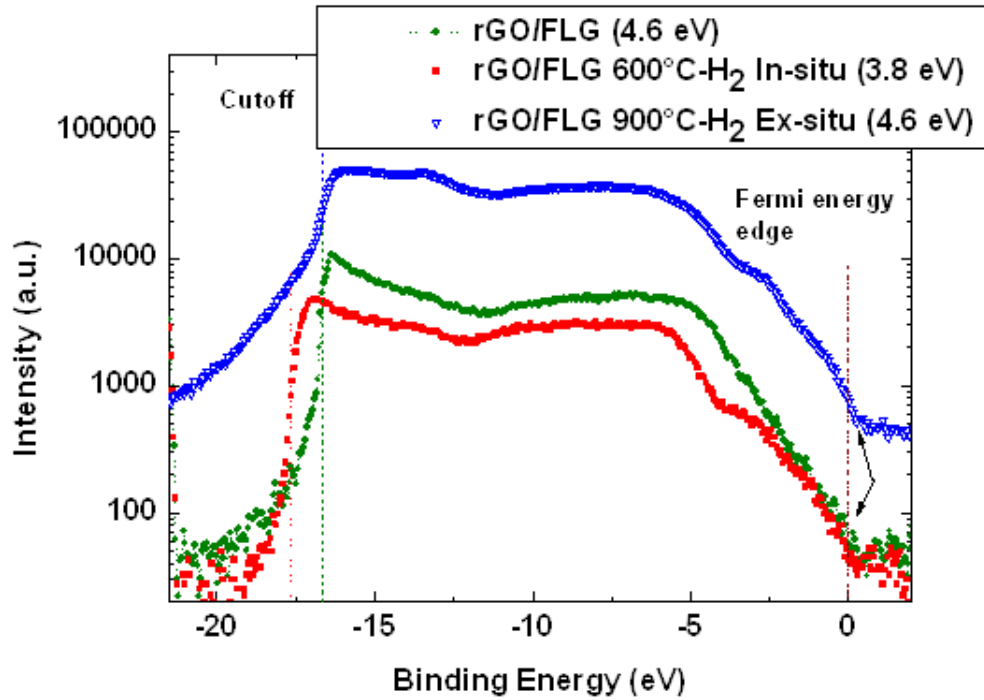


Figure 4.7: Graph showing the work-functions of rGO/FLG in different conditions.

rGO/FLG is 4.6 eV (figure 4.7) without any thermal treatment, close to that of ITO. After the ex-situ thermal treatment under H_2 at 900°C , when the UPS was performed again, the work-function remains stable to 4.6 eV. However, after an in-situ treatment (600°C under H_2) in the UPS chamber, there was a noticeable change in the work function which reduced to 3.8 eV. This is probably due to the desorption of oxygen groups and other un-intentional doping species (ions etc) from the surface of the material because the work-function of rGO is strongly dependent up on its thickness and the concentration of oxygen and other impurities [50], as it was discussed in the chapter 3. Since in this case the thermal treatment was performed in-situ and the sample was not removed from the vacuum chamber so there was no possibility for oxygen groups and other impurities present in the ambient environment to be re-adsorbed on the surface of the material contrary to the ex-situ annealed sample. A divergence in WF

for in-situ and ex-situ rGO/FLG could also rise from different temperatures annealing modes and related temperature-dependant desorption of the ad-species, it suggests also, that the acceptor type groups (such as -OH) were removed from GO during in-situ annealing. The divergence in WF of "ex-situ" and "in-situ" annealed samples shows that it is important to know proper properties and "real property" of graphene used for electronic devices, depending on the device preparation conditions. To further assess the reduction capacity of the μ -wave-assisted liquid exfoliation and reduction, the XPS spectra were performed. Thus, figure 4.8 shows different C1s-XPS spectra of GO, rGO after microwave irradiation and the same after thermal reduction at 900°C under H_2 .

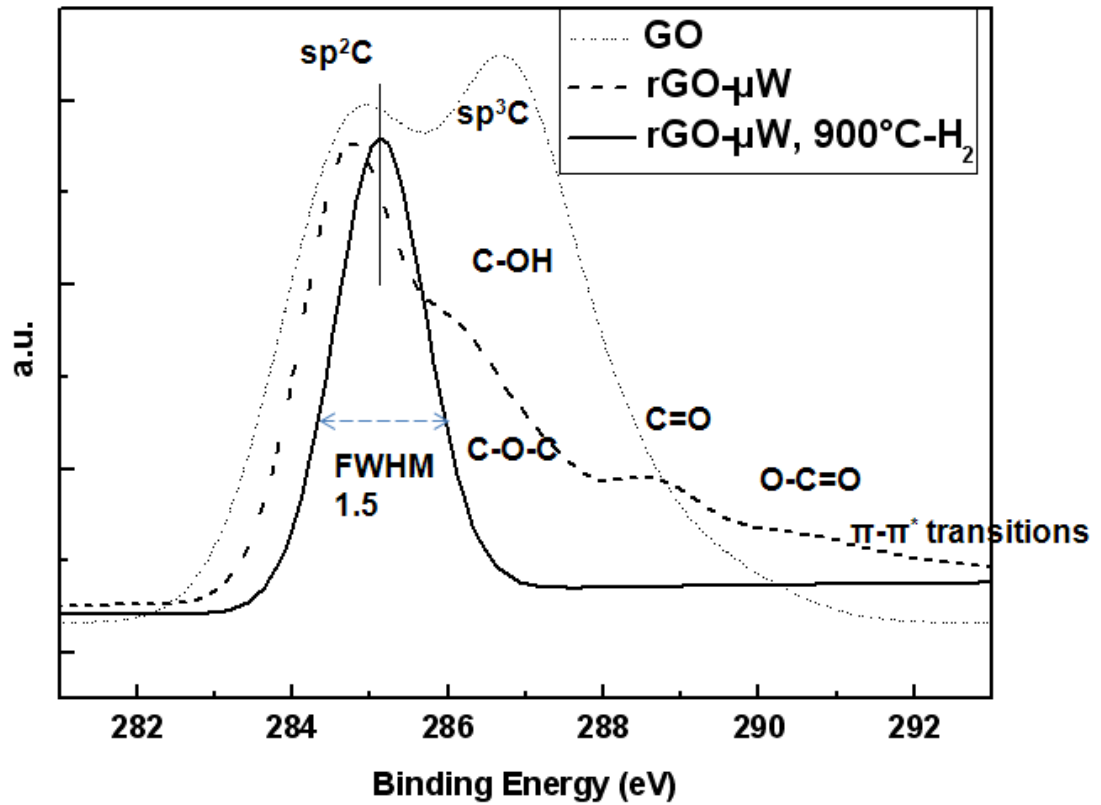


Figure 4.8: XPS C1s spectra of GO, rGO- μ w and rGO- μ w-900°C after thermal treatment under H_2 .

Note that XPS were performed for the rGO- μ w (and not the rGO/FLG)

in order to simplify the interpretation of XPS results. Graphene oxide includes bonding of carbon with various functional groups having oxygen like hydroxyl (-OH), keto (C=O), carboxyl (-COOH) or epoxy groups [225]. These species have a clear fingerprint in the C1s region for the sample before μ -waves experiment. After thermal treatment (900°C under H₂), the main peak for rGO- μ -waves-900°C-H₂ is recorded at 285.1 eV which is attributed to graphitic structure of sp² C. This peak is blue-shifted (from usual 284.6 eV for C=C) hence all other peaks relating to structural defects in the C lattice and C atoms attached to different function oxygen groups are shifted by ≈ 0.5 eV. The peaks at 287.2 eV, 288.5 eV and 289.6 eV, respectively are attributed to C-O (or C-OH), double bond C to O (C=O) and COOH [94, 258]. The last peak at 292 eV is attributed to π - π^* transitions [259]. However the oxygen peaks are considerably reduced after microwave irradiation and further after the thermal treatment. This demonstrates the impact of μ -waves on GO reduction by sp²-sp² carbon recombination. This explains why the work-function of rGO decreases after the in-situ thermal treatment. Note that the XPS peaks are shifted due to different conductivities of the samples related to different oxygen groups quantities. The percentage of O was calculated from the areas of C1s and O1s peaks. The initial percentage of oxygen content is 43 % which changes after each step of reduction to 26 % after μ -waves irradiation and further to 8% after the thermal treatment, respectively (table 4.3).

Table 4.3: *Percentage of Oxygen in GO, rGO- μ -waves and rGO- μ -waves-900°C-H₂.*

Sample	GO	GO- μ waves	GO- μ waves-900°C-H ₂
O%	43	24	8

Also, it is important to note that some % of oxygen and high R_s in rGO after the μ -waves step originates from the ethylene glycol adsorption, which has very high boiling temperature (c.a. 190°C) and was not completely removed

during the annealing process.

4.3 Percolation threshold in rGO and rGO/FLG

The minimum amount required to attain the percolation for the rGO and rGO/FLG is given for corresponding R_s (measured by FPPs) values obtained in table 4.4 for two different concentrations. The average R_s values suggest that a

Table 4.4: Percolation table for rGO and rGO/FLG materials.

rGO-μ-wave (0.25 mg/mL)		
Weight/Amount (mg)	1	1.5
$R_{s(\text{avg})} (\text{K}\Omega/\square)$		
As-prep.	251	200
After t.a. 900°C	14	3
rGO/FLG-μ-wave (0.33 mg/mL)		
Weight/Amount (mg)	1.6	2.6
$R_{s(\text{avg})} (\text{K}\Omega/\square)$		
As-prep.	255	173
After t.a. 900°C	19	4
FLG-Abl (0.25 mg/mL)		
Weight/Amount (mg)	1.5	2
$R_{s(\text{avg})} (\text{K}\Omega/\square)$		
As-prep.	644	236
After t.a. 900°C	281	89

weight of 1 mg and 1.6 mg, respectively for rGO and rGO/FLG is sufficient to cover the surface of $2 \text{ cm} \times 2 \text{ cm}$. These minimum percolation threshold value for rGO/FLG is comparable with that of FLG-Abl, while lower amount (1 mg) of rGO is sufficient to get conductive network, which is in agreement with high and homogeneous lateral size of rGO sheets.

4.4 Conclusion

Simultaneous reduction and exfoliation of graphene oxide and graphene oxide/expanded graphite, by microwave irradiation provides a viable alternative to FLG-Abl. The μ -waves-Ethylene-glycol-mediated-reduction is a high yield method with low-cost starting materials. The obtained rGO has moderate electrical properties but can be further improved by the thermal reduction treatment in an inert environment. For the charge transport devices, after thermal treatment, slightly improved results were obtained for the rGO and the rGO/FLG devices, respectively, as compared to the FLGs obtained by ablation (FLG-Abl) of pencil leads and synthetic graphite (FLG-HOPG). While the obtained sheet resistance fluctuated as compared to the values obtained by FLG-Abl, the transmittance was better (60-80%) than that of FLG-Abl (31%) and comparable with that obtained for FLG-HOPG. The fluctuations in the results give however a poor measurements predictability to obtain similar results from several rGO devices. Roughness is still one of the major challenge due the nature of material, being sheets and piled-up flakes, and due to the imperfections of the spray-deposition method. Additional stacking in the z direction and improper orientation of flakes make it difficult to grow perfectly uniform and homogeneous films on glass/quartz substrates. Taking into account very low improvement of R_s and transmittance of rGO and rGO/FLG compare to FLG-HOPG and advantages of FLG-HOPG synthesis, it seems that FLG-HOPG should be more appropriate for further investigation, provided that the roughness problem is addressed.

5 Results: Carbon Nanotubes/Few Layer Graphene Hybrids

This chapter starts with the description of preparations of CNTs/FLG hybrid devices/films in the section 5.1 followed by their characterizations in the section 5.2. The characterizations of CNTs/rGO devices are presented in the sections 5.3, followed by the work-function determination of the CNTs in the section 5.4 and the conclusion to this chapter in the section 5.5.

According to the results shown in the previous chapters, FLGs have lower conductivity of transparency than the requisite for TCE applications. One of the problems with the FLG samples is the inhomogeneous conducting path to provide continuous percolation among the flakes. Percolation threshold is high in the randomly deposited FLGs, especially for the flakes with low lateral size and inhomogeneous number of sheets within the individual flakes. So that higher amount of flakes are required to make a pathway for electron transport, which decreases the transparency and many of "extra" flakes which are deposited also in "z" direction are out of the conductive paths, strongly decreasing transparency. Further, a single sheet of graphene absorbs approximately 2.3% of the incident light, (which is earlier defined by the fine structure constant α of graphene ($\alpha\pi=2.3\%$ a fraction of white light) [183]) and each subsequent sheet contributing to the absorption, a rough maximal estimation shows that the transmission of 62% and 73% as shown in the chapter 4 corresponds to ≈ 17 and 12 graphene sheets for the the rGO/FLG and the rGO films, respectively. However, inhomogeneous distribution of the flakes and film thicknesses with voids indicate that average number of flakes and film thickness cannot be easily estimated.

A lower percolation threshold is difficult to achieve with random-sized flakes but the transmittance can be improved by reducing the number of sheets deposited. However, decreasing the number of sheets has an inverse effect on the

percolation and hence the conductivity. Thus, conductivity will decrease (hence R_s will increase) with lower thickness of graphene sheets/film.

Due to these reasons, the hybrids of FLG and rGO with Multi-wall Carbon Nano Tubes (MWCNTs) were envisaged to improve the conductivity of transparency considering the advantage of a high-aspect ratio of carbon nanotubes and their ability to form conductive mesh. This will be developed in this chapter. The advantage of using carbon nanotubes is that they provide a good percolation network with random deposition on substrates and the empty spaces between nanotubes can allow the light to pass without absorbing much of it as this was discussed for hybrids structures with carbon nanotubes and metal grids/mesh structures in the introduction (sections 1.5.0.1 and further details in the appendix 8.2). Since CNTs alone, especially SWNTs were largely investigated, the use of MWNTs and their hybrids with FLG is still scarce.

5.1 Preparations of CNTs/FLG Hybrid Films/Devices

In view of thin film preparation, to avoid potential roughness and redundant thickness, nanotubes with low external diameter of 9.5 nm were chosen (nanoscale). The average length of individual tubes is 1.5 μm which makes the aspect ratio relatively high, ~ 160 . Nanotubes were dispersed in five different solvents. Out of these, dispersions were good with only three of them, i.e. Acetonitrile (ACN), Chloroform (Chl) and Isopropanol (IPA). The other two being ethanol and dimethylformamide (DMF), could not provide good dispersion of CNTs. The CNTs/FLG-HOPG24h hybrid films were prepared by starting with CNTs deposition on the glass/quartz, followed by FLG-HOPG on top. CNTs alone devices were also prepared to understand the contribution of CNTs to charge transport and transmittance. The conditions of concentrations (wt%) of

CNTs and FLG-HOPG in solvents and deposited volumes in the preparation of devices are given in table 5.1.

Table 5.1: Summary of the prepared CNTs/FLG-HOPG24h devices

Sample/Device Name	Concentration of suspensions (mg/mL)		Vol. deposited
	CNTs	FLG-HOPG24h	CNTs/FLGHOPG24h (mg/mL)
CNTs Acetonitrile/HOPG24h	0.025 Acetonitrile	~ 0.1 Ethanol	3/3
CNTs Chloroform/HOPG24h	0.025 Chloroform	~ 0.1 Ethanol	3/3
CNTs Isopropanol/HOPG24h	0.025 Isopropanol	~ 0.1 Ethanol	3/3
CNTs Isopropanol	0.025 Isopropanol	-	6

5.2 Characterizations of CNTs/FLG-HOPG devices

5.2.1 Charge transport in CNTs/FLG-HOPG Hybrids

The representative results of charge transport devices showing $V(I)$ and transmittance spectra are shown in the figures 5.2 and 5.1, respectively, for CNTs/HOPG devices.

Since R_s and transmittance are recorded at three different locations on each sample, so average values are presented in the table 5.2 along with the conductivity of transparency, σ_{gt} . For the as-prepared CNTs/HOPG hybrid devices, the average R_s is between 5 and 12 $k\Omega/\square$, with the lowest average R_s values obtained for the CNTs ACN/HOPG ($\sim 5 k\Omega/\square$) and CNTs Chl1/HOPG24h ($\sim 6 k\Omega/\square$) devices, respectively. The difference between the three samples are due to different dispersion in solvents and/or due to the different solvents remaining adsorbants. These results suggest that there is a considerable improvement from previous CNTs-free devices (FLG-HOPG24h with $R_s=236 k\Omega/\square$ for $T=62-73\%$). These R_s values were not possible to obtain for FLG-HOPG (alone) devices without thermal treatment. Even after the thermal treatment at 900 °C in Ar,

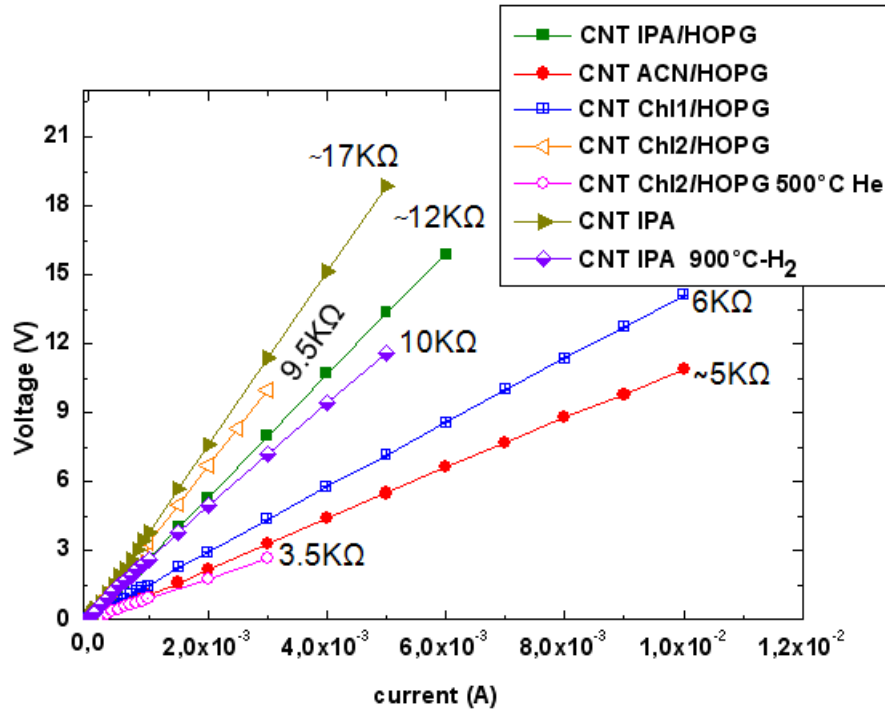


Figure 5.1: Representative $V(I)$ curves for the CNT/HOPG24h hybrid charge transport devices.

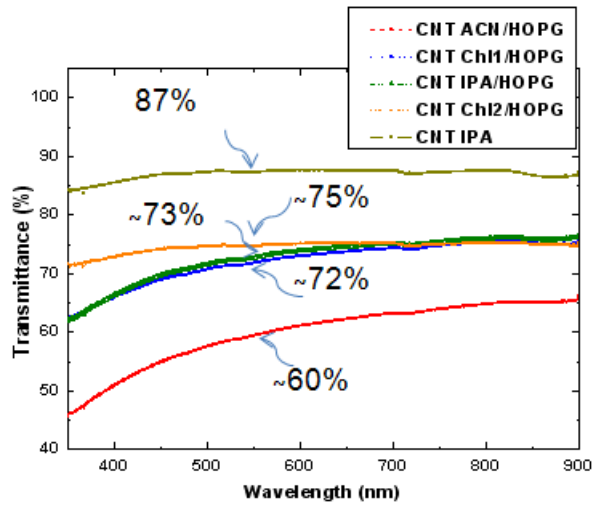


Figure 5.2: Representative transmittance spectra of the CNT/HOPG24h hybrid charge transport devices.

the R_s for FLG-HOPG24h devices was $\sim 23 \text{ k}\Omega/\square$, which is at least four times higher than $R_s=5 \text{ k}\Omega/\square$ obtained with the CNTs/FLG-HOPG24h hybrid devices without any thermal treatment. At the same time, the obtained transmittance is comparable, i.e. 62% for CNTs dispersed in acetonitrile. The transparency is higher for the CNTs dispersed in isopropanol and chloroform, which are approximately 73% and 72%, respectively, which is also comparable with the best obtained results (73%) for FLG-HOPG24h devices with superior conductivity. Thus for the same transparency, better R_s were obtained. The CNTs chloroform/HOPG sample was prepared again to see the effect of thermal treatment. The as-prepared device (CNT Chl2/HOPG) displays the average R_s $9.5 \text{ k}\Omega/\square$ (the same order to the previously obtained, $6 \text{ k}\Omega/\square$), with slightly higher transmittance of $\sim 76 \%$ (than the previously obtained 72%). However, after thermal treatment at 500° under He for 5h, the R_s lowered to $\approx 3.5 \text{ k}\Omega/\square$, which is almost three times lower than the as-prepared device. These results are better than the reported R_s $420 \text{ k}\Omega/\square$ (at $T=73\%$) for the graphene-CNT hybrid film [260].

CNTs alone (CNT IPA) device displayed an initial average R_s around $24 \text{ k}\Omega/\square$ for the as-prepared device. This is lower than any un-treated FLG (FLG-Abl= $85 \text{ k}\Omega/\square$) devices studied so far but is around four times (or one order of magnitude higher) than the R_s obtained for CNTs/FLG-HOPG ($5 \text{ k}\Omega/\square$) devices. The obtained average transmittance $\sim 87\%$ was never achieved before. This confirms the contribution of CNTs network to the percolation and transmittance in the hybrid films on one hand and also highlights the contribution of FLG in terms of R_s . Due to CNTs-FLG combination, R_s of $5 \text{ k}\Omega/\square$ with a transmittance of 72% can be achieved.

After thermal treatment, the R_s of CNTs alone after thermal treatment at 900°C decreases from 24 to around $10 \text{ k}\Omega/\square$, however it is higher than the R_s ($3.5 \text{ k}\Omega/\square$) obtained for the CNTs/FLG-HOPG24h device after thermal-treatment (500°C under He for 8h) despite higher annealing temperature. This behav-

ior is expected as carbon lattice tends to improve with thermal treatment by improving the crystalline structure and by removing the in-plane defects and adsorbed impurities. The effect of temperature confirms that the structure of CNTs is also improved, however in less important manner compared to FLG alone or CNTs-FLG hybrid. However, the crystal structure of both materials must have benefited from the heat treatment, as this is the case with most carbon materials, the FLG alone (FLG-HOPG) must have benefited more from the treatment due to the open topology of graphene, and higher number of the sensitive edges. The table 5.2 for conductivity of transparency, taking into account the average R_s and T % (at 550 nm) summarizes and compares these results with some of the best obtained previous results for FLG which are reproduced here for the sake of comparison.

Table 5.2: Conductivity of transparency σ_{gt} of CNT/HOPG devices in comparison with the best obtained results for FLG-Abl, FLG-HOPG, rGO and rGO/FLG devices, respectively.

Sample/Device	$R_{s(avg)}$ ($k\Omega/\square$)	T_{avg} (%)	Conductivity of Transparency (σ_{gt}) (S/cm)
CNT ACN/HOPG	5 ± 1	62 ± 8	302
CNT Chl1/HOPG	6 ± 2	72 ± 3	413
CNT IPA/HOPG	10 ± 6	71 ± 2	205
CNT Chl2/HOPG	9.5 ± 3	76 ± 4	261
CNT/HOPG 500°C He 8h	3.5 ± 2	76 ± 4	713
CNTs	24 ± 10	87 ± 8	203
CNTs 900°C H ₂	10 ± 3	87 ± 8	470
FLG-HOPG24h-900°C-Ar	23 ± 11	73 ± 6	61
rGO/FLG(8mL) 900° Ar/H ₂	4 ± 2	40 ± 2	190
rGO(4mL) 900°C Ar/H ₂	14 ± 5	73 ± 10	160

There is a considerable improvement in the σ_{gt} of CNTs/HOPG hybrid

devices following the improvement in the R_s and transparency. The σ_{gt} of CNTs/HOPG devices varies from 205 (S/cm) to 413 (S/cm) without thermal treatment, which is actually twice higher than the previously obtained for the FLG-Abl, FLG-HOPG24h and rGO (on 2 cm \times 2 cm substrate) devices, even after thermal treatment. The best σ_{gt} obtained for the rGO and rGO/FLG devices was 160 S/cm and 190 S/cm, respectively, with transmittance of 70 % and 40 %, for thermally-annealed/reduced (at 900 ° under Ar/H₂ environments) on 2 cm \times 2 cm substrates, while 801 S/cm was recorded for the FLG-Abl device after thermal treatment (900 °C under Ar) on 1 cm \times 1 cm device (by HE measurement). These results are still two orders of magnitude lower than that required for applications in the TCEs. In the case of CNTs hybrid, agglomeration in the dispersion or during spray could result in bundles of the CNTs on the planar surface which could serve as local insulation islands or even charge trap sites. Substrate scattering is also a common factor that can affect the charge transport in carbon materials. R_s results obtained in our studies indicate that the charge transport could have been affected by few factors, such as, agglomerates of CNTs, mis-aligned or disordered nanotubes and possibly random distribution of semi-conducting and metallic tubes in the films as well as the scattering effects due to SiO₂ substrates and impurities. However, the results obtained here are encouraging with random deposition of multi-walled nanotubes and are better than the already reported ones, which are as high as 250 (T=80%) and 440 (T=95%) k Ω /□ [124]. This should also be underlined that most of the studied CNTs in the literature are SWNTs, which have incomparable and controllable electronic properties but are also incomparably more expensive than MWNTs.

5.2.2 Morphology and Roughness Profiles of CNTs/FLG-HOPG Hybrids

Morphology was studied by SEM and representative micrographs are shown in figure 5.3 for CNTs isopropanol/HOPG devices.

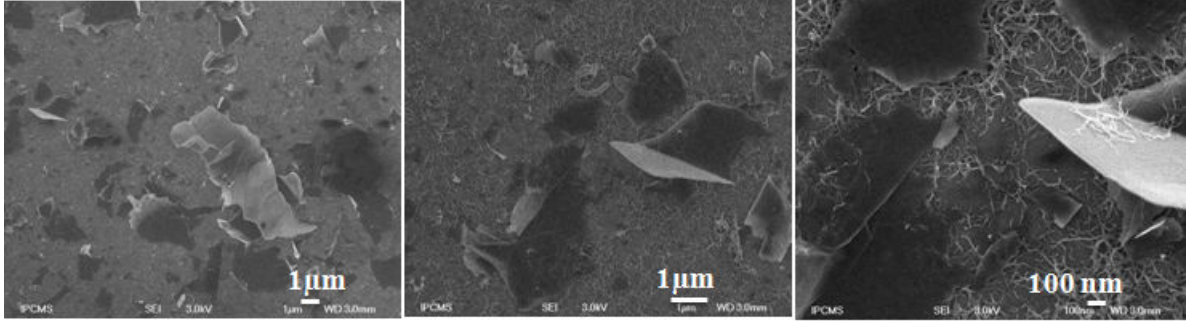


Figure 5.3: Morphology of CNT/HOPG24h hybrid charge transport devices.

From the SEM micrographs, it is clear that the surface is fully covered and conducting pathways are established between FLG flakes and CNTs. Some FLG flakes even penetrate through the open spaces among the CNT network, making superior contact/connection in the hybrid film. The contact between the π electrons in FLG and CNTs provides the conduction schema for the device. However, it is worthy to note that not all the FLG flakes are flat-lying over the underlying CNTs film and some of them are curved. The curvatures make flakes stand tangent to the underlying film and to each other, thereby making it difficult to obtain a flat and homogeneous film (while such stand up in z direction could have a positive effect for the conduction to upper layer in OSCs provided that FLG layer is fully covered to avoid shorts). This could affect the conductivity of the film in particular directions. The Figure 5.4 shows morphology of the CNT device. From the SEM micrographs, the well-connected network can be seen which is an important aspect of these type of materials in order to provide conducting pathways for current flow.

The AFM topographic profile for the CNTs/FLG-HOPG hybrid device is shown in the figure 5.5. There are several flakes of FLG-HOPG which display micro-metric height. The average roughness values are $R_a=84$ nm and $RMS=136$ nm, respectively. These values are, however much lower than FLG-HOPG alone despite double materials, which suggests that roughness has improved along with R_s and T .

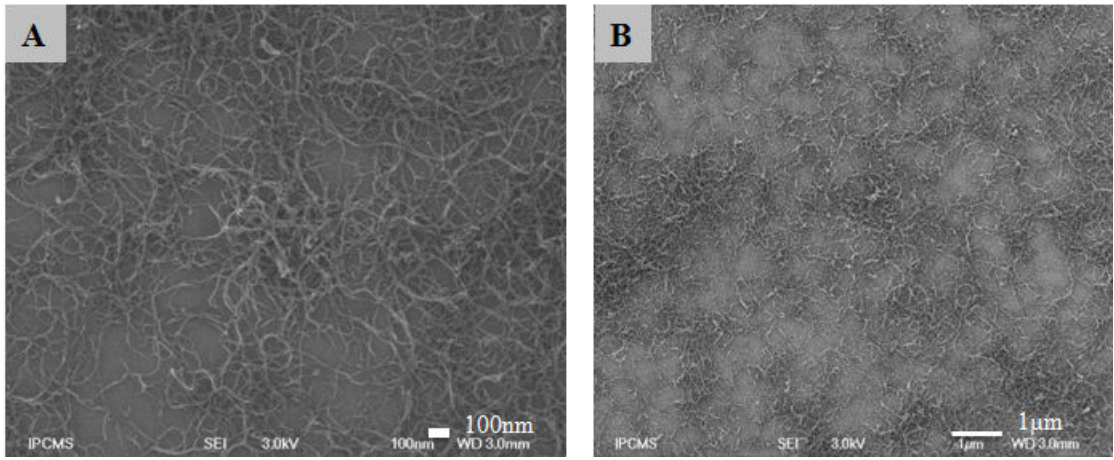


Figure 5.4: Morphology of the CNT alone device.

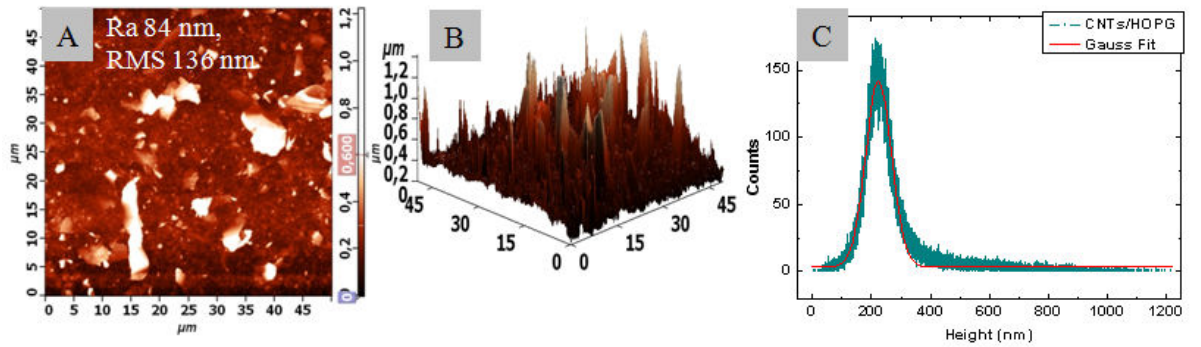


Figure 5.5: A) AFM topography profile of the CNTs/HOPG device B) 3D image and C) histograms fitted with Gaussian curve.

5.3 Charge transport in CNTs/rGO

The CNT hybrid was also studied in coupling with the rGO material. 900 °C, under Ar/H₂ for 2h. The concentrations were kept unchanged as 0.25 mg/mL and 0.025 mg/mL, respectively, for rGO and CNTs. Isopropanol was preferred for further dispersions of CNTs over the other two solvents (chloroform and acetonitrile) due to lower toxicity and second, there was no direct proof that the choice of solvent had a decisive effect on the obtained R_s results. The charge transport are shown by the illustrative V-I curves for the CNTs/rGO films for the as-prepared and thermally annealed in the figure 5.6A and transparency (the individual transmittance values can be up to 5% higher or lower than the result shown) in the figure 5.6B, respectively.

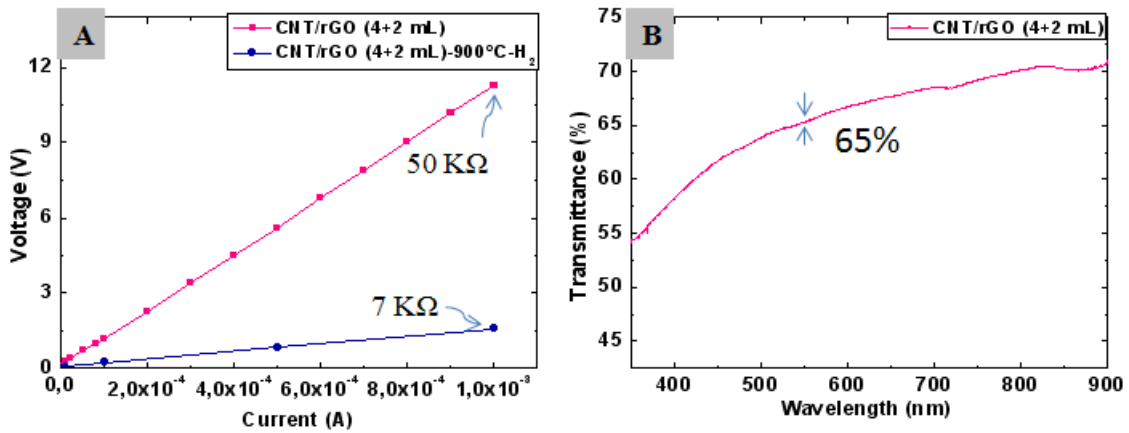


Figure 5.6: A) Representative I-V curves for the as-prepared and thermally-annealed CNTs/rGO devices, and B) transmittance for the CNTs/rGO B).

As shown by these graphs, and from the average R_s values gathered in the table 5.3, the sheet resistance for the as-prepared CNTs/rGO ($R_s \sim 55 \pm 5$ kΩ/□) device is lower the one obtained before for the rGO alone, with slightly lower transmittance (67% vs. $\sim 73\%$, see table 5.3). Similar difference is observed after thermal treatment as well.

After the thermal treatment, there is a significant decrease in the average

sheet resistance ($\sim 5 \pm 2 \text{ k}\Omega/\square$). This points out the significant improvement of structure of the composite materials and the desorption of impurities from the film due to the thermal reduction by H_2 . The R_s after thermal treatment is also lower compared to the rGO after thermal treatment ($\sim 14 \pm 5 \text{ k}\Omega/\square$)

Table 5.3: Conductivity of transparency, σ_{gt} for the as-prepared and thermally-treated CNTs/rGO hybrid devices in comparison to the rGO, and CNT/HOPG devices.

Sample/Device	$R_{s(avg)}$ ($\text{k}\Omega/\square$)	T_{avg} (%)	Conductivity of Transparency (σ_{gt}) (S/cm)
CNTs/rGO (4+2 mL)	55 ± 5	67 ± 3	31
CNTs/rGO (4+2 mL) 900 °C H_2	5 ± 2	67 ± 3	350
rGO (4mL)	250 ± 20	73 ± 10	9
rGO(4mL) 900°C Ar/ H_2	14 ± 5	73 ± 10	160
CNT Chl1/HOPG	6 ± 2	72 ± 3	413
CNT Chl2/HOPG 500° He	3.5 ± 2	76 ± 4	713

It can be argued that, the CNTs have significant role in improving the sheet resistance and transparency of the hybrid films when they are un-treated. Once they are treated under a high temperature, CNTs have a less pronounced role in the improvement of sheet resistance in the hybrid films of composite materials as it was explained in the case of CNTs/FLG-HOPG hybrid.

Conductivity of transparency, σ_{gt} quoted to 31 S/cm for the CNTs/rGO (table 5.3) is also improved compared to the rGO alone and this improvement remains considerable for the annealed sample, i.e. 350 S/cm for the CNTs/rGO vs. 160 S/cm for the rGO.

However, this also indicates that even after thermal treatment, we can not achieve a R_s around few $\text{k}\Omega/\square$ or lower without compromising the transmittance significantly by depositing more volume of these materials. This is evident for the rGO/FLG (8 mL) 900 °C Ar/ H_2 device which displays a high σ_{gt} of 190 S/cm with an average R_s of 4 $\text{k}\Omega/\square$ but with a low transmittance of 40%. This σ_{gt}

is midway to that obtained for the CNTs/rGO and the CNTs/rGO/FLG after thermal treatment (900 °C H₂) devices, but with transmittance on the lower side.

Further, with CNTs/FLG-HOPG hybrid devices, which displayed σ_{gt} between 205 S/cm and 417 S/cm for the untreated devices, there is no close comparison between the σ_{gt} of the as-prepared CNTs/rGO devices because they were very low. Only the σ_{gt} of the thermally-treated CNTs/rGO (350 S/cm) comes closer to that of the as-prepared CNTs/HOPG devices. The reason for this can be attributed to the better contribution of conductivity of FLG-HOPG as compared to that of rGO in the hybrid films. This clearly underlines, that even if rGO alone yields better results than FLG-HOPG, it is less performing in the hybrid form with CNTs. Although, one should be mindful to see the concentration and deposition amount for both graphenes in the hybrid. But overall it means that the conductivity of FLG-HOPG is higher than GO, but due to the higher thickness of the flake and their lower size, the transparency and figure of merit σ_{gt} (R_s /transparency) ratio are much lower for the FLG-HOPG flakes alone. The residual oxygen groups, such as carbonyl and hydroxyl groups linked to the sp² C atoms which are still remaining after the reduction act as defects and non-conductive islands which hamper the conductivity in the rGO.

These hybrid CNTs/rGO devices were thermally-treated in the same way as the rGO and rGO/FLG devices. However, rather than keeping the same gas during the whole process of thermal treatment, a combination of two gases was used by switching between Ar and H₂. During the ramp to 900 °C, Ar was used as inert gas, and during the plateau, it was switched on with H₂ for two hours for its ability to thermally-reduce the rGO. Then it was switched back to Ar during the cooling step. The decrease of sheet resistance after this treatment suggests that thermal treatment under Ar and H₂ gases has not only improved the structure of the hybrid materials but also further reduced the partially-reduced (by microwave irradiation) GO. Although it is difficult to compare results due to difficulty of matching experimental preparations and measurement conditions,

our results suggest that the R_s values obtained are better than R_s of 151 ($T > 90\%$) and 114 $k\Omega/\square$ ($T \approx 90\%$) which were reported for the hydrazine treated and thermally-annealed and rGO/MWNTs hybrid [261], [262].

5.3.1 Morphology and Roughness of CNTs/rGO Hybrids

Morphology is shown by SEM micrographs in the figure 5.7.

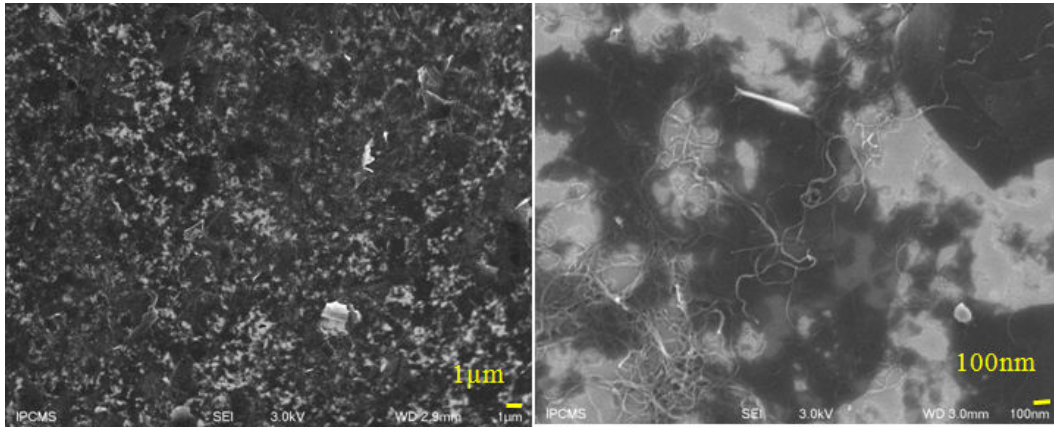


Figure 5.7: SEM images showing the morphology of CNT/rGO device.

We can clearly see anisotropic long 1D nanotubes structures as well as FLG flakes. They are randomly distributed and disoriented along the sample surface. Micrographs indicate that the surface is mostly covered by the CNTs/rGO but there are micrometric flakes at a few places which can add up to the roughness of the devices' surface due to random deposition of flakes by spray method. The orientation and packing of the FLG/rGO flakes and their inter-connection also has important role to play in the conductivity of the films and randomness of these parameters can be one of the mechanisms which hinders the establishment of several parallel paths in the film containing the rGO flakes. AFM topography profiles of the CNTs/rGO device is shown in the figure 5.8. The topography images gives the average roughness R_a and R_q (RMS) equal to 29 nm and 50 nm, respectively, for the CNTs/rGO device near the center of the film. Whereas,

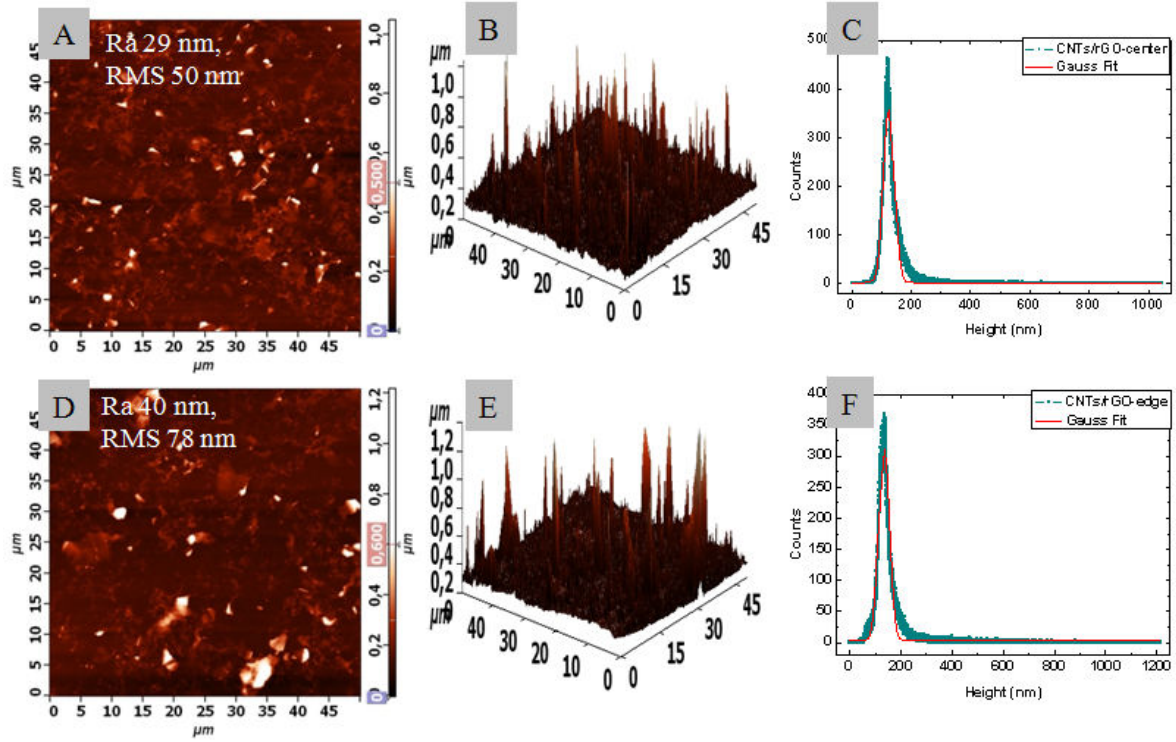


Figure 5.8: A) AFM topography profile of the CNTs/rGO device near the center, B) 3D image, C) histogram profile fitted with Gaussian curve, D) AFM topography profile of the CNTs/rGO device near the edge, E) 3D image, F) histogram profile fitted with Gaussian curve.

near the edge profile gives slightly higher R_a and RMS averages up to 40 nm and 78 nm, respectively indicating the surface at the edge is slightly more rough, which is contrary to general observations until now with other samples. This is a quite interesting difference, as such a behavior can be linked partially to the first drying (hot plate), which provides rapid attraction between the CNTs due to van der Waals which can increase local density, also at the edges. The histogram fitted with Gaussian curve reveals that most peaks are well below 150 nm (around 110-120 nm) with punctual random peaks reaching the heights up to 1000 nm and 1200 nm (also visible from the 3D profiles), for the near center and near edge profiles, respectively.

5.4 Work-function of CNTs

The work-function of the CNTs is shown in the figure 5.9. It can be noted

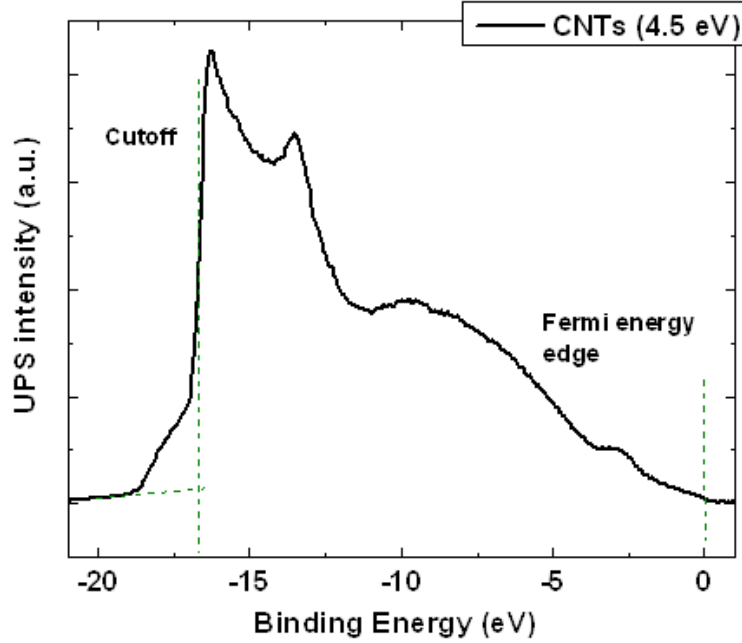


Figure 5.9: Work-function of CNTs.

that shoulder in the secondary cut-off region shows a double cut-off in this UPS measurement. The exact origin of this shoulder is not well-understood but we assume that if the secondary electron cut-off which is used to determine the work function is double, it reflects two different local surface potentials, which is an indicator for surface inhomogeneity. In this case the larger and more pronounced secondary electron cut-off is taken as the true value to calculate the work-function.

A work-function of 4.5 eV for the CNTs is then derived which is little lower than the generally reported values for multi-walled nanotubes in the literature which are between 4.6-4.9 eV [263], [264]. This could be possible because the work-function is slightly lower at the tips of nanotubes [18].

5.5 Conclusion

The CNTs network in the hybrid films serves two purposes: it helps to lower the percolation threshold in the films which allows to increase the transparency for the given R_s order. Due to its networked structure, better results, in terms of R_s and transmittance, were obtained by making the hybrid films of CNTs with FLG-HOPG and rGO. The effect of the thermal treatment improves the structure and helps to remove the adsorbed species (mostly oxygen-containing hydroxyl and carbonyl groups) from the surface of FLG and rGO. The rGO has possibly a larger content of such impurities which results in lower R_s as compared to that obtained by the FLG-HOPG24h. CNTs network has better connection and transparency than the FLG materials used in this work. This is demonstrated by R_s and transmittance results, however addition of FLG is beneficial for the R_s and the best results are obtained for hybrid, especially for the CNTs/FLG-HOPG. The rGO films obtained by this method can be used for various application in electronics, dye sensitized solar cells, Li-ion batteries, supercapacitors, and sensors as well as conductive coatings [260].

However, the imperfections of the hot-spray method make it difficult to get highly flat and homogeneous films of these carbon materials. The dispersions of these materials are although good during the preparations but while the material is being deposited through the spray needle of 0.2-3 mm diameter, there is a possibility of formation of useless agglomerates which not only make the films rough but also affect the conductivity and transparency, with the former being the worst affected.

6 Results: Organic Solar Cells based on Carbon TCES

Despite important drawbacks, which include high roughness of the films and relatively low conductivity/transparency to ITO, the tentative test as transparent electrode in organic solar cells (OSCs) to compare with ITO anode was performed with the prepared films of different carbon materials [here referred to as carbon-based transparent conductor electrodes (CTCEs)].

The organic solar cells are fabricated as per the procedure explained in the section 2.4). The figure 6.1 illustrates the structure and energy band diagram of the fabricated OSCs with ITO and CTCEs anode electrodes.

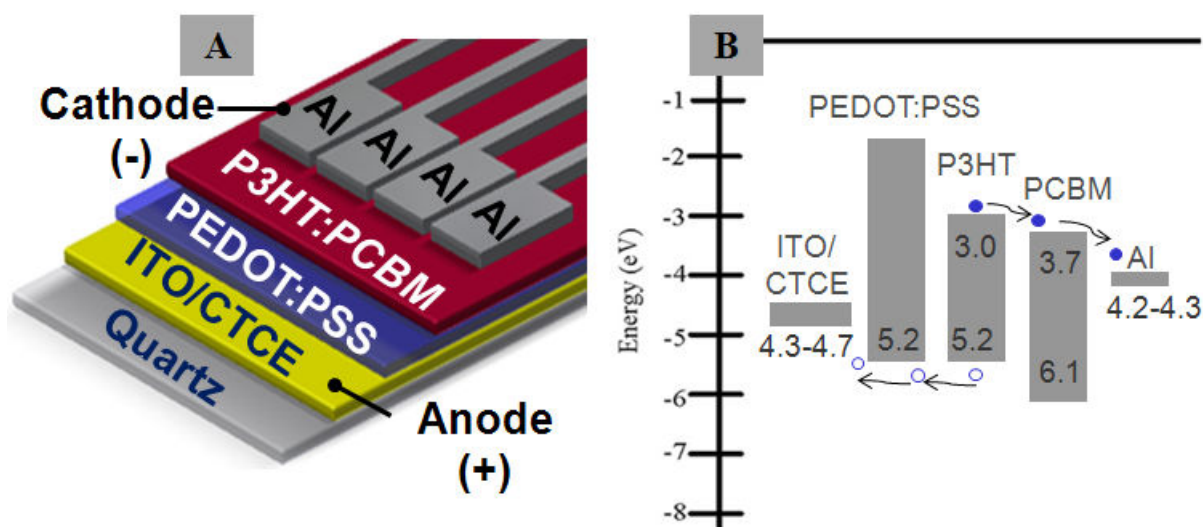


Figure 6.1: A) The structure and B) the energy band diagram showing the HOMO and LUMO levels of active layer materials along with illustrative work-functions of electrodes of the fabricated OSCs devices with ITO or CTCEs anode electrodes

Preliminary representative results are shown in figure 6.2.

The results indicate, that the device with the ITO electrode shows a normal diode-like behavior with a power conversion efficiency of 2.04%. However, the

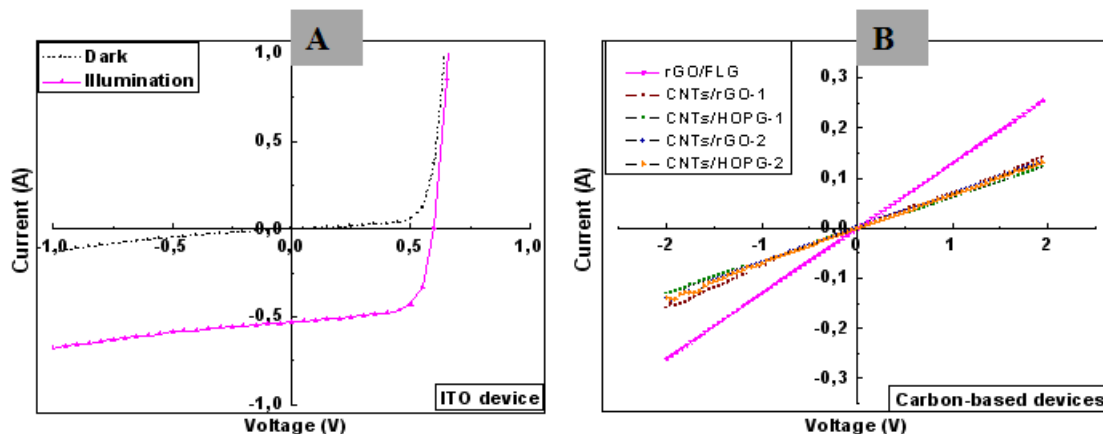


Figure 6.2: V-I curves of ITO-based A), and Carbon-based Organic Solar Cells under illumination B).

devices fabricated with carbon-based electrodes do not exhibit such a diode-like behavior, as they all resemble a resistor-like devices. We believe, this is at first because of the high roughness issues of carbon-based electrodes. The complete structure of an OSC is only around 200 nm thick, whereas, the carbon-based electrodes can have randomly-distributed peaks of several hundreds up to one thousand of nanometers. These peaks can penetrate through the PEDOT:PSS (50-70 nm thick) and the active layer consisting P3HT:PC₆₀BM blend (90-120 nm) and contact the top Al electrode. This makes a short circuit which is sufficient to destroy the solar cell. The active surface area for the solar cells is 0.12 cm² (1200 μm^2) which is quite large in a square sample with each side of 2 cm. This area can have at least several peaks going above 200 nm.

This can be explained by looking upon performing contact resistance measurements (also called series resistance and denoted as R_s and expressed in Ω) of an OSC (see figure 1.17).

The R_s is usually estimated from the current-voltage J-V curve slope at large forward voltage where the current flow is no longer limited by the internal carrier recombination but by the potential drop at R_s .

For our devices, the R_s for the ITO reference cell is calculated to be around $100\ \Omega$ whereas for the cells fabricated using carbon-based electrodes prepared by the hot-spray method, this R_s is presumably very high, from several to tens of $k\Omega$. The series resistance of these OSC devices was compared with the sheet resistance of the transparent conducting electrodes prepared in the similar conditions for comparison purpose, as shown in the table 6.1.

Table 6.1: Comparison of the sheet and series resistances of ITO and carbon-based transparent electrodes (CTCEs) in OSC devices.

OSC device/ Anode electrode type	$R_{s(series)}\ (k\Omega)$	$R_{s(sheet)}\ (k\Omega/\square)$	$T_{avg}\ (\%)$
ITO	0.1	0.03	84
rGO/FLG	7	9	64
CNTs/rGO-1	18	19	78
CNTs/HOPG-1	16	46	77
CNTs/rGO-2	17	10	66
CNTs/HOPG-2	12	15	78

The series resistance of ITO-based devices is only $100\ \Omega$ whereas, for the devices with CTCEs, this can be 7-18 $k\Omega$. This primarily indicates that the contact resistance between carbon-based electrodes and PEDOT:PSS (and the active layer as well) is so large that no photo-current could be observed through active layer at the counter metal electrode. The other reason is that the peaks from the high roughness of these carbon-based transparent conducting electrodes probably penetrate through the whole device and created many shorts (short-circuits) between the electrode and the rest of device reaching up to the counter electrode. Thus, the device behaves as a resistor and not as a normal p-n junction diode.

It can be argued that what we measure in terms of series resistance (R_s) in the carbon-based devices is actually the sheet resistance of these electrodes themselves. In general case, the sheet resistance is a two-dimensional resistance of a thin film on a planar surface, and expressed as a resistance per square. Whereas the series resistance here is the resistance which includes the contact resistance (hence the sheet resistance) of the carbon-based transparent electrode on the planar surface plus the contact resistance between all the subsequent layers in the device in vertical direction (PEDOT:PSS/P3HT:P₆₀BM/Al). The figure 6.3A shows the physical description of the device (the arrows pointing out the nature of resistance of device) and the figure 6.3B the equivalent circuit showing the contribution of different resistances in the device.

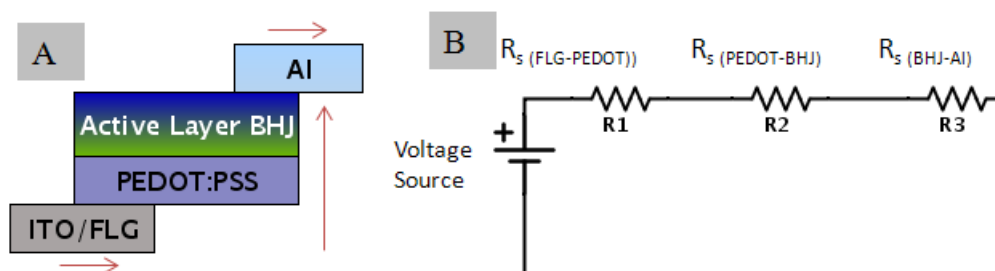


Figure 6.3: Representation of the sheet resistance and series resistance in our OSC device.

The highest peaks observed by AFM in the CTCEs are not covered completely by the PEDOT:PSS and subsequent active layer, and directly connect to the Al electrode. Hence, for the OSC devices with CTCEs $R_{series} \approx R_{sheet}$ (table 6.1) due to the high roughness. The results show that the sheet resistance values are comparable to those obtained for the series resistance for the carbon-based OSC devices. The transmittance of CTCEs is between 60-80% but we assume it has no role in the OSC devices due to high sheet resistance and roughness of these electrodes.

6.1 Conclusion

Various FLG, rGO materials and their hybrids with the CNTs have been tested as transparent conductive electrodes prepared by the hot-spray method in the fabrication of the Organic Solar Cells. The high roughness and sheet resistance of electrodes are the potential problems along with low work functions of these materials which did not allow the OSC device to be realized with normal diode characteristics. However, some of these carbon materials could be used as counter electrodes due to their favorable work-function and for conductive coatings.

7 Concluding Discussion and Perspectives

The general conclusions are pointed out in this chapter; starting with the concluding discussion in the section 7.1 and some perspectives work that should be carried out to improve this work are discussed in the 7.2.

7.1 Concluding Discussion

Transparent Conductor Electrodes (TCEs) are important components in the fabrication of solar cells of all types. The Indium Tin Oxide (ITO) and other variations of oxides provide TCEs, but the high cost of indium, their low availability pose a threat to continue the research and commercialization of solar cells, and any other devices requiring transparent electrodes. Alternate materials including polymers, silver nanowires, and carbon-based materials including graphene, few layer graphene, reduced graphene oxide and CNTs are under intensive investigation to required synthesis properties-efficiency relationship. The additional robustness of most of these materials makes them also potentially interesting for counter electrodes applications.

We studied the carbon nanomaterials starting from their synthesis, by film formation and its properties to integration in OPV. Not only synthesis methods were developed and optimized but thin film deposition and their properties were improved as well. In summary, we have studied different FLG materials obtained by mechanical exfoliation/ablation of pencil lead or HOPG, and by μ -waves-assisted liquid phase exfoliation of EG and GO; and their hybrids with CNTs. Top-down exfoliation method such as ablation of pencil lead is scalable, high yield, facile and cheap method but up to now it involves several purification and filtration steps. This method was further optimized using synthetic graphite (Highly Ordered Pyrolytic Graphite, HOPG) to get relatively more homogeneous few layer graphene (FLG) sheets and avoid harsh purification conditions as well

as decrease economic/environmental issues. A rather new method was developed in which simultaneous exfoliation and reduction was achieved by microwave-irradiation-assisted liquid phase exfoliation (LPE) to get relatively higher quality, thin and homogeneous lateral size FLG and reduced graphene oxide (rGO) materials from cheap starting materials expanded graphite and graphene oxide. This is of high interest to get high quality graphene sheets with large aspect ratio for subsequent applications.

Materials were characterized by Scanning Electron Microscopy (SEM), Transmission Electron Microscopy (TEM), Raman and Photoluminescence (PL) spectroscopies, TGA analysis to study the structural quality including defects and thickness and lateral size of FLG materials and their films. Photoelectron Spectroscopies (PES) techniques such as X-Ray Photoelectron Spectroscopy (XPS) and Ultra-violet Photoelectron Spectroscopy (UPS) were employed to study the chemical composition, binding energies, and work functions of these materials. The obtained work functions of these materials are between 4.0 eV and 4.5 eV, which are slightly lower than that of ITO (4.7 eV). Some of these materials can be used as conductive counter electrodes in the organic solar cells. These are solution-processable materials and can replace metal based counter electrodes (e.g. Al, Ag and Ca, ...) which are often deposited by costly evaporation methods. A temperature-programmed desorption couples with mass spectroscopy (TPD-MS) under vacuum at a maximum pressure of 10^{-4} Pa, were performed to understand the changes that occur during a thermal treatment to the FLG material. The TPD-MS results showed that some hydrocarbon species can be adsorbed strongly on the surface of FLGs and modify the electron states (depending upon the performed bonds) and can affect the quality of the material by behaving as defect islands. The stability of toluene up to high temperature such as 450°C which remains from the synthesis is surprisingly noteworthy in our results. This can affect the charge transport of the FLG material. This was a new evidence brought before, to the generally focused as the only oxygen content dependent

charge transport at higher temperature.

The thin films of the FLG and rGO materials including their hybrid films with carbon nanotubes (CNTs) were prepared by a low-cost, easily scalable hot-spray method which can be used to cover potentially unlimited surface as opposed to the limited surface growth of graphene by bottom-up chemical vapor deposition (CVD) method. This method is relatively more compatible for film growth due to nature of FLG material being flakes in comparison to the spray coating or drop-casting methods. The films are made up of overlapping FLG flakes and exhibit a random deposition of flakes. They apparently provide a connection among the flakes and pathways for the charge transport. In fact, a minimum percolation threshold is to be achieved in order to conduction to take place. The obtained results of charge transport of these films included in this thesis are more often at this percolation threshold. However, this cannot be obtained without adding significant number of boundaries/edges among the FLG flakes which might increase the number of hops that the electrons have to make while traveling through the FLG films. The high aspect ratio of FLGs obtained by ablation of synthetic graphite or exfoliation of expanded graphite by microwave-assisted liquid exfoliation methods, respectively, helps to lower the percolation threshold. However, larger lateral size of FLG sheets and low yield obtained by microwave-assisted liquid exfoliation require further optimization of synthesis method and a spray-gun with a large nozzle, respectively.

We studied the (opto) electronic properties of spray-coated transparent conductor films/electrodes obtained by different methods and their hybrids with CNTs as well. The electrical transport was studied by the two-point probes (2PP) and four-point probes (FPP), respectively, for measuring the resistance of singular FLG flakes and sheet resistance (R_s) of FLG films. A new configuration of mask for the Hall Effect devices was designed using a Lab View program and cutting laser to measure resistivity (ρ), carrier mobility (μ), type (electron or hole) and concentration (n) in FLG film by Hall Effect measurements sys-

tem. Further, we have shown that the overlapped FLG flakes prepared by the hot-spray technique display a significant improvement of charge transport after thermal treatment as measured by the FPP. Transmittance was studied by Ultra-Violet Visible Spectrophotometry (UV-Vis).

The R_s decreased from around $85 \text{ k}\Omega/\square$ to around $15 \text{ k}\Omega/\square$ after a 900°C Ar treatment for the FLG films prepared from FLGs obtained by mechanical ablation/exfoliation of pencil leads. This behavior is common for all the materials studied, including FLG-HOPG, rGO and their hybrids with carbon nanotubes.

This is due to desorption of adsorbed hydrocarbon impurities (toluene and its decomposition intermediates), accompanied by a low decrease of oxygen content, once annealed at 900°C . As explained above, a desorption of toluene from the FLG surface (for FLG-Abl) requires a temperature as high as 450°C under a pressure of 10^{-4} Pa , showing strong interaction of this electron-donor species with graphene materials. This information can be useful while making graphene based chemisensors. Charge transport was also studied as function of temperature. The results display a decrease in sheet resistance with increasing temperature of FLG film (toluene-free already) and suggest that FLGs have a positive temperature coefficient (PTC) which could be important information for designing the thermistor devices. These results were published in the Journal of Physical Chemistry C. Further, the figure of merit of transparent conductor electrodes (conductivity of transparency) increases from 7 S/cm to 41 S/cm after this thermal treatment. The lowest sheet resistance of $760\Omega/\square$ was recorded for the annealed FLG film. The diffusive ambipolar charge transport (both n- and p-type charge carriers) with low R_s and good mobility values were observed during Hall Effect measurements. These results of conductivity make these materials suitable for conductive coatings and electrodes. Keeping the hot-spray method constant, various materials were studied methods to find out the suitability of cheap and scalable synthesis methods.

Improved transmittance was observed for FLG-HOPG24h films as compared

to that obtained for FLG-Abl due to larger lateral size of flakes, however, the R_s was on the higher side making the conductivity of transparency comparable for both materials/films with slight increase for the later up to 61% after thermal treatment. Both materials require a high temperature thermal treatment to get better electrical transport in terms of R_s . The advantage with synthetic graphite is to avoid the harsh purification and filtration steps used in FLG-Abl synthesis as well as the larger size of flakes.

Since the R_s and transparency of these films varies depending upon the local variation of film thickness, the measurement was taken in several points and average values were extracted. This highlights that the percolation threshold has direct relation with the transparency, which needs further investigation to find out a quantitative relationship between transparency, percolation and conductivity or R_s .

The roughness of the FLG-Abl and FLG-HOPG films resulting from the useless agglomerates formed during suspension dispersion and spray are major obstacle to get the smooth film with homogeneous surface and repeatable properties. Although this problem was of lower intensity in the case of films prepared from the μ -waves-assisted rGO and rGO/FLG but still quite rough films were obtained. Apart from colloidal behavior of the suspension and related aggregates formation, the hot-spray method has few limitations to get homogeneous and repeatable films due to manual and fixed nature of the system. In addition, we assume that the use of a mobile air-gun system for a deposition of FLG could improve homogeneity and continuity of the film, and consequently, reproducibility of the measured electrical characteristics. A nano-polishing tool/mechanism or application of stress/compression by the application of force can improve the packing density of underlying film by reducing the volume and make better contact between sheets and flakes coupled with reduction in the roughness. If the volume of material is reduced (by the application of force downwards on the sample to compress the material) while keeping the mass constant, the density

will increase. A higher density will improve the contact between sheets and flakes, and will significantly reduce the number of edges/boundaries which must be overcome by electrons while hopping to the adjacent flakes. The optimization of film formations can be still done by modification of suspensions concentrations and their dispersions. Concerning the initial materials, the FLG-Abl flakes can be smoothened by the "purification" from small graphitic units and hydrocarbon via μ -waves-assisted water treatment. This process is included in published manuscript in the Journal of Colloids and Interface Science.

Larger size FLG flakes with high electrical conductivity were obtained by the means of rapid exfoliation (extraction) of expanded graphite in toluene with the assistance of μ -waves irradiations of EG. The interaction of FLG with toluene was used to advantage the extraction of FLG flakes due to its ability to penetrate through the flakes' nano-cracking as observed in the case of FLG-Abl. The difference between absorption of microwaves by the two materials also helps in exfoliation of FLG by rapid heating of expanded graphite. Significant absorption of μ -waves by EG/FLG allows to reach the low defects, high range homogeneous conductive material. Very low sheet resistance together with the large lateral size of FLG flakes, up to ten of microns or higher, are comparable to those of high quality graphenes synthesized by CVD method, while considerable sheets' size is of high interest to reach percolation in the subsequent films formation in easier way.

However, despite the advantages of large lateral size flakes and better electronic properties, FLG from microwave had problems of low yield, forming aggregates in suspension and being unsuitable for film formation (due to the small diameter spray nozzle). Therefore, further study could not be carried out at the moment.

Microwaves-and-ethylene-glycol-assisted liquid phase exfoliation/reduction of graphene oxide and graphene oxide/expanded graphite, respectively, provides a viable alternative to rGO and rGO/FLG by low-cost and high yield method which

can be used to form transparent films by hot-spray method. Such obtained FLG flakes have large lateral size and are synthesized with yield sufficient for further investigations. Although, the initially obtained rGO and rGO/FLG films have moderate electrical properties with higher transmittance up to 73%, they can be further improved by the thermal annealing/reduction treatment in the inert environment. For the charge transport devices, higher R_s and transmittance were recorded compared to the FLGs obtained by ablation of pencil leads (FLG-Abl) or synthetic graphite (FLG-HOPG24h). The obtained sheet resistance fluctuated above and below the values obtained by FLG-Abl while the transparency was better than that of FLG-Abl and comparable to that obtained for FLG-HOPG. Due to the compensation effect of transparency-resistance values, the conductivity of transparency is also comparable.

To further improve the opto-electronic properties, the hybrids of FLG and rGO with CNTs were envisaged for investigations due to the advantage of nanotubes' high-aspect ratio and ability of nanotubes to form conductive mesh.

Due to its entangled structure, the CNTs in the hybrid films form network, which helps to increase the conductivity by lowering the percolation threshold which in turn helps to improve the transparency. The obtained R_s and transmittance were superior in hybrid films of CNTs with FLG-HOPG24h and rGO to those obtained with only FLG or rGO films. The effect of the thermal treatment improves the structure and helps to remove the adsorbed species (mostly oxygen-containing hydroxyl and carbonyl groups) notably from the surface of FLG and rGO. The rGO has possibly more of such impurities, which is evident from the results of lower R_s as compared to that obtained by the FLG-HOPG24h. CNTs network alone has better connection and transparency than the FLG materials used in this work, however the R_s of CNTs alone does not improve on the same scale as the FLG and rGO obtained by annealing probably due to high crystallinity and purity. The highest values of conductivity of transparency were achieved for FLG-Abl and its hybrid with CNTs. The minimum resistance were

measured for FLG-Abl and CNTs alone, while maximum transparency for hybrid, FLG-HOPG 24h (selection of largest flake by 24h of decantation) and rGO films. The homogeneous thickness of the prepared films remains the major challenge as punctual preferential stacking in the z direction and random orientation of flakes make it difficult to form the perfectly uniform and homogeneous films on glass/quartz substrates. The roughness profile measurements were performed using tip-based Dektak profilometer and Atomic Force Microscopy (AFM). Nuclear reaction Analysis (NRA) was used for the first time to estimate the voids in FLG films by knowing the concentration of carbon in film and independently the thickness. The thickness variations obtained by profilometer and NRA measurements calculations highlighted the possibility of occurrences of voids in the films and confirmed the preferential stacking of FLG flakes in the z direction. The estimated percentage of voids in films was calculated by taking into account the variations of thickness values (this approach is worthy of further investigations).

Despite the fact that the obtained results for the studied materials are still insufficient for ideal transparent electrodes, the tentative tests of fabrication of Organic Solar Cells with various FLG, rGO, CNTs hybrids materials were performed. The high roughness of the films is the main problem, which did not allow the OSC device to be realized with normal diode characteristics.

7.2 Perspectives

7.2.1 Materials

The use of flakes which are smoothed, with lowered sheets number and high crystallization degree (for example, μ -waves water purification) could help to get more homogenous film. The inhomogeneous size of FLG flakes obtained by ablation of pencil lead and crystal quality can be improved by this methods. Thus higher transparency, conductivity and flatness can be possible in FLG films.

The concentration and dispersion degree of the carbon nanomaterials should be optimized prior to the films formation.

7.2.2 Automated Mobile Air-gun for Hot-spray

An automated mobile air-gun with controlled speed can greatly improve the homogeneity of the films by improving the probability of deposited volume on the local surface. This will not only improve the roughness profile but also the local variations in terms of R_s and transmittance.

7.2.3 Polishing/Etching to Smoothen the Surface of Films

A polishing/etching mechanism can help to reduce the roughness and smooth the surface of films.

7.2.4 Polymer as Smoothing Agent

A layer of transparent conductor polymer such as PEDOT: PSS can be used to cover the roughness and smooth the surface of FLG films as it was demonstrated in rGO film in the chapter 4. This needs further optimization. Another transparent conductor polymer such as Norland Optical Adhesive (NOA) 63 can be used to embed the films, which not only covers the surface of films but also acts as a protective layer and is ultraviolet (UV) curable as well. This was demonstrated for covering the high roughness of Ag nanowires film [265].

7.2.5 Volume-thickness Study

Due to the heterogeneous nature of the films and local variations, it is difficult to precisely determine the relationship between the deposition volume and thickness. A separate study can be carried out to establish this relationship which would add value to the suitability of hot-spray method for further use.

7.2.6 Optimization of FLG Obtained by Exfoliation of Expanded Graphite in Toluene via Microwave Irradiation and Use of Large Diameter Spray-nozzle

To improve the yield from expanded graphite, the method can be optimized by playing with different parameters such as concentration ratio between expanded graphite and toluene, controlling the temperature, ramp, and pressure during the microwave irradiation and initial sonication/stirring process. Since the FLG sheets have large lateral size up to 10 μm , a spray gun with larger nozzle diameter and lower concentration of sprayed suspension should help to avoid the agglomeration of FLGs during the spray deposition.

7.2.7 FLG as Counter Electrode for OSCs

Since the work-function of the some of the materials studied in this thesis is lower and between 4.0 and 4.5 eV they are also suitable for counter electrode to replace the metal electrodes such as Al and Ag. These metal electrodes are often deposited by costly vacuum evaporation methods and are sensitive to environmental effects. A carbon-based counter electrode can be a better and cheaper choice.

7.2.8 rGO as Buffer Layer

The rGO obtained by microwave-assisted exfoliation/reduction can be used to replace the buffer layers such as PEDOT:PSS which is a hole transporting layer in OSCs as it is thin, solution-processable and of appropriate conductivity.

Bibliography

- [1] “<http://silicontechsupport.com/services.html>.”
- [2] D. Hecht, L. Hu, and G. Irvin, “Emerging transparent electrodes based on thin films of carbon nanotubes, graphene, and metallic nanostructures,” *Adv. Mater.*, vol. 23, pp. 1482–1513, 2011.
- [3] T. Minami, “Transparent conducting oxide semiconductors for transparent electrodes,” *Semicond. Sci. Technol.*, vol. 20, pp. S35–S44, 2005.
- [4] R. G. Gordon, “Criteria for Choosing Transparent Conductors,” *MRS Bull.*, vol. 25, pp. 52–57, 2000.
- [5] T. J. Coutts and T. O. Mason, “Transparent conducting oxides: status and opportunities in basic research,” tech. rep., NREL, Colorado, 1999.
- [6] S. Eigler, “A new parameter based on graphene for characterizing transparent, conductive materials,” *Carbon N. Y.*, vol. 47, pp. 2936–2939, 2009.
- [7] A. Klein, C. Körber, A. Wachau, F. Säuberlich, Y. Gassenbauer, S. P. Harvey, D. E. Proffit, and T. O. Mason, “Transparent Conducting Oxides for Photovoltaics: Manipulation of Fermi Level, Work Function and Energy Band Alignment,” *Materials (Basel)*, vol. 3, pp. 4892–4914, 2010.
- [8] W. C. H. Choy, *Organic Solar Cells Materials and Device Physics*. Hong Kong: Bentham Science Publishers, 2006.
- [9] F. Bonaccorso, Z. Sun, T. Hasan, and a. C. Ferrari, “Graphene photonics and optoelectronics,” *Nat. Photonics*, vol. 4, pp. 611–622, 2010.
- [10] T.-B. Song and N. Li, “Emerging Transparent Conducting Electrodes for Organic Light Emitting Diodes,” *Electronics*, vol. 3, pp. 190–204, 2014.

- [11] D. Arthur, R. P. Silvy, P. Wallis, Y. Tan, J.-D. R. Rocha, D. Resasco, R. Praino, and W. Hurley, “Carbon nanomaterial commercialization: Lessons for graphene from carbon nanotubes,” *MRS Bull.*, vol. 37, pp. 1297–1306, 2012.
- [12] Y. Lee and J.-H. Ahn, “Graphene-Based Transparent Conductive Films,” *Nano*, vol. 08, p. 1330001, 2013.
- [13] R. Schlaf, H. Murata, and Z. Kafafi, “Work function measurements on indium tin oxide films,” *J. Electron Spectros. Relat. Phenomena*, vol. 120, pp. 149–154, 2001.
- [14] Z. H. Helander, M. G., Greiner, M. T., Wang, Z. B., Tang, W. M., Lu, “Work function of fluorine doped tin oxide,” *J. Vac. Sci. Technol. A*, vol. 29, pp. 011019 – 011019–4, 2011.
- [15] H. Hibino, H. Kageshima, M. Kotsugi, F. Maeda, F.-Z. Guo and Y. Watanabe, “Dependence of electronic properties of epitaxial few-layer graphene on the number of layers investigated by photoelectron emission microscopy,” *Phys. Rev. B*, vol. 79, p. 125437, 2009.
- [16] G. Giovannetti, P. A. Khomyakov, G. Brocks, V. M. Karpan, J. van den Brink and P. J. Kelly, “Doping Graphene with Metal Contacts,” *Phys. Rev. Lett.*, vol. 101, p. 026803, 2008.
- [17] M. Shiraishi and M. Ata, “Work function of carbon nanotubes,” *Carbon N. Y.*, vol. 39, pp. 1913–1917, 2001.
- [18] P. Liu, Q. Sun, F. Zhu, K. Liu, K. Jiang, L. Liu, Q. Li, and S. Fan, “Measuring the work function of carbon nanotubes with thermionic method,” *Nano Lett.*, vol. 8, pp. 647–51, 2008.
- [19] M. Terrones, A. R. Botello-Méndez, J. Campos-Delgado, F. López-Urías, Y. I. Vega-Cantú, F. J. Rodríguez-Macías, A. L. Elías, E. Muñoz Sandoval,

- A. G. Cano-Márquez, and J.-C. Charlier, “Graphene and graphite nanoribbons: Morphology, properties, synthesis, defects and applications,” *Nano Today*, vol. 5, pp. 351–372, 2010.
- [20] A. K. Geim and K. S. Novoselov, “The rise of graphene.,” *Nat. Mater.*, vol. 6, pp. 183–91, 2007.
- [21] K. S. Novoselov, A. K. Geim, S. V. Morozov, D. Jiang, Y. Zhang, S. V. Dubonos, I. V. Grigorieva, and A. A. Firsov, “Electric field effect in atomically thin carbon films.,” *Science*, vol. 306, pp. 666–9, 2004.
- [22] A. K. Geim and P. Kim, “Carbon Wonderland,” *Sci. Am.*, vol. April, pp. 90–97, 2008.
- [23] K. S. K. S. et al Kim, Y. Zhao, H. Jang, S. Y. Lee, J. M. Kim, J.-H. Ahn, P. Kim, J.-Y. Choi, and B. H. Hong, “Large-scale pattern growth of graphene films for stretchable transparent electrodes.,” *Nature*, vol. 457, pp. 706–710, 2009.
- [24] K. S. Novoselov, A. K. Geim, S. V. Morozov, D. Jiang, M. I. Katsnelson, I. V. Grigorieva, S. V. Dubonos, and A. A. Firsov, “Two-dimensional gas of massless Dirac fermions in graphene.,” *Nature*, vol. 438, pp. 197–200, 2005.
- [25] R. Garg, N. Dutta, and N. Choudhury, “Work Function Engineering of Graphene,” *Nanomaterials*, vol. 4, pp. 267–300, 2014.
- [26] I. W. Frank, D. M. Tanenbaum, A. M. van der Zande, and P. L. McEuen, “Mechanical properties of suspended graphene sheets,” *J. Vac. Sci. Technol. B Microelectron. Nanom. Struct.*, vol. 25, p. 2558, 2007.
- [27] X. Wang and Y. I. Shi, “Fabrication Techniques of Graphene Nanostructures,” in *RSC Nanosci. Nanotechnol.*, pp. 1–30, 2014.

- [28] E. Pop, V. Varshney and A. K. Roy, “Thermal properties of graphene: Fundamentals and applications,” in *MRS Bull.*, vol. 37, pp. 1273–1281, 2012.
- [29] W. Choi, I. Lahiri, R. Seelaboyina, and Y. S. Kang, “Synthesis of Graphene and Its Applications: A Review,” *Crit. Rev. Solid State Mater. Sci.*, vol. 35, pp. 52–71, 2010.
- [30] B. Partoens, F. Peeters, B. P. Peeters, and F. M., “From graphene to graphite: Electronic structure around the K point,” *Phys. Rev. B*, vol. 74, p. 075404, 2006.
- [31] W. E. Andreoni, *The Physics of Fullerene-Based and Fullerene-Related Materials*. Springer Netherlands, 23 ed., 2000.
- [32] M. S. D. R. Saito, G. Dresselhaus, *Physical Properties of Carbon Nanotubes*. Imperial College Press, 2nd ed., 1998.
- [33] J.-C. Charlier and S. Roche, “Electronic and transport properties of nanotubes,” *Rev. Mod. Phys.*, vol. 79, pp. 677–732, 2007.
- [34] V. Krsti, *Charge transport in one-dimensional molecular nanostructures : single-walled carbon nanotubes*. PhD thesis, École Polytechnique Fédérale de Lausanne, 2002.
- [35] H. Petroski, *The Pencil: A History of Design and Circumstance*. Knopf, New York ., 1st ed., 1992.
- [36] P. R. Wallace, “The band theory of graphite,” *Phys. Rev.*, vol. 71, pp. 622–634, 1947.
- [37] A. H. Castro Neto, N. M. R. Peres, K. S. Novoselov, and A. K. Geim, “The electronic properties of graphene,” *Rev. Mod. Phys.*, vol. 81, pp. 109–162, 2009.

- [38] J. Hass, W. A. de Heer, and E. H. Conrad, “The growth and morphology of epitaxial multilayer graphene,” *J. Phys. Condens. Matter*, vol. 20, p. 323202, 2008.
- [39] C.-T. Pan, J. A. Hinks, Q. M. Ramasse, G. Greaves, U. Bangert, S. E. Donnelly, and S. J. Haigh, “In-situ observation and atomic resolution imaging of the ion irradiation induced amorphisation of graphene,” *Sci. Rep.*, vol. 4, p. 6334, 2014.
- [40] I. Janowska, F. Vigneron, D. Bégin, O. Ersen, P. Bernhardt, T. Romero, M. Ledoux, and C. Pham-Huu, “Mechanical thinning to make few-layer graphene from pencil lead,” *Carbon N. Y.*, vol. 50, pp. 3106–3110, 2012.
- [41] J. I. Paredes, S. Villar-Rodil, P. Solís-Fernández, A. Martínez-Alonso, and J. M. D. Tascón, “Atomic force and scanning tunneling microscopy imaging of graphene nanosheets derived from graphite oxide,” *Langmuir*, vol. 25, pp. 5957–68, 2009.
- [42] K. S. Subrahmanyam, S. R. C. Vivekchand, A. Govindaraj, and C. N. R. Rao, “A study of graphenes prepared by different methods: characterization, properties and solubilization,” *J. Mater. Chem.*, vol. 18, p. 1517, 2008.
- [43] Z. H. Ni, H. M. Wang, J. Kasim, H. M. Fan, T. Yu, Y. H. Wu, Y. P. Feng, and Z. X. Shen, “Graphene thickness determination using reflection and contrast spectroscopy,” *Nano Lett.*, vol. 7, pp. 2758–63, 2007.
- [44] A. C. Ferrari, J. C. Meyer, V. Scardaci, C. Casiraghi, M. Lazzeri, F. Mauri, S. Piscanec, D. Jiang, K. S. Novoselov, S. Roth, and A. K. Geim, “Raman Spectrum of Graphene and Graphene Layers,” *Phys. Rev. Lett.*, vol. 97, p. 187401, 2006.
- [45] P. Blake, E. W. Hill, A. H. Castro Neto, K. S. Novoselov, D. Jiang, R. Yang,

- T. J. Booth, and A. K. Geim, "Making graphene visible," *Appl. Phys. Lett.*, vol. 91, p. 063124, 2007.
- [46] S. Zhao, Y. Lv, and X. Yang, "Layer-dependent nanoscale electrical properties of graphene studied by conductive scanning probe microscopy," *Nanoscale Res. Lett.*, vol. 6, p. 498, 2011.
- [47] C. Punckt, F. Muckel, S. Wolff, I. A. Aksay, C. A. Chavarin, G. Bacher, and W. Mertin, "The effect of degree of reduction on the electrical properties of functionalized graphene sheets," *Appl. Phys. Lett.*, vol. 102, p. 023114, 2013.
- [48] X. Hong, A. Posadas, K. Zou, C. H. Ahn, and J. Zhu, "High-Mobility Few-Layer Graphene Field Effect Transistors Fabricated on Epitaxial Ferroelectric Gate Oxides," *Phys. Rev. Lett.*, vol. 102, p. 136808, 2009.
- [49] Y.-J. Yu, Y. Zhao, S. Ryu, L. E. Brus, K. S. Kim, and P. Kim, "Tuning the graphene work function by electric field effect.," *Nano Lett.*, vol. 9, pp. 3430–4, 2009.
- [50] A. Misra, H. Kalita, A. Kottantharayil, Abhishek Misra, Hemen Kalita, and A. Kottantharayil, "Work Function Modulation and Thermal Stability of Reduced Graphene Oxide Gate Electrodes in MOS Devices," *ACS Appl. Mater. Interfaces*, vol. 6, pp. 786–94, 2014.
- [51] S.-s. Kim, S.-y. Choi, C.-g. Park, and H.-w. Jin, "Transparent conductive ITO thin films through the sol-gel process using metal salts," *Thin Solid Films*, vol. 347, pp. 155–160, 1999.
- [52] A. Reina, X. Jia, J. Ho, D. Nezich, H. Son, V. Bulovic, M. S. Dresselhaus and J. Kong, "Large area, few-layer graphene films on arbitrary substrates by chemical vapor deposition.," *Nano Lett.*, vol. 9, pp. 30–35, 2009.

- [53] L. Malard, M. Pimenta, G. Dresselhaus, and M. Dresselhaus, “Raman spectroscopy in graphene,” *Phys. Rep.*, vol. 473, pp. 51–87, 2009.
- [54] Z. Ni, Y. Wang, T. Yu, and Z. Shen, “Raman spectroscopy and imaging of graphene,” *Nano Res.*, vol. 1, pp. 273–291, 2008.
- [55] L. G. Cançado, A. Jorio, E. H. M. Ferreira, F. Stavale, C. A. Achete, R. B. Capaz, M. V. O. Moutinho, A. Lombardo, T. S. Kulmala, and A. C. Ferrari, “Quantifying defects in graphene via Raman spectroscopy at different excitation energies,” *Nano Lett.*, vol. 11, pp. 3190–6, 2011.
- [56] K. S. Novoselov, D. Jiang, F. Schedin, T. J. Booth, V. V. Khotkevich, S. V. Morozov, and A. K. Geim, “Two-dimensional atomic crystals,” *Proc. Natl. Acad. Sci. U. S. A.*, vol. 102, pp. 10451–3, 2005.
- [57] A. Nagashima, K. Nuka, H. Itoh, T. Ichinokawa, and C. Oshima, “Electronic states of monolayer graphite formed on TiC(III) surface,” vol. 291, pp. 93–98, 1993.
- [58] H. J. Park, J. Meyer, S. Roth, and V. Skákalová, “Growth and properties of few-layer graphene prepared by chemical vapor deposition,” *Carbon N. Y.*, vol. 48, pp. 1088–1094, 2010.
- [59] S. Bae, H. Kim, Y. Lee, X. Xu, J.-S. Park, Y. Zheng, J. Balakrishnan, T. Lei, H. R. Kim, Y. I. Song, Y.-J. Kim, K. S. Kim, B. Ozyilmaz, J.-H. Ahn, B. H. Hong, and S. Iijima, “Roll-to-roll production of 30-inch graphene films for transparent electrodes,” *Nat. Nanotechnol.*, vol. 5, no. 8, pp. 574–578, 2010.
- [60] M. Endo, K. Takeuchi, S. Igarashi, K. Kobori, M. Shiraishi and H. Kroto, “The production and structure of pyrolytic carbon nanotubes,” *J. Phys. Chem. Solids*, vol. 54, pp. 1841–1848, 1993.

- [61] H. Dai, A.G. Rinzler, P. Nikolaev, A. Thess, D.T. Colbert, R.E. Smalley, “Single-wall nanotubes produced by metal-catalyzed disproportionation of carbon monoxide,” *Chem. Phys. Lett.*, vol. 260, pp. 471–475, 1996.
- [62] C. Berger, Z. Song, T. Li, X. Li, A. Y. Ogbazghi, R. Feng, Z. Dai, A. N. Marchenkov, E. H. Conrad, P. N. First, and W. A. D. Heer, “Ultrathin epitaxial graphite: 2D electron gas properties and a route toward graphene-based nanoelectronics.,” *J. Phys. Chem. B.*, vol. 108, pp. 19912–19916, 2004.
- [63] J. Hass, C. A. Jeffrey, R. Feng, T. Li, X. Li, Z. Zong, W. A. de Heer, P. N. First, E. H. Conrad and C. Berger, “Highly-ordered graphene for two dimensional electronics,” *Appl. Phys. Lett.*, vol. 89, pp. 143106–1– 143106–3, 2006.
- [64] P. W. Sutter, J.-I. Flege and E. A. Sutter, “Epitaxial graphene on ruthenium.,” *Nat. Mater.*, vol. 7, pp. 406–411, 2008.
- [65] K. V. Emtsev, K. Bostwick, A. Horn, J. Jobst, G. L. Kellogg, L. Ley, J. L. McChesney, T. Ohta, A. R. Sergey, J. Röhlrl, E. Rotenberg, A. K. Schmid, D. Waldmann, , B. W. Heiko, and T. Seyller, “Towards wafer-size graphene layers by atmospheric pressure graphitization of silicon carbide.,” *Nat. Mater.*, vol. 8, pp. 203–207, 2009.
- [66] S. Stankovich, D. A. Dikin, G. H. B. Dommett, K. M. Kohlhaas, E. J. Zimney, E. A. Stach, R. D. Piner, S. T. Nguyen, and R. S. Ruoff, “Graphene-based composite materials.,” *Nature*, vol. 442, pp. 282–6, 2006.
- [67] X. Li, G. Zhang, X. Bai, X. Sun, X. Wang, E. Wang, and H. Dai, “Highly conducting graphene sheets and Langmuir-Blodgett films.,” *Nat. Nanotechnol.*, vol. 3, pp. 538–42, 2008.

- [68] I. T. Hernandez, Y. Nicolasi, V. Lotya, M. Blighe, F. M. Sun, Z. De, S. McGovern, M. Holland, B. Byrne, and Y. K. Gunk'ko, "High-yield production of graphene by liquid-phase exfoliation of graphite.," *Nat. Nanotech.*, vol. 3, pp. 563–568, 2008.
- [69] Y. Hernandez, M. Lotya, V. Nicolosi, F. M. Blighe, S. De, and J. N. Georg, D. and Coleman, "Liquid phase production of graphene by exfoliation of graphite in surfactant/water solutions.," *J. Am. Chem. Soc.*, vol. 131, pp. 3611–3620, 2009.
- [70] S. Bae, S. J. Kim, D. Shin, J.-H. Ahn, and B. H. Hong, "Towards industrial applications of graphene electrodes," *Phys. Scr.*, vol. T146, pp. 014024–014031, 2012.
- [71] A. Ciesielski and P. Samorì, "Graphene via sonication assisted liquid-phase exfoliation.," *Chem. Soc. Rev.*, vol. 43, pp. 381–98, 2014.
- [72] V. León, M. Quintana, M. A. Herrero, J. L. G. Fierro, A. de la Hoz, M. Prato, and E. Vázquez, "Few-layer graphenes from ball-milling of graphite with melamine.," *Chem. Commun.*, vol. 47, pp. 10936–8, 2011.
- [73] V. León, A. M. Rodriguez, P. Prieto, M. Prato, and E. Vázquez, "Exfoliation of graphite with triazine derivatives under ball-milling conditions: preparation of few-layer graphene via selective noncovalent interactions.," *ACS Nano*, vol. 8, pp. 563–71, 2014.
- [74] M. Cai, D. Thorpe, D. H. Adamson, and H. C. Schniepp, "Methods of graphite exfoliation," *J. Mater. Chem.*, vol. 22, p. 24992, 2012.
- [75] W. Du, X. Jiang, and L. Zhu, "From graphite to graphene: direct liquid-phase exfoliation of graphite to produce single- and few-layered pristine graphene," *J. Mater. Chem. A*, vol. 1, p. 10592, 2013.

- [76] Mustafa Lotya, Paul J King, Umar Khan, Sukanta De, and Jonathan N Coleman, “High-Concentration, Surfactant-Stabilized Graphene Dispersions,” *ACS Nano*, vol. 4, pp. 3155–3162, 2010.
- [77] C.-Y. Su, A.-Y. Lu, Y. Xu, F.-R. Chen, A. N. Khlobystov, and L.-J. Li, “High-quality thin graphene films from fast electrochemical exfoliation,” *ACS Nano*, vol. 5, pp. 2332–9, 2011.
- [78] A. A. Green, and M. C. Hersam, “Solution Phase Production of Graphene with Controlled Thickness via Density Differentiation,” *Nano Lett.*, vol. 9, pp. 4031–4036, 2009.
- [79] C. Valles, C. Drummond, H. Saadaoui, C. A. Furtado, M. He, O. Roubeau, L. Ortolani, M. Monthieux, and A. Pénicaud, “Solutions of negatively charged graphene sheets and ribbons,” *J. Am. Chem. Soc.*, vol. 130, pp. 15802–15804, 2008.
- [80] W. Zhao, M. Fang, F. Wu, H. Wu, L. Wang, and G. Chen, “Preparation of graphene by exfoliation of graphite using wet ball milling,” *J. Mater. Chem.*, vol. 20, p. 5817, 2010.
- [81] H. Li, X., Wang, X., Zhang, L., Lee, S. & Dai, X. Li, X. Wang, L. Zhang, S. Lee, and H. Dai, “Chemically derived, ultrasmooth graphene nanoribbon semiconductors,” *Science*, vol. 319, pp. 1229–1232, 2008.
- [82] W. S. Hummers, and R. E. Offeman, “Preparation of Graphitic Oxide,” *J. Am. Chem. Soc.*, vol. 80, pp. 1339–1339, 1958.
- [83] M. Sharma, D. Mondal, C. Mukesh, and K. Prasad, “Studies on the effect of bio-ionic liquid structures on the spontaneous reduction and dispersion stability of graphene oxide in aqueous media,” *RSC Adv.*, vol. 4, pp. 42197–42201, 2014.

-
- [84] S. Park and R. S. Ruoff, "Chemical methods for the production of graphenes.," *Nat. Nanotechnol.*, vol. 4, pp. 217–24, 2009.
- [85] C. Mattevi, G. Eda, S. Agnoli, S. Miller, K. A. Mkhoyan, O. Celik, D. Mastrogiovanni, G. Granozzi, E. Garfunkel, and M. Chhowalla, "Evolution of Electrical, Chemical, and Structural Properties of Transparent and Conducting Chemically Derived Graphene Thin Films," *Adv. Funct. Mater.*, vol. 19, pp. 2577–2583, 2009.
- [86] S. Park, J. An, J. R. Potts, A. Velamakanni, S. Murali, and R. S. Ruoff, "Hydrazine-reduction of graphite- and graphene oxide," *Carbon N. Y.*, vol. 49, pp. 3019–3023, 2011.
- [87] R. Cruz, D. A. Pacheco Tanaka, and A. Mendes, "Reduced graphene oxide films as transparent counter-electrodes for dye-sensitized solar cells," *Sol. Energy*, vol. 86, pp. 716–724, 2012.
- [88] X. Wang, L. Zhi, K. Müllen, L. Z. Xuan Wang, K. Müllen, and K. Wang, X., Zhi, L. & Mullen, "Transparent, conductive graphene electrodes for dye-sensitized solar cells.," *Nano Lett.*, vol. 8, pp. 323–327, 2007.
- [89] R. Rozada, J. I. Paredes, S. Villar-Rodil, A. Martínez-Alonso, and J. M. D. Tascón, "Towards full repair of defects in reduced graphene oxide films by two-step graphitization," *Nano Res.*, vol. 6, pp. 216–233, 2013.
- [90] E. Y. S. V. Tkachev and S. P. G. Buslaeva, "Graphene: A novel carbon nanomaterial," *Inorg. Mater.*, vol. 47, pp. 1–10, 2011.
- [91] M. Acik and Y. J. Chabal, "A Review on Reducing Graphene Oxide for Band Gap Engineering," *J. Mater. Sci. Res.*, vol. 2, pp. 101–112, 2012.
- [92] S. H. Tien, H. N. Van, L. H. Cuong, T. V. Kong, B.-S. Chung, J. S. Kim, E. J. Hur, "Fast and simple reduction of graphene oxide in various organic

- solvents using microwave irradiation.,” *J Nanosci Nanotechnol.*, vol. 12, no. 7, pp. 5658–5662., 2012.
- [93] Y. Zhu, S. Murali, M. D. Stoller, A. Velamakanni, R. D. Piner, and R. S. Ruoff, “Microwave assisted exfoliation and reduction of graphite oxide for ultracapacitors,” *Carbon N. Y.*, vol. 48, pp. 2118–2122, 2010.
- [94] S. Pei and H.-M. Cheng, “The reduction of graphene oxide,” *Carbon N. Y.*, vol. 50, pp. 3210–3228, 2012.
- [95] G. Gutierrez, F. Le Normand, D. Muller, F. Aweke, C. Speisser, F. Antoni, Y. Le Gall, C. Lee, and C. Cojocaru, “Multi-layer graphene obtained by high temperature carbon implantation into nickel films,” *Carbon N. Y.*, vol. 66, pp. 1–10, 2014.
- [96] J. Wu, W. Pisula, and K. Müllen, “Graphenes as potential material for electronics.,” *Chem. Rev.*, vol. 107, pp. 718–47, 2007.
- [97] V. B. Harald, B. Valerij, *Hopping Conduction in Solids*. Weinheim, Germany: Vch Pub, 1985.
- [98] J. Muster, G.T. Kim, V. Krstic, J.G. Park, Y.W. Park, S. Roth and M. Burghard, “Electrical transport through individual vanadium pentoxide nanowires,” *Adv. Mater*, vol. 12, p. 420, 2000.
- [99] J. Kondo, “Resistance Minimum in Dilute Magnetic Alloys,” *Prog. Theor. Phys.*, vol. 32, pp. 37–49, 1964.
- [100] N. S. Sankeshwar, S. S. Kubakaddi, and B. G. Mulimani, “Thermoelectric Power in Graphene,” in *Adv. Graphene Sci.*, pp. 217–271, 2013.
- [101] A. Lherbier, X. Blase, Y.-M. Niquet, F. Triozon, and S. Roche, “Charge Transport in Chemically Doped 2D Graphene,” *Phys. Rev. Lett.*, vol. 101, p. 036808, 2008.

- [102] J. Kotakoski, A. V. Krasheninnikov, U. Kaiser, and J. C. Meyer, “From Point Defects in Graphene to Two-Dimensional Amorphous Carbon,” *Phys. Rev. Lett.*, vol. 106, p. 105505, 2011.
- [103] L. Liu, M. Qing, Y. Wang, and S. Chen, “Defects in Graphene: Generation, Healing, and Their Effects on the Properties of Graphene: A Review,” *J. Mater. Sci. Technol.*, p. (in press), 2015.
- [104] N. Jing, Q. Xue, C. Ling, M. Shan, T. Zhang, X. Zhou, and Z. Jiao, “Effect of defects on Young’s modulus of graphene sheets: a molecular dynamics simulation,” *RSC Adv.*, vol. 2, p. 9124, 2012.
- [105] F. Banhart, J. Kotakoski, and A. V. Krasheninnikov, “Structural defects in graphene,” *ACS Nano*, vol. 5, pp. 26–41, 2011.
- [106] K. M. McCreary, *An Investigation of Spin and Charge Transport in Doped and Defected Graphene*. PhD thesis, University of California, Riverside, 2012.
- [107] G. Eda, Y.-Y. Lin, C. Mattevi, H. Yamaguchi, H.-A. Chen, I.-S. Chen, C.-W. Chen, and M. Chhowalla, “Blue Photoluminescence from Chemically Derived Graphene Oxide,” *Adv. Mater.*, vol. 22, pp. 505–509, 2010.
- [108] W. G. Yufeng Guo and C. Chen, “Tuning field-induced energy gap of bilayer graphene via interlayer spacing,” *Appl. Phys. Lett.*, vol. 92, p. 243101, 2008.
- [109] J. Martin, N. Akerman, G. Ulbricht, T. Lohmann, J. H. Smet, K. von Klitzing, and A. Yacoby, “Observation of electron-hole puddles in graphene using a scanning single-electron transistor,” *Nat. Phys.*, vol. 4, pp. 144–148, 2007.
- [110] E. Fradkin, “Critical behavior of disordered degenerate semiconductors. II. Spectrum and transport properties in mean-field theory,” *Phys. Rev. B*, vol. 33, p. 3263, 1986.

- [111] Andreas W. W. Ludwig, Matthew P. A. Fisher, R. Shankar and G. Grinstein, “Integer quantum Hall transition: An alternative approach and exact results,” *Phys. Rev. B*, vol. 50, p. 7526, 1994.
- [112] P. A. Lee, “Localized states in a d-wave superconductor,” *Phys. Rev. Lett.*, vol. 71, p. 1887, 1993.
- [113] N. M. R. Peres, F. Guinea and A. H. C. Neto, “Electronic properties of disordered two-dimensional carbon,” *Phys. Rev. B*, vol. 73, p. 125411, 2006.
- [114] Y. M. Nazarov, Y. V. Blanter, *Quantum Transport Introduction to Nanoscience*. New York, USA: Cambridge University Press, 1st ed., 2009.
- [115] R. Landauer, “Spatial Variation,” *IBM J. Res. Dev.*, vol. 1, pp. 223–231, 1957.
- [116] T. V. Ramakrishnan, and P. A. Lee, “Disordered electronic systems,” *Rev. Mod. Phys.*, vol. 57, p. 287, 1985.
- [117] Y.-W. Tan, Y. Zhang, K. Bolotin, Y. Zhao, S. Adam, E. H. Hwang, S. Das Sarma, H. L. Stormer, and P. Kim, “Measurement of Scattering Rate and Minimum Conductivity in Graphene,” *Phys. Rev. Lett.*, vol. 99, p. 246803, 2007.
- [118] F. Miao, S. Wijeratne, Y. Zhang, U. C. Coskun, W. Bao, and C. N. Lau, “Phase-Coherent Transport in Graphene Quantum Billiards,” *Science*, vol. 317, pp. 1530–1533, 2007.
- [119] K. Nagashio and A. Yamashita, T. Fujita, J. Nishimura, T. Kita, K. Toriumi, “Impacts of graphene/SiO₂ interaction on FET mobility and Raman spectra in mechanically exfoliated graphene films,” in *IEEE Int. Electron Devices Meet.*, pp. 23.4.1–23.4.4, 2010.

- [120] J.-H. Chen, C. Jang, S. Xiao, M. Ishigami, M. S. Fuhrer, “Intrinsic and extrinsic performance limits of graphene devices on SiO₂,” *Nat. Nanotechnol.*, vol. 3, pp. 206–209, 2008.
- [121] V. Sgobba and D. M. Guldi, “Carbon nanotubes as integrative materials for organic photovoltaic devices,” *J. Mater. Chem.*, vol. 18, p. 153, 2008.
- [122] S. M. Vemuru, R. Wahi, S. Nagarajaiah, and P. M. Ajayan, “Strain sensing using a multiwalled carbon nanotube film,” *J. Strain Anal. Eng. Des.*, vol. 44, pp. 555–562, 2009.
- [123] R. Rafiee and R. Pourazizi, “Evaluating the Influence of Defects on the Young’s Modulus of Carbon Nanotubes Using Stochastic Modeling-CNT Morphology and Defect Types,” *Mater. Res.*, vol. 17, pp. 758–766, 2014.
- [124] M. Havel, K. Behler, G. Korneva, and Y. Gogotsi, “Transparent Thin Films of Multiwalled Carbon Nanotubes Self-Assembled on Polyamide 11 Nanofibers,” *Adv. Funct. Mater.*, vol. 18, pp. 2322–2327, 2008.
- [125] L. Hu, D. S. Hecht, and G. Gru, “Carbon Nanotube Thin Films : Fabrication , Properties , and Applications,” *Chem. Rev.*, vol. 110, pp. 5790–5844, 2010.
- [126] M. Bockrath, D. H. Cobden, P. L. McEuen, N. G. Chopra, A. Zettl, A. Thess and R. E. Smalley, “Single-Electron Transport in Ropes of Carbon Nanotubes,” *Science*, vol. 275, pp. 1922–1925, 1997.
- [127] S. J. Tans, M. H. Devoret, H. J. Dai, A. Thess, R. E. Smalley, L. J. Geerligs and C. Dekker, “Individual Single-Wall Carbon Nanotubes As Quantum Wires,” *Nature*, vol. 386, pp. 474–477, 1997.
- [128] C. T. White and T. N. Todorov, “Carbon nanotubes as long ballistic conductors,” *Nature*, vol. 393, pp. 240–242, 1998.

- [129] A. Bachtold, M. S. Fuhrer, S. Plyasunov, M. Forero, E. H. Anderson, A. Zettl, P. L. McEuen, , S. A. Bachtold, M. S. Fuhrer, and P. L. McEuen, “Scanned probe microscopy of electronic transport in carbon nanotubes,” *Phys. Rev. Lett.*, vol. 84, pp. 6082–6085, 2000.
- [130] P. L. Mceuen and J.-Y. Park, “Electron Transport in Single-Walled Carbon Nanotubes,” in *MRS Bull.*, pp. 272–275, 2004.
- [131] C. Chen and Y. Zhang, *Nanowelded Carbon Nanotubes from Field-effect Transistors to Solar Microcells*. Heidelberg: Springer, 2009.
- [132] W. J. Liang, M. Bockrath, D. Bozovic, J. H. Hafner, M. Tinkham and H. Park, “Fabry-Perot interference in a nanotube electron waveguide,” *Nature*, vol. 411, pp. 665–669, 2001.
- [133] J. Kong, E. Yenilmez, T. W. Tombler, W. Kim, H. J. Dai, R. B. Laughlin and L. Liu, C. S. Jayanthi, and S. Y. Wu, “Quantum interference and ballistic transmission in nanotube electron waveguides,” *Phys. Rev. Lett.*, vol. 87, p. 106801, 2001.
- [134] S. J. Tans, and C. Dekker, “Molecular transistors-potential modulations along carbon nanotubes,” *Nature*, vol. 404, pp. 834–835, 2000.
- [135] P. L. Yaish, Y. Park, J.-Y. Rosenblatt, S. Sazonova, V. Brink, M. McEuen, “Electrical nanoprobng of semiconducting carbon nanotubes using an atomic force microscope,” *Phys. Rev. Lett.*, vol. 92, p. 046401, 2004.
- [136] Y. Zhu, S. Murali, W. Cai, X. Li, J. W. Suk, J. R. Potts, and R. S. Ruoff, “Graphene and graphene oxide: synthesis, properties, and applications,” *Adv. Mater.*, vol. 22, pp. 3906–3924, 2010.
- [137] T. M. Barnes, J. van de Lagemaat, D. Levi, G. Rumbles, T. J. Coutts, C. L. Weeks, D. A. Britz, I. Levitsky, J. Peltola and P. Glatkowski, “Optical char-

- acterization of highly conductive single-wall carbon-nanotube transparent electrodes,” *Phys. Rev. B*, vol. 75, p. 235410, 2007.
- [138] H. Ago, K. Petritsch, M. S. P. Shaffer, A. H. Windle, and R. H. Friend, “Composites of Carbon Nanotubes and Conjugated Polymers for Photovoltaic Devices,” *Adv. Mater.*, vol. 11, pp. 1281–1285, 1999.
- [139] T. V. Sreekumar, Tao Liu, Satish Kumar, Lars M. Ericson, Robert H. Hauge and R. E. Smalley, “Single-Wall Carbon Nanotube Films,” *Chem. Mater.*, vol. 15, pp. 175–178, 2003.
- [140] A. A. Mamedov, N. A. Kotov, M. Prato, D. M. Guldi, J. P. Wicksted, and A. Hirsch, “Molecular design of strong single-wall carbon nanotube/poly-electrolyte multilayer composites,” *Nat. Mater.*, vol. 1, pp. 190–194, 2002.
- [141] F. K. Laura J. Cote and J. Huang, “Langmuir-Blodgett Assembly of Graphite Oxide Single Layers,” *J. Am. Chem. Soc.*, vol. 131, pp. 1043–1049, 2009.
- [142] X. Li, L. Zhang, X. Wang, I. Shimoyama, X. Sun, W.-S. Seo, and H. Dai, “Langmuir-blodgett assembly of densely aligned single-walled carbon nanotubes from bulk materials,” *J. Am. Chem. Soc.*, vol. 129, pp. 4890–4891, 2007.
- [143] L. Li, Y. Guo, X. Zhang, and Y. Song, “Inkjet-printed highly conductive transparent patterns with water based Ag-doped graphene,” *J. Mater. Chem. A*, vol. 2, pp. 19095–19101, 2014.
- [144] A. Celzard, J. F. Maréché, G. Furdin and S. Puricelli, “Electrical conductivity of anisotropic expanded graphite-based monoliths,” *J. Phys. D Appl. Phys.*, vol. 33, pp. 3094–3101, 2000.

- [145] K. Rana, J. Singh, and J.-H. Ahn, "A graphene-based transparent electrode for use in flexible optoelectronic devices," *J. Mater. Chem. C*, vol. 2, p. 2646, 2014.
- [146] K. K. Kim, A. Reina, Y. Shi, H. Park, L.-J. Li, Y. H. Lee, and J. Kong, "Enhancing the conductivity of transparent graphene films via doping," *Nanotechnology*, vol. 21, p. 285205, 2010.
- [147] K. Y. G.-X. Ni, Y. Zheng, S. Bae, C. Y. Tan, O. Kahya, J. Wu, B. H. Hong and B. Özyilmaz, "Graphene-Ferroelectric Hybrid Structure for Flexible Transparent Electrodes," *ACS Nano*, vol. 6, pp. 3935–3942, 2012.
- [148] K. Parvez, R. Li, S. R. Puniredd, Y. Hernandez, F. Hinkel, S. Wang, X. Feng, and K. Mu, "Electrochemically Exfoliated Graphene as Solution-Processable , Highly Conductive Electrodes for Organic Electronics," *ACS Nano*, vol. 7, pp. 3598–3606, 2013.
- [149] X. Lin, J. Jia, N. Yousefi, X. Shen, and J.-K. Kim, "Excellent optoelectrical properties of graphene oxide thin films deposited on a flexible substrate by Langmuir-Blodgett assembly," *J. Mater. Chem. C*, vol. 1, p. 6869, 2013.
- [150] N. R. E. Laboratory, "Research Cell Efficiency Records," 2014.
- [151] P. Hudhomme, "An overview of molecular acceptors for organic solar cells," *EPJ Photovoltaics*, vol. 4, p. 40401, 2013.
- [152] J.-H. Choi, H.-J. Choi, J.-H. Shin, H.-P. Kim, J. Jang, H. Lee, "Enhancement of organic solar cell efficiency by patterning the PEDOT:PSS hole transport layer using nanoimprint lithography," *Org. Electron.*, vol. 14, pp. 3180–318, 2013.
- [153] G. H. Jung and J.-L. Lee, "Origin of gap states in the electron transport layer of organic solar cells," *J. Mater. Chem. A*, vol. 1, p. 3034, 2013.

- [154] T. Kietzke, “Recent Advances in Organic Solar Cells,” *Adv. Optoelectron.*, vol. 2007, pp. 1–15, 2007.
- [155] P. G. Nicholson and F. A. Castro, “Organic photovoltaics: principles and techniques for nanometre scale characterization,” *Nanotechnology*, vol. 21, p. 492001, 2010.
- [156] N. Kaur, M. Singh, D. Pathak, T. Wagner, and J. M. Nunzi, “Organic materials for photovoltaic applications: Review and mechanism,” *Synth. Met.*, vol. 190, pp. 20–26, 2014.
- [157] J. Nelson, “Organic photovoltaic films,” *Curr. Opin. Solid State Mater. Sci.*, vol. 6, pp. 87–95, 2002.
- [158] H. Hoppe and N. S. Sariciftci, “Organic solar cells: An overview,” *J. Mater. Res.*, vol. 19, pp. 1924–1945, 2011.
- [159] K. M. Coakley and M. D. McGehee, “Conjugated Polymer Photovoltaic Cells,” *Chem. Mater.*, vol. 16, pp. 4533–4542, 2004.
- [160] S. M. Sze, *Physics of Semiconductor Devices*. New York, USA: Wiley-Interscience, 3rd ed., 2006.
- [161] J. D. Servaites, M. A. Ratner, and T. J. Marks, “Organic solar cells: A new look at traditional models,” *Energy Environ. Sci.*, vol. 4, p. 4410, 2011.
- [162] B. Kippelen and J.-L. Brédas, “Organic photovoltaics,” *Energy Environ. Sci.*, vol. 2, p. 251, 2009.
- [163] W. Shockley, “The Theory of PN Junctions in Semiconductors and PN Junction Transistors,” *Bell Syst. Tech. J.*, vol. 28, pp. 435–489, 1949.
- [164] C. J. Brabec, N. S. Sariciftci, and J. C. Hummelen, “Plastic Solar Cells,” *Adv. Funct. Mater.*, vol. 11, pp. 15–26, 2001.

- [165] B. C. Thompson and J. M. J. Fréchet, "Polymer-fullerene composite solar cells," *Angew. Chemie*, vol. 47, pp. 58–77, 2008.
- [166] X. Zhu, Q. Yang, M. Muntwiler, and F. Charge, "Charge-Transfer Excitons at Organic," *Acc. Chem. Res.*, vol. 42, pp. 1779–1787, 2009.
- [167] H. Hoppe and N. S. Sariciftci, "Morphology of polymer/fullerene bulk heterojunction solar cells," *J. Mater. Chem.*, vol. 16, pp. 45–61, 2006.
- [168] J.-m. Nunzi, "Organic photovoltaic materials and devices," *C. R. Phys.*, vol. 3, pp. 523–542, 2002.
- [169] L. Koster, E. Smits, V. Mihailetschi, and P. Blom, "Device model for the operation of polymer/fullerene bulk heterojunction solar cells," *Phys. Rev. B*, vol. 72, p. 085205, 2005.
- [170] C. J. Brabec, A. Cravino, D. Meissner, N. S. Sariciftci, T. Fromherz, M. T. Rispens, L. Sanchez, and J. C. Hummelen, "Origin of the Open Circuit Voltage of Plastic Solar Cells," *Adv. Funct. Mater.*, vol. 11, pp. 374–380, 2001.
- [171] I. D. Parker, "Carrier tunneling and device characteristics in polymer light emitting diodes," *J. Appl. Phys.*, vol. 75, p. 1656, 1994.
- [172] M. C. Scharber, D. Mühlbacher, M. Koppe, P. Denk, C. Waldauf, A. J. Heeger, and C. J. Brabec, "Design Rules for Donors in Bulk-Heterojunction Solar Cells-Towards 10 % Energy-Conversion Efficiency," *Adv. Mater.*, vol. 18, pp. 789–794, 2006.
- [173] V. D. Mihailetschi, P. W. M. Blom, J. C. Hummelen, and M. T. Rispens, "Cathode dependence of the open-circuit voltage of polymer:fullerene bulk heterojunction solar cells," *J. Appl. Phys.*, vol. 94, p. 6849, 2003.

- [174] C. J. Brabec, S. E. Shaheen, C. Winder, N. S. Sariciftci, and P. Denk, "Effect of LiF/metal electrodes on the performance of plastic solar cells," *Appl. Phys. Lett.*, vol. 80, p. 1288, 2002.
- [175] S. Y. A. Hayakawa, O. Yoshikawa, T. Fujieda, K. Uehara, "High performance polythiophene/fullerene bulk-heterojunction solar cell with a TiOx hole blocking layer," *Appl. Phys. Lett.*, vol. 90, p. 163517, 2007.
- [176] C. Waldauf, M. Morana, P. Denk, P. Schilinsky, K. Coakley, S. A. Choulis and C. J. Brabec, "Highly efficient inverted organic photovoltaics using solution based titanium oxide as electron selective contact," *Appl. Phys. Lett.*, vol. 89, p. 233517, 2006.
- [177] K. Keis, E. Magnusson, H. Lindstr, S.-e. Lindquist, and A. Hagfeldt, "A 5 % efficient photoelectrochemical solar cell based on nanostructured ZnO electrodes," *Sol. Energy Mater. Sol. Cells*, vol. 73, pp. 51–58, 2002.
- [178] A. K. K. Kyaw, X. W. Sun, C. Y. Jiang, G. Q. Lo, D. W. Zhao and D. L. Kwong, "An inverted organic solar cell employing a sol-gel derived ZnO electron selective layer and thermal evaporated MoO3 hole selective layer," *Appl. Phys. Lett.*, vol. 93, p. 221107, 2008.
- [179] H. Schmidt, H. Flußlgge, T. Winkler, T. Bußlow, T. Riedl, and W. Kowalsky, "Efficient semitransparent inverted organic solar cells with indium tin oxide top electrode," *Appl. Phys. Lett.*, vol. 94, p. 243302, 2009.
- [180] S. Han, W. S. Shin, M. Seo, D. Gupta, S.-J. Moon, and S. Yoo, "Improving performance of organic solar cells using amorphous tungsten oxides as an interfacial buffer layer on transparent anodes," *Org. Electron.*, vol. 10, pp. 791–797, 2009.
- [181] C. Y. Jiang, X. W. Sun, D. W. Zhao, A. K. K. Kyaw, and Y. N. Li, "Low

- work function metal modified ITO as cathode for inverted polymer solar cells,” *Sol. Energy Mater. Sol. Cells*, vol. 94, pp. 1618–1621, 2010.
- [182] T. L. Benanti and D. Venkataraman, “Organic solar cells: an overview focusing on active layer morphology,” *Photosynth. Res.*, vol. 87, pp. 73–81, Jan. 2006.
- [183] T. J. B. R. R. Nair, P. Blake, A. N. Grigorenko, K. S. Novoselov and K. S. T. Stauber, N. M. R. Peres, and A. K. Geim, v, “Fine structure constant defines visual transparency of graphene,” *Science*, vol. 320, p. 5881, 2008.
- [184] Y. A. Akimov, “The Potential of Graphene as an ITO Replacement in Organic Solar Cells: An Optical Perspective,” *IEEE J. Sel. Top. Quantum Electron.*, vol. 20, pp. 36–42, 2014.
- [185] S. Stankovich, D. A. Dikin, R. D. Piner, K. A. Kohlhaas, A. Kleinhammes, Y. Jia, Y. Wu, S. T. Nguyen, and R. S. Ruoff, “Synthesis of graphene-based nanosheets via chemical reduction of exfoliated graphite oxide,” *Carbon N. Y.*, vol. 45, pp. 1558–1565, 2007.
- [186] Z. B. Héctor A. Becerril, Jie Mao, Zunfeng Liu, Randall M. Stoltenberg, Y. Chen, and H. A. et al. Becerril, “Evaluation of Solution-Processed Reduced Graphene Oxide Films as Transparent Conductors,” *ACS Nano*, vol. 2, pp. 463–470, 2008.
- [187] P.eter Blake, Paul D. Brimicombe, Rahul R. Nair, Tim J. Booth, Da Jiang, Fred Schedin, Leonid A. Ponomarenko, Sergey V. Morozov , Helen F. Gleeson, Ernie W. Hill, Andre K. Geim and Kostya S. Novoselov, “Graphene-Based Liquid Crystal Device,” *Nano Lett.*, vol. 8, pp. 1704–1708, 2008.
- [188] Chao Yan, Kwang-Seop Kim, Seoung-Ki Lee, Sang-Hoon Bae, Byung Hee Hong, Jae-Hyun Kim, Hak-Joo Lee, and Jong-Hyun Ahn, “Mechanical and

- Environmental Stability of Polymer Thin-Film-Coated Graphene,” *ACS Nano*, vol. 6, pp. 2096–2103, 2012.
- [189] J. Wu, H. a. Becerril, Z. Bao, Z. Liu, Y. Chen, and P. Peumans, “Organic solar cells with solution-processed graphene transparent electrodes,” *Appl. Phys. Lett.*, vol. 92, p. 263302, 2008.
- [190] S.-K. Lee, K. Rana, and J.-H. Ahn, “Graphene Films for Flexible Organic and Energy Storage Devices,” *J. Phys. Chem. Lett.*, vol. 4, pp. 831–841, 2013.
- [191] Z. Liu, J. Li, and F. Yan, “Package-free flexible organic solar cells with graphene top electrodes,” *Adv. Mater.*, vol. 25, pp. 4296–301, 2013.
- [192] E. Kymakis, K. Savva, M. M. Stylianakis, C. Fotakis, and E. Stratakis, “Flexible Organic Photovoltaic Cells with In Situ Nonthermal Photoreduction of Spin-Coated Graphene Oxide Electrodes,” *Adv. Funct. Mater.*, vol. 23, pp. 2742–2749, 2013.
- [193] H. Kim, S.-H. Bae, T.-H. Han, K.-G. Lim, J.-H. Ahn, and T.-W. Lee, “Organic solar cells using CVD-grown graphene electrodes,” *Nanotechnology*, vol. 25, p. 014012, 2014.
- [194] R. Ahmad, M. Shamsudin, M. Sahdan, M. Rusop, and S. Sanip, “Green and Economic Transparent Conductive Graphene Electrode for Organic Solar Cell: A Short Review,” *Adv. Mater. Res.*, vol. 832, pp. 316–321, 2013.
- [195] X. Xia, S. Wang, Y. Jia, Z. Bian, D. Wu, L. Zhang, and A. Cao, “Infrared-Transparent Polymer Solar Cells,” *J. Mater. Chem.*, vol. 20, pp. 8478–8482, 2010.
- [196] J. Huang, G. Li, and Y. Yang, “A Semi-transparent Plastic Solar Cell Fabricated by a Lamination Process,” *Adv. Mater.*, vol. 20, pp. 415–419, Feb. 2008.

- [197] Yu-Ying Lee, Kun-Hua Tu, Chen-Chieh Yu, Shao-Sian Li, Jeong-Yuan Hwang, Chih-Cheng Lin, Kuei-Hsien Chen, Li-Chyong Chen, Hsuen-Li Chen and C.-W. Chen, "Top Laminated Graphene Electrode in a Semi-transparent Polymer Solar Cell by Simultaneous Thermal Annealing/Releasing Method," *ACS Nano*, vol. 5, pp. 6564–6570, 2011.
- [198] Z. Liu, J. Li, Z.-H. Sun, G. Tai, S.-P. Lau, and F. Yan, "The application of highly doped single-layer graphene as the top electrodes of semitransparent organic solar cells.," *ACS Nano*, vol. 6, pp. 810–8, 2012.
- [199] Hyesung Park, Sehoon Chang, Joel Jean, Jayce J. Cheng, Paulo T. Araujo, Mingsheng Wang, Mounqi G. Bawendi, Mildred S. Dresselhaus, Vladimir Bulovic, Jing Kong, and Silvija Gradecak, "Graphene Cathode-Based ZnO Nanowire Hybrid Solar Cells," *Nano Lett.*, vol. 13, pp. 233–239, 2013.
- [200] S. Mathew, A. Yella, P. Gao, R. Humphry-Baker, B. F. E. Curchod, N. Ashari-Astani, I. Tavernelli, U. Rothlisberger, M. K. Nazeeruddin, and M. Grätzel, "Dye-sensitized solar cells with 13% efficiency achieved through the molecular engineering of porphyrin sensitizers.," *Nat. Chem.*, vol. 6, pp. 242–7, 2014.
- [201] S. Das, P. Sudhagar, V. Verma, D. Song, E. Ito, S. Y. Lee, Y. S. Kang, and W. Choi, "Amplifying Charge-Transfer Characteristics of Graphene for Triiodide Reduction in Dye-Sensitized Solar Cells," *Adv. Funct. Mater.*, vol. 21, pp. 3729–3736, 2011.
- [202] H. Choi, H. Kim, S. Hwang, W. Choi, and M. Jeon, "Dye-sensitized solar cells using graphene-based carbon nano composite as counter electrode," *Sol. Energy Mater. Sol. Cells*, vol. 95, pp. 323–325, 2011.
- [203] K. S. Lee, Y. Lee, J. Y. Lee, J.-H. Ahn, and J. H. Park, "Flexible

- and platinum-free dye-sensitized solar cells with conducting-polymer-coated graphene counter electrodes,” *ChemSusChem*, vol. 5, pp. 379–82, 2012.
- [204] S. I. Ichihashi and Toshinari, “single-shell carbon nanotubes of 1-nm diameter,” *Nature*, vol. 363, pp. 603–605, 1993.
- [205] T. Dürkop, S. A. Getty, E. Cobas, and M. S. Fuhrer, “Extraordinary Mobility in Semiconducting Carbon Nanotubes,” *Nano Lett.*, vol. 4, pp. 35–39, 2004.
- [206] A. Rinzler, J. Liu, H. Dai, P. Nikolaev, C. Huffman, F. Rodríguez-Macías, P. Boul, A. Lu, D. Heymann, D. Colbert, R. Lee, J. Fischer, A. Rao, P. Eklund, and R. Smalley, “Large-scale purification of single-wall carbon nanotubes: process, product, and characterization,” *Appl. Phys. A*, vol. 67, pp. 29–37, 1998.
- [207] H. Dai, “Carbon nanotubes: opportunities and challenges,” *Surf. Sci.*, vol. 500, pp. 218–241, 2002.
- [208] H. L. Tuller, *Flexible Electronics : Materials and Applications Electronic Materials : Science and Technology*. Springer US, 1st ed., 2009.
- [209] D. Hecht, *Properties and Applications of Carbon Nanotube Films: A Revolutionary Material for Transparent and Flexible Electronics*. Vdm Verlag Dr Mueller E, 2008.
- [210] L. Hu, D. S. Hecht, and G. Gru, “Percolation in Transparent and Conducting Carbon Nanotube Networks,” *Nano Lett.*, vol. 4, pp. 2513–2517, 2004.
- [211] S. R. M. Kaempgen, G.S. Duesberg, “Transparent carbon nanotube coatings,” *Appl. Surf. Sci.*, vol. 252, pp. 425–429, 2005.

- [212] Z. Wu, Z. Chen, X. Du, J. M. Logan, J. Sippel, M. Nikolou, K. Kamaras, J. R. Reynolds, D. B. Tanner, A. F. Hebard, and A. G. Rinzler, "Transparent, conductive carbon nanotube films.," *Science*, vol. 305, pp. 1273–6, 2004.
- [213] Q. Cao, S.-H. Hur, Z.-T. Zhu, Y. G. Sun, C.-J. Wang, M. A. Meitl, M. Shim, and J. A. Rogers, "Highly Bendable, Transparent Thin-Film Transistors That Use Carbon-Nanotube-Based Conductors and Semiconductors with Elastomeric Dielectrics," *Adv. Mater.*, vol. 18, pp. 304–309, 2006.
- [214] D. Zhang, K. Ryu, Xi.Liu, E. Polikarpov, J. Ly, Mark E. Thompson, and C. Zhou, "Transparent, Conductive, and Flexible Carbon Nanotube Films and Their Application in Organic Light-Emitting Diodes," *Nano Lett.*, vol. 6, pp. 1880–1886, 2006.
- [215] M. B. Jakubinek, M. A. White, G. Li, C. Jayasinghe, W. Cho, M. J. Schulz, and V. Shanov, "Thermal and electrical conductivity of tall, vertically aligned carbon nanotube arrays," *Carbon N. Y.*, vol. 48, pp. 3947–3952, 2010.
- [216] A. D. Pasquier, H. E. Unalan, A. Kanwal, S. Miller, and M. Chhowalla, "Conducting and transparent single-wall carbon nanotube electrodes for polymer-fullerene solar cells," *Appl. Phys. Lett.*, vol. 87, p. 203511, 2005.
- [217] M. W. Rowell, M. a. Topinka, M. D. McGehee, H.-J. Prall, G. Dennler, N. S. Sariciftci, L. Hu, and G. Gruner, "Organic solar cells with carbon nanotube network electrodes," *Appl. Phys. Lett.*, vol. 88, p. 233506, 2006.
- [218] J. De Lagemaat, T. Barnes, G. Rumbles, T. Coutts, S. Shaheen, C. Weeks, P. Glatkowski, I. Levitsky, and J. Peltola, "Efficient Organic Excitonic Solar Cells with Carbon Nanotubes Replacing In₂O₃:Sn as the Transpar-

- ent Electrode,” in *IEEE 4th World Conf. Photovolt. Energy Conf.*, vol. 1, pp. 183–185, Ieee, 2006.
- [219] R. C. Tenent, T. M. Barnes, J. D. Bergeson, A. J. Ferguson, B. To, L. M. Gedvilas, M. J. Heben, and J. L. Blackburn, “UltrasMOOTH, Large-Area, High-Uniformity, Conductive Transparent Single-Walled-Carbon-Nanotube Films for Photovoltaics Produced by Ultrasonic Spraying,” *Adv. Mater.*, vol. 21, pp. 3210–3216, 2009.
- [220] T. M. Barnes, J. D. Bergeson, R. C. Tenent, B. a. Larsen, G. Teeter, K. M. Jones, J. L. Blackburn, and J. van de Lagemaat, “Carbon nanotube network electrodes enabling efficient organic solar cells without a hole transport layer,” *Appl. Phys. Lett.*, vol. 96, p. 243309, 2010.
- [221] D. Y. L. Won Jae Lee, Easwaramoorthi Ramasamy and J. S. Song, “Efficient Dye-Sensitized Solar Cells with Catalytic Multiwall Carbon Nanotube Counter Electrodes,” *ACS Appl. Mater. Interfaces*, no. 6, pp. 1145–1149, 2009.
- [222] V. C. Tung, L.-M. Chen, M. J. Allen, J. K. Wassei, K. Nelson, R. B. Kaner, and Y. Yang, “Low-Temperature Solution Processing of Graphene-Carbon Nanotube Hybrid Materials for High-Performance Transparent Conductors,” *Nano Lett.*, vol. 9, pp. 1949–1955, 2009.
- [223] P. J. King, U. Khan, M. Lotya, S. De, and J. N. Coleman, “Improvement of transparent conducting nanotube films by addition of small quantities of graphene,” *ACS Nano*, vol. 4, pp. 4238–46, 2010.
- [224] Q. Zhang, X. Wan, F. Xing, L. Huang, G. Long, N. Yi, W. Ni, Z. Liu, J. Tian, and Y. Chen, “Solution-processable graphene mesh transparent electrodes for organic solar cells,” *Nano Res.*, vol. 6, pp. 478–484, 2013.

- [225] I. Janowska, K. Chizari, O. Ersen, S. Zafeiratos, D. Soubane, V. D. Costa, V. Speisser, C. Boeglin, M. Houllé, D. Bégin, D. Plee, M.-J. Ledoux, and C. Pham-Huu, “Microwave synthesis of large few-layer graphene sheets in aqueous solution of ammonia,” *Nano Res.*, vol. 3, pp. 126–137, 2010.
- [226] T. T. Thanh, H. Ba, L. Truong-Phuoc, J.-M. Nhut, O. Ersen, D. Begin, I. Janowska, D. L. Nguyen, P. Granger, and C. Pham-Huu, “A few-layer graphene-graphene oxide composite containing nanodiamonds as metal-free catalysts,” *J. Mater. Chem. A*, vol. 2, p. 11349, 2014.
- [227] F. Smith, “Measurement of sheet resistivities with four-point probe,” *Bell Syst. Tech. Journal*, p. 711, 1958.
- [228] L. van der Pauw, “A method of measuring specific resistivity and Hall effect of discs of arbitrary shape. Philips Research Reports 13:,” tech. rep., 1958.
- [229] R. Green, “Hall Effect Measurements in Materials Characterization Who Needs to Measure Hall Effect ? Growing Interest in the Use of Hall Effect Measurements,” 1879.
- [230] E. H. Hall, “On a New Action of the Magnet on Electric Currents,” *Am. J. Math.*, vol. 2, pp. 287–292, 1879.
- [231] J. Wang, K. K. Manga, Q. Bao, and K. P. Loh, “High-Yield Synthesis of Few-Layer Graphene Flakes through Electrolyte,” *J. Am. Chem. Soc.*, vol. 133, pp. 8888–8891, 2011.
- [232] A. Malesevic, R. Vitchev, K. Schouteden, A. Volodin, L. Zhang, G. V. Tendeloo, A. Vanhulsel, and C. V. Haesendonck, “Synthesis of few-layer graphene via microwave plasma-enhanced chemical vapour deposition,” *Nanotechnology*, vol. 19, p. 305604, 2008.

- [233] Z. Luo, J. Shang, S. Lim, D. Li, Q. Xiong, Z. Shen, J. Lin, and T. Yu, “Modulating the electronic structures of graphene by controllable hydrogenation,” *Appl. Phys. Lett.*, vol. 97, p. 233111, 2010.
- [234] A. Benayad, H.-J. Shin, H. K. Park, S.-M. Yoon, K. K. Kim, M. H. Jin, H.-K. Jeong, J. C. Lee, J.-Y. Choi, and Y. H. Lee, “Controlling work function of reduced graphite oxide with Au-ion concentration,” *Chem. Phys. Lett.*, vol. 475, pp. 91–95, 2009.
- [235] Jin Ok Hwang, Ji Sun Park, Dong Sung Choi, Ju Young Kim, Sun Hwa Lee, Kyung Eun Lee, Yong-Hyun Kim, Myoung Hoon Song, Se-unghyup Yoo, and Sang Ouk Kim, “Workfunction-Tunable, N-Doped Reduced Graphene Transparent Electrodes for High-Performance Polymer Light-Emitting Diodes,” *ACS Nano*, vol. 6, pp. 159–167, 2012.
- [236] Derek J. Gardiner, Pierre R. Graves, *Practical Raman Spectroscopy*. Berlin: Springer-Verlag, 1989.
- [237] C Ghimbeu, C Decaux, P Brender, M Dahbi, D Lemordant, E Raymundo-pinero, M Anouti, F Beguin, C Vix-guterl, “Influence of Graphite Characteristics on the Electrochemical Performance in Alkylcarbonate LiTFSI Electrolyte for Li-Ion Capacitors and Li-Ion Batteries,” *J. Electrochem. Soc.*, vol. 160, pp. A1907–A1915, 2013.
- [238] G. Gavrilov, A. Krivchitch, and V. Lebedev, “Application of nuclear reaction analysis for aging investigations of detectors,” *Nucl. Instruments Methods Phys. Res. Sect. A Accel. Spectrometers, Detect. Assoc. Equip.*, vol. 515, pp. 108–117, 2003.
- [239] M. S. Moldovan, Y. J. Dappe, I. Janowska, C. Pham-huu, O. Ersen, and M. Simona Moldovan, Herve Bulou, Yannick J. Dappe, Izabela Janowska,

- Dominique Begin, Cuong Pham-Huu, and Ovidiu Ersen, "On the Evolution of Pt Nanoparticles on Few-Layer Graphene Supports in the High-Temperature Range," *J. Phys. Chem. C*, vol. 116, pp. 9274–9282, 2012.
- [240] G. L. Becker, J. A., Green, C. B. and Pearson, "Properties and Uses of Thermistors- Thermally Sensitive Resistors," *Bell Syst. Tech. Journal*, Vol., vol. 65, pp. 170–212, 1947.
- [241] C. Dimitrakopoulos, M. Freitag, and P. Avouris, "Layer Number Determination and Thickness-Dependent Properties of Graphene Grown on SiC," *IEEE Trans. Nanotechnol.*, vol. 10, pp. 1196–1201, 2011.
- [242] V. Coropceanu, A. Demetrio, S. Filho, Y. Olivier, R. Silbey, and J.-l. Bre, "Charge Transport in Organic Semiconductors," *Chem. Rev.*, vol. 107, pp. 926–952, 2007.
- [243] G. Melinte, I. Florea, S. Moldovan, I. Janowska, W. Baaziz, R. Arenal, A. Wisnet, C. Scheu, S. Begin-Colin, D. Begin, C. Pham-Huu, and O. Ersen, "A 3D insight on the catalytic nanostructuration of few-layer graphene.," *Nat. Commun.*, vol. 5, p. 4109, 2014.
- [244] H. Malekpour, K.-H. Chang, J.-C. Chen, C.-Y. Lu, D. L. Nika, K. S. Novoselov, and A. A. Balandin, "Thermal conductivity of graphene laminate," *Nano Lett.*, vol. 14, pp. 5155–61, 2014.
- [245] X. Xiao, P. Liu, J. S. Wang, M. Verbrugge, and M. P. Balogh, "Vertically aligned graphene electrode for lithium ion battery with high rate capability," *Electrochem. commun.*, vol. 13, pp. 209–212, 2011.
- [246] C.-H. Liu and X. Yu, "Silver nanowire-based transparent, flexible, and conductive thin film.," *Nanoscale Res. Lett.*, vol. 6, p. 75, Jan. 2011.
- [247] A. A. Pirzado, L. Truong-Phuoc, V. Papaefthimiou, C. Matei Ghimbeu, F. Le Normand, H. Ba, T. Thanh-Tung, C. Pham-Huu, and I. Janowska,

- “Activation of few layer graphene by μ W-assisted oxidation in water via formation of nanoballs -Support for platinum nanoparticles,” *J. Colloid Interface Sci.*, vol. 451, pp. 221–230, 2015.
- [248] K. C. Kwon, K. S. Choi, B. J. Kim, J.-l. Lee, and S. Y. Kim, “Work-Function Decrease of Graphene Sheet Using Alkali Metal Carbonates,” *J. Phys. Chem. C*, vol. 116, pp. 26586–26591, 2012.
- [249] A. A. Pirzado, Y. Jouane, F. Le Normand, R. Akilimali, V. Papaefthimiou, C. Matei Ghimbeu and I. Janowska, “Electrical Transport in Few Layer Graphene Film Prepared by Hot-Spray Technique; the Effect of Thermal Treatment.,” *J. Phys. Chem. C*, vol. 118, pp. 873–880, 2014.
- [250] J. Menéndez, A. Arenillas, B. Fidalgo, Y. Fernández, L. Zubizarreta, E. Calvo, and J. Bermúdez, “Microwave heating processes involving carbon materials,” *Fuel Process. Technol.*, vol. 91, pp. 1–8, 2010.
- [251] A. B. Bourlinos, V. Georgakilas, R. Zboril, T. a. Steriotis, and A. K. Stubos, “Liquid-phase exfoliation of graphite towards solubilized graphenes.,” *Small*, vol. 5, pp. 1841–5, 2009.
- [252] A. Celzard, E. McRae, J.F. Mareche, G. Furdin, M. Dufort, C. Deleuze, “Composites based on micron-sized exfoliated graphite particles: electrical conduction, critical exponents and anisotropy,” *J. Phys. Chem. Solids*, vol. 57, pp. 715–718, 1996.
- [253] Hassan M. A. Hassan, A Victor Abdelsayed, A Abd El Rahman S. Khder, A Khaled M. AbouZeid, A James Turner, A M. Samy El-Shall, A Saud I. Al-Resayesb and Adel A. El-Azhary B, “Microwave synthesis of graphene sheets supporting metal nanocrystals in aqueous and organic media,” *J. Mater. Chem.*, vol. 19, p. 3832, 2009.

- [254] V. Lopez, R. S. Sundaram, C. Gomez-Navarro, D. Olea, M. Burghard, J. Gomez-Herrero, F. Zamora, and K. Kern, "Chemical Vapor Deposition Repair of Graphene Oxide: A Route to Highly-Conductive Graphene Monolayers," *Adv. Mater.*, vol. 21, pp. 4683–4686, 2009.
- [255] D. K. Ferry, "Short-range potential scattering and its effect on graphene mobility," *J. Comput. Electron.*, vol. 12, pp. 76–84, 2013.
- [256] S. Saha, O. Kahya, M. Jaiswal, A. Srivastava, A. Annadi, J. Balakrishnan, A. Pachoud, C.-T. Toh, B.-H. Hong, J.-H. Ahn, T. Venkatesan, and B. Özyilmaz, "Unconventional transport through graphene on SrTiO: a plausible effect of SrTiO phase-transitions," *Sci. Rep.*, vol. 4, p. 6173, 2014.
- [257] H. Hu, Z. Zhao, Q. Zhou, Y. Gogotsi, and J. Qiu, "The role of microwave absorption on formation of graphene from graphite oxide," *Carbon N. Y.*, vol. 50, pp. 3267–3273, 2012.
- [258] V. Penmatsa, T. Kim, M. Beidaghi, H. Kawarada, L. Gu, Z. Wang, and C. Wang, "Three-dimensional graphene nanosheet encrusted carbon micropillar arrays for electrochemical sensing," *Nanoscale*, vol. 4, p. 3673, 2012.
- [259] V. Datsyuk, M. Kalyva, K. Papagelis, J. Parthenios, D. Tasis, A. Siokou, I. Kallitsis, and C. Galiotis, "Chemical oxidation of multiwalled carbon nanotubes," *Carbon N. Y.*, vol. 46, pp. 833–840, 2008.
- [260] V. Mani, S.-m. Chen, and B.-s. Lou, "Three Dimensional Graphene Oxide-Carbon Nanotubes and Graphene-Carbon Nanotubes Hybrids," *Int. J. Electrochem. Sci.*, vol. 8, pp. 11641–11660, 2013.
- [261] Y.-K. Kim and D.-H. Min, "Durable large-area thin films of graphene/carbon nanotube double layers as a transparent electrode," *Langmuir*, vol. 25, pp. 11302–6, 2009.

- [262] T. Mihara, Shota; Tsubota, Toshiki; Murakami, Naoya; Ohno, “Improvement of Electrical Conductivity While Maintaining a High-Transmittance of Graphene Oxide/MWCNT Film by Hydrazine Reduction,” *J. Nanosci. Nanotechnol.*, vol. 12, pp. 6930–6934(5), 2012.
- [263] W. Su, T. Leung, and C. Chan, “Work function of single-walled and multiwalled carbon nanotubes: First-principles study,” *Phys. Rev. B*, vol. 76, p. 235413, 2007.
- [264] Z. P. Ruiping Gao¹ and Z. L. Wang¹, “Work function at the tips of multiwalled carbon nanotubes,” *Appl. Phys. Lett.*, vol. 78, p. 1757, 2001.
- [265] S. Nam, M. Song, D.-H. Kim, B. Cho, H. M. Lee, J.-D. Kwon, S.-G. Park, K.-S. Nam, Y. Jeong, S.-H. Kwon, Y. C. Park, S.-H. Jin, J.-W. Kang, S. Jo, and C. S. Kim, “UltrasMOOTH, extremely deformable and shape recoverable Ag nanowire embedded transparent electrode,” *Sci. Rep.*, vol. 4, p. 4788, 2014.
- [266] J. T. Littleton, “INSULATOR (OCR),” 1938.
- [267] J. M. Mochel, “ELECTRICALLY CONDUCTING COATING ON GLASS AND OTHER CERAMIC BODIES,” 1951.
- [268] “ITO Transparent Conductive Film http://www.tdk.co.jp/techjournal_e/vol17_itofilm/contents03.htm,” 2014.
- [269] E. Arca, K. Fleischer, and I. V. Shvets, “Magnesium, nitrogen codoped Cr₂O₃: A p-type transparent conducting oxide,” *Appl. Phys. Lett.*, vol. 99, p. 111910, 2011.
- [270] D. R. Cairns, R. P. W. Li, D. K. Sparacin, S. M. Sachsman, D. C. Paine, and G. P. Crawford, “Strain-dependent electrical resistance of tin-doped indium oxide on polymer substrates,” vol. 76, pp. 2000–2002, 2000.

- [271] M. A. Green, "Estimates of Te and In Prices from Direct Mining of Known Ores," *Prog. Photovoltaics Res. Appl.*, vol. 17, pp. 347–359, 2009.
- [272] U.S. Geological Survey, "MINERAL COMMODITY SUMMARIES 2012," tech. rep., Virginia, 2012.
- [273] A. M. Alfantazi and R. R. Moskalyk, "Processing of indium: a review," *Miner. Eng.*, vol. 16, pp. 687–694, 2003.
- [274] D. Bleiwas, "Byproduct Mineral Commodities Used for the Production of Photovoltaic Cells Circular 1365," tech. rep., U.S. Geological Survey, Virginia, 2010.
- [275] "Mapping resource prices : the past and the future Final report," tech. rep., ECORYS Nederland BV, Rotterdam, 2012.
- [276] "Transparent Conductive Film ELECRYSTA
<http://www.nitto.com/jp/en/products/group/optical/structure/009/>," 2014.
- [277] V. Arivazhagan and S. Rajesh, "Influence of In / Sn ratio on nanocrystalline indium tin oxide thin films by spray pyrolysis method," *Arch. Phys. Res.*, vol. 2, pp. 19–25, 2011.
- [278] M. Sandoval-Paz and R. Ramírez-Bon, "Indium tin oxide films deposited on polyethylene naphthalate substrates by radio frequency magnetron sputtering," *Thin Solid Films*, vol. 517, pp. 2596–2601, Feb. 2009.
- [279] C. O. Dwyer, M. Szachowicz, G. Visimberga, V. Lavayen, S. B. Newcomb, and C. M. S. Torres, "Bottom-up growth of fully transparent contact layers of indium tin oxide nanowires for light- emitting devices," *Nat. Nanotechnology*, vol. 4, pp. 239–244, 2009.

- [280] M. Yamaguchi, A. Ide-Ektessabi, H. Nomura, and N. Yasui, “Characteristics of indium tin oxide thin films prepared using electron beam evaporation,” *Thin Solid Films*, vol. 447-448, pp. 115–118, 2004.
- [281] K. Maruyama, Toshiro and Fukui, “Indium tin oxide thin films prepared by chemical vapor deposition,” *J. Appl. Phys.*, vol. 70, pp. 3848–3851, 1999.
- [282] H. Mbarek, M. Saadoun, and B. Bessaïs, “Porous screen printed indium tin oxide (ITO) for NO_x gas sensing,” *Phys. Status Solidi*, vol. 4, pp. 1903–1907, 2007.
- [283] K. A. Sierros, D. R. Cairns, J. S. Abell, and S. N. Kukureka, “Pulsed laser deposition of indium tin oxide films on flexible polyethylene naphthalate display substrates at room temperature,” *Thin Solid Films*, vol. 518, pp. 2623–2627, 2010.
- [284] Sutapa Roy Ramanan, “Dip coated ITO thin-films through sol-gel process using metal salts,” *Thin Solid Films*, vol. 389, pp. 207–212, 2001.
- [285] S. Heusing, P. de Oliveira, E. Kraker, A. Haase, C. Palfinger, and M. Veith, “Wet chemical deposited ITO coatings on flexible substrates for organic photodiodes,” *Thin Solid Films*, vol. 518, pp. 1164–1169, 2009.
- [286] Q. Wan, E. N. Dattoli, W. Y. Fung, W. Guo, Y. Chen, X. Pan, and W. Lu, “High-performance transparent conducting oxide nanowires,” *Nano Lett.*, vol. 6, pp. 2909–15, 2006.
- [287] T. Minami, “Substitution of transparent conducting oxide thin films for indium tin oxide transparent electrode applications,” *Thin Solid Films*, vol. 516, pp. 1314–1321, 2008.
- [288] J. V. Deelen, A. Illiberi, A. Hovestad, I. Barbu, L. Klerk, and P. Buskens, “Transparent conducting materials : overview and recent results,” in *SPIE, Thin Film Sol. Technol.*, vol. 8470, pp. 84700P–1–84700P–8, 2012.

- [289] Y.-S. Hsiao, W.-T. Whang, C.-P. Chen, Y.-C. Chen, "High-conductivity poly(3,4-ethylenedioxythiophene):poly(styrene sulfonate) film for use in ITO-free polymer solar cells,," *J. Mater. Chem.*, vol. 2008, pp. 5948–5955, 18.
- [290] E. Ahlswede, W. Mußhlheisen, M. W. bin Moh Wahi, J. Hanisch, and M. Powalla, "Highly efficient organic solar cells with printable low-cost transparent contacts," *Appl. Phys. Lett.*, vol. 92, p. 143307, 2008.
- [291] F. Krebs, "Fabrication and processing of polymer solar cells: a review of printing and coating techniques," *Sol. Energy Mater. Sol. Cells*, vol. 93, pp. 394–412, 2009.
- [292] C. J. Emmott, A. Urbina, and J. Nelson, "Environmental and economic assessment of ITO-free electrodes for organic solar cells," *Sol. Energy Mater. Sol. Cells*, vol. 97, pp. 14–21, 2012.
- [293] P. B. Y. Galagan, J.-E.J.M. Rubingh, R. Andriessen, C.-C. Fan and J. K. S.C. Veenstra, "ITO-free flexible organic solar cells with printed current collecting grids," *Sol. Energy Mater. Sol. Cells*, vol. 95, pp. 1339–1343, 2011.
- [294] P. P. W. Gaynor, G.F. Burkhard, M.D. McGehee, "Smooth nanowire/ polymer composite transparent electrodes," *Adv. Mater.*, vol. 23, pp. 2905–2910., 2011.
- [295] S.-I. Na, G. Wang, S.-S. Kim, T.-W. Kim, S.-H. Oh, B.-K. Yu, T. Lee, D.-Y. Kim, "Evolution of nanomorphology and anisotropic conductivity in solventmodified PEDOT:PSS films for polymeric anodes of polymer solar cells,," *J. Mater. Chem.*, vol. 19, pp. 9045–9053, 2009.
- [296] Y.-F. Lim, S. Lee, D. J. Herman, M. T. Lloyd, J. E. Anthony, and G. G. Malliaras, "Spray-deposited poly(3,4-

- ethylenedioxythiophene):poly(styrenesulfonate) top electrode for organic solar cells,” *Appl. Phys. Lett.*, vol. 93, p. 193301, 2008.
- [297] J. G. Tait, B. J. Worfolk, S. A. Maloney, T. C. Hauger, A. L. Elias, J. M. Buriak, and K. D. Harris, “Spray coated high-conductivity PEDOT:PSS transparent electrodes for stretchable and mechanically-robust organic solar cells,” *Sol. Energy Mater. Sol. Cells*, vol. 110, pp. 98–106, 2013.
- [298] D. S. Ghosh, L. Martinez, S. Giurgola, P. Vergani, and V. Pruneri, “Widely transparent electrodes based on ultrathin metals,” *Opt. Lett.*, vol. 34, pp. 325–7, 2009.
- [299] Matthias Fahland, T. Vogt, W. Schoenberger, N. Schiller, “Optical properties of metal based transparent electrodes on polymer films,” *Thin Solid Films*, vol. 516, pp. 5777–5780, 2008.
- [300] M.-G. Kang and L. J. Guo, “Nanoimprinted Semitransparent Metal Electrodes and Their Application in Organic Light-Emitting Diodes,” *Adv. Mater.*, vol. 19, pp. 1391–1396, 2007.
- [301] M.-g. Kang, H. J. Park, S. H. Ahn, T. Xu, and L. J. Guo, “Toward Low-Cost, High-Efficiency, and Scalable Organic Solar Cells with Transparent Metal Electrode and Improved Domain Morphology,” *IEEE J. Sel. Top. QUANTUM Electron.*, vol. 16, pp. 1807 – 1820, 2010.
- [302] M.-G. Kang, M.-S. Kim, J. Kim, and L. J. Guo, “Organic Solar Cells Using Nanoimprinted Transparent Metal Electrodes,” *Adv. Mater.*, vol. 20, pp. 4408–4413, 2008.
- [303] Sukanta De, Thomas M. Higgins, Philip E. Lyons, Evelyn M. Doherty, Peter N. Nirmalraj, Werner J. Blau, John J. Boland and Jonathan N. Coleman, “Silver Nanowire Networks as Flexible, Transparent, Conducting Films:

- Extremely High DC to Optical Conductivity Ratios,” *ACS Nano*, vol. 3, pp. 1767–1774, 2009.
- [304] Daniel Azulai, Tatyana Belenkova, Hagit Gilon, Zahava Barkay and Gil Markovich, “Transparent Metal Nanowire Thin Films Prepared in Mesostructured Templates,” *Nano Lett.*, vol. 9, pp. 4246–4249, 2009.
- [305] Po-Chun Hsu, Shuang Wang, Hui Wu, Vijay K. Narasimhan, Desheng Kong, Hye Ryoung Lee & Yi Cui, “Performance enhancement of metal nanowire transparent conducting electrodes by mesoscale metal wires,” *Nat. Commun.*, vol. 4, pp. 1–7, 2013.
- [306] Y. Chang , M. L. Lye, H. C. Zeng, “Large-Scale Synthesis of High-Quality Ultralong Copper Nanowires,” *Langmuir*, vol. 21, pp. 3746–3748, 2005.
- [307] J. Zou, H.-L. Yip, S. K. Hau, and A. K.-Y. Jen, “Metal grid/conducting polymer hybrid transparent electrode for inverted polymer solar cells,” *Appl. Phys. Lett.*, vol. 96, p. 203301, 2010.
- [308] J. J. Takehiro Tokuno, Masaya Nogi and K. Suganuma, “Hybrid transparent electrodes of silver nanowires and carbon nanotubes: a low-temperature solution process,” *Nanoscale Res. Lett.*, vol. 7, p. 281, 2012.
- [309] Jin-A. Jeong, Jihoon Kim, Han-Ki Kim, “Ag grid/ITO hybrid transparent electrodes prepared by inkjet printing,” *Sol. Energy Mater. Sol. Cells*, vol. 95, pp. 1974–1978, 2011.
- [310] P. Lin, W. C. H. Choy, D. Zhang, F. Xie, J. Xin, and C. W. Leung, “Semi-transparent organic solar cells with hybrid monolayer graphene/metal grid as top electrodes,” *Appl. Phys. Lett.*, vol. 102, p. 113303, 2013.
- [311] Sung Man Kim, Bright Walker, Jung Hwa Seo and Seong Jun Kang, “Hybrid Transparent Conductive Films of Multilayer Graphene and Metal Grid for Organic Photovoltaics,” *J. Appl. Phys.*, vol. 52, p. 5103, 2013.

- [312] J. S. Woo, J. T. Han, S. Jung, J. I. Jang, H. Y. Kim, H. J. Jeong, S. Y. Jeong, K.-J. Baeg, and G.-W. Lee, “Electrically robust metal nanowire network formation by in-situ interconnection with single-walled carbon nanotubes.,” *Sci. Rep.*, vol. 4, p. 4804, 2014.
- [313] B. Murali, D.-G. Kim, J.-W. Kang, and J. Kim, “Inkjet-printing of hybrid transparent conducting electrodes for organic solar cells,” *Phys. Status Solidi*, vol. 211, pp. 1801–1806, 2014.
- [314] M. Song, H. Park, S. Kim, D.-h. Kim, Y.-c. Kang, and S.-h. Jin, “Highly flexible and transparent conducting silver nanowires / ZnO composite film for organic solar cells,” *Nano Res*, vol. 7, pp. 1370–1379, 2014.
- [315] G. Jo, M. Choe, S. Lee, W. Park, Y. H. Kahng, and T. Lee, “The application of graphene as electrodes in electrical and optical devices.,” *Nanotechnology*, vol. 23, p. 112001, 2012.
- [316] W. A. D. Heer, C. Berger, M. Ruan, M. Sprinkle, X. Li, Y. Hu, and B. Zhang, “Large area and structured epitaxial graphene produced by confinement controlled sublimation of silicon carbide,” in *PNAS*, vol. 108, pp. 16900–16905, 2011.
- [317] L. C. Isett, J.M. Blakely, “Segregation Isosteres for Carbon at the (100) Surface of Nickel,” *Surf. Sci.*, vol. 58, pp. 397–414, 1976.
- [318] C. Enderlein, *Graphene and its Interaction with Different Substrates Studied by Angular-Resolved Photoemission Spectroscopy*. PhD thesis, 2010.
- [319] C. Riedl, C. Coletti, T. Iwasaki, A. A. Zakharov, and U. Starke, “Quasi-Free-Standing Epitaxial Graphene on SiC Obtained by Hydrogen Intercalation,” *Phys. Rev. Lett.*, vol. 103, p. 246804, 2009.
- [320] B. Alexander, E. K. Michael, “Pyrolytic Formation of Highly Crystalline Graphite Films,” *J. Appl. Phys.*, vol. 37, pp. 2179–2181, 1966.

- [321] A. A. Obraztsov, A. N. Obraztsova, E. A. Tyurnina, A. V. Zolotukhin, “Chemical vapor deposition of thin graphite films of nanometer thickness,” *Carbon N. Y.*, vol. 45, pp. 2017–2021, 2007.
- [322] X. Li, W. Cai, J. An, S. Kim, J. Nah, D. Yang, R. Piner, A. Velamakanni, I. Jung, E. Tutuc, S. K. Banerjee, L. Colombo, and R. S. Ruoff, “Large-area synthesis of high-quality and uniform graphene films on copper foils,” *Science*, vol. 324, pp. 1312–4, 2009.
- [323] J. M. Eizenberg, M. Blakely, “Carbon monolayer phase condensation on Ni(111),” *Surf. Sci.*, vol. 82, pp. 228–236., 1979.
- [324] V. Yong and H. T. Hahn, “Graphene growth with giant domains using chemical vapor deposition,” *CrystEngComm*, vol. 13, p. 6933, 2011.
- [325] T. Kobayashi, M. Bando, N. Kimura, K. Shimizu, K. Kadono, N. Umezu, K. Miyahara, S. Hayazaki, S. Nagai, Y. Mizuguchi, Y. Murakami, and D. Hobara, “Production of a 100-m-long high-quality graphene transparent conductive film by roll-to-roll chemical vapor deposition and transfer process,” *Appl. Phys. Lett.*, vol. 102, p. 023112, 2013.
- [326] M. Choucair, P. Thordarson, and J. A. Stride, “Gram-scale production of graphene based on solvothermal synthesis and sonication,” *Nat. Nanotech.*, vol. 4, pp. 30–33, 2009.
- [327] O. D. Jurchescu, J. Baas, and T. T. M. Palstra, “Effect of impurities on the mobility of single crystal pentacene,” *Appl. Phys. Lett.*, vol. 84, p. 3061, 2004.
- [328] I. McCulloch, M. Heeney, C. Bailey, K. Genevicius, I. Macdonald, M. Shkunov, D. Sparrowe, S. Tierney, R. Wagner, W. Zhang, M. L. Chabiny, R. J. Kline, M. D. McGehee, and M. F. Toney, “Liquid-

- crystalline semiconducting polymers with high charge-carrier mobility,” *Nat. Mater.*, vol. 5, pp. 328–33, 2006.
- [329] P. Lienerth, *Elaboration and characterization of field-effect transistors based on organic molecular wires for chemical sensing applications*. PhD thesis, University of Strasbourg, 2014.
- [330] D. B. Farmer, R. Golizadeh-Mojarad, V. Perebeinos, Y. S. Lin, Tulevski G., J. C. Tsang, and P. Avouris, “Chemical doping and electron-hole conduction asymmetry in graphene devices,” *Nano Lett.*, vol. 9, pp. 388–392, 2009.
- [331] L. A. Majewski, R. Schroeder, and M. Grell, “Low-Voltage, High-Performance Organic Field-Effect Transistors with an Ultra-Thin TiO₂ Layer as Gate Insulator,” *Adv. Funct. Mater.*, vol. 15, pp. 1017–1022, 2005.
- [332] D. Zielke, A. C. Humblert, U. Hahn, N. Brandt, M. Bartzsch, U. Fußlgmann, T. Fischer, J. Veres, and S. Ogier, “Polymer-based organic field-effect transistor using offset printed source/drain structures,” *Appl. Phys. Lett.*, vol. 87, p. 123508, 2005.
- [333] S. V. Novikov, “Hopping charge transport in organic materials,” *Russ. J. Electrochem.*, vol. 48, pp. 388–400, 2012.
- [334] L.-B. Lin, C.-W. Cheng, C.-A. Dai, and Y.-P. Lee, “Extrinsic charge traps in disordered organic materials,” *J. Appl. Phys.*, vol. 112, p. 073715, 2012.

8 Appendix

8.1 ITO and Related TCOs

ITO consists of 90/10 atomic ratio of indium (III) oxide (In_2O_3) and tin (IV) oxide (SnO_2). Several other metal oxide combinations as Indium (In_2O_3), Tin (SnO_2) and Zinc (ZnO); Gallium doped Zinc Oxide (GZO) and Fluorine doped Tin Oxide (FTO), have been used as TCEs during last several decades. TCOs have been under investigation since 1930s. The experiments by Corning laboratories team working on metal oxide insulators lead accidentally to transparent conductor electrodes in 1930s (US Patent 2118795, filed Sept. 21, 1931) [266]. Later, an other patent was deposited by them with some advancements explaining the mixture of Indium and Tin in 1940s (US Patent 2564707) [267]. The observation of strong midnight blue color of the mixture encouraged the scientists at Corning to spend more effort into it[2]. Later, with the advent of transistor, integrated circuits and fabrication technologies and techniques, the demand for the devices with transparent electrodes came in to the limelight. Over the next few decades, thin and thick films of several metal oxides were grown by various physical and chemical methods. Film preparation techniques have grown over to be mature since the first studies of TCO deposition. Chemical Vapor Deposition (CVD), magnetron sputtering, pulsed laser deposition (PLD) and spray pyrolysis, are the common deposition techniques at the forefront of the growth of thin transparent and conducting films [4]. Thus, these developments accelerate the race to find optimum performance of transparent conductors. Soon, TCEs become the commercially available on the market. The TCE market is ever-increasing by 10-20 % since two decades. Figure 8.1 shows some of the most common film coating/deposition methods used today [268].

Figure 8.2 shows the basic principles of ITO film coating via physical vapor

□ Main coating generation methods

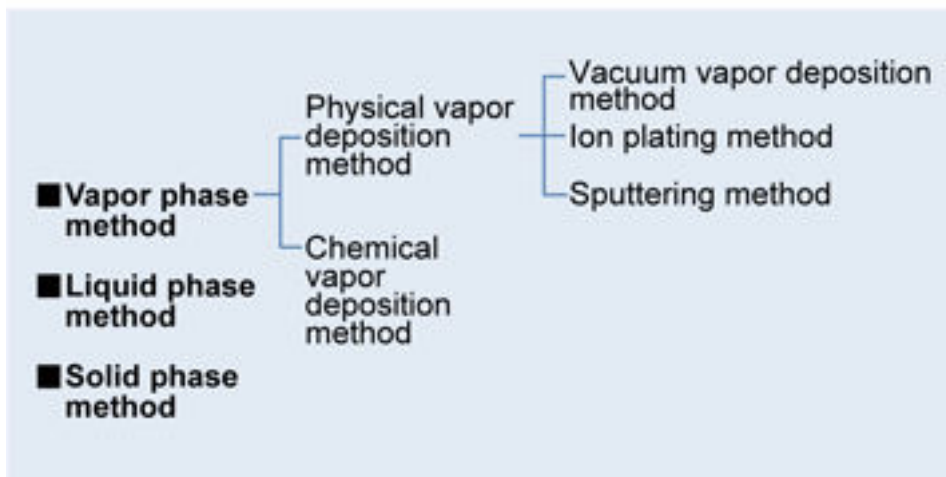
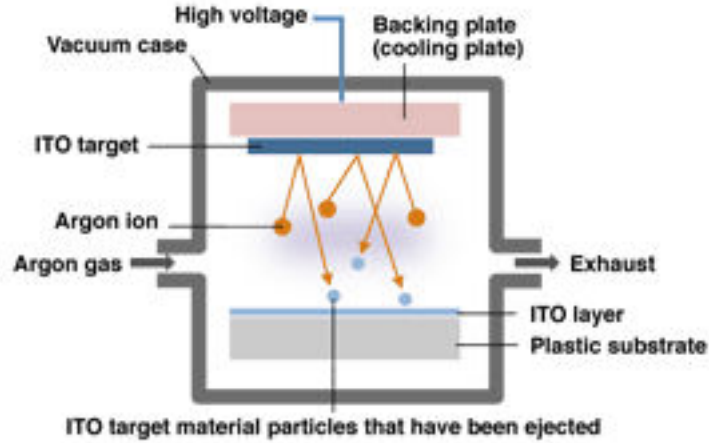


Figure 8.1: Main coating generation methods (Courtesy TDK Corporation) [268].

deposition (PVD) technique by sputtering the ions of ITO target on the flexible Polyethylene terephthalate (sometimes written poly(ethylene terephthalate and commonly abbreviated PET) substrate. PVD is a technique that employs an inert gas (e.g. Argon) which is charged and behaves as plasma inside the vacuum chamber. The ions of plasma are excited by high voltage which collide onto the surface of target (ITO in this case) with high kinetic energy. This causes the particles from target to eject and travel towards the substrate. The substrate usually is down, so the particles fall down and settle on the substrate forming a thin film. This action is called sputtering of particles.

Among other criteria, the Work function of TCO plays an important role to harness the charge in the organic solar cells. The work function is defined as the minimum energy required to remove an electron from the conduction band to the vacuum [4]. Thus, a suitable work function is important for collecting the charge at the interface of active layer and electrode in OSCs. Table 8.1 shows work function of few TCOs examples. Although most TCOs employed in the fabrication of solar cells are typically n-type semiconductors [3], p-type TCOs have been

□ Basic principles of ITO layer coating through the sputtering method



■ Sputtering method

A thin-film generation method that is classified as a PVD (physical vapor deposition) method. When a substrate is placed in a vacuum device and the ions collide on the target surface, the particles of the target material are ejected, fall down (sputter) and gather on the substrate, and form a thin-film.

Figure 8.2: Basic principles of ITO layer coating through sputtering method.

(Courtesy TDK Corporation) [268].

Table 8.1: Work functions of some transparent conductors [4].

Work Functions of Some Transparent Conductors.		
Material	Work Function (eV)	Electron Concentration (cm ⁻³)
ZnO:F	4.2	2×10^{20}
ZnO	4.5	7×10^{19}
In ₂ O ₃ :Sn	4.8	$>10^{20}$
SnO ₂ :F	4.9	4×10^{20}
ZnSnO ₃	5.3	6×10^{19}

reported as well [269]. Due to Indium paucity, rising demand of ITO in emerging applications and potential challenges make the ITO dominance questionable [2]. ITO is liable to cracks and brittleness at low cycles of bending/strain due to its ceramic character and unsuitability as a ductile material. A small strain of up to

3 % can seriously deteriorate the conductivity of ITO [270]. Repeated cyclic testing can severely degrade ITO by introducing micro cracks, propagating into the device employing ITO and eventually contribute to decreasing the device performance by the means of degradation of conductivity. Further, the environmental effects as salts, acids, humidity present in the device operating environment can affect the lifetime of ITO as TCO or device employing it. Due to these reasons, damage in the form of cracks of the film during manufacturing, handling, and device fabrication significantly leads to loss of expensive material and decreases the yield before the device approaches to the market. Even after the ITO film has reached the facility for device fabrication without damage, a risk of material damage during fabrication of organic solar cells or other devices can not be excluded. Due to its relatively higher index of refraction ($n \sim 2.0$), patterning on to lower index substrates and materials, leads to another potential problem of redundant reflection which can be solved by the use of anti-reflective coatings but not without increasing the fraction of the cost. However, for rigid devices, ITO is still the most viable option in the absence of alternatives at industrial stage. Most other TCOs still have to come up to the technological readiness.

The greatest challenge of ITO is associated with its preparation cost and film deposition of Indium and tin materials. Indium comprises approximately 75 % (compared to only 25% of tin) of the total mass of ITO electrode for LCD (which accounts for 83 % of Indium usage) touch screens, flat panel displays, semiconductors and OSCs [2, 271]. An massive 3/4 of total global consumption of Indium is consumed by ITO alone [272]. Indium is a rare metal (ranking 61st in abundance in the Earth's crust - about three times more abundant than silver or mercury), which comes largely as a byproduct of zinc ores' processing in China, Peru, and Australia (in decreasing order of quantity produced) [273, 274]. Alternate sources of Indium come from mining of tin, copper, lead, and precious metals. Common deposition technique for ITO is sputtering process which itself is inefficient with yield of 3-30 % (Indium reaching the substrate/film). About 70 % of ITO resides

in the spent ITO target and other parts of sputtering system [272]. Due to scarcity of Indium and fluctuation in the prices of Indium, ITO recycling is gaining more importance. However, the cost of recycling is influenced by the price of primary Indium. Further improvements in the processing technology and methods for recovery of Indium will help offset the Indium scarcity and price fluctuations but this Indium recovery and reclamation is still insufficient to achieve optimum and efficient recovery of good quality Indium [272], [275]. As deposition of ITO films is usually done by slow and costly vacuum-based techniques, and supply of indium which is prone to mining and geo-political issues, the prices have been unstable for Indium and ITO. The magnitude of price swings for indium during the last decade is important to note. The cost of indium increased ~ 5 times during last one and half decade (Source: Alex Freundlich of the University of Houston citing data from the U.S. Geological Survey) [2].

ITO manufacturers are concentrating also to resolve strain-induced propagatable micro-cracks issue in the ITO film [270]. It was reported that mechanical properties of ITO film may be improved by laminating it to an other PET substrate via optically clear adhesive [276] or by altering the ratio of Indium to tin. However, increasing the wt % of tin or reducing the wt % of Indium can affect the electro-optical properties of film [2]. It was demonstrated that band gap of the film increases with increasing the wt % of In, from 3.2 eV for the ratio 50:50 to 3.7 eV for In/Sn ratio of 80:20 for a film prepared by spray pyrolysis method, with >90 % transparency and best conductivity. The conductivity and transparency decrease with increase of Sn wt % [277]. Various film growth/deposition techniques such as spray pyrolysis, DC and RF magnetron sputtering, [278], molecular beam epitaxy (MBE), [279], electron beam evaporation (EBE) [280], chemical vapor deposition (CVD) [281] screen printing [282], pulsed laser deposition [283] and sol-gel spin-coated techniques [51] and dip coated through sol-gel [284] have been reported in order to reduce the cost and increase the yield of material being used. When ITO films are prepared by solvent-based process

they necessitate thermal annealing to improve the conductivity and transparency of the films by removing the traces of solvents, impurities and improving the structural quality of films [2]. ITO nanoparticles dispersed in solvent and deposited by gravure printing process exhibit a sheet resistance of $500 \Omega/\square$ after low temperature irradiation and thermal annealing steps [285]. ITO nanowires film with R_s close to $3k \Omega$ in device having transparency of 85 per cent was reported also [286]. Apart from nanomaterials, minimizing or excluding the amount/content of In in TCOs is under study. Low In content examples are $ZnO-In_2O_3$, $In_2O_3-SnO_2$, and $Zn-In-Sn-O$. Aluminum and Gallium doped Zinc Oxide (AZO, and GZO), and Fluorine doped tin oxide (FTO) have been used as TCOs without Indium. Although, these materials have cost benefit but they lag in opto-electronic properties. Electrical conductivity of thin films of AZO, GZO (less than 100 nm), fluctuates when exposed to air environment with high relative humidity, thus making thinner than 100 nm films unsuitable for humid environments [287]. However, due to the low cost of film preparation and suitable properties, fluorine doped SnO_2 and aluminum doped ZnO (AZO) are among the most widely used TCOs for thin film solar cells [288].

8.2 Other Candidates for TCEs

As GTCEs continue to provide alternative to TCEs, and the advancement in nano-materials assembly and control is pushing for several other alternatives. Conducting polymers, metal nanowires and printable metal grids have been studied for this purpose. Here, we will cover their material properties and suitability to function as TCEs in current/future optoelectronics especially OSCs. Conducting polymers have become a mature material which are used for various functions in organic solar cells, as active layer (P3HT:PCBM) and as buffer layers (PEDOT:PSS). A low-cost, solution-processable polymer mixture poly(3,4-ethylenedioxythiophene)/poly(styrenesulfonate) (PEDOT:PSS) is investigated

due to its flexibility, light weight, and compatibility with solution-based deposition techniques such as gravure printing, slot die coating, knife-over-edge, coating, slide coating, and spray coating [289],[290], [291]. The cost of PEDOT is much lower (two orders of magnitude lower) than that of ITO and the metal-base electrodes [12], [292]. The mixture of PEDOT:PSS have conductivity inferior to that of ITO, hence it is either doped or used in conjunction with metal grids [293], silver nanowires [294], and other additives [295]. PEDOT:PSS, one of the crucial layers which performs several key functions, such as, buffer layer placed between the cathode and the active layer. Its primary work is to serve as a hole transporter and electron blocking layer. Additionally, it also smooths out the ITO surface, acts as impermeable to oxygen and as cathode material thereby protecting active layer from oxidation and generation of unwanted trap sites [182]. Due to very good conductivity and relative transparency, it is also applied as electrode in organic solar cells. The first good replacement of ITO was demonstrated with an easily processable low-cost, spin coated transparent contacts based on high conductivity formulations of PEDOT:PSS anode in conventional OSC. The authors claimed that, up to 3 % efficiencies were possible to achieve with this method. This highlighted that PEDOT:PSS can be a very low-cost alternate to vacuum-deposited ITO [290]. A solar cell with spray-deposited PEDOT:PSS as cathode/top electrode was demonstrated in an attempt to replace the thermally evaporated metal electrode in an inverted P3HT:PCBM structure. The PEDOT:PSS layer showed R_s of 900 Ω /square and device achieved a PCE of 2.0 % [296].

In a recent study, it was pointed out that a multiple solvent ink containing Ethylen Glycol (EG) can contribute to enhance optoelectronic properties of PEDOT:PSS followed by post-deposition annealing of ink over PEDOT:PSS electrode. Sheet resistance of 24-259 Ω/\square with transparency of 71-95 % can be achieved and efficiency of 3.2 % was reported on a flexible device which showed better electrical/mechanical stability in comparison to ITO device [297]. We can

conclude from these reports that there is ongoing progress underway to capitalise the advantages of materials development, deposition methods, characterization and optimization of the electrical, optical and mechanical properties of PEDOT:PSS electrodes.

Metallic structures in the form of thin metal films, patterned metal grids and metal nanowires can be used as transparent conductor electrodes when their average thickness is sufficiently thin. Metals are most conductive materials due to high free-electron density but are not very transparent. Since metals can be made to grow thin films, to maximise the transparency, they can function as transparent electrodes while maintaining good electrical conductivity. Thin films of 10 nm or less have been demonstrated with sufficient optical transmittance [298], [299]. These metal films can be deposited by DC sputtering method in ultrahigh vacuum in Argon environment. Various metals can be used to grow thin films, such as, chromium, nickel, copper and silver. Chromium and Nickel are relatively less expensive than ITO and compatible with fabrication process and organic materials.

An innovative way to improve the transmission of thin metal films is to grow them in patterned grid structures whereby, leaving free space on the substrate to harness the light transmission. Hundred percent light can pass through these empty spaces in the grid where as, electrical contact is served by solid metal lines of grid. This approach requires careful design of grid dimensions; spacing and width of grid lines to get optimum sheet resistance and transmittance for the electrode [2], [300], [301], [302], [303], [304], [305]. Organic solar cells were fabricated by 40 nm thick, wire-grid patterned Au, Cu, and Ag electrodes prepared by nanoimprint Lithography as anode materials to compare with ITO electrode [302]. The authors demonstrated comparable performance using metal grid electrodes with transparency of around and over 80% and sheet resistance between 23 and 28 Ω/\square . Figure 8.3 shows transmittance and device characteristics for

the nanoimprinted metal electrodes alongwith ITO.

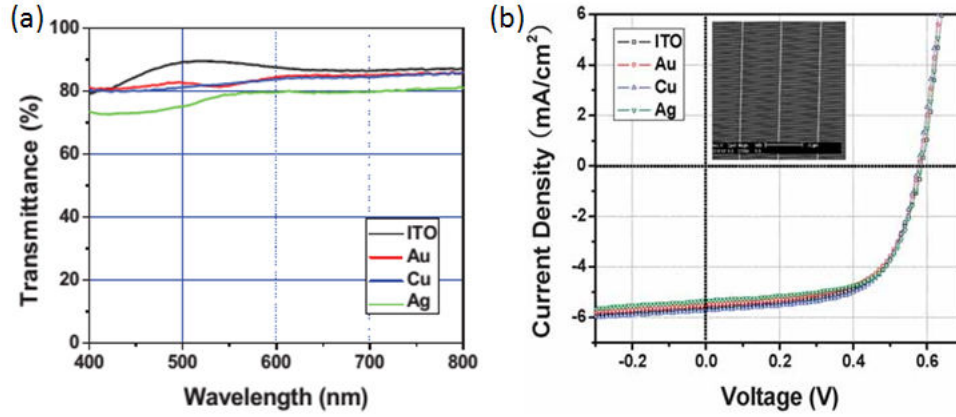


Figure 8.3: (a) UV-Vis transmittance of nanoimprinted metal electrodes Ag, Cu, Au and ITO, inset shows the SEM image of an as-fabricated metal electrode on glass (b) Current density versus voltage characteristics of organic solar cells (OSCs) fabricated using different electrodes, nanopatterned Au, Cu, and Ag as well as conventional ITO electrodes (Intensity: AM1.5G 100 mW.cm⁻²) [302]

As it is evident from the J-V characteristics, the efficiency is almost the same for metal electrodes as for ITO. Table 8.2 summarises the performance of each electrode.

Table 8.2: Device characteristics of solar cells fabricated using nanopatterned Au, Cu, and Ag and conventional ITO electrodes (Intensity: AM1.5G 100 mW.cm⁻²) [302].

Transparent Electrode	J_{sc} [mA · cm ⁻²]	V_{oc} [V]	FF [%]	Efficiency [%]
ITO	5.59	0.59	0.61	2.00
Au	5.50	0.57	0.62	1.96
Cu	5.71	0.57	0.63	2.06
Ag	5.34	0.58	0.65	2.00

The criteria for nanowires puts emphasis on the growth of small diameter,

smooth, long lateral size, and highly pure metallic nanowires for this purpose with low production cost. Silver nanowires (AgNWs) have demonstrated potential for transparent conductor applications with electron density which brings high intrinsic conductivity of silver to the arena. Nanoscale diameter (40-200nm) and micrometer length (1-20 μ m) AgNWs can be grown [2], [246]. However, several challenges impair the large scale use of AgNWs as electrodes, such as, high surface roughness, instability towards oxidation and moisture environments, and adhesion to substrates which is still poor [265]. Figure 8.4 shows schematic and SEM image of AGNWs on flexible substrates.

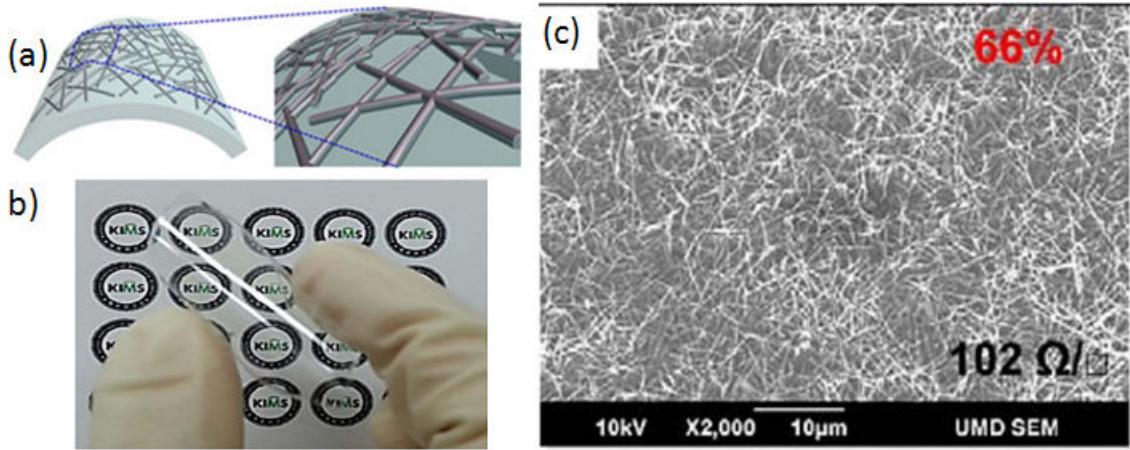


Figure 8.4: (a) Schematic illustration of the fabrication process of AgNWs embedded NOA 63 transparent electrode, (b) Photograph of a fabricated AgNWs embedded flexible transparent electrode (7 cm \times 37 cm) illustrating their high transparency and flexibility [265], (c) SEM images of the surface of NW film on PET with 102 Ω/\square , $T = 66\%$ [246].

To solve instability and roughness issues, a study demonstrated the fabrication of a flexible transparent electrode with superior mechanical, electrical and optical properties by embedding a AgNWs film into a transparent polymer matrix (a commercial ultraviolet (UV) curable polymer of Norland Optical Adhesive (NOA) 63 as the transparent substrate) which serves both as flexible electrode

and protector for AgNWs network. An ultra-smooth and extremely deformable transparent electrode having have sheet resistance and transmittance comparable with those of an ITO electrode could be produced with this technique. The OSC devices showed PCE of 3.07 with excellent performance after several bending cycles and stability after weeks.

Copper (Cu) NWs have been reported in the literature as well, which offers even lower cost solution than AgNWs. The report demonstrated that CuNWs with diameters of 90 ± 10 nm and a length of $10\mu\text{m}$ can be synthesized by a simple room-temperature solution process [306]. An other study reported production of Cu NWs synthesized by solution processing. The CuNWs network, when printed on the glass substrate formed the film having a sheet resistance of $20 \Omega/\square$ at 60 % transmittance. Further, the potential of CuNWs (NW diameter was from 20 to 70 nm, with an average diameter of 44nm) as transparent electrode was demonstrated by fabricating a small molecule device, which showed 3.1 % efficiency on flexible substrate compared to 4.0 % for the ITO reference.

Apart from these emerging materials, several hybrids and composites have been reported for OSC to take advantage of materials' combination. These include, solution-processable Graphene-Carbon Nanotube hybrid [?], metal grid/conducting polymer hybrid transparent electrode for inverted polymer solar cells [307], a low-temperature solution processable silver nanowires and carbon nanotubes [308], Ag grid/ITO prepared by inkjet printing [309], monolayer graphene/Au metal grid as top electrode [310], multilayer graphene (MLG) and metal grids (Ag) [311], dispersant-free AgNW/SWCNT hybrid films [312], Metal-grid hybrid TCEs prepared by inkjet-printing with PEDOT:PSS and Ag nanoparticle inks [313], silver nanowires /ZnO composite film[314]. Table 8.3 summarises the status of most important emerging and commercialised TCEs.

Table 8.3: Comparison of graphene (unoptimized and optimized) with other materials such as ITO, Ag nanowires, CNTs and PEDOT:PSS. The table is adapted from reference [315].

Material	$T(\%)$	$R_S (\Omega/\square)$	Status	Issue
ITO	>85	15–30	Standard	Cost, brittle, corrosion by salts or acids, slow vacuum process
Ag nanowire	>80	0.4–116	Commercialized, emerging	Roughness, environmental stability, haze, light scattering
CNT	90	50	Emerging	High resistance, doping stability, roughness
PEDOT:PSS	80	100	Limited use	Electrical/environmental stability, color tinge
Graphene (unoptimized)	85	400 or more	Emerging	High resistance, doping stability
Graphene (optimized)	85	Less than 30	Emerging	More doping up to few Ω/\square , doping stability

8.3 Bottom Up Techniques: Epitaxial Growth, CVD and Chemical Synthesis

8.3.1 Epitaxial Growth

SiC crystal is heated and cooled down to produce single-bi-few layer graphene [316]. This technique is also known as carbon segregation from silicon carbide (SiC) or metal substrates and requires a good control of conditions, such as, temperature, heating rate and pressure to get the desired quality and thickness of graphene [62],[63], [65], [64]. Graphene from SiC was produced and patented in 1896. Graphene segregation from Ni(111), however is studied since 1976 [317]. The Ni(111) surface has a favourable lattice structure for graphene, having a lattice constant mismatch near 1.3 %. In Ni diffusion method, a thin layer of Ni is evaporated onto a SiC crystal. When heated, the carbon diffuses through the Ni layer forming a graphene on the surface. This method has a potential advantage of facility to detach graphene layer from surface as compared to SiC crystal without Ni [318]. However, the growth of graphene takes place at random locations simultaneously, forming islands of graphene which assemble together. Due to this random growth and subsequent assembly, graphene is not perfectly homogeneous, mainly due to defects and/or grain boundaries [84]. Thus, the graphene suffers in quality when compared to exfoliated graphene unless grown on a perfect single crystal where size of graphene is dictated by the size of crystal itself. Mass production and upscaling is still a challenge for this method. Large size, high-quality layers are grown on SiC in an argon atmosphere currently [65] and detachment is made possible by hydrogen treatment [319].

8.3.2 Chemical Vapor Deposition and Transfer

CVD is a well-known process and the earliest report of CVD grown FLG was reported more than 40 years ago [320]. The gaseous hydrocarbons compounds are

feed in the CVD chamber and decompose at high temperatures in order to grow thin films of SLG and FLG on various substrates [321]. The thickness/number of sheets depends upon the thickness of substrate (Ni) and solubility of carbon in metal. Patterning of Ni film helps control the shape of graphene as well. Graphene has to be subsequently transferred onto other substrates for further study/applications. Ni is used as catalyst due to its high solubility of carbon and several layers of graphene can be grown over precedent layers on Ni. Copper (Cu) catalyst allows to grow mostly SLG and FLG with less than 5% due to low solubility of carbon in Cu [322]. Cu has solubility of 0.04 % in comparison to that of Ni (2.7 %), at higher temperatures, and the carbon solubility is affected by temperature as well showing a decreases with decrease of temperature [323]. Much of these films are micro meter to centimeter by lateral size [23], [322]. Millimeter size sheets of graphene have also been reported to grow on Platinum (Pt) surface with the thickness of films strongly depends upon the thickness of Pt[324]. The necessity to grow larger sheets for flexible electronics displays and TCEs motivated to grow 30-inch graphene on copper substrates by CVD using roll-to-roll process, subsequently transferred onto flexible PET substrate [59]. Further doping with HNO_3 can help decrease the sheet resistance of CVD grown graphene. Stacking few (4) layers of this graphene showed a sheet resistance of approximately $30 \Omega/\square$ with very high transparency of 90 %. Recently, an other group reported a 100-meter-long high-quality graphene transparent conductive film by roll-to-roll chemical vapor deposition and transfer process with sheet resistance of $150 \Omega/\square$ and transmittance above 80 per cent [325]. However the cost of production (cost of substrates, catalysts and thermal budget for CVD is grown on high temperature of 1000°C), dependency on size-of-wafer and complexity involved in transfer to arbitrary substrates are cons [70].

8.3.3 Chemical Synthesis

Graphene or carbon nanosheets production by chemical synthesis methods have been reported in the literature as well. Such synthesis yields carbon nanosheets in gram-scale quantities in a bottom-up approach which can then be assembled to form larger [326]. Ordered layers are formed by nanographenes with control of orientation and spacing. The interaction of nanoribbons helps control and tune its optoelectronic properties [96].

8.4 Charge Transport in Organic Semiconductors

Before, we discuss the charge transport in graphene, it is worthwhile to briefly introduce the basics of charge transport in disordered organic semiconductors. Generally, the organic semiconductors with conjugated π system are most interesting among the class of organic semiconductors for organic electronics. When a carbon (C) atom has a double bond to another C atom, two p and one s orbital form three degenerated and coplanar sp^2 hybridized orbitals, each occupied by one electron. The fourth valence electron of the C atom is in the residual p_z orbital, which is perpendicular to the plane of the sp^2 orbitals. This electron interacts with the electron in the p_z orbital of the other C atom and forms a π bond while the electrons in the sp^2 orbitals form σ bonds. In a benzene ring, six C atoms are distributed on a hexagonal shape, each one bound to the two adjacent C atoms and one H atom. The six electrons in the p_z orbitals, one at each C atom, allow the formation of three π bonds which are delocalized over the benzene ring. Each atom contributes only one electron to the π bond, occupying only the energetically lower π orbitals in the ground state. These energy levels are also referred to as the highest occupied molecular orbital (HOMO) and contribute to the bonding of the atoms. The anti-bonding π^* orbital is the lowest unoccupied molecular orbital (LUMO). In a planar molecule with several adjacent benzene rings, the p_z electrons are delocalized over the whole conjugated part of the molecule. As the number of benzene rings increases, the conjugation length increases too. The highest number of bonding and anti-bonding π orbitals reduces the band gap of the resulting molecule. While a single benzene ring has a band gap of ≈ 8 eV, tetracene, consisting of three benzene rings, has a band gap of ≈ 4 eV and pentacene ≈ 2 eV. In semiconducting polymers conjugated units are connected by single carbon-carbon bonds which introduce high rotational freedom between neighboring units. As a consequence of the distorted planarity and the spatial alignment of the polymer, the conjugation can only extend over

a couple of monomers leading to typical band gaps around 2 eV or lower.

Due to the band gap between HOMO and LUMO, pure organic semiconductors are not conductive in the dark at low temperatures and low applied voltage. This requires the creation of excess charge carriers by injection through the electrodes, the internal photo-effect or by chemical doping, the organic semiconductors become conductive. Neighboring molecules interact only weakly through Van der Waals forces or by dipole-dipole interactions, so the wave functions of excess charge carriers are localized at only a few or even one individual molecule, resulting in a negative or positive charged ions. This polarizes the surrounding molecules. As the relaxation time of the polarized molecule is ≈ 100 times shorter than the transfer time needed for the electron or hole to tunnel with the thermal assistance to the next molecule, the polarization follows the charged molecule. Therefore, electrons in the LUMO are also called the negative polarons, while the holes in the HOMO are called positive polarons. Ordered crystals exhibit a homogeneous polarization energy throughout the crystal and a larger overlap of adjacent π orbitals, than disordered molecules. However, due to weak delocalization of the π orbitals, the HOMO and LUMO energy levels have a bandwidth below 100 meV and the orbitals extend only over a few oligomers. As a consequence the highest charge carrier mobilities obtained for hole transport are around $35 \text{ cm}^2/\text{Vs}$ at room temperature and up to $58 \text{ cm}^2/\text{Vs}$ at 225 K, about one order of magnitude smaller than Silicon mobility of $450 \text{ cm}^2/\text{Vs}$ at room temperature [327]. In amorphous organic semiconductors, locally different molecular environments change the polarization energy, which leads to a Gaussian distributed density of states with in a range of 80 to 120 meV. Hopping between adjacent states results in mobilities below $0.1 \text{ cm}^2/\text{Vs}$ [328].

While the position of the fermi level can be tuned in the production process by doping of inorganic semiconductor, organic semiconductors are rather classified as p or n-type materials as a function of energy of HOMO and LUMO levels with respect to the source and drain electrode in the Field Effect Transistor

(FET) structure [329].

The charge transport in disordered organic semiconductors is via hopping simply because the charge carriers have to overcome large barriers between the molecules or localization sites [330]. The charge carrier mobility is relatively high in a region of crystalline order due to short and organized (hopping) distance among molecules. The hopping site arrangement varies both positionally and energetically within a disordered material. Disorder includes structural disorder (such as defects) and the presence of impurities and chemical inhomogeneities [331]. These abnormalities behave as trapping sites. These sites have various origins or reasons to occur, including due to presence of water, chemical residues and grain boundaries in semi-crystalline materials [332], [333], [334]. Relatively low charge carrier mobility in disordered organic semiconductors (OSs) is linked to and is consequence of weak intermolecular interactions and resulting localization of charge carriers or trapping by chemical impurities and other trap states formed by structural disorder. Mobility is an important parameter that is used to understand charge transport in OSs. Major factors on which mobility of an organic material is dependent on are its temperature, applied electric field, atmospheric conditions and molecular ordering. Several ways are employed to experimentally determine mobility. Most frequently it is determined from the current-voltage characteristics of FET. Recently, however time-of-flight (TOF) is emerging as a viable method to assess mobility in FET-like structures.

8.5 Four-point Probes manual for calculation of geometrical factor

4.1 Resistivity Measurements

The most direct approach to measuring the resistivity of semiconductor materials is to pass a current through the sample and to measure the voltage drop across a known distance. This is most readily achieved with a four-point resistivity probe with appropriate current supplies and voltage measuring circuitry. Similar apparatus can also be used to measure other characteristics, such as mobility.

Four-Point Probe Method

Figure 4-1 illustrates the use of a collinear four-probe array for resistivity measurements. Four correction factors are applied, as necessary, to obtain accurate measurements. They are

F_{SP} = probe spacing correction factor

$F\left(\frac{W}{S}\right)$ = thickness correction factor

F_2 = geometrical correction factor

C = correction factor for conducting skin of finite thickness (wraparound diffusion).

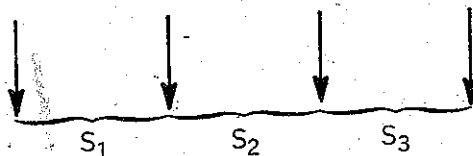
Resistivity, then, is defined as $R_S = \frac{V}{I} \times \text{correction factor}$,

The probe spacing correction factor, F_{SP} , is defined as

$$F_{SP} = 1 + 1.082 \left(1 - \frac{S_2}{S} \right),$$

where

$$S = 1/3 (S_1 + S_2 + S_3).$$



Thus, $R_S = \frac{V}{I} \times F_{SP}$.

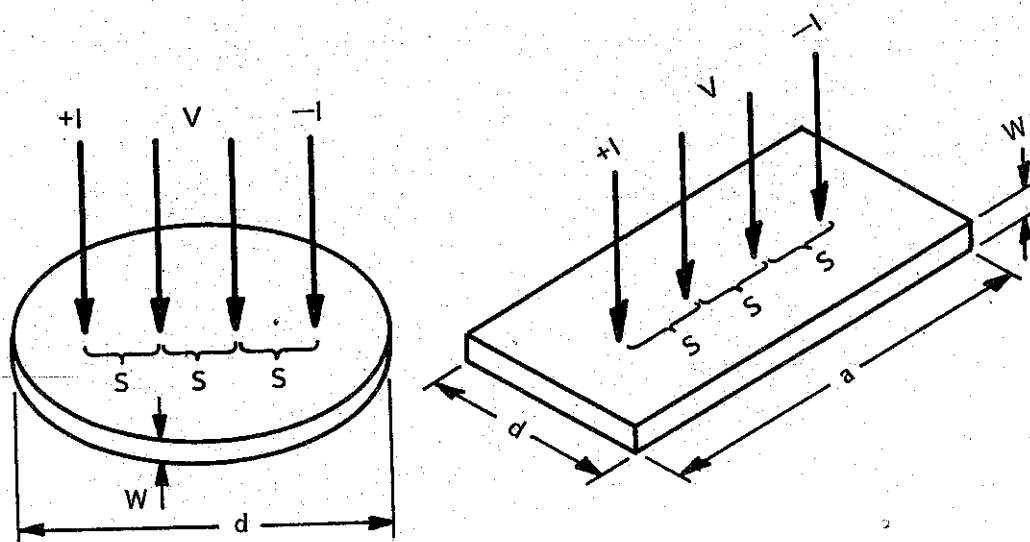
The thickness correction factor, $F\left(\frac{W}{S}\right)$, is obtained from the table below.

$\left(\frac{W}{S}\right)$	$F\left(\frac{W}{S}\right)$
0.5	0.997
0.6	0.992
0.7	0.982
0.8	0.966
0.9	0.944
1.0	0.921

Thus, $R_S = \frac{V}{I} \times F\left(\frac{W}{S}\right)$.

Figure 4-2 illustrates the use of the geometrical correction factor, F_2 , and Figure 4-3 illustrates the use of correction factor C .

4-4 MEASUREMENTS



APPARATUS: collinear four-probe array

APPLICATION: silicon slices: diameter > 16 mm
thickness < 1.6 mm

PARAMETERS: I = current applied through outer probes

V = voltage measured across inner probes

d = diameter of sample (in rectangular case, dimensions perpendicular to probe direction)

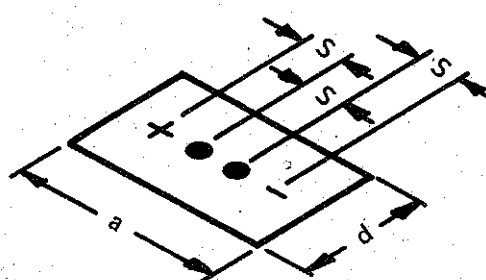
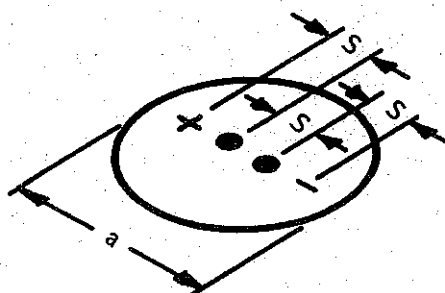
a = sample dimension parallel to probe direction

W = thickness of sample

S = probe spacing

Figure 4-1 — Four-Point Probe Measurement of Resistivity

$$S = 0,635 \text{ mm}$$



$$R_S = \frac{V}{I} \times F_2$$

$\frac{d}{s}$	CIRCLE	$\frac{a}{d} = 1$	$\frac{a}{d} = 2$	$\frac{a}{d} = 3$	$\frac{a}{d} \geq 4$
1.00				0.9988	0.9994
1.25				1.2467	1.2248
1.50			1.4788	1.4893	1.4893
1.75			1.7196	1.7238	1.7238
2.00			1.9454	1.9475	1.9475
2.50			2.3532	2.3541	2.3541
3.00	2.2662	2.4575	2.7000	2.7005	2.7005
4.00	2.9289	3.1137	3.2246	3.2248	3.2248
5.00	3.3625	3.5098	3.5749	3.5750	3.5750
7.50	3.9273	4.0095	4.0361	4.0362	4.0362
10.00	4.1716	4.2209	4.2357	4.2357	4.2357
15.00	4.3646	4.3882	4.3947	4.3947	4.3947
20.00	4.4364	4.4516	4.4553	4.4553	4.4553
40.00	4.5076	4.5120	4.5129	4.5129	4.5129
inf	4.5324	4.5324	4.5324	4.5324	4.5324

Figure 4-2 — Geometrical Correction Factor F_2 (for Sample Thickness or Junction Depth $< \frac{S}{2}$)

List of Figures

1.1	Transparent Electrodes applications in LCDs [1].	8
1.2	Sheet resistance requirement for different applications of TCEs. . .	10
1.3	I-V curves for different electrical and electronic devices: for a large resistance (resistor) A); a small resistance B); a p-n junction diode C) and a battery D).	11
1.4	Family of carbon allotropes [22].	19
1.5	Schematic of the in-plane σ bonds and the p orbitals perpendicular to the plane of the graphene sheets forming π bonds A) and three most common stacking sequences of graphene flakes B) [38]. . . .	21
1.6	TEM micro-graphs of the FLG borders with different graphene sheets numbers A), TEM micro-graph and electron diffraction of a single layer graphene B), SEM image showing the presence of thick FLG in the sample C), [40].	22
1.7	Comparison of Raman spectra at 514 nm for bulk graphite and graphene (scaled to have similar height of the 2D peak at 2700 cm^{-1}) (a). Evolution of the spectra at 514 nm with the number of layers (b). Evolution of the Raman spectra at 633 nm with the number of layers (c). Comparison of the D band at 514 nm at the edge of bulk graphite and single layer graphene (d). The fit of the D_1 and D_2 components of the D band of bulk graphite is shown. The four components of the 2D band in 2 layer graphene at 514 and 633 nm (e) [44]. Raman spectrum of a graphene fragment, recorded at an edge, showing the main Raman features, i.e. the D, G, D' and G' bands taken with a laser excitation energy of 2.41 eV [53].	24

1.8	General strategies for preparation of graphene oxide/graphene from graphite followed by types of reduction treatments A) and chemical structure of graphite oxide B).	30
1.9	Low energy DFT 3D band structure and its projection on k_x close to k point K for graphene showing graphene honeycomb lattice and the Brillouin zone (a), bilayer graphene (b), trilayer graphene (c) and graphite (d). The Dirac point (i.e., relativistic fermion characteristic) is lost in bilayer graphene (b), but appears again in trilayer graphene (c); (d) shows the 3D graphite structure which displays a semimetallic band structure with parabolic-like bands. The Fermi level has been set at zero in all cases [19] An enlargement close to the K and K' point shows Dirac cones [37, 100].	33
1.10	Examples of structural defects and oxygen groups in single sheet of graphene. The 5-8 double vacancy A), stone-wales defects B), adatoms C) oxygen functional groups mainly on the edges D). Interlayer double vacancy structures in bilayer graphene V_2^1 ($\beta\beta$) E), V_2^2 ($\beta\beta$) F), and spiro-interstitial (a four-coordinated carbon atom between the layers) G) [105].	35
1.11	Disorder in graphene obtained by micromechanical exfoliation (scotch tape) of synthetic graphite. Using a scanning single electron transistor the spatial density fluctuations in graphene are measured. The black line shows the contour between electron (red) and hole (blue) puddles at an average carrier density of zero [109].	37
1.12	Schematic structure of MWNTs A) and chiralities of single wall CNTs B) [123, 124].	39
1.13	The graph shows the record solar-cell efficiencies over time, highlighting the progress in different solar cells and technologies up to the end of 2014. [150].	45
1.14	P3HT and PCBM materials, and their blended D/A structure [?].	46

1.15	Structure of conventional OSC with ITO anode and Al cathode electrodes, highlighting the importance of WF [151].	48
1.16	Four device architectures of conjugated polymer-based photo-voltaic cells: (a) single-layer PV cell; (b) bilayer PV cell; (c) disordered bulk hetero-junction; (d) ordered bulk hetero-junction [159].	50
1.17	The commonly used equivalent circuit for a p-n junction diode A) and the current density equation B) for solar cells. Note that the diode represents recombination current [160, 161].	50
1.18	Bulk heterojunction in organic solar cells described by the $p - n$ junction in inorganic solar cells.	51
1.19	Illustration of the principle of charge separation in solar cell [8]. .	55
1.20	Graph of current (J) versus Voltage for photo-voltaic devices. The figure shows how the device characteristics change upon illumination. Key points on the graph are also indicated,[182].	56
1.21	Transmission of SLG, and BLG (a), and up to five layer FLG (b), and AFM height as function of thickness of graphene (height obtained by AFM tapping-mode profile) up to 8 layers of graphene (c) [183], [46].	59
1.22	Organic Solar Cell structure using GTCEs. (a) Conventional device (Glass/LrGO/PEDOT:P3HT:PCBM/Al) structure for using LrGO as an anode, (b) Inverse structure device on flexible substrate (PI(substrate)/Metal/ZnO/P3HT:PCBM/PEDOT:PSS (Au)Graphene/PMMA) with CVD graphene used as cathode, (c) J-V characteristics of OPVs with different number of layers of graphene anode doped with PEDOT:PSS+Au or PEDOT:PSS only, and (d) J-V curves of the solar cells with various LrGO film thicknesses [192], [191].	61

1.23	(a) Organic Solar Cell structure using modified PEDOT:PSS (Gr-HEL) and (b) J-V curves of the solar cells with varying film thickness/sheets of graphene [193].	62
1.24	(a) Organic Solar Cell structure using small molecules and graphene-based TCE (b) J-V curves of the solar cells for different bending cycles [189].	63
2.1	A) Optical photo showing the main part of the mechanical set-up to produce the FLG from the pencil lead by a mechanical ablation where: (1) is the glass disk with rough surface, (2) pencil leads, (3) an ultrasonication bath containing solvent, B) suspension of the FLG in the ethanol medium.	75
2.2	A) Raw materials, B) Sonication and exfoliation procedure before the microwave experiment.	79
2.3	(a) FLG dispersion in ethanol, (b) set-up of spray coating by air-gun on hot plate.	82
2.4	A) Device configuration with variable gaps between electrodes (2.5, 5, 10 and 20 μm) for two probes measurement (T=top, B= bottom, R= right and L=left) and B) SEM image of the 2.5 μm device after FLG deposition.	85
2.5	A) Scheme showing the geometry of sample and probes in FPPS measurement, B) scheme showing the measurement principle, where extreme probes are used to inject the current in the sample under investigation and middle probes measure the voltage drop caused by the induced current across the sample. The spacing between probes is equal to s and is constant for all four probes from 1 to 4 as shown in A. The distance among probes in B is arbitrarily exaggerated for a better visualization only.	86

2.6	A) Geometry for charge transport device sample with dimensions of electrodes and spacing (s) between them, B) Optical image of actual device after electrodes deposition.	88
2.7	Schematic of principle of Hall Effect (a) and sample geometries for Van der Pauw configuration for resistivity and Hall effect measurements (b-d)	89
2.8	A) Schematic for the van der Pauw configuration device for Hall Effect measurement, B) Optical image of the device. Practically, the four contact electrodes have each $1.5 \times 1.5 = 2.25 \text{ mm}^2$ over a surface of $10 \times 10 = 100 \text{ mm}^2$ with a thickness $t = 200 \text{ nm}$ ($t/a = 200 \times 10^{-9}/10 \times 10^{-3} = 2 \times 10^{-6}$).	90
2.9	Principle of SEM and TEM respectively, showing back-scattered electrons and transmitted electrons.	94
2.10	A) The basic apparatus required and B) the schemes of photoelectron spectroscopy, XPS and UPS.	97
2.11	The simple model representing the energies in XPS.	99
2.12	A simple example of UPS spectra for Au(111) surface.	101
2.13	A) Raman and Rayleigh scattering of light, B) Energy diagrams. Note that difference of thickness of lines for Rayleigh and Raman, respectively, indicates the intensity of each scattering by which Rayleigh scattering is stronger/more intense in comparison to Raman scattering which is weak.	103
2.14	Surface roughness: Ra and Rq.	107
2.15	A) Schematic of the cantilever-tip assembly used in an AFM, B) Schematic of light source, cantilever, and photo detector reassembling the basic components of the light-lever AFM detection system.	108
2.16	Probe-sample interaction potential.	108
2.17	Principle of the Nuclear Reaction Analysis.	110

3.1	V(I) characteristics of FLG-Abl charge transport device, as-prepared and after thermal annealing A), Transmittance spectrum B). Inset: optical image of the device.	133
3.2	Log-log scale V(I) characteristics of FLG-Abl charge transport device, as-prepared and after thermal annealing (as figure 3.1). . . .	134
3.3	V(I) curves for low-to-high and high-to low currents to see hysteresis.	135
3.4	Measurement of resistance of FLG film by two-probes technique. .	136
3.5	Comparison of two-probes and four probes techniques by log-log scale of V(I) curves on left. The log-log plot is magnified between 10^{-4} A and 10^{-3} A on the right.	137
3.6	SEM images showing the morphology of the charge transport device.	138
3.7	A) V(I) characteristics of FLG-HOPG24h charge transport devices, as-prepared and thermally annealed at 900 °C under Ar, B) transmittance.	140
3.8	The difference and variation of lateral size of sheets within FLGs depending upon the raw materials used. A) FLG-Abl from pencil lead, [239] B) FLG-HOPG from HOPG.	143
3.9	SEM micrographs showing morphology of FLG-HOPG24h transport devices.	143
3.10	TEM micrograph of initial FLG with hydrocarbons layer adsorbed on the sheets (flashes lines), A) TEM micrograph of FLG after μ -waves assisted treatment in water (FLG-H ₂ O), displaying the highly crystallized FLG sheets, B). TGA (derivatives) profiles of initial FLG (FLG), FLG after μ -waves treatment in water (FLG-H ₂ O) and FLG after μ -waves treatment in water and additional oxidation at 650°C (FLG-H ₂ O+650°Cox), C) and FLG and FLG after μ -waves treatment in water (FLG-H ₂ O) D.	145
3.11	Surface profile for average roughness values for a FLG-Abl device.	147

3.12	A) AFM topography profile image of FLG-Abl device, B) 3D image of the profile, C) Histogram profile fitted by Gaussian curve, D) AFM image at a different location with a big micrometric flake, E) 3D image of profile with large flake F), 2D image of the inset showing smoother area in the profile, G) Histogram profile fitted by Gaussian curve of image in D.	148
3.13	A-B) AFM topography profile image of FLG-HOPG24h device at edge and related 3D image, C) Histogram of the profile fitted using Gaussian curve, D-E) AFM topography profile image at center of the device and related 3D image, F) Histogram of the profile fitted using Gaussian curve.	150
3.14	NRA profile simulated and experimental for the FLG-HOPG24h-40mL device.	152
3.15	Thickness of FLG film obtained by the Dektak profilometer by calculating the average height of the film.	153
3.16	A) A possible schematic description of FLG flakes arranged in the film assuming additional stacking in the z direction, B) surface profile of FLG film.	155
3.17	UPS work functions of FLG materials.	156
3.18	Percolation table for FLG-Abl.	158
3.19	SEM micrographs of the expanded graphite A) after sonication B).	160
3.20	A and B. Temperature-time profiles obtained for toluene, EG-toluene and graphite-toluene medium under μ -waves irradiation with two different conditions of μ -wave experiment.	161
3.21	TEM micrographs A-C) and XPS C1s peak of FLG D).	162
3.22	A) Representative Raman spectra on FLG flakes. B-D) I_G , I_D and I_D/I_G Raman intensity cartographies obtained (calculated for I_D/I_G) from area of the flake presented at the insert of the image in A.	163

3.23	A) Representative images of measured FLG flakes between two electrodes in a FET-like device, B-D) The I(V) curves obtained for few FLG flakes with varied electrodes distance at B) 2.5, C) 5 and D) 10 μm , respectively.	164
3.24	The R_{avg} device, FLG flakes count for each device width/distance of 2.5, 5 and 10 μm , respectively A) table enlisting the R_{avg} device, and R_{flake} for each device width/distance along with the flakes count B).	165
4.1	Representative V(I) curves of rGO and rGO/FLG charge transport devices by four-point probes. A) as-prepared, B) thermally annealed at 900 °C under Ar/H ₂ for 2h.	171
4.2	Representative transmittance spectra of the rGO and the rGO/FLG devices.	172
4.3	SEM micrographs of the rGO/FLG charge transport device. . . .	176
4.4	AFM roughness analyses of rGO/FLG microwave device.	177
4.5	AFM roughness analyses of PEDOT:PSS/rGO/FLG microwave device.	178
4.6	SEM of PEDOT:PSS/rGO/FLG microwave device.	178
4.7	Graph showing the work-functions of rGO/FLG in different conditions.	179
4.8	XPS C1s spectra of GO, rGO- μw and rGO- μw -900°C after thermal treatment under H ₂	180
5.1	Representative V(I) curves for the CNT/HOPG24h hybrid charge transport devices.	187
5.2	Representative transmittance spectra of the CNT/HOPG24h hybrid charge transport devices.	187
5.3	Morphology of CNT/HOPG24h hybrid charge transport devices. .	191
5.4	Morphology of the CNT alone device.	192

5.5	A) AFM topography profile of the CNTs/HOPG device B) 3D image and C) histograms fitted with Gaussian curve.	192
5.6	A) Representative I-V curves for the as-prepared and thermally-annealed CNTs/rGO devices, and B) transmittance for the CNTs/rGO B).	193
5.7	SEM images showing the morphology of CNT/rGO device.	196
5.8	A) AFM topography profile of the CNTs/rGO device near the center, B) 3D image, C) histogram profile fitted with Gaussian curve, D) AFM topography profile of the CNTs/rGO device near the edge, E) 3D image, F) histogram profile fitted with Gaussian curve.	197
5.9	Work-function of CNTs.	198
6.1	A) The structure and B) the energy band diagram showing the HUMO and LUMO levels of active layer materials along with illustrative work-functions of electrodes of the fabricated OSCs devices with ITO or CTCEs anode electrodes	200
6.2	V-I curves of ITO-based A), and Carbon-based Organic Solar Cells under illumination B).	201
6.3	Representation of the sheet resistance and series resistance in our OSC device.	203
8.1	Main coating generation methods (Courtesy TDK Corporation) [268].	257
8.2	Basic principles of ITO layer coating through sputtering method. (Courtesy TDK Corporation) [268].	258

- 8.3 (a) UV-Vis transmittance of nanoimprinted metal electrodes Ag, Cu, Au and ITO, inset shows the SEM image of an as-fabricated metal electrode on glass (b) Current density versus voltage characteristics of organic solar cells (OSCs) fabricated using different electrodes, nanopatterned Au, Cu, and Ag as well as conventional ITO electrodes (Intensity: AM1.5G 100 mW.cm⁻²) [302] 264
- 8.4 (a) Schematic illustration of the fabrication process of AgNWs embedded NOA 63 transparent electrode, (b) Photograph of a fabricated AgNWs embedded flexible transparent electrode (7 cm³7 cm) illustrating their high transparency and flexibility [265], (c) SEM images of the surface of NW film on PET with 102Ω/□, T=66 % [246]. 265

List of Tables

1.1	Criteria for choosing TCO materials [4].	9
1.2	Strengths and weaknesses of TCF technologies [11].	16
1.3	Properties of various materials for TCF technologies [12].	17
1.4	Work Function of current TCEs and Carbon-based TCEs.	18
1.5	Five representative methods of graphene production [70].	27
1.6	Sheet resistance, transmittance and conductivity of transparency (σ_{gt}) of graphene, graphene oxide and doped graphene films pro- duced by various methods.	43
1.7	Performance of GTCFs in organic solar cells [145].	64
2.1	Summary of carbon/graphitic materials used.	71
2.2	List of solvents and their use.	72
2.3	Summary of methods of producing FLG/rGO materials.	80
3.1	HE measurements results: the carrier concentration n , resistivity ρ and mobility μ for A) the FLG-Abl as-prepared device and B) for the FLG-Abl-900°C-Ar device at room temperature.	129
3.2	Conductivity of transparency (σ_{gt}) of FLG-Abl charge transport devices with R_s given for the FPP and HE in comparison to com- mercially available ITO electrodes.	139
3.3	Conductivity of transparency of FLG-HOPG24h charge transport devices.	141
4.1	Conductivity of transparency (σ_{gt}), of the rGO and the rGO/FLG devices.	173
4.2	R_s of the rGO (films) suspended paper. Insert showing the optical image.	174
4.3	Percentage of Oxygen in GO, rGO- μ -waves and rGO- μ -waves- 900°C-H ₂	181

4.4	Percolation table for rGO and rGO/FLG materials.	182
5.1	Summary of the prepared CNTs/FLG-HOPG24h devices	186
5.2	Conductivity of transparency σ_{gt} of CNT/HOPG devices in comparison with the best obtained results for FLG-Abl, FLG-HOPG, rGO and rGO/FLG devices, respectively.	189
5.3	Conductivity of transparency, σ_{gt} for the as-prepared and thermally-treated CNTs/rGO hybrid devices in comparison to the rGO, and CNT/HOPG devices.	194
6.1	Comparison of the sheet and series resistances of ITO and carbon-based transparent electrodes (CTCEs) in OSC devices.	202
8.1	Work functions of some transparent conductors [4].	258
8.2	Device characteristics of solar cells fabricated using nanopatterned Au, Cu, and Ag and conventional ITO electrodes (Intensity: AM1.5G 100 mW.cm ⁻² [302].	264
8.3	Comparison of graphene (unoptimized and optimized) with other materials such as ITO, Ag nanowires, CNTs and PEDOT:PSS. The table is adapted from reference [315].	267

CONFERENCES AND PUBLICATIONS

The electrical property of large few layer graphene flakes obtained by μ -waves assisted exfoliation (extraction) in toluene

Azhar A. Pirzado, Guillaume Dalmas, Lam Nguyen-Dinh, Ivan Komissarov, Francois Le Normand, Izabela Janowska

« Under preparation »

Macronization (densification) of graphenes via vibratory compaction

Izabela Janowska, Dr; Thierry Dintzer, Dr; Azhar Pirzado

Submitted to: Manufacturing Letters

Activation of few layer graphene by μ W-assisted oxidation in water via formation of nanoballs - support for Pt nanoparticles

Azhar A Pirzado, Mr; Lai Truong-Phuoc, Ph.D.; Vasiliki Papaefthimiou, Ph.D.; Camelia Matei Ghimbeu, Ph.D.; François Le Normand, Ph.D.; Housseinou Ba, Mr; Cuong Pham-Huu, Ph.D.; Tung Tran-Thanh, Ph.D.;

Journal of Colloid and Interface Science Volume 451, 1 August 2015, Pages 221–230,

DOI: 10.1016/j.jcis.2015.03.063

Electrical Transport in “Few-Layer Graphene” Film Prepared by the Hot-Spray Technique: The Effect of Thermal Treatment

Pirzado, Y. Jouane, F. Le Normand, R. Akilimali, V. Papaefthimiou, C. Matei Ghimbeu, I. Janowska

The Journal of Physical Chemistry C (Impact Factor: 4.81). 12/2014; 2(118):873–880. DOI:10.1021/jp4103433

Few Layer Graphene (FLG) and FLG/Carbon Nanotubes (CNTs) Transparent Conductive Films (TCF) prepared by hot-spray technique

Pirzado, Y. Jouane, F. Le Normand, I. Janowska

E-MRS Spring Meeting 2013: Oral presentation

Investigation of Electronic properties of few layers graphene (FLG) prepared by hot spray technique

Pirzado, Y. Jouane, F. Le Normand, I. Janowska

GDR Conference 2013: Poster presentation

ACKNOWLEDGEMENTS

I would like to thank my Supervisors Dr. Francois Le Normand and Dr. Izabela Janowska for their continued support in from planning to execution of experiments and further during entire process of PhD work and valuable corrections/discussions during the write up. Also for the financial support that I received from ICPEES laboratory and the ICUBE.

I would like to thank the laboratory staff and colleagues at ICUBE and ICPEES who helped me in number of ways during the PhD work.

I would like to thank all the members of jury who kindly accepted to be on my jury.

In the last, I would like my parents/family and wife for their support and patience throughout the tough times during my studies.

Résumé de la thèse en français

En bref, nous avons étudié différents matériaux de fines couches de graphite (FLG) obtenus par exfoliation mécanique et exfoliation assisté par micro-ondes en milieu liquide de têtes de crayon papier, de graphite pyrolytique hautement orienté (HOPG), et de graphite expansé (EG), respectivement.

La fabrication du FLG par ablation de têtes de crayon papier comprend plusieurs étapes de filtration, mais c'est un procédé à haut rendement, facile et qui peut être étendu à grande échelle. Les fragments ne sont pas plus grands que 2-3 μm . Les mesures de transport de charge ont été obtenues par effet Hall, par des méthodes 2-pointes et 4-pointes (FPPs) montrées dans la fig. 1. Pour des dispositifs préparés à partir de ces matériaux.

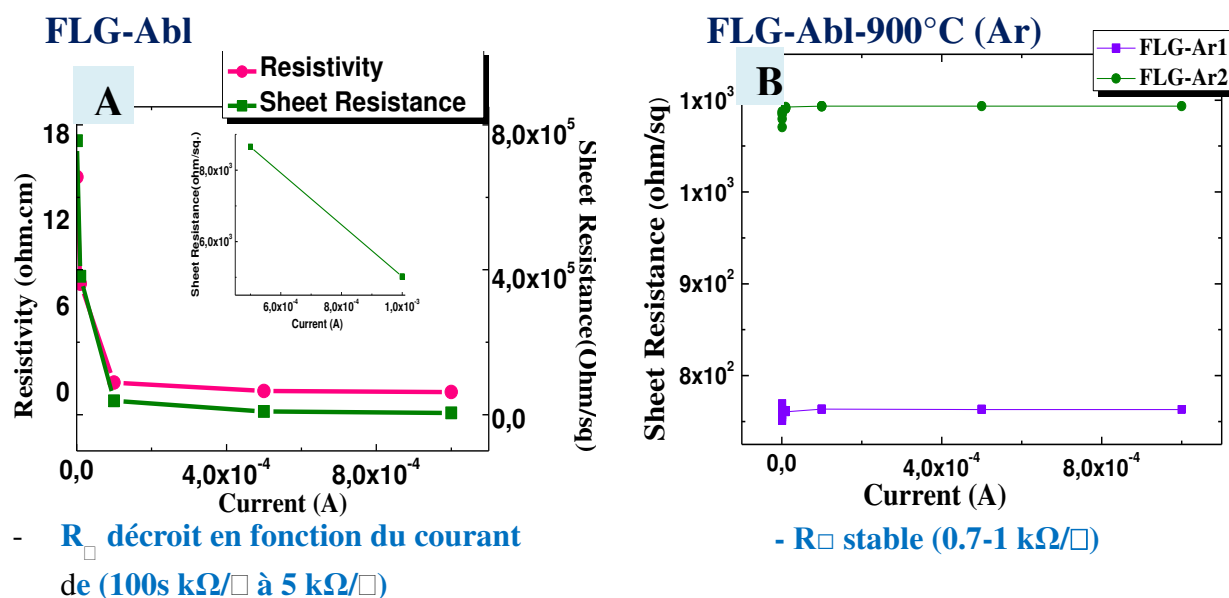


Figure 1: Mesures FPP de transport de charge pour des dispositifs FLG-Abl.

Par la suite, nous avons montré que l'échantillon préparé par pulvérisation à chaud conduit à des films de fragments FLG avec un dépôt aléatoire. Ces films montrent une amélioration significative des propriétés de transport de charge après un traitement thermique. Ceci est dû à la désorption d'hydrocarbures adsorbés qui sont des impuretés (toluène et ses intermédiaires de décomposition), accompagnée d'une désorption d'oxygène, après un traitement thermique à 900 °C. La désorption du toluène à partir d'une surface de requiert une température aussi grande que 450 °C sous une pression de 10^{-4} Pa, montrant de fortes interactions de cette espèce donneur d'électron avec les matériaux graphiques (fig. 2).

Ce résultat peut être considéré comme important à prendre en compte si l'on veut développer et définir des capteurs chimiques. Un mécanisme de transport diffusif du transport des électrons de même que un coefficient de température négatif du film de FLG a été observé lors de mesures d'effet Hall ce qui peut être utile pour des applications potentielles dans des dispositifs thermistors.

La plus faible résistance superficielle a été mesurée à $760 \Omega/\square$ pour des films de FLG film traités thermiquement. Ces résultats de conductivité font de ces matériaux de possibles électrodes et dépôts conducteurs et leurs faibles travaux de sortie sont encourageants pour des électrodes cathode de cellules organiques solaires (OSCs).

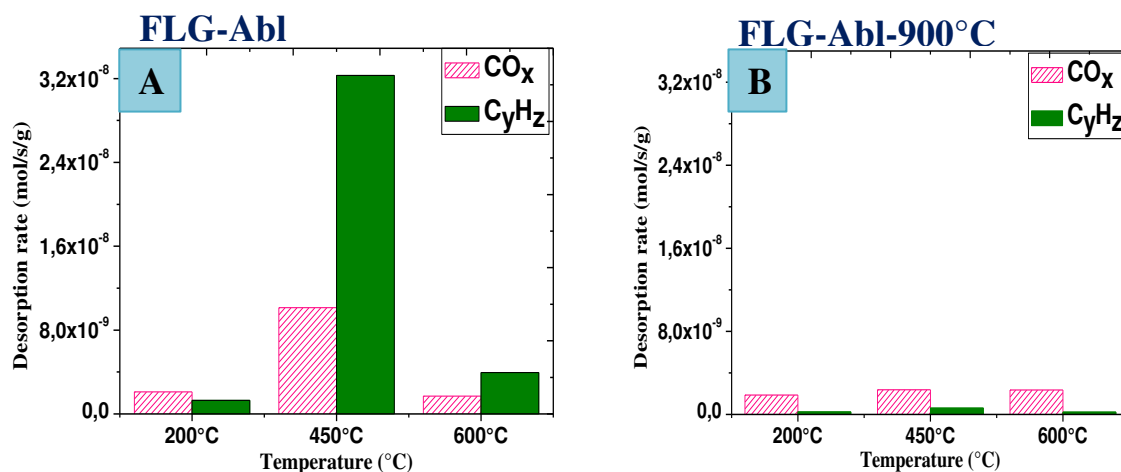
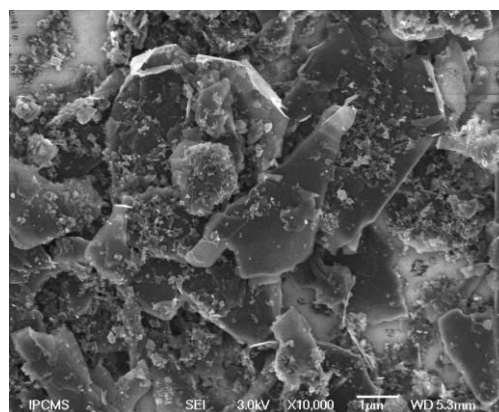
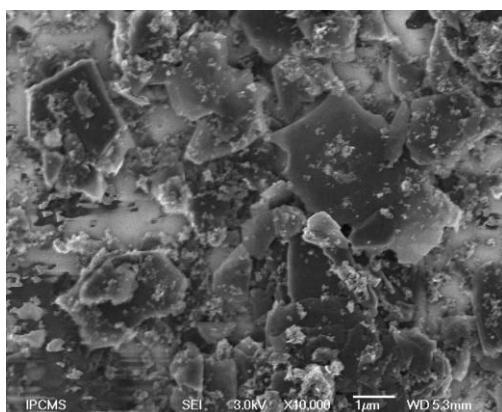


Figure 2: Désorption thermo-programmée couplée à la spectroscopie de masse (TPD-MS): Evolution de l'oxygène (CO_x) et des hydrocarbures (CyHz) en fonction de la température à trois températures différentes.

Le principal problème est la déposition aléatoire par la pulvérisation et la faible la percolation entre les fragments, ce qui est dû au procédé multi-étapes de préparation du FLG à partir des têtes de crayon papier (FLG-Abl) et à la non-homogénéité et à la faible taille des fragments (fig. 3).

FLG-Abl



HOPG24h

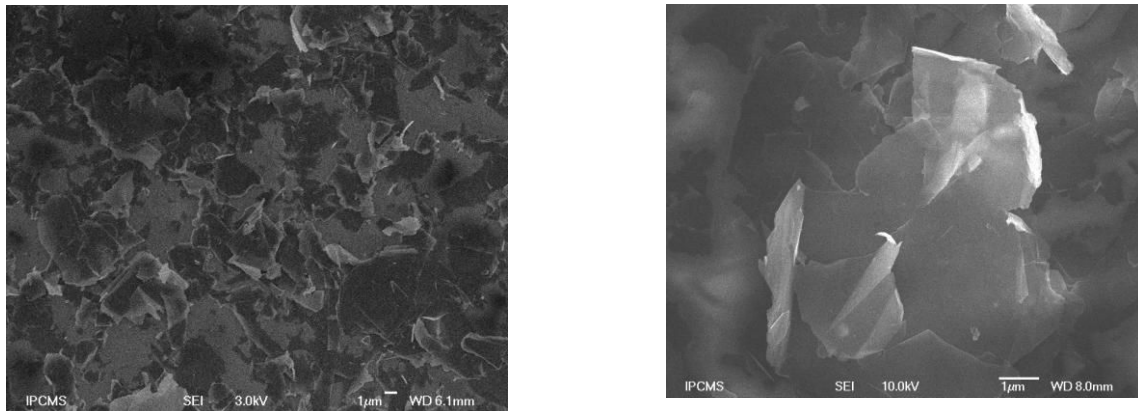


Figure 3: Images SEM (Scanning electron microscopy) montrant la morphologie des échantillons FLG-Abl et FLG-HOPG24.

La rugosité des deux films FLG-Abl et FLG-HOPG, résultant de l'agglomération inutile de fragments formés durant la dispersion et la pulvérisation, est un obstacle majeur pour obtenir des films homogène et une surface plane avec des propriétés reproductibles. Cependant, une amélioration significative dans la transmittance a été obtenue dans le cas du film FLG-HOPG24. Des fragments de FLG-Abl ont été améliorés par traitements micro-ondes dans l'eau à 650 °C.

Finalement, de fines couches de graphite (FLG) ont été obtenues par exfoliation liquide du graphite expansée EG, procédé assisté par des irradiations micro-ondes. Il a été observé que quelques couches de graphène avec une grande dimension des fragments et une forte conductivité électrique obtenues par cette méthode. Une absorption significative par les micro-ondes des échantillons EG/FLG permet d'atteindre une faible densité de défauts avec de meilleures propriétés d'homogénéité et de conductivité. De très faibles résistances surfaciques, conjuguées avec des grandes tailles latérales des fragments de FLG, de dix jusqu'à des dizaines de microns, sont comparable aux graphènes de haute qualité synthétisés par les méthodes CVD, alors que des dimensions considérablement augmentées est d'un grand intérêt pour atteindre une percolation facile pour les films à suivre.

Cependant, en dépit des avantages obtenus avec des fragments à grande tailles latérales et de meilleures propriétés électroniques, les FLG obtenu à partir des micro-ondes sont formés avec des rendements faibles, ils forment des agrégats en suspension et il apparait difficile pour ces échantillons d'opérer dans un système de pulvérisation standard pour

former les films à cause du petit diamètre du gicleur. Pour décroître le nombre de feuillets dans les fragments individuels de FLG et augmenter la percolation dans les films, les échantillons hybrides rGO-FLG et CNT-FLG, ont été étudiées. La réduction et l'exfoliation simultanées de l'oxyde de graphène et l'hybride oxyde de graphène/ graphite expansé par by irradiation micro-ondes apporte une alternative viable au FLG-Abl. La réduction activée dans l'éthylène glycol est une méthode à haut rendement avec un faible cout des matériaux intrants. L'oxyde de graphène réduit (rGO) obtenu possède des propriétés électriques modérées mais ces propriétés peuvent être encore améliorées par un traitement thermique de réduction en atmosphère inerte.

Pour les dispositifs de transport de charge, après traitement thermique, des résultats légèrement améliorés ont été obtenus pour les dispositifs rGO et rGO/FLG, respectivement, en comparaison des échantillons FLGs obtenus par ablation (FLG-Abl) des têtes de crayon papier et de graphite synthétique (FLG-HOPG). Alors que les résistances superficielles obtenues fluctuant en comparaison avec les valeurs obtenues avec les échantillons FLG-Abl, la transmittance est meilleure (60-80%) que les échantillons FLG-Abl (31%) et comparable avec les valeurs obtenues pour les échantillons FLG-HOPG. Les fluctuations dans les résultats de dispositifs similaires conduisent cependant à une faible prédiction dans les mesures. La forte rugosité reste encore un des problèmes majeur due à la nature du matériau, formé de feuillets empilés, et due aux imperfections de la méthode de dépôt par pulvérisation. Une orientation additionnelle des fragments dans la direction z perpendiculaire au plan du substrat rend difficile une croissance parfaitement uniforme et homogène des films sur des substrats de verre ou de quartz. Prenant en compte une amélioration très faible de la résistance superficielle et de la transmittance des échantillons rGO et rGO/FLG comparée aux échantillons FLG-HOPG et les avantages du mode de synthèse de ces derniers, il semble que les échantillons FLG-HOPG devraient être plus appropriées pour des investigations supplémentaires, pourvu que le problème de la rugosité soit pris en compte.

Le réseau des nanotubes de carbone (CNTs) dans les films hybrides a deux buts: il aide à abaisser le seuil de percolation dans les films permettant ainsi d'augmenter la transparence pour une résistance superficielle donnée. Due à sa structure en réseau, de meilleurs résultats, en termes de R_s et de transmittance ont été obtenus en réalisant des films hybrides de CNTs avec FLG-HOPG and rGO (fig. 4 and 5). L'effet du traitement thermique améliore la structure et aide à la désorption de surface des espèces adsorbées (principalement des groupes contenant de l'oxygène tels que les groupes hydroxyles et

carbonyles) de FLG et rGO. Le rGO a une plus grande quantité de telles impuretés. Il en résulte de plus faibles résistances superficielles R_s comparées aux valeurs obtenues avec les échantillons FLG-HOPG24h. Le réseau de CNTs produit à la fois de meilleures connections et transparences que le matériau FLG utilisé dans ce travail. Ceci est démontré par les résultats de R_s et de transmittance, cependant l'addition de FLG est bénéfique pour R_s et les meilleurs résultats sont obtenus pour des échantillons hybrides, en particulier pour les échantillons CNTs/FLG-HOPG (fig. 4).

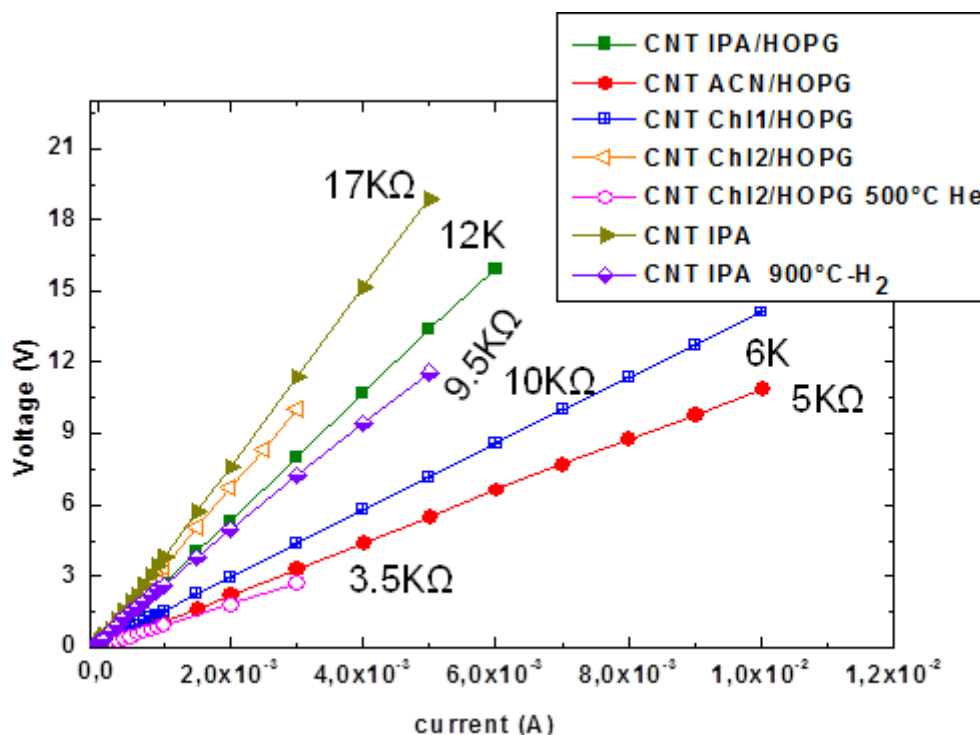


Figure 4: Courbes de transport de charge des dispositifs hybrides CNTs/FLG-HOPG24h.

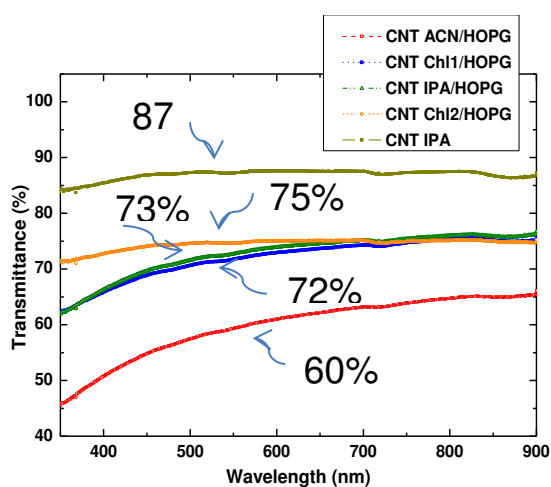


Figure 5: Transmittance des dispositifs hybrides CNTs/FLG-HOPG24h.

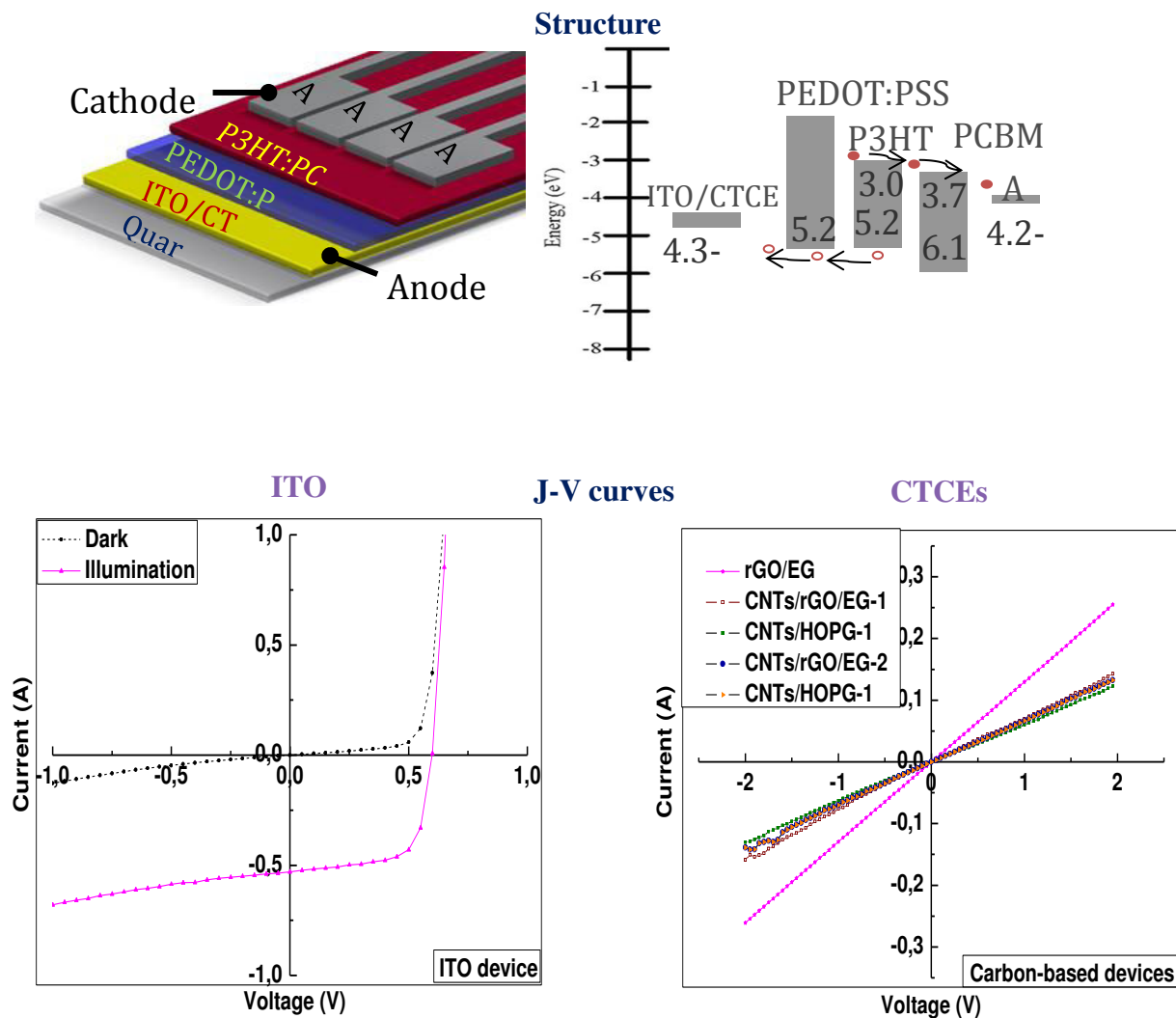


Figure 6: Dispositifs OSC comprenant des électrodes transparentes à base de carbone.

Cependant les imperfections de la méthode de pulvérisation à chaud rendent difficiles d'obtenir des films plats et homogène de ces matériaux carbonés. Les dispersions de ces matériaux sont cependant bonnes durant les préparations mais alors que le matériau a été déposé au travers d'un gicleur de diamètre 2-3 mm, il y a la possibilité de formation d'agglomérats inutiles qui non seulement contribuent à la rugosité des films mais aussi affectent la conductivité et la transparence, la première étant la plus fortement affectée.

Différents matériaux FLG et rGO ainsi que leurs hybrides avec les CNTs ont été testés comme électrodes transparentes conductrices préparées par la méthode de la pulvérisation à chaud dans la fabrication des cellules solaires organiques (OSC). La forte rugosité mais aussi

les fortes résistances superficielles des électrodes sont des problèmes potentiels ainsi que le faible travail de sortie de ces matériaux qui ne permettent pas d'envisager une application comme OSC avec des caractéristiques d'une diode normale. Cependant, quelques-uns de ces matériaux carbonés pourraient être utilisés comme contre-électrodes à cause de leur travail de sortie favorable et de leurs propriétés de films conducteurs.

Nous allons maintenant présenter quelques éléments de discussion et de perspectives section.

1. Discussion

Les électrodes transparentes conductrices (TCEs) sont des composants importants dans la fabrication des cellules solaires de tous types. L'Indium Tin Oxyde (ITO) et d'autres variations parmi ces oxydes donne des TCEs, mais le coût prohibitif de l'indium, sa disponibilité limitée constitue un défi pour la réussite de la recherche et de la commercialisation des cellules solaire, et de toutes autres dispositifs nécessitant des électrodes transparentes. Des matériaux alternatifs incluant les polymères, les nanofils d'argent, et les matériaux à base de carbone parmi lesquels le graphène monocouche ou à faible nombre de couches, l'oxyde de graphène réduit, et les CNTs sont l'objet d'investigations intenses pour obtenir une synthèse entre la relation entre propriétés et l'efficacité. La robustesse additionnelle de la plupart de ces matériaux rend ces matériaux potentiellement intéressant dans des applications comme contre-électrodes.

Nous avons étudiés des nanomatériaux de carbone en partant de leur synthèse, depuis la formation du film et ses propriétés pour l'intégration comme OPV. Non seulement les méthodes de synthèse ont été développées et optimisées mais le dépôt de film fin ainsi que leurs propriétés ont été améliorées. En résumé, nous avons étudié différents matériaux FLG obtenus exfoliation/ablation mécanique de têtes de crayon papier ou de graphite HOPG, et par exfoliation assistée par microondes en phase liquide de matériaux EG et GO et leurs hybrides avec CNTs. La méthode d'exfoliation top-down telle que l'ablation de têtes de crayon papier est extensible à large échelle avec un grand rendement, facile and bon marché mais jusqu'à présent elle comporte plusieurs étapes de purification et de filtration. Cette méthode a été par la suite optimisée en utilisant du graphite synthétique (Highly Ordered Pyrolytic Graphite, HOPG) pour obtenir des feuilles de graphène multicouches (FLG) relativement plus homogène et pour éviter une purification dans des conditions sévères tandis qu'elle permet

une diminution des problèmes économiques et environnementaux. Une méthode plutôt nouvelle a été développée dans laquelle une exfoliation et une réduction simultanées ont été réalisées par exfoliation assistée par microondes en phase liquide (LPE) pour obtenir des films de graphène (FLG) de relativement bonne qualité, fins et homogènes en taille latérale (FLG) et de l'oxyde de graphène réduit (rGO) à partir de matériaux de départ bon marché tels que le graphite expansé et l'oxyde de graphite. Ceci est d'un grand intérêt pour obtenir du graphène de haute qualité sous forme de feuilles avec un grand rapport d'aspect pour des applications à suivre.

Les matériaux ont été caractérisés par microscopie électronique à balayage (SEM), Microscopie électronique à transmission (TEM), spectroscopies Raman et de Photoluminescence (PL), analyses thermogravimétriques (TGA) pour étudier la qualité structurale des matériaux, incluant les défauts, l'épaisseur et la taille latérale des matériaux et films FLG. Les spectroscopies de photoélectrons (PES) à partir d'une source RX (XPS) ou ultraviolette (UPS) ont été employées pour étudier la composition chimique, les énergies de liaison, et les travaux de sortie de ces matériaux. Les travaux de sortie obtenus sont compris entre 4.0 eV et 4.5 eV, qui sont légèrement plus faibles que ceux de ITO (4.7 eV). Ce sont des matériaux qui peuvent être mis en oeuvre en solution et peuvent remplacer les contre-électrodes à base de métal (Al, Ag and Ca, ...) qui sont souvent déposés par des méthodes d'évaporation couteuses. La désorption programmée en température couplée avec la spectroscopie de masse (TPD-MS) sous vide à une pression maximum de 10^{-4} Pa, ont été réalisées pour comprendre les changements durant le traitement thermique du matériau FLG. Les résultats de TPD-MS montrent que quelques espèces d'hydrocarbures sont fortement adsorbées à la surface des FLGs et modifient les états électroniques qui dépendent de la nature des liaisons et peuvent affecter la qualité du matériau en laissant des îlots de défauts. La stabilité du toluène adsorbé après la synthèse jusqu'à des températures aussi hautes que 450°C est surprenamment remarquable dans nos résultats. Ceci peut affecter le transport des charges dans le matériau FLG. Ceci est une nouvelle évidence que d'autres fonctionnalités que celles contenant de l'oxygène influent sur les propriétés de transport de charge.

Les films fins des matériaux FLG et rGO incluant leurs hybrides avec des nanotubes de carbone (CNTs) ont été préparés par des méthodes de pulvérisation à chaud à bas coût, aisément extensible pour couvrir des surfaces potentiellement non-limitées en opposition aux surfaces limitées obtenues par la croissance de graphène par un procédé « bottom-up » tel

que le dépôt chimique en phase vapeur (CVD). Cette méthode est relativement plus compatible pour la croissance du film due à la nature des matériaux FLG qui sont formés de fragments en comparaison des méthodes de dépôts en pulvérisation ou de dépôt en gouttes. Les films sont constitués de fragments de FLG se recouvrant d'une manière aléatoire. Ce recouvrement permet une interconnexion entre les fragments et de ce fait des chemins pour le transport de charge. En fait, un minimum du seuil de percolation est obtenu pour mettre en œuvre la conduction. Les résultats de transport de charge obtenus avec ces films dans ce travail sont souvent obtenus au-delà de ce seuil de percolation, et même bien au-delà. Cependant ceci ne peut être obtenu sans ajout d'un nombre significatif de bords et de frontières parmi les fragments de FLG ce qui peut augmenter le nombre de sauts d'électrons au cours de leur traversée des films FLG. Le grand rapport d'aspect des FLGs obtenus par des méthodes d'ablation du graphite synthétique ou par exfoliation assistée par microondes en phase liquide du graphite expansé, respectivement, aident fortement à abaisser ce seuil de percolation. Cependant, la plus grande taille moyenne latérale des fragments de FLG et les faibles rendements de la méthode d'exfoliation assistée par microondes en phase liquide requiert une optimisation de la méthode de synthèse dans le futur et un gicleur avec une ouverture plus grande, respectivement.

Nous avons étudié les propriétés (opto) électroniques des dépôts par pulvérisation à chaud de films/électrodes conductrices transparentes obtenues par différentes méthodes et aussi leurs hybrides avec CNTs. Le transport électrique a été étudié par la méthode deux pointes (2PP) et la par la méthode 4-point (FPP), respectivement, pour la mesure de la résistance de fragments uniques de FLG et la résistance superficielle (R_s) de films FLG. Une nouvelle configuration de masque pour les dispositifs à effet Hall a été dessinée en utilisant le logiciel Lab View et un laser de coupe. Cela a permis de mesurer la résistivité de Hall (ρ), la mobilité des porteurs de charge (μ), la nature des porteurs de charge (électron ou trou) et enfin leur concentration (n) dans le film FLG. Par la suite, nous avons montré que les fragments empilés de FLG préparés par la méthode de pulvérisation à chaud montrent une amélioration significative du transport de charge après traitement thermique à partir de mesures FPP. La transmittance a été par ailleurs obtenue par spectrophotométrie ultra-violette et visible (UV-Vis).

La résistance superficielle R_s décroît d'environ $85 \text{ k}\Omega/\square$ à environ $15 \text{ k}\Omega/\square$ après un traitement thermique à 900°C dans l'Argon pour les films FLG préparés à partir de FLGs

obtenus par ablation/exfoliation by mécanique de têtes de crayon papier. Ce comportement est commun à tous les matériaux étudiés, incluant FLG-HOPG, rGO et leurs hybrides obtenus avec des nanotubes de carbone. Ceci est dû à la désorption d'hydrocarbures adsorbés comme impuretés (toluène et ses intermédiaires de décomposition), accompagné par une lente décroissance de la concentration d'oxygène, une fois chauffé à 900 °C. Comme cela est expliqué auparavant, une désorption de toluène de la surface FLG (pour FLG-Abl) requiert une température aussi haute que 450 °C sous une pression de 10^{-4} Pa, montrant une forte interaction de cette espèce donneuse d'électrons avec le graphène. Cette information peut être utile pour faire des capteurs chimiques à base de graphène. Le transport de charge a aussi été étudié en fonction de la température. Les résultats montrent une décroissance de la résistance superficielle avec la température des films FLG (libres de toluène) et suggèrent que les FLGs ont un coefficient de température positif (PTC), ce qui peut s'avérer utile et intéressant pour des dispositifs à thermistors. Ces résultats ont été publiés dans le Journal of Physical Chemistry C. Par la suite, la figure de mérite intitulée conductivité en transparence d'électrodes transparent conductrices augmente de 7 S/cm à 41 S/cm après un traitement thermique. La plus faible résistance superficielle de $760 \Omega/\square$ a été enregistrée pour un film FLG recuit. Le transport de charge montre un caractère diffusif ambipolaire (porteurs de charges de type à la fois n-type et p-type) avec de faibles R_s et une bonne mobilité ont été obtenues avec des mesures d'effet Hall. Ces résultats de conductivité font que ces matériaux sont applicables pour des revêtements et des électrodes conductrices.

Dans le cadre de la méthode de pulvérisation à chaud, des matériaux variés ont été étudiés pour sonder leurs possibilités d'application avec des élaborations simples, bon marché et extensible à grande échelle.

Une transmittance améliorée a été observée pour des films de FLG-HOPG24h en comparaison avec les résultats obtenus pour des films FLG-Abl. Ceci a été expliqué par les plus grandes tailles latérales des fragments. Cependant la résistance superficielle R_s reste suffisamment élevée pour que la conductivité en transparence soit comparable pour les deux types de matériaux/films, avec cependant une légère augmentation pour le dernier jusqu'à 61% après traitement thermique. Ces deux matériaux requièrent une forte température de traitement thermique pour obtenir un meilleur transport électrique en termes de R_s . L'avantage avec le graphite synthétique est d'éviter des étapes de purification et de filtration

conduites dans des conditions sévères dans le cas de la synthèse de FLG-Abl ainsi que d'obtenir de plus grandes tailles des fragments.

Comme R_s et la transparence de ces films varient suivant les variations locales de l'épaisseur des films, les mesures ont été reproduites en plusieurs points and des valeurs moyennes ont été extraites. Ceci souligne que le seuil de percolation est en relation directe avec la transparence. Ceci requiert cependant d'autres investigations pour trouver une relation quantitative entre transparence, percolation, conductivité et/ou résistance superficielle R_s . La rugosité des films FLG-Abl et FLG-HOPG résultant de la formation d'agglomérats inutiles Durant la suspension et la dispersion et les dimensions du gicleur sont les principaux obstacles pour obtenir des films moins rugueux avec une surface homogène et des propriétés reproductibles. Quoique ce problème soit de moindre importance dans le cas de films préparés à partir d'un traitement assisté par microondes pour les films rGO et O/FLG, des films encore trop rugueux ont été encore obtenus. En plus du comportement colloïdal de la suspension et la formation concomitante d'agrégats, la méthode de pulvérisation à chaud a quelques limitations pour obtenir des films homogènes et reproductibles due à la nature manuelle et fixe du dispositif expérimental. En plus, nous assumons que l'utilisation d'un système mobile avec un canon à air pour le dépôt de FLG peut améliorer l'homogénéité et la continuité des films, et en conséquence la reproductibilité des caractéristiques électriques mesurées. Un système de nano-polissage et/ou l'application d'une compression ou contrainte by par l'application d'une force peut améliorer la densité d'empilement de la couche en réduisant le volume et obtenir de meilleurs contacts entre les feuillets et les fragments en plus d'une réduction de la rugosité. Si le volume du matériau est réduit par l'application d'une force appliquée perpendiculaire au film pour le comprimer tout en gardant sa masse constante, la densité augmentera. Une plus forte densité augmentera le contact entre les feuillets et les fragments, et réduira de façon significative le nombre de joints et de bords que doivent franchir les électrons par sauts sur le fragment adjacent. L'optimisation de la formation des films peut encore être obtenue par modification des concentrations de la suspension et de leur dispersion. Concernant les matériaux de départ, les fragments de FLG-Abl peuvent être aplanis par "purification" de petites unités graphitiques et d'hydrocarbures par traitement dans l'eau assisté par les microondes. Ce procédé est utilisé dans un récent papier publié dans le "Journal of Colloids and Interface Science ».

Des fragments FLG de plus grande taille avec une grande conductivité électrique ont été obtenus au moyen d'une exfoliation rapide (extraction) de graphite expansé dans le

toluène avec l'assistance d'irradiations microondes. L'interaction de FLG avec le toluène a été utilisée pour favoriser l'extraction de fragments FLG à cause de la possibilité de pénétrer à travers les nano-cracking des fragments, effet observé dans le cas de FLG-Abl. La différence entre l'absorption des microondes par les deux matériaux aide aussi dans l'exfoliation du FLG par un chauffage rapide du graphite expansé. Une absorption significative des radiations microondes par les films EG/FLG permet d'obtenir peu de défauts et un matériau fortement homogène et conducteur. De très faibles résistances superficielle conjuguées avec la présence de fragments FLG à grandes dimensions latérales, jusqu'à des dizaines de microns ou plus, sont comparables aux valeurs obtenues avec des graphènes de haute qualité synthétisés par des méthodes CVD, tandis que des feuillets de taille considérablement agrandie est d'un grand intérêt pour atteindre la percolation pour les films de façon plus aisée.

Cependant, en dépit des avantages des grandes dimensions latérales et de meilleures propriétés électroniques, les films FLG obtenus à partir d'activation microondes ont des problèmes d'avoir de faible rendement, de former des agrégats en suspension et d'être inapproprié pour la formation de film, à cause du petit diamètre du gicleur. Aussi des études supplémentaires ne peuvent être entreprises pour le moment dans cette direction. Due à des problèmes inhérents à l'ablation FLG (petite taille latérale et présence d'impuretés, telle que le toluène), un recuit à haute température est nécessaire pour améliorer la structure et pour restaurer les propriétés électroniques des FLG.

L'exfoliation/réduction assistée en phase liquide éthylène-glycol et par microonde de l'oxyde de graphène et de l'oxyde de graphène/graphite expansé, respectivement, constitue une alternative viable au rGO et au rGO/FLG par son faible coût, son haut rendement et elle peut être utilisée pour former des films transparents à partir de la pulvérisation à chaud. De tels fragments FLG obtenus ont de grandes tailles latérales et sont synthétisés avec des rendements suffisants pour de futures investigations. Cependant, les films rGO et rGO/FLG ont des propriétés électriques modérées avec des transmittances aussi élevées que 73%, mais ils peuvent être encore améliorés dans le futur par des traitements thermiques de recuit/réduction dans un environnement inerte. Pour les dispositifs de transport de charge à la fois de plus grandes résistances superficielles et transmittances ont été enregistrées en comparaison avec les FLGs obtenus par ablation de têtes de crayon papier (FLG-Abl) ou du graphite synthétique (FLG-HOPG24h). Les résistances superficielles obtenues alors fluctuent en dessous et au-dessus des valeurs obtenues par les FLG-Abl tandis que la transparence est meilleure que celle des FLG-Abl et comparable à celle des FLG-HOPG. A cause d'un effet de

compensation du couple de valeurs transparence-résistance la conductivité en transparence est aussi comparable.

Pour améliorer encore dans le futur les propriétés opto-electroniques, les hybrides de FLG et rGO avec les CNTs ont été envisagés pour investigations à cause de l'avantage des nanotubes pour leur fort rapport d'aspect et leur possibilité de former une maille conductrice. A cause de sa structure enchevêtrée les CNTs dans les films hybrides forment un réseau qui aide à augmenter la conductivité en abaissant le seuil de percolation, ce qui aide à augmenter la transparence. Les résistances superficielles obtenus R_s et les transmittances sont alors supérieures dans les films hybrides de CNTs avec FLG-HOPG24h et rGO par rapport aux valeurs obtenues avec des films FLG ou rGO seuls. L'effet d'un traitement thermique améliore la structure et aide à enlever notablement les espèces adsorbées (principalement les groupes fonctionnels contenant de l'oxygène comme les hydroxyles et les carbonyles) de la surface de FLG et rGO. Les films rGO ont probablement plus de telles impuretés, ce qui est évident à partir des résultats de plus faibles R comparés à ceux obtenus par les FLG-HOPG24h. Le réseau de simples CNTs a de meilleures connections et transparences que le matériau FLG utilisé dans ce travail, cependant la résistance superficielle R_s des CNTs seuls n'augmente pas à la même échelle que FLG et rGO obtenus par recuit, probablement à cause de la grande cristallinité et pureté. Les plus grandes valeurs de conductivité en transparence ont été obtenues pour FLG-Abl et ses hybrides avec les CNTs. La résistance minimum a été mesurée pour FLG-Abl et CNTs seul, tandis que la transparence maximum a été obtenue pour les hybrides, FLG-HOPG 24h (sélection de plus grands fragments par une décantation de 24h) et les films rGO.

L'épaisseur homogène des films préparés reste un des problèmes majeur car un empilement ponctuel préférentiel dans la direction z et une orientation aléatoire des fragments rendent difficile de former des films parfaitement uniformes et homogènes sur des substrats verre/ quartz. Les mesures de profil de rugosité ont été réalisées en utilisant un profilomètre Dektak basé sur une pointe et la Microscopie à force Atomique (AFM). L'analyse de réaction nucléaire (NRA) a été utilisée pour la première fois pour estimer le volume non rempli dans les films FLG connaissant la concentration de carbone dans le film et de façon indépendante l'épaisseur. Les variations d'épaisseur obtenues par profilométrie et analyses NRA soulignent la présence de vides dans les films et confirment un empilement préférentiel de fragments FLG dans la direction z . Le pourcentage estimé de vides dans le film a été calculé en prenant en compte les variations d'épaisseurs (cette approche est prometteuse pour de futures

investigations). En dépit du fait que les résultats obtenus pour les matériaux étudiés sont encore insuffisants pour obtenir des électrodes transparentes idéales, les tests de fabrication de cellules solaires organiques avec FLG, rGO, et des hybrides avec les CNTs ont été entrepris. La forte rugosité des films demeure le problème principal, qui ne permet pas d'obtenir un dispositif OSC avec des caractéristiques d'une diode normale.

2. Perspectives

Matériaux

L'utilisation de fragments qui sont peu rugueux avec un nombre de feuillets et un fort degré de cristallisation (par exemple, purification microondes en milieu aqueux) pourrait aider pour obtenir des films plus homogènes. La taille non-homogène des fragments FLG obtenus par ablation de têtes de crayon papier et la qualité cristalline peuvent être améliorées par ces méthodes. Ainsi de plus fortes transparences, conductivités et de faibles rugosités sont possibles dans les films FLG. La concentration et le degré de dispersion des nanomatériaux devraient être optimisés avant la formation des films.

Pulvérisation à chaud par un canon à air automatique mobile

La pulvérisation à chaud par un canon à air automatique mobile avec une vitesse contrôlée peut grandement améliorer l'homogénéité des films en augmentant la probabilité de volume déposé sur une surface locale. Ceci n'améliorera pas non seulement le profil de rugosité mais aussi les variations en termes de résistance superficielle et de transmittance.

Polissage/Gravure pour aplanir la surface des films

Un polissage/gravure peut aider à réduire la rugosité et à aplanir la surface des films.

Polymère comme agent aplanissant

Une couche de polymère transparent conducteur telle que PEDOT: PSS peut être utilisée pour aplanir la surface et éliminer la rugosité de films FLG comme cela a été démontré dans un film rGO dans le chapitre 4. Ceci nécessite une future optimisation. Un autre polymère transparent conducteur tel que le Norland Optical Adhesive (NOA) 63 peut être utilisé pour encadrer les films, ce qui non seulement recouvre les films mais constitue aussi

une couche de protection ultraviolette (UV). Ceci a été démontré pour le recouvrement de films de nanofils d'argent à grande rugosité.

Etude volume-épaisseur

A cause la nature hétérogène des films et des variations locales, il est difficile de déterminer précisément la relation entre le volume de déposition et l'épaisseur. Une étude séparée peut être entreprise pour établir cette relation ce qui renforcera l'intérêt pour la potentialité de la méthode de pulvérisation à chaud.

Optimisation des FLG obtenus par exfoliation de graphite expansé dans le toluène via irradiation microonde et l'utilisation d'un gicleur de pulvérisation à plus grand diamètre

Pour améliorer le rendement à partir de graphite expansé, la méthode peut être optimisée en jouant sur différents paramètres tels que le rapport de concentration entre graphite expansé et toluène, en contrôlant la rampe de température et la pression durant l'irradiation microonde et les étapes de sonication/agitation mécanique.

Comme les feuillets de FLG ont de grandes dimensions latérales jusqu'à 10 microns, un pulvérisateur avec un gicleur possédant un grand diamètre de de plus faibles concentrations dans les suspensions de pulvérisation devraient aider à éviter les agglomérations de FLGs durant la pulvérisation.

FLG comme contre-électrode for OSCs

Comme le travail de sortie de quelques-uns des matériaux étudiés dans cette thèse sont plus bas que ou entre 4.0 et 4.5 eV ils peuvent aussi utilisables comme contre électrode pour remplacer les électrodes métalliques telles que Al et Ag. Ces électrodes métalliques sont souvent déposées par des techniques d'évaporation couteuses et sont sensibles aux effets environnementaux. Une contre-électrode à base de carbone peut se révéler un meilleur choix technique et financier.

rGO comme couche tampon

Les rGO obtenus par exfoliation/réduction assistée par irradiation microondes peuvent être utilisés pour remplacer des couches tampon telle que PEDOT:PSS qui est une couche collectant les trous dans OSCs. En effet c'est une couche fine, utilisable en solution et dont la conductivité est appropriée.

Azhar Ali Ayaz Pirzado

Integration of Few Layer Graphene Nanomaterials in Organic Solar Cells as (Transparent) Conductor Electrodes

Résumé

Les électrodes conductrices transparentes (TCE) sont des éléments importants dans les écrans tactiles et les applications photovoltaïques. L'augmentation de la rareté et le coût des dispositifs actuellement utilisés, tels que l'oxyde d'étain-indium (ITO), exigent la recherche de matériaux alternatifs efficaces et peu coûteux. Dans cette thèse des films à base de graphène ont été étudiés comme des alternatives viables. Elle met l'accent sur des couches fines de graphène (FLG), sur l'oxyde de graphène réduit (RGO) et sur leurs hybrides avec des nanotubes de carbone (NTCs) pour les applications des TCE dans les cellules solaires organiques (OSC). Les FLGs et RGOs ont été préparés par les méthodes d'exfoliation mécanique ou en phase liquide assistée par micro-ondes. Ensuite des couches minces de ces nanomatériaux carbonés ont été produites par la méthode de pulvérisation de ces matériaux dilués dans un solvant liquide à chaud. Des caractérisations de transport de charge ont été obtenues par différentes méthodes: deux pointes, quatre pointes, et par la méthode de Van der Pauw. Par ailleurs ces échantillons ont été caractérisés par des mesures de transparence UV-Visible, ainsi que par des études morphologiques et topographiques déterminant les profils de rugosité et l'épaisseur des couches minces. Par ailleurs le travail de sortie des matériaux a été déterminé par spectroscopie de photoémission ultra-violet (UPS). La nature morphologique et chimique des films déposés a été étudiée par MEB, TEM, XPS, Raman et photoluminescence. Enfin, des résultats préliminaires sur des dispositifs OSC à base de carbone sont présentés.

Mots-clé: électrodes transparentes conductrices, films de graphène multicouches, graphène par exfoliation, transport de charge, hybrides de graphène et de nanotubes de carbone, travail de sortie, transmission de la lumière.

Summary

Transparent conductors electrodes (TCE) are important components in displays, touch screens and photovoltaics. The scarcity and cost increase of the presently used, like Indium Tin oxide (ITO), demand search for efficient and economically interesting alternatives. Graphene materials have been researched as viable alternatives in this thesis. Current study focuses on few layer graphene (FLG), reduced graphene oxide (rGO) and their hybrids with carbon nanotubes (CNTs) for TCE applications in organic solar cells (OSCs). FLGs and rGO have been prepared by mechanical and microwave-assisted exfoliation methods. Thin films of these materials, alone or mixed as composite with CNTs, have been produced by hot-spray method. Results of charge transport characterizations including two probes, four-point probes, Van der Pauw methods and UV-Vis measurements, along with morphological and topographic studies with roughness and thickness profiles of the films have been presented. UPS studies were performed to determine a work-function. The morphology and chemical analyses carried out by SEM, TEM, XPS, Raman and Photoluminescence studies are provided as well. Finally, tentative results of carbon-based OSC devices are presented.

Key words: transparent conductor electrodes, few layer graphene, graphene by exfoliation, charge transport, FLG-CNTs hybrid, work function, light transmission